Solar Energy Storage:

Novel Solar-to-Fuel and Solar-to-Electric Approaches

"Use of sunlight and water to power the world"

MORENO DE RESPINIS

SOLAR ENERGY STORAGE: NOVEL SOLAR-TO-FUEL AND SOLAR-TO-ELECTRIC APPROACHES

"Use of sunlight and water to power the world"

Proefschrift

ter verkrijging van de graad van doctor

aan de Technische Universiteit Delft,

op gezag van de Rector Magnificus Prof. ir. K.Ch.A.M. Luyben;

voorzitter van het College voor Promoties,

in het openbaar te verdedigen op

vrijdag 14 oktober 2016 om 10:00 uur

door

Moreno DE RESPINIS

Master of Science in Engineering, Technical University of Denmark,

geboren te Milaan, Italië

This dissertation has been approved by the

promotor: Prof. dr. B. Dam	Delft University of Technology
promotor: Prof. dr. ir. R. van de Krol	Helmholtz-Zentrum Berlin für Materialen und Energie GmbH and Technische Universität Berlin, Germany

Composition of the doctoral committee:

Rector Magnificus	chairman
Prof. dr. B. Dam	Delft University of Technology
Prof. dr. ir. R. van de Krol	Helmholtz-Zentrum Berlin für Materialen und Energie GmbH and Technische Universität Berlin, Germany

Independent members:

Prof. dr. E.H. Brück	Delft University of Technology
Prof. dr. M.T.M. Koper	Leiden University
Prof. dr. ir. J.R. van Ommen	Delft University of Technology
Dr. W.G. Haije	Delft University of Technology
Dr. B. Seger	Technical University of Denmark, Denmark

Cover artwork by Tomaso Albertini
e: tomasoalbertini@hotmail.it; w: http://www.tomasoalbertini.com/

ISBN numer: 978-94-6332-091-7
Printed by: GVO drukkers & vormgevers B.V.

The work described in this thesis was carried out in the Materials for Energy Conversion and Storage (MECS) group, Department of Chemical Engineering, Faculty of Applied Sciences, TU Delft. This research was funded by the *BioSolar Cells consortium.*

Contents

Chapter 1
Introduction

The global energy picture

In the coming decades our society will experience a transformation of the energy sector: the shift from a fossil fuel based society to a so-called renewable based society.[1,2,3] There are three main drivers for the need of a transition in the energy sector towards sustainability: a) the depletion of easily accessible fossil fuel resources,[2,3,4,23] b) the socio-economic and geo-political consequences of (local) air pollution and climate changes,[5,6,7,8] c) the expected increase in energy demand.[9] The timeline for such an energy transition depends, among other factors,[10] on the social awareness of the costs-benefits of a transition towards sustainable energy. In this introduction additional background information is provided to the reader to illustrate the complexity of the energy problem.

Fossil fuel companies are benefitting from global subsidies of $5.3 trillion a year, equivalent to $10 million a minute every day, according to a startling new estimate by the International Monetary Fund.[11] The $5.3 trillion subsidy estimated for 2015 is greater than the total health spending of all the world's governments. Nicholas Stern, climate economist at the London School of Economics, commented: *"This very important analysis shatters the myth that fossil fuels are cheap by showing just how huge their real costs are. There is no justification for these enormous subsidies for fossil fuels, which distort markets and damage economies, particularly in poorer countries."*[12] As an example, the World Health Organisation published a report which states that air pollution caused about one in eight deaths in 2012 and had by then become the single biggest environmental health risk.[13] Ending the subsidies to fossil fuels would also slash the number of premature deaths from outdoor air pollution by 50%, about 1.6 million lives a year.[13] Another consequence would be that the need for subsidies for renewable energy, a relatively tiny $120 billion a year, would also disappear, if fossil fuel prices reflected the full cost of their impacts.[11] The comparison for the subsidies received by the renewables and by the fossil fuels is shown in **Figure 1.1**. Additionally, several studies have reported evidences for net job creation from policy support for energy efficiency and renewable energy, compared to fussil fuels.[14,15,16]

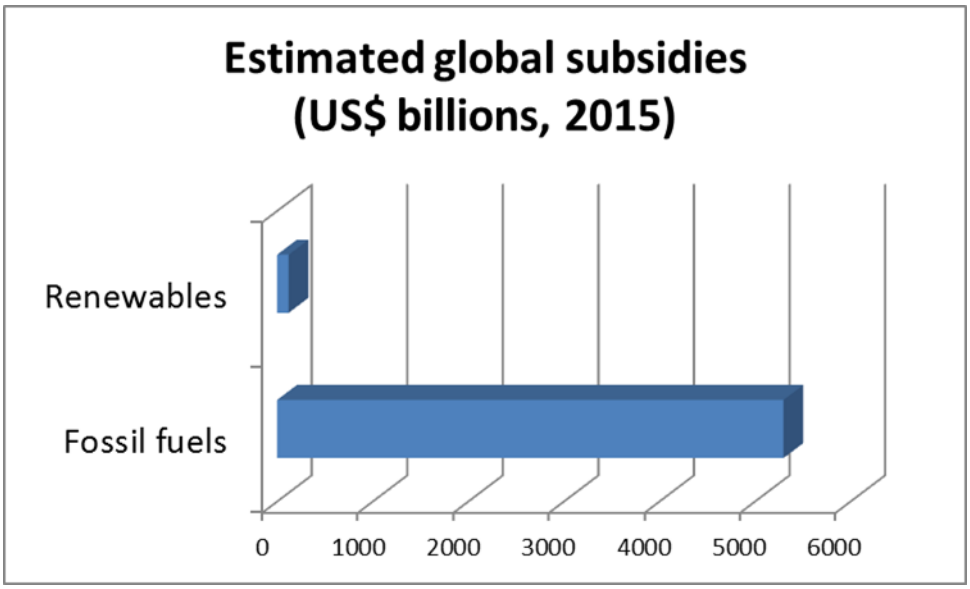

Figure 1.1. Annual global subsidies for renewables and fossil fuels. Source: IMF [11]

What has to be done, what has been done, and what is questionable, about how to get into a sustainable era

A 2008 paper by James Hansen, former director of NASA's Goddard Institute for Space Studies and expert on climate change, showed that to bring the CO_2 levels down below the safety threshold (350 ppm, or 2 °C global increase since pre-industrial level), we must not only cease emitting CO_2 as soon as possible but also actively remove the gas from the air and store the carbon in a stable form.[17,18] For instance via reforestation (photosynthesis), and by developing technologies for carbon storage (i.e. artificial photosynthesis). The recent outcome of the COP21 conference in Paris, at which world leaders (including USA and China) agreed to keep the global temperature to no more than 2 °C higher than the pre-industrial value, appears as a milestone which paves the way towards a quicker transition.[19]

Nearly the entire scientific community agrees on the man-made origin of the climate change.[20] Furthermore there is agreement on the urgency of an immediate action in order to mitigate the socio-economic impact of climate change and adapt to its consequences.[6,8,20] If this urgency is not perceived as such is partly because in the media, equal time is often given to representatives of the majority of the scientific literature as to its opponents. This is a dangerous approach, since each position will seem equally credible to the general audience.[21,22]

The approaches needed for tackling the socio-economic and geo-political impacts of resource scarcity, (local) air pollution, and climate change are the same: moving away from the

dependence on fossil-fuel resources[23] and relying on decentralized energy production based on renewables. At the forefront of this transformation of the energy and transportation sectors are countries like Denmark, whose government has ratified the *"Energy Strategy 2050"*, a plan to turn the city of Copenhagen carbon-neutral by 2025,[24] and the whole country being independent from fossil fuels by 2050.[25] Norway is pioneering in electric mobility, its fleet of plug-in electric vehicles is the largest per capita in the world, with about 24 per cent of the country's cars running on electricity.[27] Considering that 99% of the electricity generated in the country comes from hydropower,[26] Norway's fleet of electric cars is one of the cleanest in the world. Furthermore the government plans to ban new sales of fuel-powered cars by 2025.[27] In the Netherlands, Dutch people are frontrunners with respect to lightweight mobility. In fact, 31.2% of the people lists the bike as their main mode of transport for daily activities.[28] Lately, the range of travelled distance has extended by the introduction of electric bikes, whose market share has boomed up to 20% of the total new bikes sales.[29] Also the big countries are taking important steps towards renewables energies. The german government has approved and promoted the "*Energiewende*", a green energy deal to regulate a concrete energy transition.[30] The state of California in the USA is a world-class leader in solar PV installation and electric vehicles mobility.[31,32] And China is already the world's largest investor in renewable energy.[33]

Why, and how, storage of solar energy into batteries and H_2

Currently the debate about the diffusion of renewable (solar) energies is mostly centered on their intermittent character, and the technological readiness and cost of the technologies for their storage. Globally we get 10 TW/year of useful energy from 15 TW/year of primary energy from fossil fuels, biomass and nuclear power plants.[34] The difference is due to energy losses and inefficiencies in the conversion and transmission processes. The sunlight striking the surface of the continents on the Earth amounts to 23000 TW/year and it is the primary source of energy for the whole terrestrial ecosystem.[35] Or in other words, *the energy that is provided by the sun in one hour is equal to the world's annual energy consumption*. It is therefore meaningful to look at the sun as a source to satisfy the mankind's energy needs. As sunlight presents daily and seasonal variability, energy from the sun needs not only to be harvested, it needs to be stored, and (eventually) transported to the final users. Whether this can be done in a cheap way on the TW scale is the great challenge. The simplest way to store solar energy is to use batteries or to store it in the form of chemical bonds. The electrical storage in batteries can serve as short term storage, as well as a medium for short distance transportation. Chemical storage in the form of e.g. H_2 will be of paramount

importance for seasonal storage and as a fuel for transportation (also for ammonia synthesis or synthesis of higher hydrocarbons).[36] At present the storage of solar energy into batteries or into hydrogen through electrolysis, is generally not cost competitive.[37,39] Thus it is of paramount importance to extend the efficiency, self-discharge time, capacity, and operational activity of storage devices, alongside with reducing their cost.

The simplest of the options (in principle) for solar-to-fuel conversion consists of water splitting for hydrogen production, possibly followed by the reaction of hydrogen with CO_2 to make syngas and thereby chemical fuels.[38] A handful of pathways is available for the conversion of sunlight and water into hydrogen. Those can be classified into three groups according to their interfaces (see **Figure 1.2**):[40] a) the direct PEC approach where a semiconductor/liquid junction is formed; b) the buried PEC approach which is a monolithic device where the semiconductor light absorbers are separated from the electrolyte by one or more interfacial layers; c)-d) the modular PV-electrolysis approach where the light absorption and charge separation occurs in a device which powers the electrochemical reactions occurring in a second device. Solar H_2 production is achieved via the latter approach for \$8/Kg H_2 (as of 2011).[39] This can be considered as the benchmark. Direct photoelectrolysis of water in a single device, via approaches a) and b), can in principle be more desirable due to the high fabrication and system costs arising from the use of a three component system PV - electrolyzer – converter (d). Two obvious drawbacks, however, are that a device for direct photoelectrolysis cannot generate electricity, nor serve as daily electricity storage. A potential solution would be to couple the PV module directly to an electrolyzer, without the need for a converter (c). The last chapter of this thesis explores a similar pathway, where a further integration of battery and electrolyzer functionalities enables a highly efficient direct coupling with the PV. For the re-conversion of hydrogen to electricity a fuel cell is needed. Several design targets have been published in the past few years with changing boundary conditions. At this early technological readiness level of the PEC solar-to-hydrogen technology, however, nobody knows what the necessary targets are. As a general guideline, we report the design targets described in 2011 by *Keable and Holcroft*:

- 10% solar-to-hydrogen (STH) efficiency (alias 8 mA/cm^2 at both the anode and cathode)
- 15 years lifetime
- Capital cost of \$160/m^2

With this considered, PEC hydrogen production must cost less than \$3/Kg.[39]

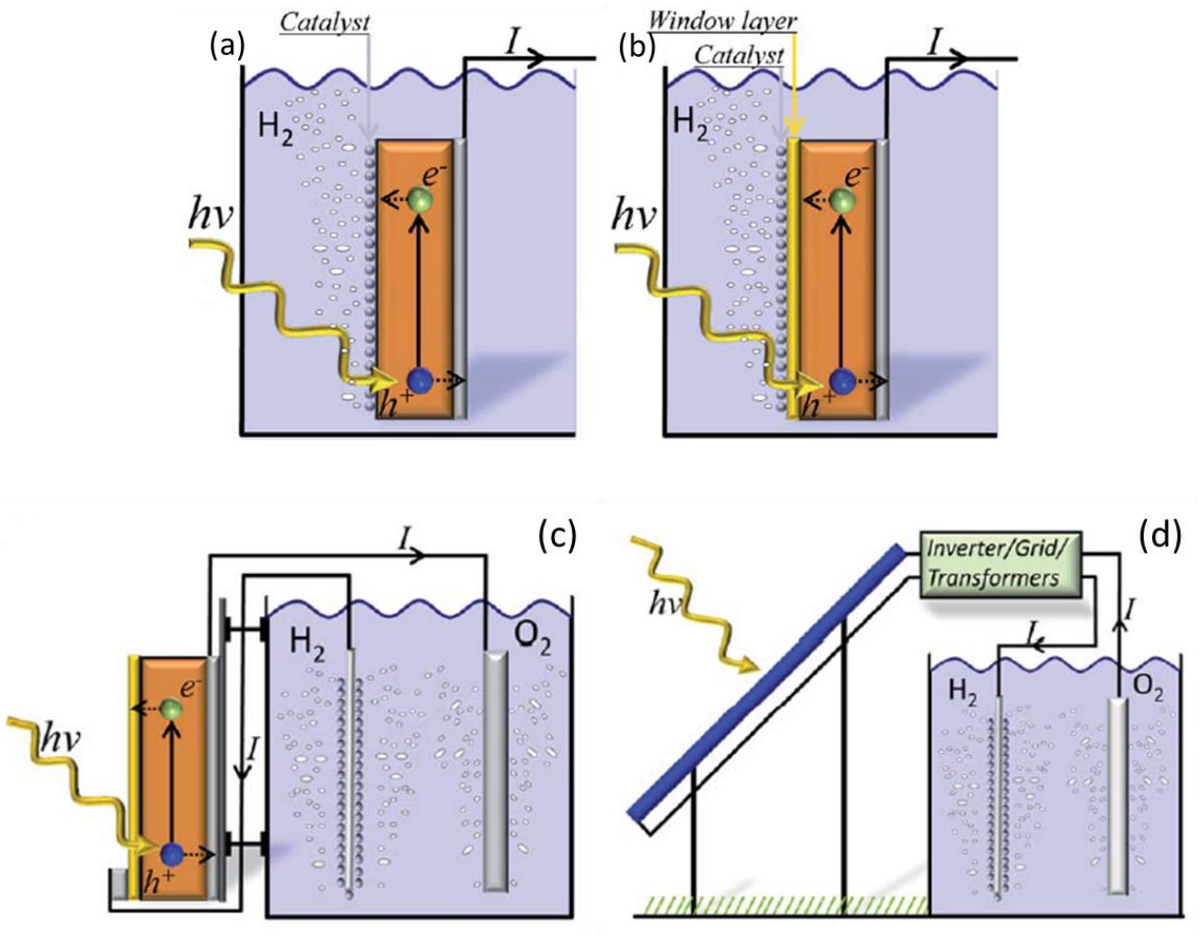

Figure 1.2. Schematic representation of solar water electrolysis approaches. (a) Direct PEC where a semiconductor/electrolyte junction is formed; (b) the buried PEC approach which is a monolithic device where the semiconductor light absorbers are separated from the electrolyte by one or more interfacial layers; (c-d) the modular PV-electrolysis approach where the light absorption and charge separation occurs in a device which powers the electrochemical reactions occurring in a second device. Source: Jacobsson et al., 2014 [40]

PEC approach to solar water splitting: possibilities and limitations

This PhD research focused in part on photoelectrochemical water splitting based on metal-oxide or (oxy)nitride semiconductor photoelectrodes. The key characteristic of PEC water splitting is that it takes advantage of the intrinsic electric field generated at the semiconductor-electrolyte interface to act as charge separator (see ***Figure 1.3***). Several further advantages are related to this approach. The water reduction and oxidation reactions

occur at two separate electrodes (or two sides of one electrode), making it relatively easy to keep the hydrogen and oxygen separated. Serious safety concerns are thus avoided. Moreover, the entire process can be carried out at room temperature and, in principle, with seawater. In addition, photoelectrochemical water splitting can be made in a monolithic device, avoiding extra costs and efficiency losses related to multi-device approaches such as the conventional photovoltaic + electrolysis systems. Finally, as the main components are inorganic metal oxides or oxynitrides, cost-effectiveness and non-toxicity are achieved.

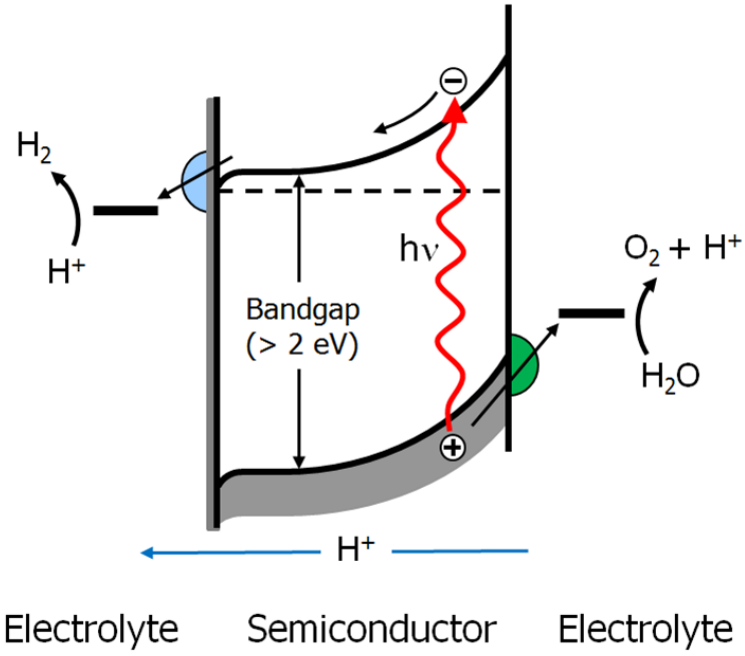

Figure 1.3. *Simplified energy diagram of a photoelectrochemical (PEC) cell based on a single photoelectrode. The processes of light absorption, charge separation, charge transport and charge transfer at interfaces for the catalytic water splitting are shown.*

Figure 1.3 shows a simplified energy diagram of a photoelectrochemical (PEC) cell based on a single photoelectrode. The main component of the PEC cell is the semiconductor, which converts incident photons to electron-hole pairs. These electrons and holes are spatially separated from each other due to the presence of an electric field inside the semiconductor, which originates from the transfer of the majority charge carriers from the semiconductor to the electrolyte. The photo-generated electrons are swept towards the conducting back-contact, and are eventually transported to the metal counter-electrode via an external wire. At the metal, the electrons reduce water to form hydrogen gas. The photogenerated holes are swept towards the semiconductor/electrolyte interface, where they oxidize water to form oxygen gas.

In the overall process of solar water splitting, most of the critical processes occur at the photoelectrode. Those are light absorption, charge separation, charge transport and charge transfer at interfaces.[41,42] For a long lifetime, the semiconductor must be stable in aqueous environment. Finally, Earth-abundant materials and low cost fabrication are required. Stringent requirements are therefore imposed on the ideal photoelectrode. None of the semiconductor materials explored so far gets even close to meeting all the above demands. Major trade-offs need to be made in order to develop composite photoelectrodes in which each functionality is fulfilled by a particular material. Two directions have been pursued in this thesis to overcome these challenges: developing strategies to improve the limiting factors in existing materials for PEC water splitting, along with the development of an alternative approach to the conversion and storage of solar energy.

Aim of this thesis

The aim of this thesis is to investigate materials and devices for the conversion and storage of solar energy. This will be pursued by two approaches: a) the direct conversion of solar energy into hydrogen and oxygen in a photoelectrochemical (PEC) cell and b) a modular device composed of a PV cell and a battery/electrolyzer cell for combined solar electricity production with electrical and chemical storage, depending on the incoming potential provided by the solar cell. In the PEC approach, the focus will be on the oxygen evolving electrode, where the energetically more difficult reaction of the water splitting is performed. Electrocatalysts will be investigated as electrodes, and in combination with a light absorbing semiconductor as photoelectrodes. The class of semiconductors of choice is metal oxides because of the non-toxicity, inexpensiveness and stability towards oxidation. As drawbacks they have poor visible light absorption and low charge carrier mobility. The aim is to develop strategies to mitigate these drawbacks. Two directions have been pursued in this thesis to overcome these challenges: investigating methods to improve the limiting factors in existing materials for PEC water splitting, along with the development of an alternative approach to the conversion and storage of solar energy. Our PEC investigation reveals that 1) in the materials considered, the drawbacks can be mitigated via optimized semiconductors-catalyst junctions (Chapter 2.2), via nanostructuring (Chapter 3), and via bandgap engineering (Chapter 4.1) 2) the conductor-semiconductor and semiconductor-catalyst-electrolyte interface is a key factor limiting the performance and lifetime of the device and 3) the ideal semiconductors/catalysts combinations are yet to be found. The extra requirement of a high control over the interfaces is a problem which is circumvented in the modular device where the solid-state processes (i.e., light absorption and charge separation) are separated from

the electrocatalytic processes of electrical/chemical storage. Compared to a pure photo-electrochemical approach, this approach has the further advantage of improved compatibility with the daily and seasonal variations of light intensity. It does so by having the electrical storage proceed at potentials where the chemical storage is not possible. Moreover, since the electrochemical cell is directly connected to the solar cell, the additional balance-of-system costs compared to the PEC approach are limited. In this prototype device, Earth-abundant materials such as Si (solar cell), Mg, Ti and Ni (electrochemical cell) constitute the main components. Moreover, the fabrication of Si solar cells is a well-developed industrial process and electrodes in the electrochemical cell are deposited with cheap and scalable techniques such as Physical Vapor Deposition (PVD) and electrodeposition. As drawbacks, 1) triple or quadruple junction solar cells are needed to provide the required potential for the electrochemical reactions, 2) the capacity of the chosen Ni electrode is limited, and 3) Pd, a rare-Earth element, is used as a catalyst for the Mg-based electrode. Lastly, the cyclic stability has not been tested.

Outline of this thesis

With low cost and generally good chemical stability against photocorrosion as main advantages, absorbers based on metal oxides often suffer from modest light absorption, poor charge transport and slow surface reaction kinetics. The purpose of this research project is to tackle these challenges by introducing heterogeneous catalysts, by morphology control via nano-structuring, by band-gap engineering, and interfacial protection layers. The focus of the following 3 chapters (Chapter 2-4) will be on the investigation of the various interfaces on several electrodes for the water oxidation reaction. In the last chapter, Chapter 5, an approach alternative to the direct PEC water splitting will be proposed.

In **Chapter 2.1** the basic concepts for electrochemical water splitting will be provided in order to understand the catalyst-electrolyte interface and the origin of the overpotential for the water oxidation reaction. Experiments on first-row transition metal oxide catalysts will be used to show the effect of different electrolyte anions, pH, and concentration. Finally, possible strategies to reduce this overpotential are proposed. In **Chapter 2.2** the energetics at the semiconductor-electrolyte and semiconductor-catalyst-electrolyte interfaces are analyzed using $BiVO_4$ as a model metal oxide semiconductor. Charge recombination determines the overpotential required to oxidize water. As a way to alter the surface recombination a Ru-based molecular catalyst is compared to a porous Co double hydroxide

catalyst and RuO_2 nanoparticles in a phosphate buffer. The difference between efficiency in electrocatalysis and in co-catalysis will be shown together with the advantages of coupling molecular catalysts to semiconductors. The specific challenges for surface-attached molecular catalysts will be discussed. We will show that the main point of improvement to be addressed remains the stability of the molecular assembly (and semiconductor) under continuous operation.

Solar absorbers based on metal oxides suffer from a modest optical absorption coefficient and poor (minority carrier) charge transport properties. This generates a mismatch between the thickness required for the light absorption and the distance photogenerated carriers can travel. This mismatch can be tackled by nanostructuring. One of the main challenges in developing highly efficient nanostructured photoelectrodes is to achieve good control over the desired morphology and good electrical conductivity. In **Chapter 3** an efficient plasma-processing technique to form porous structures in tungsten substrates is presented. The interface between the bulk substrate and the porous surface is very sensitive to the anneal conditions. While the substrate needs to remain metallic to preserve its conductive properties, the porous surface should be fully oxidized into WO_3 to get good semiconducting characteristics. We developed a two-step anneal procedure to transform mesoporous tungsten into photoactive monoclinic WO_3, leaving the substrate in its original metallic state. We will show that the excellent control over the feature size and good contact between the crystallites with the plasma technique offers an exciting new synthesis route to nanostructure materials for e.g. solar water splitting. Also, we identify as limitations the energy intensiveness of the process and the high temperature reached by the substrate during the plasma etching.

The poor carrier conductivity and large bandgap typical of metal oxide semiconductors can be tackled also via materials engineering. To reduce the bandgap, we have explored the possibility to incorporate nitrogen into the metal oxide lattice, leading to nitrogen-doped oxide, oxynitride or nitride phases. Among the various nitride and oxynitride compounds considered, tantalum nitride (Ta_3N_5) and tantalum oxynitride (β-TaON) are particularly attractive because of their relatively small bandgaps (2.1 eV and 2.4 eV, respectively) and the high energetic position of Ta 5d orbitals, which form the conduction band in these materials. However, the recipes to synthesize the desired Ta-O-N phases used by various groups are difficult to reproduce. In **Chapter 4.1** an in-situ UV-vis monitoring technique called 'oxynitrogenography' is proposed as an approach towards the controlled and reproducible synthesis of thin films of different Ta-O-N phases, including the elusive β-TaON

phase. We identify the thermodynamic equilibrium conditions to obtain these various phases, and a phase diagram is constructed. Finally, a correlation is found between the carrier mobility and lifetime in tantalum (oxy)nitride thin films as a function of the nitrogen content in the material. As drawbacks, β-TaON and Ta_3N_5 show a semiconductor-liquid interface of poor quality. Furthermore, their intrinsic instability in water under illumination is a major hurdle for their use in photoelectrochemical water splitting. In **Chapter 4.2** multilayered, multifunctional coatings are investigated to mitigate the drawbacks and exploit a significant fraction of the potential of β-TaON and Ta_3N_5. Interestingly, while the surface layers improve the performance of Ta_3N_5, they are marginally affecting β-TaON. These results point towards the importance of the β-TaON–Pt interface in the growth of high quality β-TaON.

The results presented in chapters 2-4 show that drawback in the materials considered, e.g. the modest light absorption, poor charge transport and catalytic properties, can be singularly addressed. However, the ultimate photoanode that meets all the requirements, after the current efforts, is yet to be reached. The presence of other unresolved issues points towards the complexity of the direct PEC approach compared to approaches with separate functionalities. The PEC approach tackles issues from the engineering standpoint (reduce the number of devices and the balance-of-system), but poses new stringent requirements on the materials employed. The quest for multifunctional materials to efficiently convert sunlight to charges and run the electrochemical reactions at high rate and stability seems of difficult solution. The analysis performed in chapters 2-4 suggests that a higher control over the interfaces among the materials is needed. These observations set the basis for the proposal and investigation of an alternative strategy for the conversion of solar energy. In **Chapter 5** a new approach is proposed: a modular device inspired by the PV-electrolysis approach where solid state physics processes of light absorption, charge separation and charge transport are separated from the electrocatalytic process. The novelty consists in integrating the electrical and chemical storage into one cell, thereby providing battery and electrolyzer functionalities depending on the incoming potential from the PV cell. The advantages and points of improvement are illustrated.

REFERENCES CHAPTER 1

1. Zittel, W.; Zerhusen, J.; Zerta, M.; Ludwig-Bölkow; Arnold, N. Fossil and Nuclear Fuels – the Supply Outlook, Energy Watch Group / Ludwig-Boelkow-Foundation /Reiner-Lemoine-Foundation, **2013**
2. David Hughes, J. *Nature* **2013**, 494, 307.
3. David Hughes, J. Drill, Baby, Drill: Can Unconventional Fuels Usher in a New Era of Energy Abundance?, **2013**, Post Carbon Institute.
4. David Hughes, J. Drilling deeper: a reality check on U.S. government forecasts for a lasting tight oil & shale gas boom, **2014**, Post Carbon Institute.
5. Randers, J. 2052: A Global Forecast for the Next Forty Years, the Club of Rome, **2012**.
6. http://carbontracker.live.kiln.it/Unburnable-Carbon-2-Web-Version.pdf
7. Whiteman, G.; Hope, C.; Wadhams, P. *Nature* **2013**, 499, 401.
8. Hagel, Climate Change Adaptation Roadmap, **2014**, Department of Defense of the USA
9. International Energy Outlook **2013** DOE/EIA-0484(2013)
10. O'Brien, K. Political agency: The key to tackling climate change *Science* **2015**, 350, 1170
11. http://www.imf.org/external/pubs/ft/wp/2015/wp15105.pdf
12. http://www.theguardian.com/environment/2015/may/18/fossil-fuel-companies-getting-10m-a-minute-in-subsidies-says-imf
13. http://www.who.int/mediacentre/news/releases/2014/air-pollution/en/
14. Will, B.; Gross, R.; Speirs, J.; Sorrell, S.; Nicholls, J.; Dorgan, A.; Hughes, N. Low carbon jobs: The evidence for net job creation from policy support for energy efficiency and renewable energy, **2014**, UK Energy Research Centre (UKERC)
15. Wei, M.; Patadia, S.; Kammen, D. M. Putting renewables and energy efficiency to work: How many jobs can the clean energy industry generate in the US? *Energy Policy*, 38, 2, **2010**, 919–931
16. Kammen, D. M.; Kapadia, K.; Fripp, M. Putting Renewables to Work: How Many Jobs Can the Clean Energy Industry Generate? *RAEL Report*, **2004**
17. www.columbia.edu/~jeh1/2008/TargetCO2_20080407.pdf
18. http://spectrum.ieee.org/energy/renewables/what-it-would-really-take-to-reverse-climate-change
19. http://www.theguardian.com/environment/2015/dec/13/paris-climate-deal-cop-diplomacy-developing-united-nations
20. Pachauri, R.K.; Meyer, L.A. Climate Change 2014: Synthesis Report. Contribution of Working Groups I, II and III to the Fifth Assessment Report of the Intergovernmental Panel on Climate Change, IPCC, **2014**
21. Boykoff, M.T.; Boykoff, J.M. Balance as bias: Global warming and the US prestige press, *Global Environmental Change* **2004**, 14, 125–136.
22. Schneider, S. Mediarology: The role of citizens, journalists, and scientists in debunking climate change myths, **2011**
23. Oil's tipping point has passed, *Nature* **2012**, 481, 434
24. http://denmark.dk/en/green-living/copenhagen/
25. http://denmark.dk/en/green-living/strategies-and-policies/independent-from-fossil-fuels-by-2050
26. Facts about hydropower, Norsk Hydro ASA, **2016**
27. http://www.independent.co.uk/environment/climate-change/norway-to-ban-the-sale-of-all-fossil-fuel-based-cars-by-2025-and-replace-with-electric-vehicles-a7065616.html
28. Why is cycling so popular in the Netherlands? *BBC News*, **2013**
29. Oortwijn, J. Huge Growth in Dutch E-Bike Sales in 2015, *Bike Europe*, **2016**.
30. Morris, C.; Pehnt, M. Energy Transition: The German Energiewende, Heinrich Böll Foundation, **2012**
31. Solar Energy Industries Association, **2016**, www.seia.org
32. Cobb, J. Americans Buy Their Half-Millionth Plug-in Car, *Hybrid Cars*, **2016**
33. Global Trends in Renewable Energy Investment, Frankfurt School-UNEP Centre/BNEF, **2016**
34. 2014 Key World Energy Statistics, *IEA*, **2014**, 6-38
35. Gust, D.; Moore, T. A.; Moore, A. L. *Acc. Chem. Res.*, **2009**, 42, 1890–1898
36. Mulder, F. M. Implications of diurnal and seasonal variations in renewable energy generation for large scale energy storage *J. Renewable Sustainable Energy* **2014**, 6, 033105
37. Genoese F. Low-cost batteries will not disrupt (all) energy utilities, *CEPS commentary,* **2015**

38. Haije, W.; Geerlings, H. Efficient production of solar fuel using existing large scale production technologies, *Environ. Sci. Technol.* **2011**, 45, 8609.
39. Van de Krol R. et al., Photoelectro-chemical hydrogen production, *Springer*, **2012**
40. Jacobsson, T. J.; Fjällström, V.; Edoff, M.; and Edvinsson, T. Sustainable solar hydrogen production: from photoelectrochemical cells to PV-electrolyzers and back again *Energy Environ. Sci.*, **2014**, 7, 2056.
41. Van de Krol, R.; Liang, Y.; Schoonman, J. *J. Mater. Chem.* **2008**,18, 2311-2320
42. Walter, M. G.; Warren E. L.; Boettcher S. W.; Mi, Q.; McKone, J. R.; Santori, E. A.; Lewis, N. S.; Solar Water Splitting Cells, *Chem. Rev.* **2010**, 110, 6446-6473

Chapter 2 Water oxidation at the catalyst-electrolyte and semiconductor-catalyst-electrolyte interfaces

2.1 Water oxidation at the catalyst-electrolyte interface

Introduction

The conversion of renewable (solar) energy into fuels such as hydrogen, alcohols, hydrocarbons, etc. is highly desirable as a mean of energy storage. The water splitting process plays a pivotal role in the renewable production of fuels. In all approaches, water is oxidized to oxygen releasing protons and electrons for the fuel production reactions.[39] However the efficiency of the water oxidation reaction is low, limited by its slow kinetics. In this section we will discuss the thermodynamic reasons for the low efficiency in the electrocatalytic water oxidation. The reader will be briefly guided through a basic understanding of the free energy diagram and the Sabatier principle. Then the concept of scaling relations will be introduced. Our experimental results will illustrate the effect of different metal catalytic sites, electrolyte anions, pH, and concentration. We chose electrocatalysts based on transition metal oxides as test materials because of the broad literature available and their typical stability towards oxidation conditions. Finally, possible routes to allow for water splitting with low overpotential will be presented.

Theory on electrochemical water splitting, Sabatier principle, scaling relations

The overall electrochemical water splitting reaction proceeds according to:[41,42]

$$2H_2O(l) \leftrightarrow 2H_2(g) + O_2(g) \qquad (2.0)$$

The overall reaction is divided into two half-cell redox reactions. The reduction process at the cathode (hydrogen evolution reaction, HER) and the oxidation process at the anode (oxygen evolution reaction, OER).

For an alkaline electrolyte,

$$4H_2O + 4e^- \leftrightarrow 2H_2 + 4OH^- \qquad E_{red} = +0.828 \text{ V vs. NHE} \qquad (2.1)$$

$$4OH^- + 4h^+ \leftrightarrow 2H_2O + O_2 \qquad E_{ox} = -0.401 \text{ V vs. NHE} \qquad (2.2)$$

For an acidic environment, from Eqs. (2.1) and (2.2) subtract or add the dissociation reaction of water into protons and hydroxyl ions:

$4H^+ + 4e^- \leftrightarrow 2H_2$ $E_{red} = +0.000$ V vs. NHE (2.3)

$2H_2O + 4h^+ \leftrightarrow 4H^+ + O_2$ $E_{ox} = -1.229$ V vs. NHE (2.4)

Here, E_{red} and E_{ox} are the electrochemical potentials of the reactions at standard temperature (298 K) and concentrations (1 mol/L, 1 bar); NHE stands for normal hydrogen electrode. The corresponding change in Gibbs free energy becomes $\Delta G = -nF \cdot \Delta E$. Where n is the number of electrons involved in the reaction; F the Faraday constant; ΔE the electrochemical cell voltage. A ΔE of -1.229 V according to reactions (2.1)–(2.4) corresponds to a Gibbs free energy change of ΔG=+237 kJ/mol H_2. Therefore the water splitting reaction is thermodynamically uphill and non-spontaneous. When operating at this cell voltage the reactions are endothermic, thus heat energy must be absorbed from the surrounding environment for the increase in entropy associated with the water splitting which converts two liquid molecules into three gas molecules. For the reaction to proceed at isothermal conditions, a higher amount of energy equal to the enthalpy $\Delta H = \Delta G + T\Delta S$ (=+286 kJ/mol at standard conditions) must be supplied. The voltage corresponding to this condition is called the thermoneutral voltage and is given by $V_{tn} = \Delta H/nF = 1.48$ V. In practical devices energy losses, associated with reaction kinetics as well as charge transport through electrical leads and the electrolyte, necessitate electrolyzer operation at voltages that are even above 1.48 V. The additional voltage required to overcome the losses in the cell and obtain the desired output in terms of current density or production rate of hydrogen from the cell represents the overvoltage of the cell.[43] In PEC approaches to water splitting the thermodynamic potential $\Delta V_{td} = 1.23$ V is normally used for efficiency calculations, because the required thermal energy is provided by the direct solar illumination. In electrochemical approaches the thermoneutral potential $V_{tn} = 1.48$ V is generally used as reference, since the extra heat has to be provided by the voltage source. In commercial electrolyzers however, the high current density of operation requires potentials in the order of 1.9 V, and the energy losses provide the required thermal energy.

The electrocatalytic activity is to a large extent determined by the binding strength of the reaction intermediates to the electrode surface. The intermediate should not bind too weakly nor too strongly to the surface; thus, there is an optimum binding energy for which the activity of multi-step catalytic reactions is at a maximum. This is called the "Sabatier principle". Plotting the activity as a function of binding energy can give a so-called volcano

plot. With this considered, we can introduce the proposed reaction mechanism for water oxidation. It consists of four consecutive proton and electron transfer steps and a schematic reaction mechanism is shown in **Figure 2.1**.

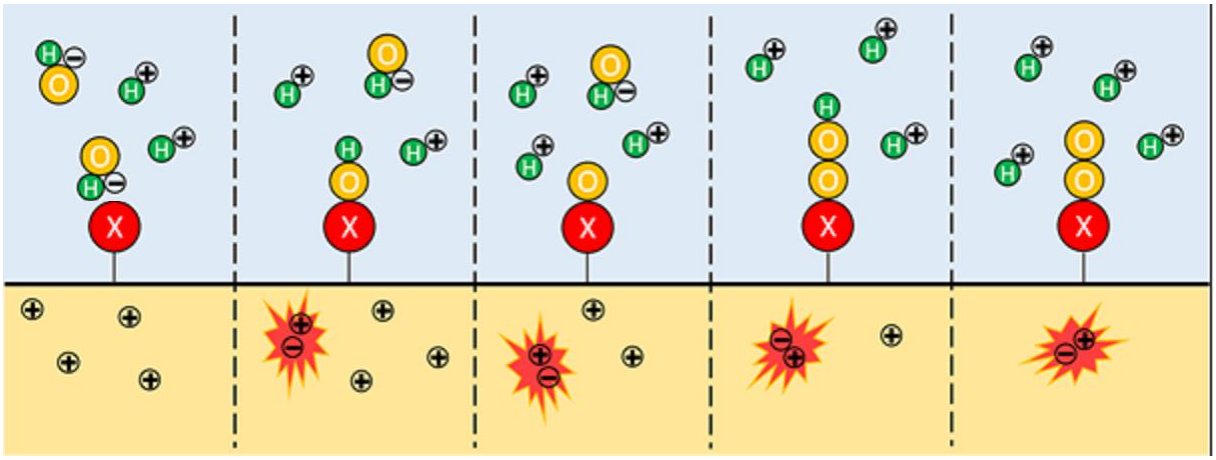

Figure 2.1. *Schematic illustrating the reaction intermediates for electrocatalytic water splitting by catalyst X. The bond strength between the atom X and the first O atom depends on the atom X. The catalytic activity follows the bond strength according to the Sabatier principle. During the oxidative reaction four holes from the substrate recombines with four electrons from the adsorbed species.*

For the water oxidation reaction in acidic and neutral media, the following reaction paths are usually considered:

$$* + H_2O(l) \leftrightarrow *OH + H^+ + e^- \quad (2.5)$$

$$*OH \leftrightarrow *O + H^+ + e^- \quad (2.6)$$

$$*O + H_2O(l) \leftrightarrow *OOH + H^+ + e^- \quad (2.7)$$

$$*OOH \leftrightarrow * + O_2(g) + H^+ + e^- \quad (2.8)$$

In alkaline media the surface of metal oxide catalysts is readily covered with hydroxyl species. Therefore reaction (2.5) is replaced by reaction (2.9). For the same reason, the surface *O species formed in reaction (2.6) can be attacked by a second hydroxyl anion according to reaction (2.10).[44,45,46]

$$* + OH^- (l) \leftrightarrow *OH + e^- \quad (2.9)$$

$$*OH \leftrightarrow *O + H^+ + e^- \quad (2.6)$$

$$*O + OH^- (l) \leftrightarrow *OOH + e^- \quad (2.10)$$

$$*OOH \leftrightarrow * + O_2(g) + H^+ + e^- \quad (2.8)$$

Where * is a catalytic site on the surface of the catalyst.

To evaluate the thermodynamics of these reactions, free energy diagrams can be constructed. An example of this is given in **Figure 2.2**. Four individual one-electron reaction steps are needed for water oxidation, so the total energy change is 4 x 1.23 eV = 4.92 eV. If each of the four individual steps would require exactly the same energy (1.23 eV), the reaction would occur at zero overpotential. Let's now look at the formation of the HO* and HOO* intermediates, which represent two of these steps (Figure 2.2). Since two proton and electron transfer steps separate the two intermediates, their energy levels should be separated by 2 x 1.23 eV = 2.46 eV. However, as outlined in a recent review by M. Koper[48], the binding strengths of HO* and HOO* differ from each other by $\Delta E_{HOO*} - \Delta E_{HO*} = 2.98$ eV. The difference in the energetics of these two steps between actual OER catalysts and an ideal one, (2.98–2.46 eV)/2e, gives a minimum thermodynamic overpotential of 0.26 V.

To reduce this overpotential to zero, one would need to change the difference in binding energies of the HO* and HOO* species. Unfortunately, quantum chemical modelling (density functional theory, DFT) from DTU and the Nørskov group[47], but also using thermodynamics approach as proposed by Koper's group[48], revealed that the difference in binding energies is constant. More generally, it was shown that scaling relationships can be established between the binding energies of HO*, HOO*, and O* species on oxide surfaces, which makes it impossible to change any one these binding energies independently.

The scaling relations suggest that there is only one free parameter, e.g. the O* binding energy, that determines the free energy diagram and thereby the activity. This conveniently allows us to plot the activity for the OER reaction as a function this single parameter, which then acts as a 'descriptor' for the catalytic activity. The result is a volcano-shaped relationship between catalytic activity and the calculated oxygen adsorption energy. Such a plot graphically shows that the activity for surfaces that strongly bind O* is limited by the formation of HOO* species, whereas for surfaces that bind oxygen too weakly, the activity is limited by the oxidation of HO*. Moreover, it shows that the top of the vulcano curve is off-set from the thermodynamic OER potential (1.23 V) by the minimum thermodynamic overpotential of 0.26 V.

It should be noted that the theoretical overpotential is independent of the pH or the potential values, because the free energies obtained by using Reactions (2.5)–(2.8) vary in the same way with pH and potential. Thus, the potential determining step remains the same.

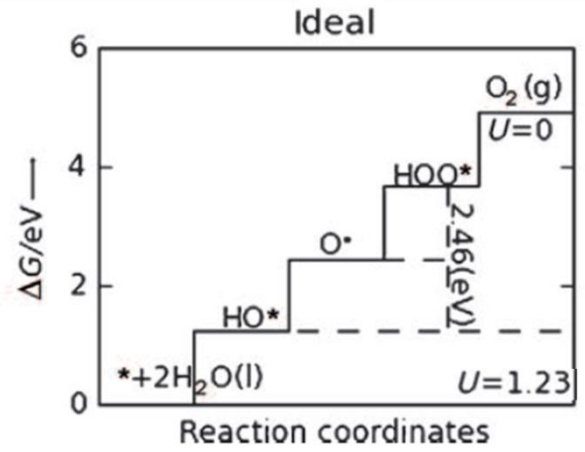

Figure 2.2. *Standard free energy diagram for the oxygen evolution reaction at zero overpotential, where all steps proceed at the equilibrium potential for oxygen evolution (U=1.23), at pH 0 and T=298 K over the ideal catalyst. The* $\Delta G_{HOO*}-\Delta G_{HO*}$ *(vertical dashed line) for the ideal catalyst is equal to 2.46 eV. Modified from ref. [47].*

From the point of view of the surface, HO* and HOO* look very similar. To avoid the limitations defined by the universal scaling relation, the challenge is to find a way to modify oxide surfaces or the electrochemical interface, such that the relative stability of HOO* and HO* changes. It is possible that 3-dimensional structures, such as rough surface structures, layered structures, zeolites or co-adsorbates on the surface could achieve this relative stabilization of HOO*. Effects such as these are likely present in enzymes that catalyze water oxidation very effectively in nature.

One must be careful in distinguishing between this thermodynamic analysis and an analysis based on rate-determining steps, which is based on the knowledge of the activation barriers and the rate laws of the different steps. The kinetics of water oxidation quantify how much a change in the free energy difference driving the first hole transfer reduces the activation barrier. In photochemical or electrochemical studies, the dependence of steady-state product evolution on the free energy difference driving the hole transfer is used to extract activation barriers. In the literature, it is common to extrapolate the kinetic rate due to the activation barrier when that free energy difference is zero, i.e., at the Nernstian potential.[49,50,51]

Results and discussion

Before presenting the polarization curves for different catalysts, we introduce the current response to an applied voltage (JV) curve itself. In Figure 2.3 we give a schematic representation of the JV characteristics of different catalysts. In the absence of other reactions than water splitting, no anodic (positive) current can be evolved at potentials below the reversible potential for water oxidation, 1.23 V vs. RHE. An ideal catalyst that does not present thermodynamic losses will have an onset potential at 1.23 V vs. RHE and the current density would increase exponentially (a). Such a catalyst is operating endothermically. A catalyst which onsets at the thermoneutral potential is shown as curve (b). A catalyst that obeys the scaling relations will have a thermodynamic overvoltage of ~0.26 V (c). Curve (d) shows a catalyst with a higher onset potential whose current density increases linearly. A linear behaviour in the JV characteristic of an electrocatalyst is related to resistive losses, which can be caused by e.g. electrical contacts, mass transport limitations (e.g. in the electrolyte). Curve (e) shows an electrocatalyst with higher onset potential and lower response to the increasing applied bias. The latter is a consequence of lower catalytic activity.

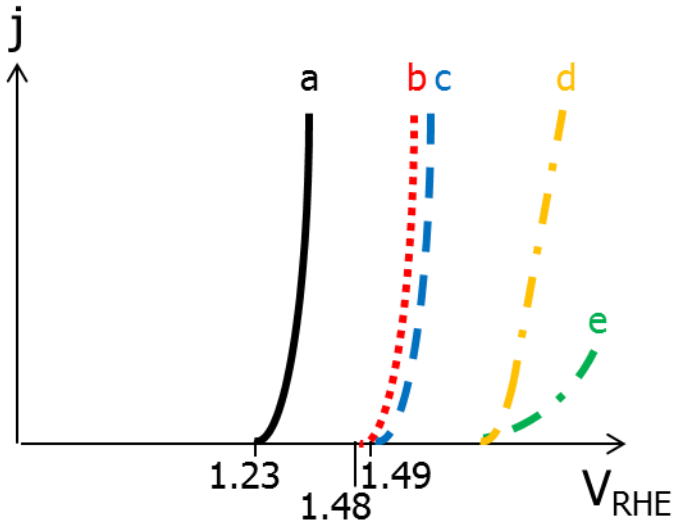

Figure 2.3. *Schematic illustrating the current-voltage response of (a) an ideal catalyst operating at the thermodynamic potential for water oxidation; (b) a catalyst operating at the thermoneutral potential; (c) a catalyst operating at the lowest potential given by the scaling relations (0.26 V overvoltage); (d) a JV curve showing linear slope due to resistive losses; (e) a JV curve of a poor catalyst, showing high onset potential and low response of J to the applied V.*

It is important to mention that one must be careful when comparing results from polarization curves. In particular the scan rate must be the same for all measurements. **Figure 2.2** shows an example of a catalyst that undergoes a redox change before the water oxidation reaction is enabled. This appears as redox peaks around 1.4 V vs. RHE due to the Ni^{2+}/Ni^{3+} transition. This transition happens prior to the onset of water oxidation. When this occurs, its JV characteristics are affected by the scan rate. The rate dependency occurs when the charge transfer is associated with slow processes, occurring in a time scale comparable to the scan rate. These slow processes could originate from the structural response of the catalyst upon application of an electric field and/or charge accumulation, possibly involving ion rotations, displacement, and lattice distortion.[75]

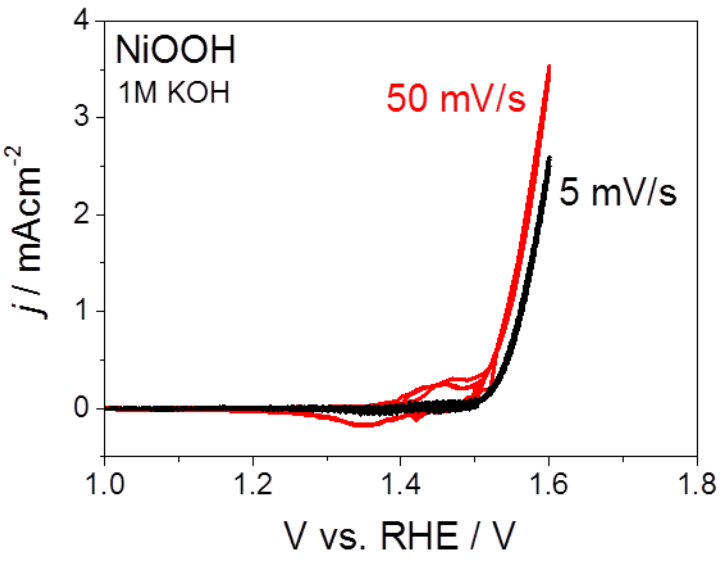

Figure 2.2. *Effect of scan rate. NiOOH undergoes a redox change from a rest state into an active state before the water oxidation reaction is enabled. Its JV characteristic is affected by the scan rate.*

Another challenge is to properly account for the influence of the specific surface area, which is often not precisely known. While important when quantitatively comparing different electrocatalysts, it usually cannot be determined accurately. Thus it will be considered only qualitatively in the rest of this chapter.

According to theory explained above, the electrocatalytic activity is to a large extent determined by the binding strength of the reaction intermediates to the electrode surface. This can be verified by comparing the effect of catalysts with different metal sites which lead to different binding energies of the water oxidation intermediates, under otherwise identical experimental conditions. Therefore, we tested the electrocatalytic activity for water oxidation

of metal double hydroxide/oxyhydroxide catalysts in 1 M KOH (pH=13.6), where the metal center is either Ni, Fe or Co as shown in **Figure 2.3** and **2.4**. Note that these I-V curves are not corrected for resistive losses (i-R drops). The cyclic voltammogram shows that NiOOH has the lowest onset potential (V_{on} = ~1.55 V vs. RHE at 1 $mAcm^{-2}$), while for CoOOH and FeOOH a negligible current is flowing through the electrode up to an applied potential of ~1.6 V vs. RHE. The potential for the reversible water oxidation reaction is at 1.23 V vs. RHE, which implies an overpotential of ~0.3 V for NiOOH and ~0.4 V at 1 $mAcm^{-2}$ for CoOOH and FeOOH. As explained in the theory section in this chapter, the lowest thermodynamic overpotential one can expect from oxide-based catalysts is 0.26 V, according to the scaling relations. This suggests that the NiOOH catalyst is close to ideal. Our results agree with literature reports, where the same trend in overpotential was observed and explained as the Ni binding site provides a more optimal binding energy to the water oxidation intermediates compared to Co and Fe.[52] In this literature example, the relationship between overpotential and binding strength of the reaction intermediates correlates well with the experimental data, despite the fact it does not take into account the kinetics of the reaction.

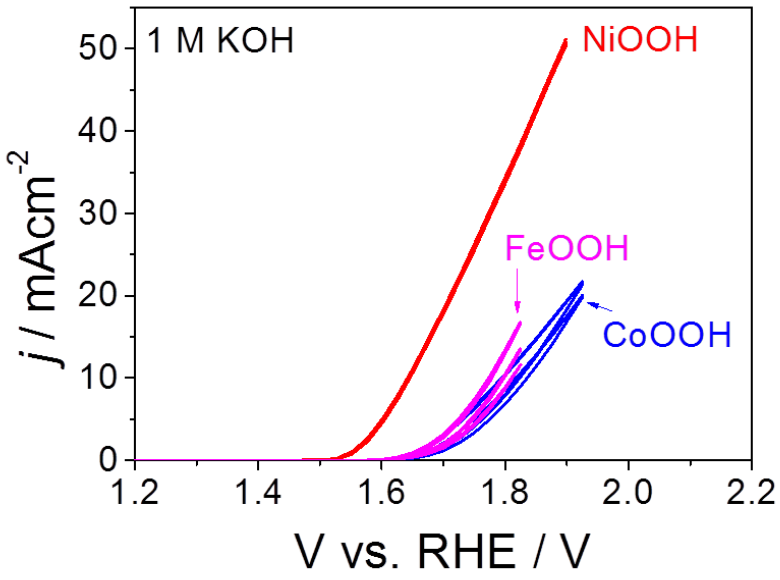

Figure 2.3. *Effect of different metal sites which lead to different binding energies of the water oxidation intermediates. Catalysts deposited on FTO-coated glass.*

Based on the scaling relations, the relatively low overpotential achieved by NiOOH (which is NiO_x in alkaline media) is somehow counterintuitive. In order to explain this apparent contradiction we need to introduce the concept of three-dimensional layered structures as a

possible way to avoid the limitations defined by the universal scaling relation. The reasoning is based on the fact that the scaling relations exist because, from the point of view of the surface, HO* and HOO* look very similar. In this context, the key feature of layered structures is to provide a second catalytic surface with the water oxidation intermediates, which interact with the intermediates from the opposite catalytic surface (alter the relative stability of HOO* and HO*). In **Figure 2.4** we show the layered structure of the Ni double hydroxide catalyst. It has been shown that the sheets are held together by non-covalent interactions allowing for the movement of water and ions between the sheets and throughout the structure when it undergoes redox chemistry.[53,54,63,64] From this water and ionic movement it has been hypothesized that the layered structure of the hydroxide catalysts is especially active because the catalytic sites are sandwiched in-between redox-active transition-metal-cation sheets that modify the energetics of the reaction intermediates differently than is possible on the surface of a dense oxide.[53,64] In between such layers, the water oxidation intermediates OH and OOH from one layer can feel the influence of the other intermediates from the opposite layer. In other words there is a second catalytic surface from which viewpoint OH and OOH do not look identical. As a further point of surface modification, the presence of dopants in the catalyst structure, as well as cations and anions in the electrolyte, has been shown to alter the overall catalytic properties by influencing the bond strength of the intermediates.[55,56,57,58,59,60,61,62,67] This approach seems a promising way to design catalysts by breaking the scaling relations.

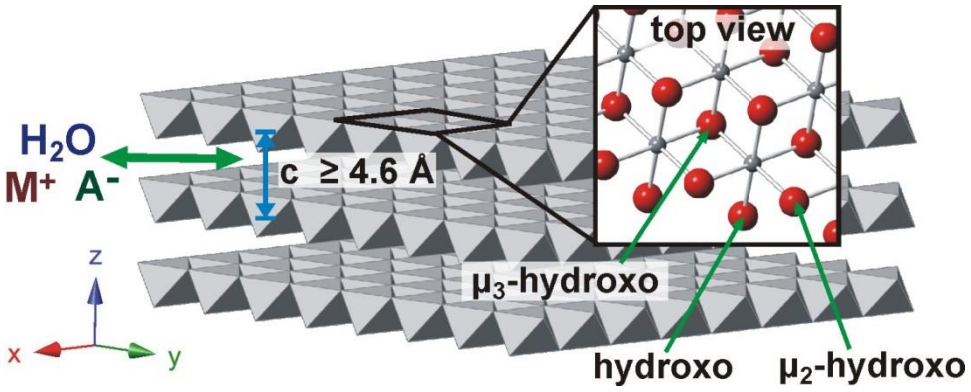

Figure 2.4. *$Ni(OH)_2$/NiOOH structure. The crystalline structure shown above is β-$Ni(OH)_2$. Structures with larger sheet spacing and more disorder are known as the α-$Ni(OH)_2$. The edge of the sheets are likely terminated with hydroxo and m_2-hydroxo groups that are under-coordinated relative to the "bulk" m_3-hydroxo bridges. Ions can move in-between the sheets.*[63,64]

We investigate now the effect of the thickness of the catalytic layer. We expect that increasing the number of sites available for the water oxidation reaction is beneficial as long as the catalyst has a porous, open structure and is electrically connected throughout its thickness and in contact with the electrolyte. Moreover, the electrical conductivity of the catalyst materials should be high enough to avoid ohmic losses at the current densities of interest. The three examples in **Figure 2.5** indeed show that the JV characteristics of Fe-, Co-, and Ni-based catalysts improves as the thickness increases. The increase in activity of thicker films suggests that there is electrical conductivity between the sheets. In the case of FeOOH, however, an optimal performance is observed after 30 min. deposition time. We hypothesize that ohmic losses become dominant for thicker films.

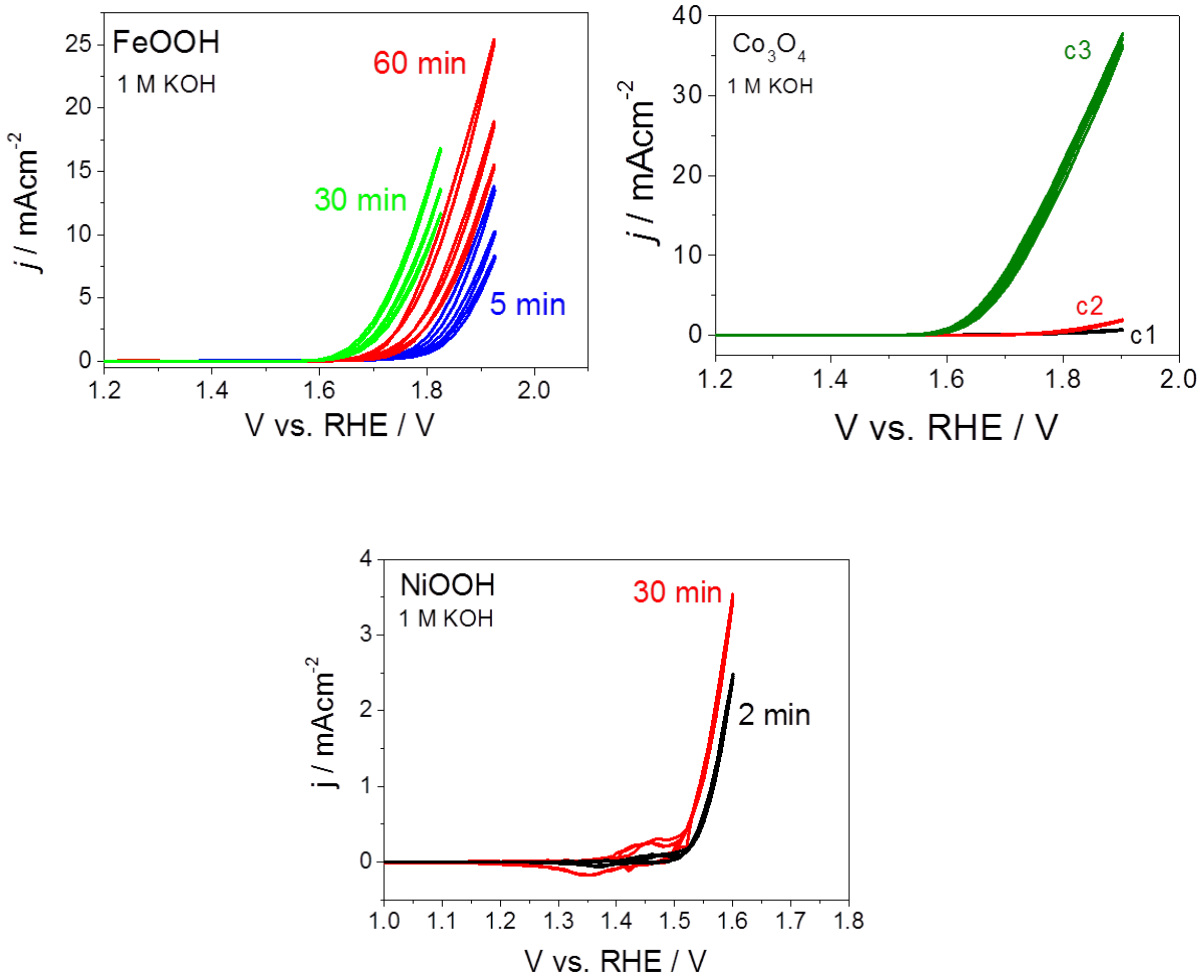

Figure 2.5. *Effect on the electrocatalytic activity of catalyst's deposition time or catalyst concentration (which represents the increased thickness in both cases). The deposition conditions can be found in the experimental section. CoOOH is deposited as Co_3O_4 nanoparticles. Their surface is*

readily converted into CoOOH in 1 M KOH.[65] The concentrations of Co_3O_4 used were $1.3*10^{-10}$ (c1), $2.3*10^{-9}$ (c2) and $1.73*10^{-8}$ mol/cm^2 (c3).

An alternative strategy to reduce the overpotential is to find pathways in which one of the intermediates is avoided. In heterogeneous electrocatalytic reactions, such as the electrocatalytic water oxidation in acidic and neutral media, it is typically assumed that the proton(s) and the electron(s) transfer simultaneously at each step in the mechanism (reactions (2.5-2.8)). This assumption is also made in arriving at the idea of the scaling relations. In enzymes, however, such mechanism is rather untypical, and the transfer of electrons and protons is usually decoupled. This may also occur in the electrocatalytic water oxidation in alkaline media, as in reactions (2.9-2.10). Because of such a decoupling, intermediates that do not feature in the suggested mechanisms could be involved. As a result of the decoupling of the transfer of protons and electrons, the pH of the electrolyte solution would play a key role in the catalysis, while it plays virtually no role in the existing thermodynamic theories of electrocatalysis.[48]

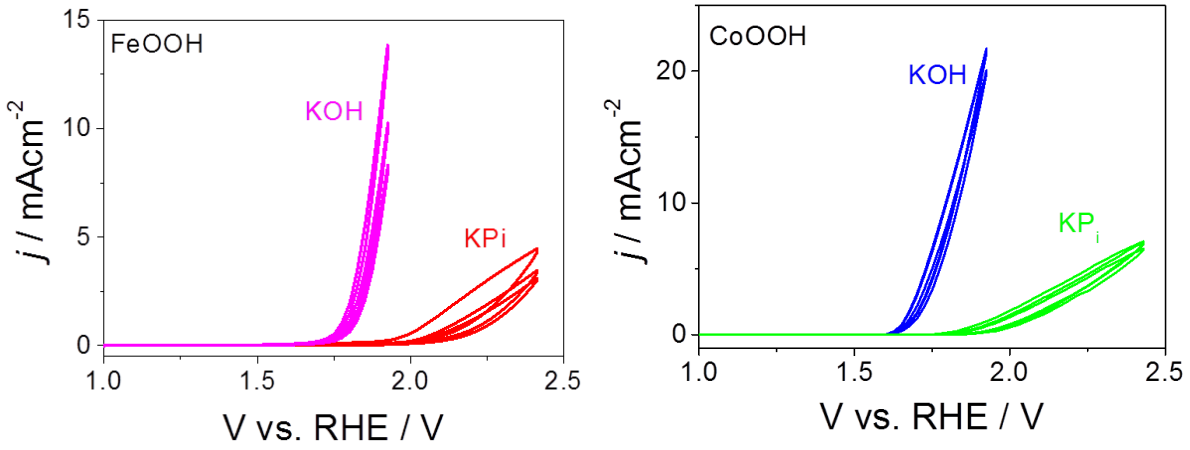

Figure 2.6. *Effect on activity of electrolyte pH and anion type. Kpi electrolyte is a 0.1 M mono- and di-basic potassium hydrogen phosphate solution of pH = 7. KOH electrolyte is a 0.1 M potassium hydroxide solution of pH = 13.*

To test this hypothesis, we investigated the influence of the pH. **Figure 2.6** shows the increased catalytic activity for FeOOH and CoOOH from a KPi electrolyte to a KOH electrolyte. The trend observed shows the importance of the electrolyte anion and/or its pH for the water oxidation catalysis. In KOH the onset potential shifts cathodically and the JV slope is steeper, compared to the measurement in KPi. A similar behavior was observed also in the literature for Ir complexes in different electrolytes.[66] In analogy, we can explain the varying strength of the coordination of the anions to the iron or cobalt center of the catalyst

as the most likely explanation for the shift in onset potential. The different slope can be related to the faster kinetics for the water oxidation reaction in alkaline electrolyte. In this specific case however, the fact that phosphate salts are less conducting than OH salts (at equal molarities) is also playing a role in the slope. The above results suggest that the catalytic activity of a given catalyst for water oxidation can be tuned by carefully controlling the electrolyte pH and/or the anions.

To decouple the effect of electrolyte pH from that of the anions, we performed experiments with a Co hydroxide catalyst in a phosphate electrolyte (CoPi) at different pHs.

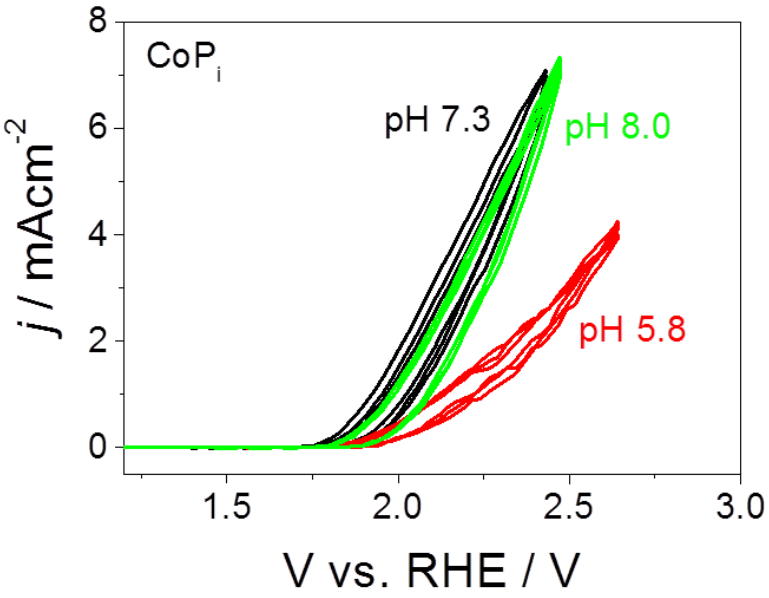

Figure 2.7. *Effect of pH in 0.1M KP$_i$ solution. A CoP$_i$ catalyst has a maximum of activity at a certain pH, based on its pK value.*

The current–potential profiles for water oxidation over Co hydroxide is shown in **Figure 2.7**. Interestingly, there is a maximum in activity at a pH close to 7.3, while the activity drops in acidic pH. This observation suggests the existence of a pH for which the activity reaches a maximum value between pH 5.8 and 8, at least in phosphate media.

Finally, for a meaningful understanding of pH effects, the reversible hydrogen electrode (RHE) is a suitable potential reference, as it takes into account the pH dependence of the overall reaction. Therefore, on the RHE scale reactivities are automatically compared at the same overpotential, revealing the real intrinsic pH dependence. As has been recently shown, a pH dependence of the catalytic activity on the RHE scale suggests the importance of decoupled proton–electron transfer steps in the overall OER mechanism.[66] The poor catalytic

activity of the CoPi at a more acidic pH might be related to a chemical conversion of the molecular complex into an inactive species (e.g. CoOH).[66] It has be shown that the deprotonation of the catalyst in acidic media inhibits the catalytic activity in NiOOH-based catalysts for water oxidation.[67] In order to validate this statement also in the case of CoPi, IR spectroscopy or NMR could be employed.

Conclusion

In this chapter we have discussed the thermodynamic reasons of the slow kinetics in the electrocatalytic water oxidation. We have introduced the concepts of free energy diagram, the Sabatier principle and the scaling relations. We have illustrated the effect on the catalytic activity of 1) metal catalytic sites, 2) electrolyte anions, pH, and catalyst thickness. Increasing the specific surface area of the catalyst layer (via the thickness) is beneficial as long as the catalyst is electrically connected throughout its thickness and in contact with the electrolyte, until ohmic losses prevail. Moreover, the water oxidation reaction over catalysts with a double-hydroxide structure are favored in alkaline media compared to a neutral electrolyte. Importantly, we have shown that certain catalysts such as CoPi possess a peak in catalytic activity at a certain pH, based on its pK value. Finally, we proposed that 3D structures such as in layered catalysts may provide a viable route to allow for water splitting with low overpotential.

Experimental section

Electrochemical measurements

The substrates used are TEC-15 FTO-coated glass (15Ω/sq; Hartford Glass Co.). Electrochemical characterization was carried out either in an aqueous 0.1M potassium phosphate electrolyte solution (pH ~7.1), or in an aqueous 1M potassium hydroxide (pH ~13.6). The solution was purged with nitrogen prior and during the measurements to remove any dissolved oxygen. The working area of the electrodes exposed to the electrolyte was 28.3 mm^2 (6 mm diameter) for all samples. The potential of the working electrode was controlled by a potentiostat (EG&G PAR 283). In three-electrode measurements, a coiled Pt wire and an Ag/AgCl electrode (XR300, saturated KCl and AgCl solution; Radiometer Analytical) were used as the counter and reference electrodes, respectively. Cyclic

voltammetry measurements were performed with a scan rate of 50 mVs^{-1}, unless otherwise stated. Electrical contact to the sample was made using a silver wire and graphite paste.

Synthesis of the Catalyst Complexes:

Co_3O_4. Co_3O_4 NPs were prepared according to a previous recipe.[68,69] 1.63 g PVP (polyvinylpyrrolidone) was dissolved in 20 ml ethanol and sonicated for 5 min. Then 0.40 g $Co(CH_3COO)_2 \cdot 4H_2O$ was added and the solution was sonicated for 30 min. 2.00 ml 25% ammonia was added while stirring and the resulting solution was put in an 120 ml autoclave at 150 °C for 4.5 hours. The formed nanoparticles were separated by centrifuging 30 min at 6000 rpm. The deposition was redispersed in ethanol and separated by centrifuging 30 min at 7500 rpm. The deposition was dried, weighted and redispersed in ethanol. Samples were prepared by dropcasting diluted solutions and were finished with annealing at 360 °C for 10 h.

CoPi. A 30 nm CoPi catalyst was electrodeposited according to the recipe from Kanan and Nocera.[70] The CoPi catalyst solution is prepared by adding 0.5 mM $Co(NO_3)_2$ (Acros Organics ≥99%) to a 0.1 M potassium phosphate buffer. The pH is adjusted in the range 5.8-8.1 by controlling the ration of K_2HPO_4 (Sigma Aldrich ≥98%) and KH_2PO_4 (Sigma Aldrich 99.5%-100.5%) dissolved in Milli-Q distilled water. Electrodeposition at +1.1V versus Ag/AgCl is carried out for a duration of 15 and 30 minutes. Care was taken to always keep the electrodeposited CoPi layer wet, as intermediate drying of the CoPi was found to adversely affect the stability.

CoOOH. CoOOH was prepared by a potentiostatic electrochemical deposition.[71] The sample had a round contact surface with the electrolyte with a diameter of 1 cm. A 3 M Ag/AgCl reference electrode (REF321) and a platinum counter electrode were used. The electrolyte was made by adding 25% ammonia to a 0.1 M solution of cobalt nitrate until all deposition initially formed was dissolved. The deposition was done directly after the solution was made, because the solution is not stable in air. Cycling was used to find an optimum voltage for deposition. CoOOH was deposited at 0.79 V vs. Ag/AgCl for 30 minutes.

FeOOH. FeOOH was synthesized in a buffer of pH 4.1 consisting of 100 ml 0.1 M Potassium Hydrogen Phthalate (Sigma Aldrich ≥99.95%) and 2.6 ml of 0.1 M NaOH (Sigma Aldrich 99%).[72] This pH was chosen, because then Fe(3+) precipitates and forms a thin film on a substrate.[73] After that $FeCl_2 \cdot 4H_2O$ (Acros Organics 99+%) was added in a concentration of 0.02 M. The applied voltage was 1.2 Volt vs Ag/AgCl.[74]

NiOOH. NiOOH was synthesized by electro deposition at 300 microA/cm^2 of a solution containing 0.005 M $NiSO_4$ (J.T. Baker ≥98.0%) and 0.015 M $(NH_4)_2SO_4$ (Sigma Aldrich ≥99.0%) for 10 and 30 minutes.[75] The pH was adjusted by adding NH_4OH (Sigma Aldrich) until a pH of 8.5 was reached. Above a pH of 8 amine complex ions are formed and the colour changes from green to light blue. After electrodeposition, the sample is gently dried under a nitrogen stream before it is placed in a furnace. A heat treatment of 15 minutes at 250ºC with a heating ramp of 5ºC per minute and under a stream of air improves the catalyst by evaporating structural water.

2.2 Solar Water Splitting Combining a $BiVO_4$ Light Absorber with a Ru-based Molecular Co-catalyst

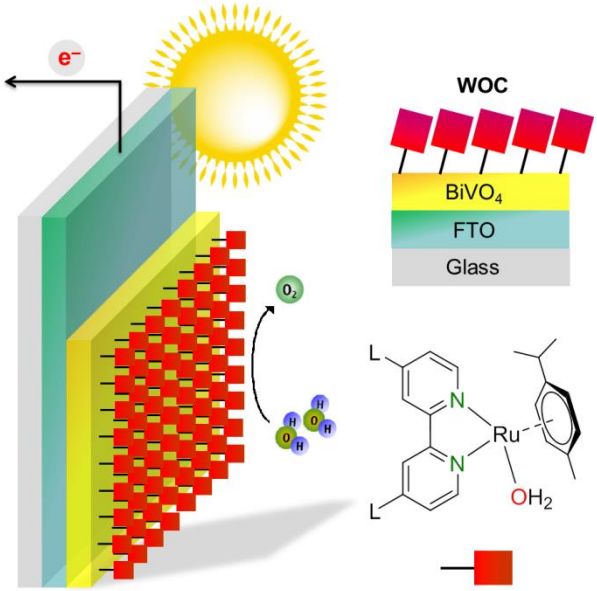

We demonstrate here for the first time the photoelectrochemical properties of a $BiVO_4$ photoanode in conjunction with a *molecular* catalyst. When the Ru-based molecular catalyst (RuCat) is coupled to a $BiVO_4$ light-absorber the performance of this photoanode improves particularly in the low-bias region (<1.0V vs. RHE). The RuCat-$BiVO_4$ photoanode shows a higher photocurrent than CoP_i-$BiVO_4$ under front illumination, and a 0.1 V more cathodic onset potential. The former can be partly explained by the low light absorption of the RuCat (<5% light absorption in the UV-vis-NIR range). For the latter, we propose that the linkers in the RuCat reduce the surface recombination in $BiVO_4$ to a greater extent than CoP_i. Finally, we observe that the fill factor of the RuCat-$BiVO_4$ JV characteristic improves after the stability test. The results presented herein not only show the feasibility and potential of the solid state/molecular heterojunctions, they also represent a proof of principle to improve conventional all-solid state systems such as CoP_i-$BiVO_4$.

This chapter is based on:
de Respinis, M.; Joya, K. S.; De Groot, H. J. M.; D'Souza, F.; Smith, W. A.; van de Krol, R.; & Dam, B. J. Phys. Chem. C 2015, *119*, 7275-7281.

Introduction

One of the challenges in solar water splitting is to control the semiconductor-electrolyte interface.[39,76] In many cases, the presence of defects and traps results in high surface recombination rates.[77] In addition, slow water oxidation kinetics often reduces the solar-to-chemical conversion efficiency. In order to optimize the light absorption in the solar spectrum, approaches with multiple bandgap heterojunction absorbers should be favored.[78] To avoid losses, one needs to improve the photoanode efficiency at low applied bias. This be achieved by nano-structuring,[79,80,81,82] by the application of surface passivation layers,[83] and by the decoration with an efficient surface catalyst.[84] It is imperative to identify alternative catalysts or combinations of surface passivation layers and catalysts, that are able to reduce the recombination losses and enhance the reaction kinetics at a potential $V < 1$ V. In addition, the catalyst should not compete for the absorption of light with the semiconductor onto which it is deposited. While solid state junctions have attracted much attention, molecular/solid state heterojunctions remain largely unexplored. Recent advances on molecular catalysts have made them highly efficient, with activities comparable to that of photosystem II.[85,86,87,88,89,90,91,92,93] The focus on hybrid molecular/solid state approaches thus far has been mostly limited to the dye sensitized solar cell approach to water splitting, where light absorption was conducted by the molecular compounds.[94,95,96] Only recently a photoelectrode with an Fe-based molecular catalyst on WO_3 was demonstrated. In this case, the use of a molecular catalyst increased the current for photoelectrochemical water oxidation in non-neutral pH conditions, but the optical transparency and surface passivation effects of the catalyst were not considered.[97] In this study $BiVO_4$ is the semiconductor of choice due to the relatively deep understanding of its properties both in the particulate form,[98,99,100] as well as a thin film photoanode.[101,102] Here we report for the first time the surface functionalization of $BiVO_4$ photoanodes with a molecular catalyst, a *p*-cymene ruthenium bipyridine aqua complex $[(cy)Ru^{II}(L_2bpy)OH_2]^+$ (L=linker 4,4′-dicarboxylic acid) that has a catalytic cycle with consecutive electron transfer events coupled to efficient proton release. This leads to redox leveling of catalytic intermediates and a narrow density of states localized at the catalyst.[87,88,89,90,91,92,93] The proton-NMR spectrum of the mono ruthenium complexes is shown in **Figure 2.1**. For simplicity, undoped $BiVO_4$ samples are used in this study. We examine the performance of this planar molecular–solid state hybrid system in conjunction with all-solid state systems such as the well-studied CoP_i-$BiVO_4$ in which CoP_i has been shown to be one of the most effective co-catalysts,[103] and RuO_2-$BiVO_4$. In addition, we

compare their functionality to the case where the same catalysts are used as electrocatalysts on FTO.

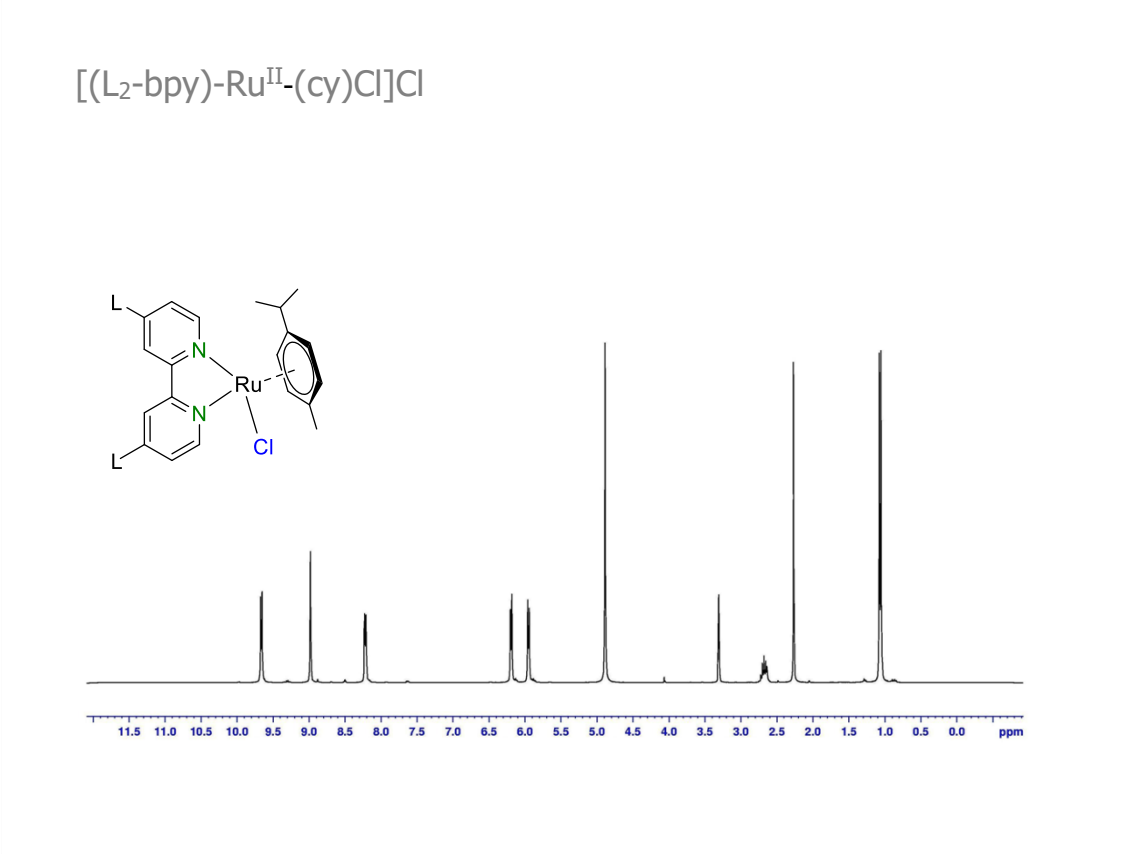

Figure 2.1 *Proton-NMR spectrum of the mono ruthenium complexes [(L₂-bpy)-Ru^{II}-(cy)Cl]Cl.*

Experimental section

(Photo-)electrochemical measurements

As a photoanode, we synthesized 200 nm dense films of $BiVO_4$ by spray pyrolysis. The spray deposition rate is ~1 nm per 5 seconds (1 cycle). The recipe for the preparation of the precursor solution and the spray pyrolysis setup are described elsewhere.[84,103] Before every deposition, ~80 nm of SnO_2 layer was deposited onto FTO substrate to prevent recombination of electrons and holes at the FTO/$BiVO_4$ interface.[102] The substrates used are TEC-15 FTO-coated glass (15Ω/sq; Hartford Glass Co.). After the deposition, all samples were annealed for 2 h at 450 ºC in air to further improve the crystallinity. A 30 nm Co-Pi catalyst was electrodeposited according to the recipe from Kanan and Nocera.[96,104] The electrodeposition was performed at a constant voltage of 1.7 V versus RHE for 15 min. Care

was taken to always keep the electrodeposited Co-Pi layer wet, as intermediate drying of the Co-Pi was found to adversely affect the stability. The $BiVO_4$ photoanodes and the FTO anodes were functionalized with molecular water oxidation catalyst by immobilizing the p-cymene ruthenium derived bipyridine complex $[(cy)Ru^{II}(L_2bpy)OH_2]^+$. The catalyst was dispersed into an aqueous solution and the deposition was obtained by dip-coating the substrates into the catalyst solution for periods of 1.5 to 3 hours. RuO_2 NPs were synthesized by the solvothermal method and calcined in air at 300°C for 3 h.[105] An aqueous solution (2 ml) of catalyst (5 mg) was prepared and mixed in an ultrasonic bath. 20 µl of aqueous solution of catalyst was deposited on the FTO or $BiVO_4$ substrates. Photoelectrochemical characterization was carried out in an aqueous 0.1M potassium phosphate electrolyte solution (pH ~7.1). The solution was purged with nitrogen prior and during the measurements to remove any dissolved oxygen. The working area of the electrodes exposed to the electrolyte was 28.3 mm^2 (6 mm diameter) for all samples. The potential of the working electrode was controlled by a potentiostat (EG&G PAR 283). In three-electrode measurements, a coiled Pt wire and an Ag/AgCl electrode (XR300, saturated KCl and AgCl solution; Radiometer Analytical) were used as the counter and reference electrodes, respectively. Cyclic voltammetry measurements were performed with a scan rate of 50 mVs^{-1}. White light photocurrent measurements were performed under simulated AM1.5 solar illumination (100mWcm2) with a Newport Sol3A Class AAA solar simulator (type 94023 ASR3). Electrical contact to the sample was made using a silver wire and graphite paste. A Keithley 2001 multimeter was used as the ammeter in the current versus time measurements, and as an auxiliary high-impedance voltmeter (> 10 GΩ) connected to the working (WE) and counter (CE) electrodes to measure the two-electrode voltage. The UV-visible-near IR absorption was measured with a balanced deuterium-halogen lamp as the light source and a Maya 2000 spectrophotometer as the detector.

Electrochemical Quartz Crystal Nanobalance

EQCN experiments, with simultaneous cyclic voltammetry and piezoelectric gravimetry measurements, were performed with an Elchema EQCN-600 nanobalance and an Elchema PS-605B potentiostat. Both instruments were computer-controlled with the Elchema Voltscan program (version V.4.1). A conventional three-electrode cell configuration was used; the counter electrode was a platinum foil, and an Ag/AgCl/KCl electrode (Bioanalytical Systems, Inc.) served as the reference. The working electrode was a 14 mm diameter quartz crystal (AT cut, plano-plano, 10 MHz) coated with a gold/chromium conducting surface (approximate electroactive surface area: 0.256 cm^2). The quartz crystal disc was mounted in

an EQCM-5710 quartz crystal holder of the Polish Academy of Sciences. The frequency response of the quartz crystal was additionally monitored before and during experiments using a Fluke PM6680B high-resolution frequency counter.

Synthesis of the Catalyst Complexes:

Chloro complex $[(cy)Ru^{II}(L_2bpy)Cl]Cl$

4,4′-dicarboxylic acid-2,2′-bipyridine (L_2bpy: 0.244 g, 1.0 mmol) was dissolved in 0.5 mL water containing NaOH (0.08 g, 2.0 mmol) and MeOH (25 mL) was added to it. This mixture was poured into a stirred mixture of $[RuCl_2(p\text{-cymene})]_2$ dimer (0.362 g, 0.5 mmol) in absolute MeOH (20 mL). The whole reaction mixture was further stirred for 2 hours at 40-45 °C. The solution was cooled to room temperature and the pH was lowered to 1-2 by addition of 0.5 M HCl. The free ligand was filtered off and the solvent mixture was evaporated under vacuum. The solid orange chloro complex $[(cy)Ru^{II}(L_2py)Cl]Cl$ thus obtained was re-precipitated from MeOH or acetone by addition of ether/hexane. Yield 0.43 g, 78 %. ^{1}H NMR (CD_3OD, 295 K, δ ppm, J Hz): 9.66 (d, 2H, $H^{6,6'}{}_{dcabpy}$, J 5.76); 8.99 (s, 2H, $H^{3,3'}{}_{dcabpy}$); 8.22 (dd, 2H, $H^{5,5'}{}_{dcabpy}$, J 1.49, J 5.79); 6.19 (d, 2H, $Ar_{p\text{-cy}}$, J 6.33); 5.95 (d, 2H, $Ar_{p\text{-cy}}$, J 6.33); 2.66 (sep, 1H, -C<u>H</u>$(CH_3)_2$ $_{p\text{-cy}}$); 2.27 (s, 3H, CH_3 $_{p\text{-cy}}$); 1.06 (d, 6H, -CH(C<u>H</u>$_3)_2$ $_{p\text{-cy}}$, J 6.91), Analysis found: C, 45.56%; H, 4.41%; N, 4.85%. Calculated: C, 45.74%; H, 4.36%; N, 4.86% for $C_{22}H_{22}N_2O_4Ru_1Cl_2.1.5H_2O$ complex.

Catalyst Complex $[(cy)Ru^{II}(L_2bpy)\text{-}OH_2]^{2+}$ (RuCat)

The chloro complex $[(cy)Ru^{II}(L_2bpy)Cl]Cl$ was converted into the aqua (OH_2) catalyst $[(cy)Ru^{II}(L_2bpy)\text{-}OH_2]^{2+}$ by stirring with aqueous solution containing 2.1 eq. of $AgNO_3$ or silver hexafluorophosphate in methanol (1:1, H_2O/MeOH) for 30 minutes. The white precipitates were filtered off and the solvent mixture was evaporated under vacuum. The yellow solid aqua complex thus obtained was re-precipitated from acetone or MeOH by addition of ether/hexane.

RuCat deposition

$[RuCl_2(p\text{-cymene})]_2$ dimer and $RuCl_3.nH_2O$ were obtained from Sigma-Aldrich Co., and used as received. L_2bpy (4,4'-diphosphonic acid-2,2'-bipyridine) was prepared using literature procedures.[106,107] Unless otherwise specified, the solutions were prepared in ultra-pure water (Millipore MilliQ® A10 gradient, 18.2 MΩ cm, 2–4 ppb total organic content). Compounds, ligands and catalyst complexes were synthesized in argon/nitrogen atmosphere. The

glassware and the electrochemical cell were cleaned as described previously.[108] Proton NMR spectra were obtained with a Bruker WM-300 MHz spectrophotometer. Immobilization of the catalyst on FTO coated glass slides (1 × 2.5 cm) and $BiVO_4$ coated FTO was carried out according to our previously described procedure.[109]

Results and discussion

In this study, we choose to perform all (photo-)electrochemical measurements at pH 7.1 in 0.1M phosphate buffer, conditions under which the performance and stability of the CoP_i are optimal. A study on the effect of the electrolyte anions and pH may reveal conditions under which the performance of RuCat is even higher than herein reported. First we compared the electrocatalytic activity for water oxidation on the bare FTO substrate, with that for FTO coated with CoP_i, RuO_2 and the RuCat catalysts, as shown in **Figure 2.2.** The cyclic voltammogram shows that RuO_2 has the lowest onset potential (V_{on} = ~1.4 V vs. RHE), while for CoP_i and RuCat a negligible current is flowing through the cell up to an applied potential of 1.75 V vs. RHE. The potential for the reversible water oxidation reaction is at 1.23 V vs. RHE, which implies an overpotential of 0.7 V and 0.8 V at 1 $mAcm^{-2}$ for CoP_i and RuCat, respectively. Therefore RuO_2 is, as expected, the most active electrocatalyst on FTO.

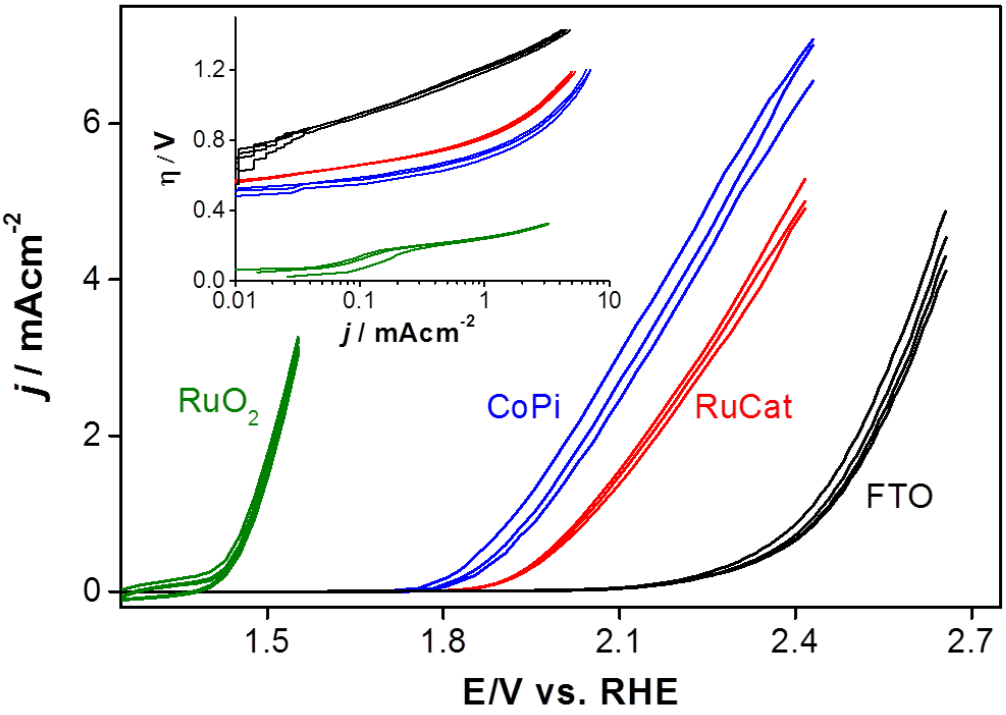

Figure 2.2 *JV curve for RuCat@FTO (red), CoP_i@FTO (blue), RuO_2@FTO (green) and bare FTO (black). The numbers on the right hand side of the CoP_i, RuCat and FTO represent the cycle number. The inset is the Tafel plot. Measurements performed at 50 mV sec^{-1}.*

Next, we studied the light driven water oxidation catalysis in conjunction with a $BiVO_4$ light absorber. **Figure 2.3** shows the linear sweep voltammogram under chopped illumination for a $BiVO_4$ photoanode with and without anchoring the RuCat. The photocurrent density of the RuCat-$BiVO_4$ photoanode increases at all potentials. The enhancement is most pronounced at low potential, resulting in an improved fill factor of the polarization curve. The improved fill factor for the RuCat-$BiVO_4$ system can be attributed to reduced surface recombination, enhanced charge injection (i.e., oxygen evolution kinetics), or both. In fact, the more pronounced current transients between 0.6 V – 1.7 V for the RuCat-$BiVO_4$ suggest that the photogenerated charges live longer.[103] This favors an explanation in terms of reduced surface recombination at low current density. It is also corroborated by the absence of cathodic transients when the light is turned off, which would indicate an accumulation of holes at the semiconductor-catalyst interface due to slow catalysis. The fact that the photocurrent improves at low potentials, but not at higher potentials is fully consistent with the explanation that the photocurrent is limited by surface states. For unmodified $BiVO_4$ at low potentials, electrons in the conduction band may be injected into the surface states, so passivation of these states would help. At higher applied potentials, conduction band

electrons are more strongly driven away from the surface, and cannot reach the surface states anymore. Therefore passivation of the surface states does not help at these potentials.[110] All in all we find that the current density for the RuCat-$BiVO_4$ is 5.5 times higher than the one for bare $BiVO_4$ at 0.8 V vs. RHE, where 0.8 V is a typical operating voltage when using this anode in conjunction with e.g. a single-junction amorphous silicon solar cell. The improved JV characteristic is a sign that RuCat has been successfully deposited, since the presence of RuCat enhances the oxidative power of the substrate. At this stage however, the exact nature and structure of the RuCat during catalysis in a phosphate buffer is unknown. The characterization of the $BiVO_4$-RuCat interface will be the subject of further work.

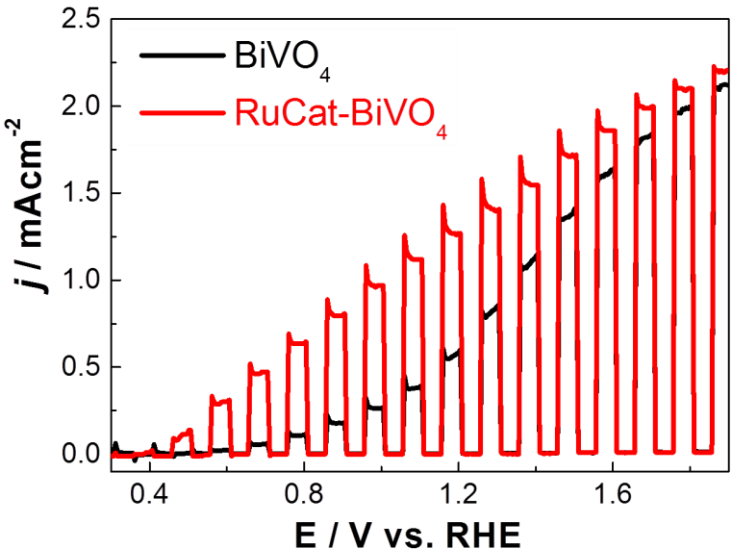

Figure 2.3 *JV curve for a bare $BiVO_4$ (black), and for Ru-catalysts on $BiVO_4$ (red). Measurement performed at 10 mV/sec, under chopped AM 1.5 back illumination.*

In **Figure 2.5A** and **B** we show the current density of RuCat-$BiVO_4$ and CoP_i-$BiVO_4$, under continuous frontside and backside illumination. Interestingly, in both configurations the onset potential (V at 0.1 $mAcm^{-2}$) for RuCat-$BiVO_4$ is comparable to that for CoP_i-$BiVO_4$. In contrast, the electrocatalytic measurements in **Figure 2.2** show that CoP_i@FTO has a lower onset for water oxidation than RuCat@FTO. Comparable results are obtained in the dark with RuCat or CoP_i deposited on $BiVO_4$ instead of FTO (**Figure 2.4**). This apparent contradiction suggests that the cathodic shift in the onset potential for the RuCat-$BiVO_4$ is not due to enhanced water oxidation catalysis, but to reduced surface recombination (since surface recombination does not play a role in the electrocatalytic experiments shown in **Figure 2.2**).

The cathodic shift in onset potential between the electrocatalysis (**Figure 2.2**) and the photoelectrocatalysis (**Figure 2.5A** and **B**) is related to the photovoltage of $BiVO_4$. We use open circuit potential (OCV) measurements in **Figure 2.6** to shine light on this concept. When $BiVO_4$ is immersed in the electrolyte, the OCV in the dark equilibrates at ~0.9 V vs. RHE. This value is consistent with literature reports and has been attributed to the energy of surface states in $BiVO_4$.[111] When $BiVO_4$ is catalyzed with CoP_i or RuCat, the OCV is 0.8 V vs. RHE. A likely reason for the new value is the energetic equilibrium of the $BiVO_4$-catalyst interface, where the catalyst is in its rest state. After the electrocatalysis, the OCV in the dark for $BiVO_4$ is unchanged. The value for CoP_i-$BiVO_4$ starts at 1.23 V vs. RHE and slowly decreases. For RuCat-$BiVO_4$ instead, its value shows a more pronounced temporal variation towards 0.85 V vs. RHE. We attribute the decrease in OCV to the discharge of the capacitance of the catalyst film.[112] Under illumination, the OCV for the $BiVO_4$ is at around 0.4 V vs. RHE under both front and back illumination. For CoP_i-$BiVO_4$ a significant difference is observed between back and front illumination, whose OCV are at 0.3 and 0.5 V vs. RHE. The difference can be ascribed to the light absorption by the CoP_i layer. For CoP_i-$BiVO_4$ the OCV equilibrates at 0.2 V vs. RHE. The OCV value under illumination is related to the thermodynamic V_{on} with the chosen semiconductor. The real V_{on} includes also the catalytic losses. Moreover the difference between the OCV in the dark and the OCV under illumination is defined as the so-called photovoltage. In order to get the highest photovoltage out of a semiconductor (and therefore the smallest V_{on} under illumination), it is favorable for the hole quasi-Fermi level $E_{F,h}$ to equilibrate as closely as possible to the valence band top, and the electron quasi-Fermi level $E_{F,e}$ as closely as possible to the conduction band bottom. To understand this concept, one needs to consider that the photovoltage of a semiconductor in an aqueous medium is often limited by the Fermi-level pinning due to recombination at surface states (**Figure 2.7A**). By passivating these surface states through the application of a suitable catalyst such as CoP_i, the $E_{F,e}$ becomes unpinned resulting in a higher photovoltage ΔV_{photo} (smaller V_{on}) which is then limited by recombination of conduction band electrons with the holes accumulating in the catalyst (**Figure 2.7B**). It has been shown that CoP_i effectively passivates the surface states in Fe_2O_3 and promotes near-complete suppression of surface recombination in $BiVO_4$.[113,114,115] The comparable onset potential of the RuCat-$BiVO_4$ presumably means that the RuCat is as effective as CoP_i in passivating the $BiVO_4$ surface states. In the case of RuCat, possibly the recombination is further reduced by its linkers which increase the distance (introduce a tunneling barrier) between the conduction band electrons and the holes accumulating in the reaction center (Ru), which in turn increases the $E_{F,e}$ (**Figure 2.7C**). Note, that the molecular catalyst is expected to be

both ion-permeable and redox-active, which leads to the formation of a so-called *adaptive junction.*[116] In such a junction, the oxidation of a catalyst intermediate increases its redox potential (i.e. it lowers the catalyst electrochemical potential) and thus lowers the $E_{F,h}$. This also contributes to an increase in ΔV_{photo}.

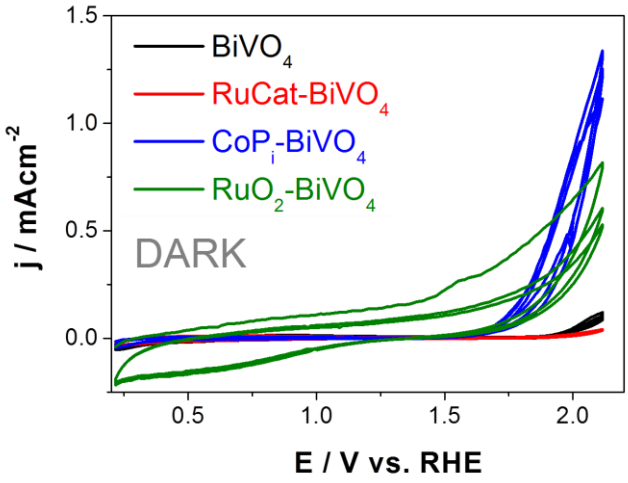

Figure 2.4 *JV scans in the dark for a bare $BiVO_4$ substrate, RuCat-$BiVO_4$, CoP_i-$BiVO_4$, and RuO_2-$BiVO_4$. For RuO_2-$BiVO_4$, the first peak at ~1.5 V vs. RHE is probably the beginning of the water oxidation reaction. The reaction efficiency is possibly dampened by catalyst instability (agglomeration of nanoparticles and/or detachment).*

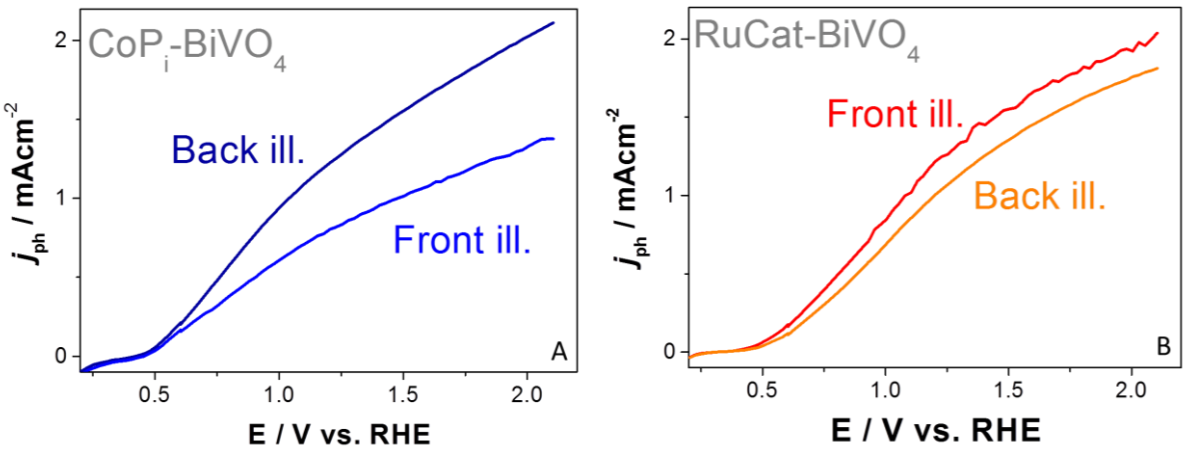

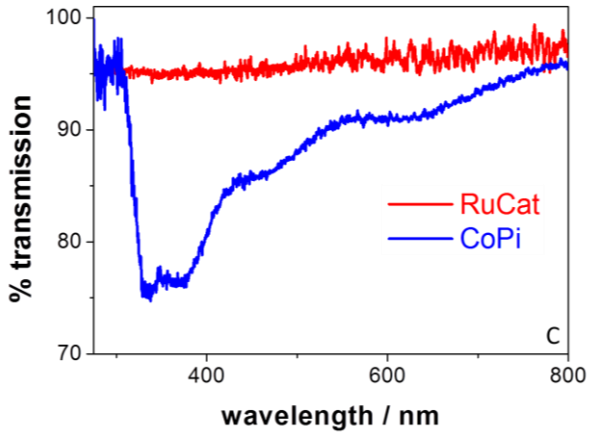

Figure 2.5 *JV scans for CoP_i-$BiVO_4$ (A) and RuCat-$BiVO_4$ (B) under front illumination (light from the electrolyte/catalyst interface) and under back illumination (light from the FTO-glass). Transmission spectrum for CoP_i@FTO as recorded at the end of the deposition is compared with the ex-situ UV-vis spectrum for RuCat on glass (C). The strong absorbance of the FTO precludes the measurement at wavelengths below 330 nm. CoPi deposition done in potentiostatic mode at 1.7 V vs. RHE. In 900 seconds a 30 nm thin film has deposited, which is the optimal thickness for CoP_i-catalyzed $BiVO_4$ [84]).*

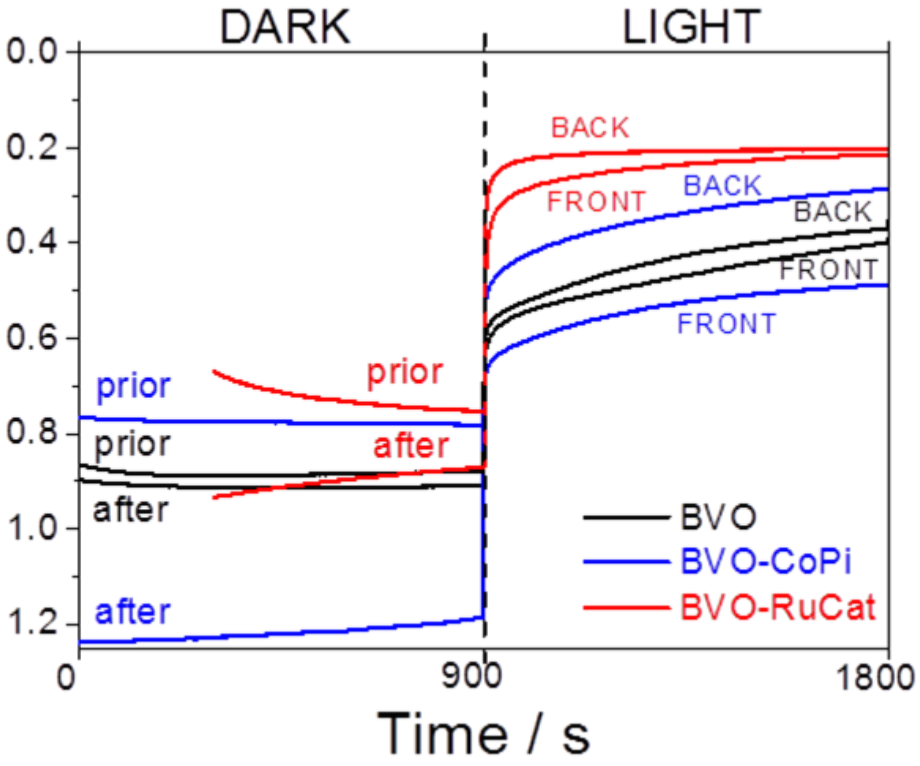

Figure 2.6 *Open circuit voltage (OCV) plot for A) $BiVO_4$ (black) and for CoP_i-catalyzed $BiVO_4$ (blue); and B) $BiVO_4$, CoP_i-catalyzed $BiVO_4$ and RuCat-catalyzed $BiVO_4$. Time in seconds on the x-axis, potential vs. RHE in volts on the y-axis. First 900 seconds with closed shutter followed by 900 seconds*

with open shutter and back illumination. In the dark 'prior' indicates the OCV measured prior to the water oxidation electrocatalysis, 'after' indicates the OCV measured after the water oxidation electrocatalysis. Under light 'BACK and 'FRONT' refer to the illuminated side.

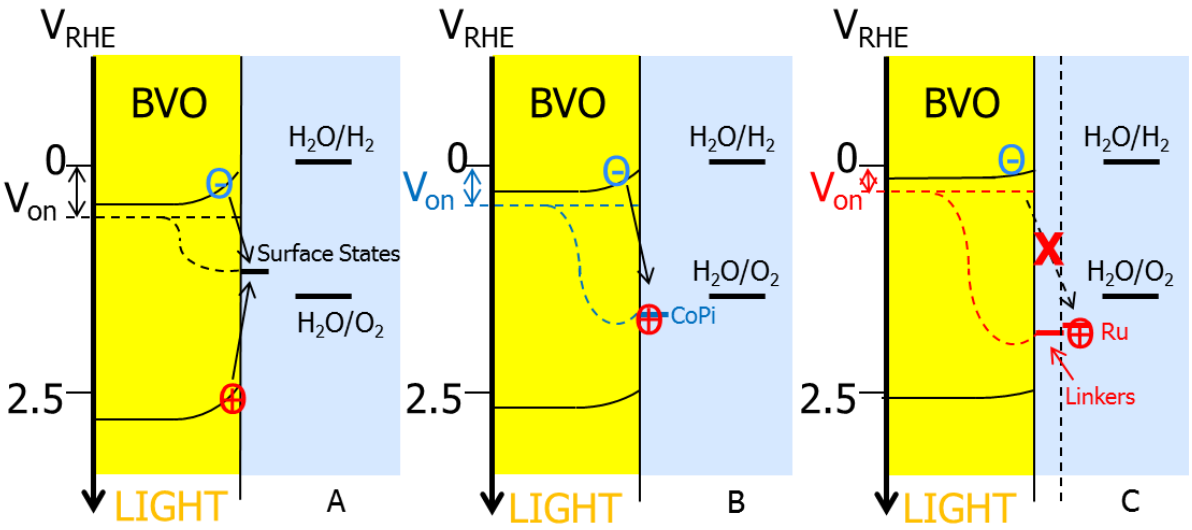

Figure 2.7 *A schematic energy diagram under reaction conditions (low applied bias) including the conduction and valence bands, the quasi-Fermi levels of $BiVO_4$ in the dark and under illumination, in the presence of surface states and with a catalyst; the redox level of the CoP_i catalyst and the Ru-based molecular complex; the redox potential for water oxidation. A) Photovoltage and recombination at surface states on an uncatalyzed $BiVO_4$. B) Passivation of surface states, increased photovoltage and recombination on Co sites in CoP_i-$BiVO_4$. C) Further increased photovoltage and reduced recombination on RuCat-$BiVO_4$.*

We observe that V_{on} for CoP_i-$BiVO_4$ under front illumination is slightly more anodic than under back illumination (**Figure 2.8**), and the saturation current density is lower in the former (**Figure 2.5A**). These differences do not occur in RuCat-$BiVO_4$ (**Figure 2.5B** and **Figure 2.8**) and can be attributed to the parasitic light absorption by the CoP_i. Our UV-vis measurements of the CoP_i@FTO, compared with the absorption through the RuCat, are shown in **Figure 2.5C**. CoP_i absorbs up to 25% of the light at wavelengths shorter than the bandgap of $BiVO_4$ while RuCat only absorbs 5%. It was shown that Co^{IV} species are formed at potentials positive of 1.5 V vs. RHE,[117] and that they are characterized by dark coloration.[118] Thus those are the species formed when we deposit the CoP_i film at 1.7 V vs. RHE, and the ones which are required to evolve oxygen.[117]

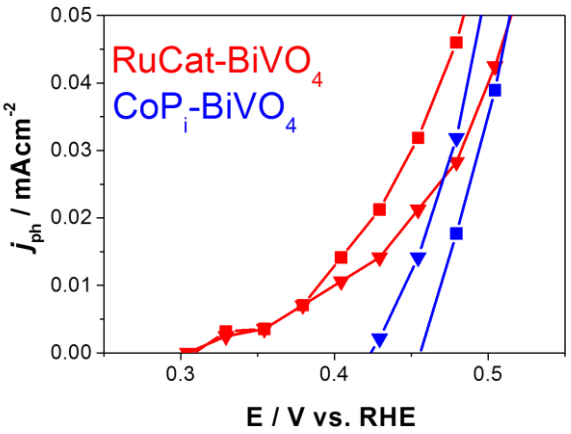

Figure 2.8 *JV scans for a CoP_i-catalyzed $BiVO_4$ and RuCat-catalyzed $BiVO_4$. Measurements performed at 50 mV sec^{-1} under front illumination (full squares) and back illumination (full triangles).*

The stability of the CoP_i-$BiVO_4$ and RuCat-$BiVO_4$ samples at 1.23 V vs. RHE, under AM1.5 illumination were measured over a period of 6500 seconds as shown in **Figure 2.9**. While the photoanode performance under constant bias and illumination is slowly degrading over time, we observe that the cyclic voltammogram under illumination of the RuCat-$BiVO_4$ samples after the stability test shows an improved fill factor compared to a freshly made sample (**Figure 2.10A**). In this experiment, for each cyclic voltammetry three cycles are taken. As those cycles overlap, we can say that between them there is no evidence for degradation. Given the limited thickness of the as deposited RuCat catalyst, this strongly suggests that the observed photocurrent is due to oxygen evolution rather than catalyst degradation.

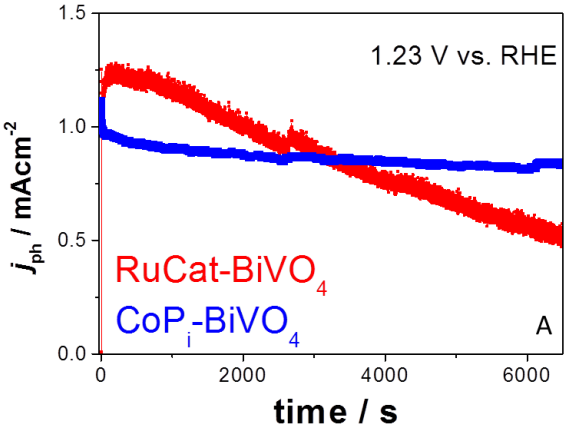

Figure 2.9 *Stability measurement for a RuCat-catalyzed $BiVO_4$ (red), and CoP_i-catalyzed $BiVO_4$ (blue); measurements performed at 1.23 V vs. RHE, under AM 1.5 illumination.*

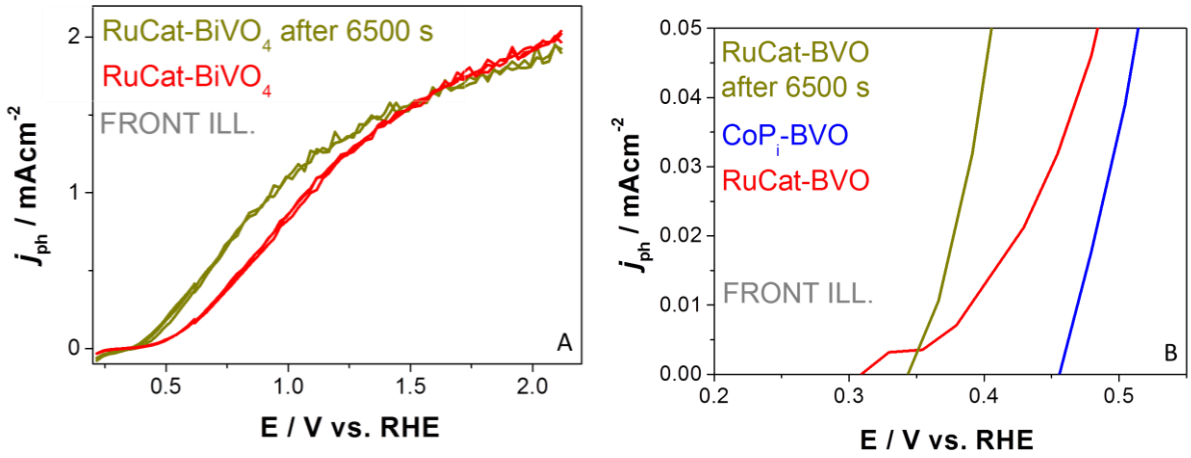

Figure 2.10 *JV scans before and after 2.5 hours of reaction under illumination for a RuCat-catalyzed $BiVO_4$ (A). JV scans for a CoP_i-catalyzed $BiVO_4$ and RuCat-catalyzed $BiVO_4$. For RuCat-$BiVO_4$ the JV after the stability test is compared. Measurements performed at 50 mV sec^{-1} under front illumination (light from the electrolyte/catalyst interface) (B).*

The reason for the fill factor improvement is unclear, however reasonable interpretations could be a reduced surface recombination due to an improved semiconductor/catalyst interface, or improved catalysis over the RuCat. The latter explanation is supported by the electrocatalytic measurements before and after the stability test shown in **Figure 2.11**, where the dark currents of the RuCat-$BiVO_4$ and RuCat@FTO slightly increase after the stability test. By zooming in around the V_{on}, we observe that after the stability test V_{on} is at around 0.35 V vs. RHE, unchanged compared to before the stability test. Moreover we observe that this value is 0.1 V more cathodic than for CoP_i-$BiVO_4$ (**Figure 2.10B**). This difference further supports our interpretation of reduced surface recombination as compared to CoP_i. To exclude the possibility that the improvement after the continuous reaction is due to the oxidation of RuCat to RuO_x, we deposited RuO_2 onto $BiVO_4$ for comparison. In fact, in **Figure 2.12** we observe that the photocurrents for RuO_2-$BiVO_4$ are significantly lower than for RuCat-$BiVO_4$. Furthermore, a comparison of **Figure 2.5** and **Figure 2.12** shows that while RuO_2 NPs are excellent catalysts for the electrocatalytic oxidation of water, they do not enhance the photoelectrocatalytic performance of $BiVO_4$. Furthermore, we tested the molecular integrity of RuCat by *in situ* electrochemical quartz crystal nanobalance (EQCN) experiments (**Figure 2.13**). The EQCN data reveal only small reversible mass changes and show no sign of persistent mass gain in the potential window for water oxidation.

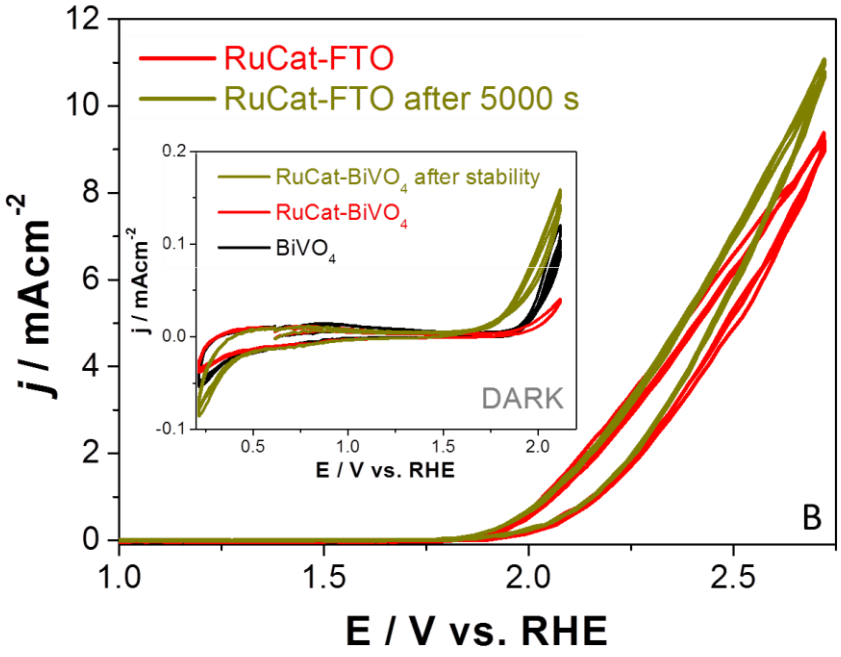

Figure 2.11 *JV scans before and after 5000 seconds of reaction in the dark for a RuCat-catalyzed FTO; the inset compares the dark JV scans of $BiVO_4$, RuCat-catalyzed $BiVO_4$, and RuCat-catalyzed $BiVO_4$ after 2 hours of reaction under illumination.*

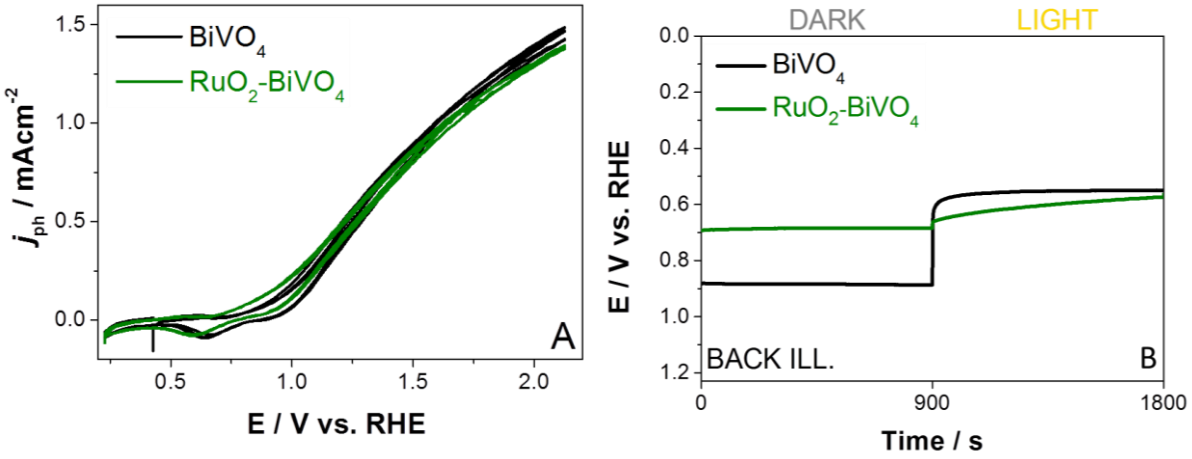

Figure 2.12 *(A) JV scans for a $BiVO_4$ (black) and RuO_2-catalyzed $BiVO_4$ (green) under back illumination. (B) Open circuit potential plot for $BiVO_4$ (black) and for RuO_2-catalyzed $BiVO_4$ (green). Time in seconds on the x-axis, potential vs. RHE in volts on the y-axis. First 900 seconds with closed shutter followed by 900 seconds with open shutter and back illumination.*

To exclude the possibility that the improvement after the continuous reaction is due to the oxidation of RuCat and the formation of RuO_x, we synthesized RuO_2 nanoparticles and dispersed them into an aqueous solution. The colloidal solution was then drop casted onto

FTO and $BiVO_4$ for comparison. By comparing ***Figure 2.12*** with ***Figure 2.10***A, we observe that the photocurrents for RuO_2-$BiVO_4$ are significantly lower than for RuCat-$BiVO_4$. As there is no reason to believe that the decomposition product of RuCat in the form of RuO_x would outperform an excellent water oxidation catalyst such as the synthesized RuO_2 NPs, we can therefore exclude the possibility that the improved performance after the stability measurements (**Figure 2.10A**) is due to oxidation of RuCat to RuO_x. Furthermore, a comparison of **Figure 2.2** and **Figure 2.12** shows that while RuO_2 NPs are excellent catalysts for the electrocatalytic oxidation of water, they do not enhance the photoelectrochemical performance of $BiVO_4$. $BiVO_4$-RuO_2 forms a poor heterojunction which leads to a substantial reduction of ΔV_{photo}. In this case, the higher (electro)catalytic activity of RuO_2 is counteracted by the fact that the applied bias does not induce band bending in the $BiVO_4$, and the potential drop takes place in the Helmoltz layer instead of the space charge region. This phenomenon is known as Fermi-level pinning.[110,119]

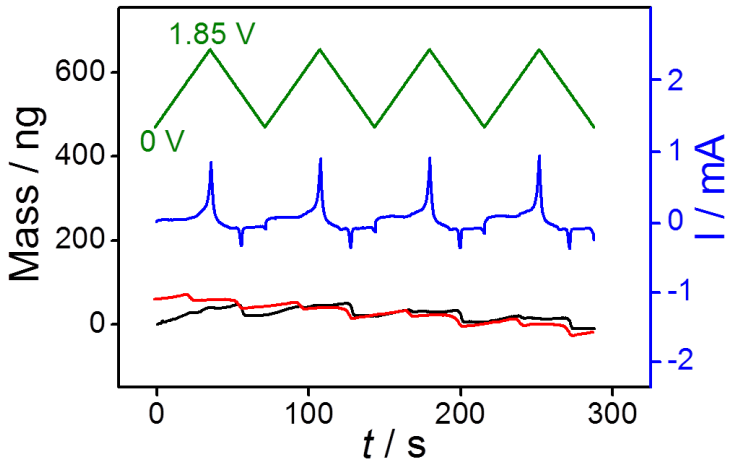

Figure 2.13 *In situ EQCN mass response as a function of time during four consecutive potential scans between 0–1.85 V vs. NHE (0.6–2.45 V vs. RHE) for Cat.Ru–COOH (red line) in deoxygenated 0.1 M HNO_3 solution. The black line corresponds to the background signal. The Ru catalyst was in a ~2 mg/15 mL solution. The green line is the linear cyclic voltammetry between 0-1.85 V vs. NHE. The blue line is the current response of the anode. The EQCN is a measurement system for monitoring extremely small variation in the mass of a working electrode attached to a vibrating quartz single crystal.*[109,120] *The EQCN data reveal only small reversible mass changes and show no sign of persistent mass gain in the potential window for water oxidation for the RuCat immobilized on the gold-piezoelectric (Au-PZT) disk.*

Conclusions

In summary, we explored the (photo-)electrochemical performance of $BiVO_4$ photoanodes for water oxidation modified with a ruthenium derived aqua complex $[(cy)Ru^{II}(bpy)OH_2]^+$ molecular catalyst (RuCat). We find that the electrocatalytic activity of a catalyst cannot be used to determine its effectiveness as a co-catalyst, since RuCat and CoP_i outperform RuO_2 as a co-catalyst for $BiVO_4$ photoanodes. The limited thickness of the molecular catalyst results in a light absorption of only 5% across the UV-vis-NIR spectrum, which allows for a higher saturation current density under front illumination as compared to CoP_i. In addition, we find that the RuCat-$BiVO_4$ photoanode shows a 0.1 V more cathodic onset potential compared to CoP_i-$BiVO_4$. This we attribute to the larger distance between the conduction band electrons and the reaction center (Ru). Finally, while the photocurrent at constant potential is slowly decreasing in time, we observe that the fill factor of the RuCat-$BiVO_4$ JV-characteristic improves after the stability test. Electrocatalytic measurements suggest an improved catalysis over the RuCat, however, a reduced surface recombination due to an improved semiconductor/catalyst interface could also contribute. The improved fill factor, the smaller onset potential and the enhanced stability make the use of such a molecular catalyst an interesting proposition when designing a heterojunction tandem device where light must first pass through the catalyst layer.

REFERENCES

43. Engel, T. et al. *Physical Chemistry*, Pearson, **2014**.
44. Dau, H.; Limberg, C.; Reier, T.; Risch, M.; Roggan, S.; Strasser, P. *ChemCatChem* **2010**, 2, 724.
45. Rossmeisl, J.; Logadottir, A.; Norskov, J.K. *Chem. Phys.* **2005**, 319, 178.
46. Rossmeisl, J.; Qu, Z.W.; Zhu, H.; Kroes, G.J.; Norskov, J.K. J. *Electroanal. Chem.* **2007**, 607, 83.
47. Man, I. C.; Su, H.-Y.; Calle-Vallejo, F.; Hansen, H.; Jos, A.; Martinez, I.; Inoglu, N. G.; Kitchin, J.; Jaramillo, T. F.; Nørskov, J. K.; Rossmeisl, J. Universality in Oxygen Evolution Electrocatalysis on Oxide Surfaces *ChemCatChem* **2011**, 3, 1159 – 1165
48. Koper, M. T. M. Thermodynamic theory of multi-electron transfer reactions: Implications for electrocatalysis *J. Electroanal. Chem.* **2011**, 660, 254–260.
49. Surendranath, Y.; Kanan, M. W.; Nocera, D. G. *J. Am. Chem. Soc.* **2010**, 132, 16501−16509.
50. Bediako, D. K.; Surendranath, Y.; Nocera, D. G. *J. Am. Chem. Soc.* **2013**, 135, 3662−3674.
51. Waegele, M. M.; Chen, X.; Herlihy, D. M.; and Cuk T. How Surface Potential Determines the Kinetics of the First Hole Transfer of Photocatalytic Water Oxidation *J. Am. Chem. Soc.* **2014**, 136, 10632−10639
52. Subbaraman, R.; Tripkovic, D.; Chang, K.-C.; Strmcnik, D.; Paulikas, A. P.; Hirunsit, P.; Chan, M,; Greeley, J.; Stamenkovic, V.; Markovic N. M. Trends in activity for the water electrolyser reactions on 3d M(Ni,Co,Fe,Mn) hydr(oxy)oxide catalysts, *Nature Mater.* **2012**, 11, 550–557
53. Hall, D. S.; Lockwood, D. J.; Bock C.; MacDougall, B. R. Nickel hydroxides and related materials: a review of their structures, synthesis and properties *Proc. R. Soc. A* **2014**, 471, 07
54. van der Ven, A.; Morgan, D.; Meng, Y. S.; Ceder, G. Phase stability of Nickel Hydroxides and Oxyhydroxides *Journal of The Electrochemical Society* **2006**, 153, A210-A215.
55. Diaz-Morales et al., Guidelines for the Rational Design of Ni-Based Double Hydroxide Electrocatalysts for the Oxygen Evolution Reaction *ACS Catal.* **2015**, 5, 5380−5387.
56. Trotochaud et al., Nickel−Iron Oxyhydroxide Oxygen-Evolution Electrocatalysts: The Role of Intentional and Incidental Iron Incorporation *J. Am. Chem. Soc.* **2014**, 136, 6744−6753.
57. Smith et al., Contributions to activity enhancement via Fe incorporation in Ni-(oxy)hydroxide/borate catalysts for near-neutral pH oxygen evolution *Chem. Commun.* **2015**, 51, 5261-5263.
58. Bediako et al., Mechanistic Studies of the Oxygen Evolution Reaction Mediated by a Nickel−Borate Thin Film Electrocatalyst *J. Am. Chem. Soc.* **2013**, 135, 3662−3674.
59. Zhiyi Lu et al., Three-dimensional NiFe layered double hydroxide film for high-efficiency oxygen evolution reaction *Chem. Commun.* **2014**, 50, 6479—6482.
60. Xiaohong Li et al., Nickel based electrocatalysts for oxygen evolution in high current density, alkaline water electrolysers *Phys. Chem. Chem. Phys.* **2011**, 13, 1162–1167.
61. Corrigan, D. A. The Catalysis of the Oxygen Evolution Reaction by Iron Impurities in Thin Film Nickel Oxide Electrodes *J. Electrochem. Soc.* **1987**,134, 2, 377-384.
62. Gong et al., An Advanced Ni−Fe Layered Double Hydroxide Electrocatalyst for Water Oxidation *J. Am. Chem. Soc.* **2013**, 135, 8452−8455.
63. Trotochaud, L.; Ranney, J. K.; Williams, K. N.; Boettcher, S. W. Solution-Cast Metal Oxide Thin Film Electrocatalysts for Oxygen Evolution. *J. Am. Chem. Soc.* **2012**, DOI 10.1021/ja307507a.
64. https://wiki.uoregon.edu/display/BOETTCHERLAB/Research+Vision
65. Chivot, J.; Mendoza, L.; Mansour, C.; Pauporté, T.; Cassir, M. New insight in the behaviour of Co–H2O system at 25–150 °C, based on revised Pourbaix diagrams *Corrosion Science* **2008**, 50, 62–69
66. Diaz-Morales, O.; Hersbach, T.J.P., Hetterscheid, D.G.H.; Reek, J.N.H; Koper, M.T.M. *J. Am. Chem. Soc.* **2014**, 136, 10432-10439.
67. Trześniewski, B. J.; Diaz-Morales, O.; Vermaas, D. A.; Longo, A.; Bras, W.; Koper, M. T.M.; Smith, W. A. In Situ Observation of Active Oxygen Species in Fe-Containing Ni-Based Oxygen Evolution Catalysts: The Effect of pH on Electrochemical Activity *J. Am. Chem. Soc.* **2015**, 137, 15112–15121
68. Zhang, M.; de Respinis, M.; Frei, H. M. *Nature Chem.* **2014**, 6, 362-367.
69. Jiao, F.; Frei, H. Nanostructured Cobalt Oxide Clusters in Mesoporous Silica as Efficient Oxygen-Evolving Catalysts, *Angew. Chem. Ed.* **2009**, 48, 1841-1844
70. Kanan, M. W.; Nocera, D. G. In Situ Formation of an Oxygen-Evolving Catalyst in Neutral Water Containing Phosphate and Co2+ *Science* **2008**, 321, 1072–1075.

71. Jagadale, A.D.; Dubal, D.P.; Lokhande C.D. Electrochemical behavior of potentiodynamically deposited cobalt oxyhydroxide (CoOOH) thin films for supercapacitor application, *Materials Research Bulletin* **2011**, 47, 672–676
72. Robinson, R.A.; Stokes, R.H. Electrolyte solutions 2nd edition, rev London, Butterworths, **1968**
73. Spray, R. L.; Choi, K.-S. Photoactivity of Transparent Nanocrystalline Fe2O3 Electrodes Prepared via Anodic Electrodeposition, *chem. mater.* **2009**, 21, 3701-3709
74. McDonald, K. J.; Choi, K.-S. A new electrochemical synthesis route for a BiOI electrode and its conversion to a highly efficient porous BiVO4 photoanode for solar water oxidation, *energy environ. Sci* **2012**, 5, 8553-8557
75. Morisaki, S.; Kawakami, K.; Baba, N. Formation of Nickel Oxyhydroxide Thin Films by Electrodeposition and Their Electrochromic characteristics, *Japanese journal of Applied Physics* **1988**, 27, 314-318
76. Joya, K. S.; Faheem, Y.; Ocakoglu, K.; van de Krol, R. Water-Splitting Catalysis and Solar Fuel Devices: Artificial Leaves on the Move *Angew. Chem. Int. Ed.* **2013**, 52, 10426–10437.
77. Sivula, K. Metal Oxide Photoelectrodes for Solar Fuel Production, Surface Traps, and Catalysis *J. Phys. Chem. Lett.* **2013**, 4, 1624-1633.
78. Abdi, F. F.; Han, L.; Smets, A. H. M.; Zeman, M.; Dam, B.; van de Krol R. Efficient Solar Water Splitting by Enhanced Charge Separation in a Bismuth Vanadate-Silicon Tandem Photoelectrode *Nature Comm.* **2013**, 4, 2195.
79. van de Krol, R.; Liang, Y.; Schoonman, J. Solar Hydrogen Production with Nanostructured Metal Oxides *J. Mater. Chem.* **2008**, 18, 2311-2320.
80. Osterloh, F.E. Inorganic Nanostructures for Photoelectrochemical and Photocatalytic Water Splitting. *Chem.Soc.Rev.* **2013**, 42, 2294-2320.
81. de Respinis, M.; De Temmerman, G.; Tanyeli, I.; van de Sanden, M. C. M.; Doerner, R. P.; Baldwin, M. J.; van de Krol, R. Efficient Plasma Route to Nanostructure Materials: Case Study on the Use of m-WO3 for Solar Water Splitting. *ACS Appl. Mater. Interfaces* **2013**, 5, 7621–7625.
82. Maijenburg, A. W.; Hattori, A. N.; de Respinis, M.; McShane, C. M.; Choi, K.-S.; Dam, B.; Tanaka, H.; ten Elshof, J. E. Ni and p-Cu2O Nanocubes with a Small Size Distribution by Templated Electrodeposition and Their Characterization by Photocurrent Measurement. *ACS Appl. Mater. Interfaces* **2013**, 5, 10938-10945.
83. Liang, Y.; Messinger, J. Improving BiVO4 Photoanodes for Solar Water Splitting through Surface Passivation. *Phys. Chem. Chem. Phys.* **2014**, 16, 12014-12020.
84. Abdi, F. F.; Firet, N.; van de Krol, R. Efficient BiVO4 Thin Film Photoanodes Modified with Cobalt Phosphate Catalyst and W-doping. *Chem Cat. Chem.* **2013**, 5, 490-496.
85. Duan, L.; Bozoglian, F.; Mandal, S.; Stewart, B.; Privalov, T.; Llobet, A.; Sun, L. A Molecular Ruthenium Catalyst with Water-Oxidation Activity Comparable to that of Photosystem II. *Nature Chemistry* **2012**, 4, 418–423.
86. Tong, L.; Duan, L.; Xu, Y.; Privalov, T.; Sun, L. Structural Modifications of Mononuclear Ruthenium Complexes: A Combined Experimental and Theoretical Study on the Kinetics of Ruthenium-Catalyzed Water Oxidation. *Angew. Chem. Int. Ed.* **2011**, 50, 445–449.
87. Vallés-Pardo, J. L.; Guijt, M. C.; Iannuzzi, M.; Joya, K. S.; de Groot, H. J. M.; Buda, F. Ab Initio Molecular Dynamics Study of Water Oxidation Reaction Pathways in Mono-Ru Catalysts. *ChemPhysChem* **2012**, 13, 140–146.
88. Joya, K.S.; de Groot, H.J.M. Efficient Water Splitting by Single Site Ruthenium Catalyst. Proceedings 4th European conference on chemistry and life sciences (4th ECCLS), **2011**, 51–54.
89. Joya, K.S. Molecular Catalytic System for Efficient Water Splitting. Ph.D. Thesis, Leiden University, The Netherlands, **2011**.
90. Joya, K. S.; Vallés-Pardo, J. L.; Joya, Y. F.; Eisenmayer, T.; Thomas, B.; Buda, F.; de Groot, H. J. M. Molecular Catalytic Assemblies for Electrodriven Water Splitting. *ChemPlusChem* **2013**, 78, 35–47.
91. Joya, K. S.; de Groot, H. J. M. Artificial Leaf Goes Simpler and More Efficient for Solar Fuel Generation. *ChemSusChem* **2014**, 7, 73–76.
92. Joya, K.S.; Joya, Y.F.; de Groot, H.J.M. Ni-Based Electrocatalyst for Water Oxidation Developed In-Situ in a HCO3−/CO2 System at Near-Neutral pH. *Adv. Energy Mater.* **2014**, 4, 1301929
93. Joya, K.S.; Takanabe, K.; de Groot, H.J.M. Surface Generation of a Cobalt-Derived Water Oxidation Electrocatalyst Developed in a Neutral HCO3−/CO2 System. *Adv. Energy Mater.* **2014**. DOI: 10.1002/aenm.201400252.
94. Swierk, J. R.; Mallouk, T. E. Design and Development of Photoanodes for Water-Splitting Dye-Sensitized Photoelectrochemical Cells. *Chem. Soc. Rev.* **2013**, 42, 2357.

95. Jiao, F.; Frei, H. Nanostructured Cobalt Oxide Clusters in Mesoporous Silica as Efficient Oxygen-Evolving Catalysts. *Angew. Chem.* **2009**, 121, 1873–1876.
96. Zhang, M.; de Respinis, M.; Frei, H. M. Time-Resolved Observations of Water Oxidation Intermediates on a Cobalt Oxide Nanoparticle Catalyst. *Nature Chem.* **2014**, 6, 362-367.
97. Klepser, B. M.; Bartlett, B. M. Anchoring a Molecular Iron Catalyst to Solar-Responsive WO3 Improves the Rate and Selectivity of Photoelectrochemical Water Oxidation. *J. Am. Chem. Soc.* **2014**, 136, 5, 1694–1697.
98. Tokunaga, S.; Kato, H.; Kudo, A. Selective Preparation of Monoclinic and Tetragonal BiVO4 with Scheelite Structure and Their Photocatalytic Properties. *Chem. Mater.* **2001**, 13, 4624-4628.
99. Yu J.; Kudo A. Effects of Structural Variation on the Photocatalytic Performance of Hydrothermally Synthesized BiVO4. *Adv. Funct. Mater.* **2006**, 16, 2163–2169.
100. Aiga, N.; Jia, Q.; Watanabe, K.; Kudo, A.; Sugimoto, T.; Matsumoto Y. Electron−Phonon Coupling Dynamics at Oxygen Evolution Sites of Visible-Light-Driven Photocatalyst: Bismuth Vanadate. *J. Phys. Chem. C* **2013**, 117, 9881−9886.
101. Abdi, F. F.; Savenije, T. J.; May, M. M.; Dam, B.; van de Krol, R. The Origin of Slow Carrier Transport in BiVO4 Thin Film Photoanodes: A Time-Resolved Microwave Conductivity Study. *J. Phys. Chem. Lett.* **2013**, 4, 2752–2757.
102. Liang, Y. Q.; Tsubota, T.; Mooij, L. P. A.; van de Krol, R. Highly Improved Quantum Efficiencies for Thin Film BiVO4 Photoanodes. *J. Phys. Chem. C* **2011**, 115, 17594–17598.
103. Abdi, F. F.; van de Krol, R. Nature and Light Dependence of Bulk Recombination in Co-Pi-Catalyzed BiVO4 Photoanodes. *J. Phys. Chem. C* **2012**, 116, 17, 9398–9404.
104. Kanan, M. W.; Nocera, D. G. In Situ Formation of an Oxygen-Evolving Catalyst in Neutral Water Containing Phosphate and Co2+. *Science* **2008**, 321, 1072–1075.
105. Cruz, J. C.; Baglio, V.; Siracusano, S.; Antonucci, V.; Aricò, A. S.; Ornelas, R.; Ortiz-Frade, L.; Osorio-Monreal, G.; Durón-Torres, S. M.; Arriaga, L. G. Preparation and Characterization of RuO2 Catalysts for Oxygen Evolution in a Solid Polymer Electrolyte. *Int. J. Electrochem. Sci.* **2011**, 6, 6607-6619.
106. Hoertz, P. G.; Staniszewski, A.; Marton, A.; Higgins, G. T.; Incarvito, C. D.; Rheingold, A. L.; Meyer, G. J. Toward Exceeding the Shockley-Queisser Limit: Photoinduced Interfacial Charge Transfer Processes that Store Energy in Excess of the Equilibrated Excited State. *J. Am. Chem. Soc.* **2006**, 128, 8234–8245.
107. Ferrere, S. New Photosensitizers Based upon [Fe(L)2(CN)2] and [Fe(L)3] (L = Substituted 2,2'-Bipyridine): Yields for the Photosensitization of TiO2 and Effects on the Band Selectivity. *Chem. Mater.* **2000**, 12, 1083–1089.
108. Joya, K. S.; de Groot, H.J.M. Electrochemical in situ Surface Enhanced Raman Spectroscopic Characterization of a Trinuclear Ruthenium Complex, Ru-red. *J. Raman Spec.* **2013**, 44, 1195–1199.
109. Joya, K. S.; Subbaiyan, N. K.; D'Souza, F.; de Groot, H. J. M. Surface-Immobilized Single-Site Iridium Complexes for Electrocatalytic Water Splitting. *Angew. Chem. Int. Ed.* **2012**, 51, 9601.
110. Peter, L. M.; Wijayanthab K. G. U.; Tahir A. A. Kinetics of light-driven oxygen evolution at α-Fe2O3 electrodes. *Faraday Discuss.* **2012**, 155, 309-322.
111. Trześniewski, B. J.; and Smith W. A. Photocharged BiVO4 photoanodes for improved solar water splitting *J. Mater. Chem. A* **2015** DOI: 10.1039/C5TA04716A.
112. Bediako, D. K.; Surendranath, Y.; and Nocera D. G. Mechanistic Studies of the Oxygen Evolution Reaction Mediated by a Nickel−Borate Thin Film Electrocatalyst *J. Am. Chem. Soc.* **2013**, 135, 3662−3674.
113. Barroso, M.; Mesa, C. A.; Pendlebury, S. R.; Cowan, A. J.; Hisatomi, T.; Sivula, K.; Gratzel, M.; Klug, D. R.; Durrant, J. R. Dynamics of Photogenerated Holes in Surface Modified α-Fe2O3 Photoanodes for Solar Water Splitting. *Proc. Natl. Acad. Sci. U.S.A.* **2012**, 109, 15640-15645.
114. Zhong, D. K.; Choi, S.; Gamelin, D. R. Near-Complete Suppression of Surface Recombination in Solar Photoelectrolysis by "Co-Pi" Catalyst-Modified W:BiVO4. *J. Am. Chem. Soc.* **2011**, 133, 18370-18377.
115. Klahr, B.; Gimenez, S.; Fabregat-Santiago, F.; Bisquert, J.; Hamann, T. W. Photoelectrochemical and Impedance Spectroscopic Investigation of Water Oxidation with "Co–Pi"-Coated Hematite Electrodes. *J. Am. Chem. Soc.* **2012**, 134, 16693−16700.
116. Mills, T. J.; Lin, F.; Boettcher, S. W. Theory and Simulations of Electrocatalyst-Coated Semiconductor Electrodes for Solar Water Splitting. *Phys. Rev. Lett.* **2014**, 112, 148304.
117. Surendranath, Y.; Kanan, M. W.; Nocera, D. G. Mechanistic Studies of the Oxygen Evolution Reaction by a Cobalt-Phosphate Catalyst at Neutral pH. *J. Am. Chem. Soc.* **2010**, 132, 16501–16509.
118. Trotochaud, L.; Mills, T. J.; Boettcher, S. W. An Optocatalytic Model for Semiconductor–Catalyst Water-Splitting Photoelectrodes Based on In Situ Optical Measurements on Operational Catalysts. *J. Phys. Chem. Lett.* **2013**, 4, 931–935.

119. Liu, R.; Zheng, Z.; Spurgeon, J.; Yang, X. Enhanced Photoelectrochemical Water-Splitting Performance of Semiconductors by Surface Passivation Layers. *Energy Environ. Sci.* **2014**, 7, 2504-2517.
120. Schley, N. D.; Blakemore, J. D.; Subbaiyan, N. K.; Incarvito, C. D.; D'Souza, F.; Crabtree, H. R.; Brudvig, G. W. Distinguishing Homogeneous from Heterogeneous Catalysis in Electrode-Driven Water Oxidation with Molecular Iridium Complexes. *J. Am. Chem. Soc.* **2011**, 133, 10473–10481.

Chapter 3

An efficient approach to nanostructure the surface of materials. The role of interfaces in W – WO_3 systems for solar water splitting

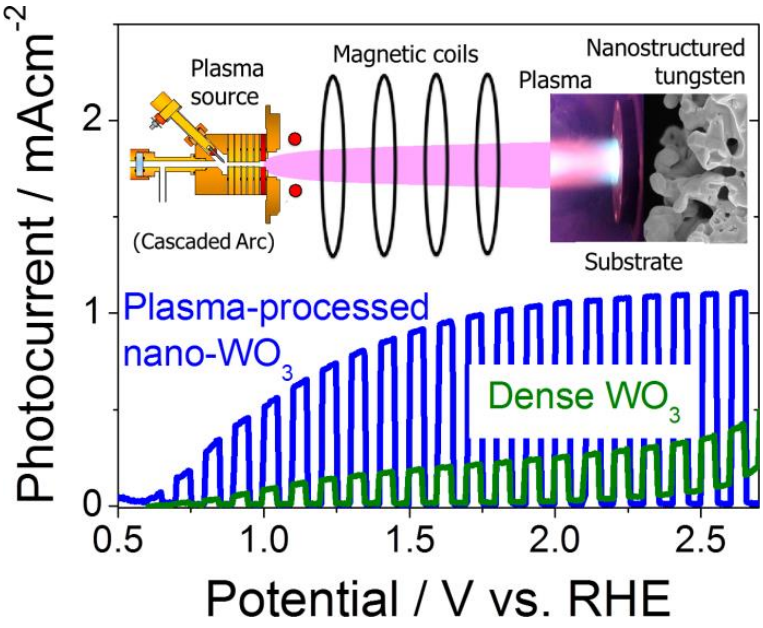

One of the main challenges in developing highly efficient nanostructured photoelectrodes is to achieve good control over the desired morphology and good electrical conductivity. In this chapter we present an efficient plasma-processing technique to form porous structures in tungsten substrates. The interface between the bulk substrate and the porous surface turned out to be very sensitive to the anneal conditions. While the substrate needs to remain metallic to preserve its conductive properties, the porous surface should be fully oxidized into WO_3 to get good semiconducting characteristics. After an optimized two-step anneal procedure, the mesoporous tungsten transforms into photoactive monoclinic WO_3, leaving the substrate in its original metallic state. The excellent control over the feature size and good contact between the crystallites with the plasma technique offers an exciting new synthesis route for nanostructured materials for e.g. solar water splitting.

This chapter is based on:
de Respinis, M., De Temmerman, G., Tanyeli, I., van de Sanden, M. C., Doerner, R. P., Baldwin, M. J., & van de Krol, R. Efficient Plasma-Route to Nanostructure Materials: Case Study on m-WO_3 for Solar Water Splitting *ACS applied materials & interfaces*, 2013, *5* (15), 7621-7625.

Introduction

One of the grand challenges for the 21st century is to secure the availability of energy on demand on the terawatt scale.[121] Moreover, environmental concerns result in the need for renewable energy sources to satisfy this demand. Direct photo-electrochemical conversion of solar energy into storable fuels, based on cheap and earth-abundant semiconductors and catalysts, has the potential to satisfy these requirements. Metal oxide semiconductors are particularly appealing candidates for practical applications due to their low-cost, non-toxicity, abundance, and stability towards corrosion.[122]

Despite intensive research efforts over the past 40 years, the efficiency of direct solar water splitting using metal oxides processed via scalable techniques still remains low.[123,124] One of the main bottlenecks for achieving high efficiencies with metal oxides is the mismatch between the absorption depth of visible light, up to micrometers, and the distance that the photo-generated charge carriers can travel before they recombine. The latter is often one order of magnitude shorter than the penetration depth of the light. A second limiting factor is the slow reaction kinetics at the surface of most metal oxides, especially for water oxidation.

Morphology control can overcome these challenges. Specifically, geometries with a large surface-to-volume ratio, such as nanowire arrays and porous nanostructures, will decrease the distance over which charge transport has to occur, and increase the amount of available surface area for catalytic reactions.[41,125,126] Although a great variety of techniques is nowadays available to fabricate nanostructured materials, it is often difficult to achieve the desired combination of properties. For example, standard approaches such as wet-chemical processing can give very homogeneous particle sizes, but the contact between the particles is often poor and a necking treatment may be needed to alleviate this limitation.[127]

In this chapter we propose a novel processing technique based on surface treatment of tungsten substrates by a high flux of low-energy helium ions. This provides an efficient route for the formation of porous metallic nanostructures that, after oxidation, can be used as photoanode for solar water splitting. Exposure of metal surfaces at elevated temperatures to high fluxes of low energy (<100 eV) helium ions has been shown to lead to the formation of a nanostructured surface morphology consisting of nanometric filaments.[128] The structure size can be controlled by the processing temperature, while the thickness of the

nanostructured layer depends on the processing time.[129] The porosity of the processed material is very high (up to 90%) and this yields a very high light absorption (up to 99%) across the whole visible spectrum[130]. Moreover, the continuous structure ensures that efficient charge transport through the structure is possible, without the need for post-deposition necking treatments.

Tungsten is chosen as case-study due to the high photocatalytic activity of its oxide, WO_3, in the monoclinic phase. Nanostructuring is essential for this material in order to address the mismatch between the intrinsically low light absorption coefficient ($1/\alpha$ = 6 μm at λ = 327 nm[131]) and the modest minority (hole) carrier diffusion length (~150 nm[12]). Previous studies have shown that nanoporosity indeed improves the incident photon-to-current efficiency (IPCE) of WO_3 photoanodes.[132] Santato *et al.* have reported on mesoporous nanocrystalline WO_3 photoanodes that showed an IPCE as high as 97% under UV illumination (380 nm) in the presence of a sacrificial hole scavenger (MeOH).[133,134,135] Berger *et al.* have shown that randomly oriented porous layers of WO_3 generate significantly higher photocurrents than compact layers due to different mechanisms of charge separation.[136] Tungsten oxide photo-electrodes for photo-electrochemical water splitting are mostly synthesized via sol-gel methods[126-128,137] or hydrothermal synthesis followed by calcination[138,139], and to lesser extent via CVD, pulsed electrodeposition, and reactive sputtering[140,141]. With most of these techniques, stoichiometric WO_3 is obtained during the synthesis process, and a standard thermal anneal is required to form the desired highly crystalline monoclinic phase. Other studies have been published on the formation of dense tungsten oxide films directly from tungsten metal by thermal treatment at elevated temperature[142,143,144,145]. However, poor control over the stoichiometry[136] and thickness of the oxide layer[137,138] have prevented any efficient application in solar water splitting. In this chapter, we will show how the novel plasma treatment technique can overcome these issues.

Experimental section

Polycrystalline tungsten discs (25 mm diameter, 1 mm thick) were cut from a rod of rolled tungsten (Plansee, 99.95 wt% purity) and mechanically polished to a mirror finish. After polishing they were rinsed in alcohol and acetone and no further treatment was applied. Surface nanostructuring was performed using high fluxes of low energy helium ions in a plasma generator (**Figure 3.1**). It has been previously demonstrated that the helium-induced nanostructure formation on tungsten surfaces worked best when the particle flux to the surface is higher than 7×10^{21} $m^{-2}s^{-1}$. The helium plasma is generated by a magnetically

confined arc discharge.[146] The nanorod dimensions (length, diameter) depend on the processing time and temperature respectively. For this case study, nanorod diameters in the range 100-200 nm were chosen. The nanostructure was formed by exposure to 150 eV helium ions with a flux of $8x10^{23}$ $m^{-2}s^{-1}$ at a surface temperature of 1700 K (1427°C) for a duration of 1000 s.

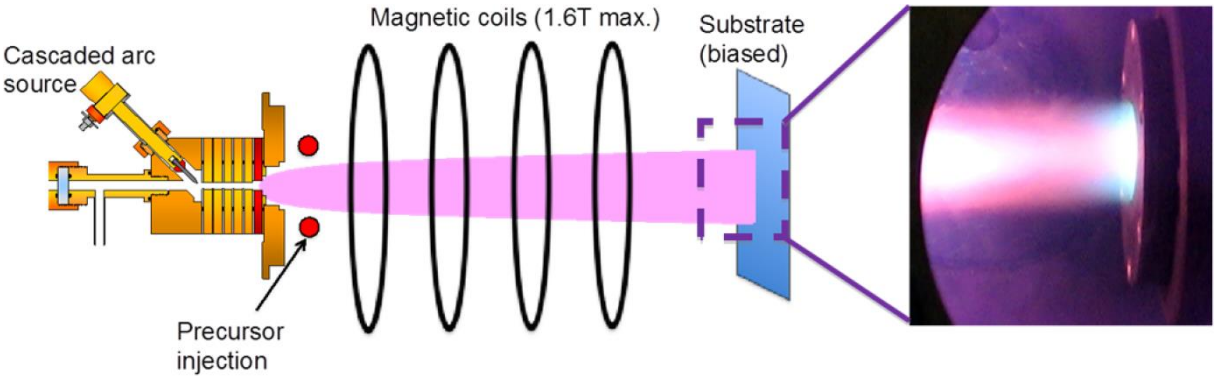

Figure 3.1 *Schematic overview of the high-flux plasma generator used to generate the helium-induced nanostructured surfaces. The plasma is generated by a cascaded arc discharge and confined by a strong magnetic field. The picture on the right side shows the high-intensity helium beam interacting with a tungsten surface.*

Nanostructured tungsten targets are annealed either with a single-step treatment at either of 500-550-600°C for 8 hours following a modified procedure from the literature[127], or via an optimized two-step thermal oxidative anneal to form WO_3. The procedure consists of a short-time thermal treatment of 2 hours at 550°C, followed by further annealing at 450°C for 4 hours (all in flowing O_2). Polished samples are annealed either under the same two-step procedure, or with a single-step treatment at 700°C for 60 minutes following a modified procedure from the literature.[135,138]

The crystal structure of the samples was determined using a Bruker D8 Advance X-ray diffractometer equipped with LynxEye linear detector in a Bragg-Brentano configuration. In-situ XRD was performed inside a Anton-Paar XRK-900 reactor chamber at in air at atmospheric pressure, a temperature ramp rate of 5°C/min, a temperature dwell of 20 min prior to the XRD measurement, at room temperature, then at steps of 50°C from 300°C to 600°C, cooling down at natural rate, at steps of 50°C. A Perkin Elmer Lambda 900 UV/VIS/NIR double-beam spectrophotometer with an integrating sphere was used for diffuse reflectance measurements.

Photoelectrochemical characterization was carried out in an aqueous 3M H_2SO_4 (95-97%, Sigma-Aldrich) solution. The faradaic efficiency of WO_3 in different electrolytes has recently been examined and it is noted that in H_2SO_4, WO_3 may produce persulfate more favorably than O_2.[152] However, this is not expected to change the photocurrent and the application of the right co-catalyst probably overcomes the issue. The solution was purged with nitrogen prior and during the measurements to remove any dissolved oxygen. Potential control was provided by a potentiostat (EG&G PAR 283) in a three-electrode cell with a fused silica window.[114] An Ag/AgCl electrode (XR300, Radiometer Analytical) and a coiled Pt wire were used as the reference and counter electrodes, respectively. White-light photocurrent densities were measured under simulated AM1.5 solar illumination (100 mW/cm^2) with a Newport Sol3A Class AAA solar simulator (type 94023A-SR3), whereas quantum efficiencies were measured with 300 W Xe-arc lamp (L.O.T. Oriel LSB530U), coupled into a grating monochromator (Acton SpectraPro 150i). An electronic shutter (Uniblitz LS6) and high-pass colored glass filters (Schott, two filters of 3 mm thickness each) were placed between the monochromator and the sample to remove second-order diffracted light. The intensity of the monochromatic light was measured with a calibrated photodiode (Ophir PD300-UV).

Results and discussion

Helium bombardment of tungsten surfaces may lead to strong microstructural changes such as dislocation loops, helium holes and bubbles, and formation of a fiber-formed nanostructure. The occurrence of those effects is strongly dependent on the surface temperature. The formation of helium-induced nanostructures on tungsten surfaces has been studied by our collaborators at the *Dutch Institute for Fundamental Energy Research* DIFFER. Tungsten samples were exposed to high fluxes (around 10^{24}m^{-2}s^{-2}) of pure helium plasma's in the temperature range 600-2400 °C.[122] **Figure 3.2** illustrates the effect of the surface temperature on the helium-induced morphology changes of tungsten surfaces bombarded by 45 eV helium ions. There is a strong correlation between the temperature during plasma exposure and the resulting surface structure size. At 1000 °C, nanoscopic filaments with a diameter lower than 20 nm are formed. When the temperature is increased to 1500 °C, the structure size is in the range 100–200 nm while micrometric voids are observed on the surface of the sample exposed at 2000 °C. A sharp boundary exists between the plasma-modified area and the undamaged bulk material. The thickness of the plasma-modified zone increases with the surface temperature similarly to the size of the near-surface voids.

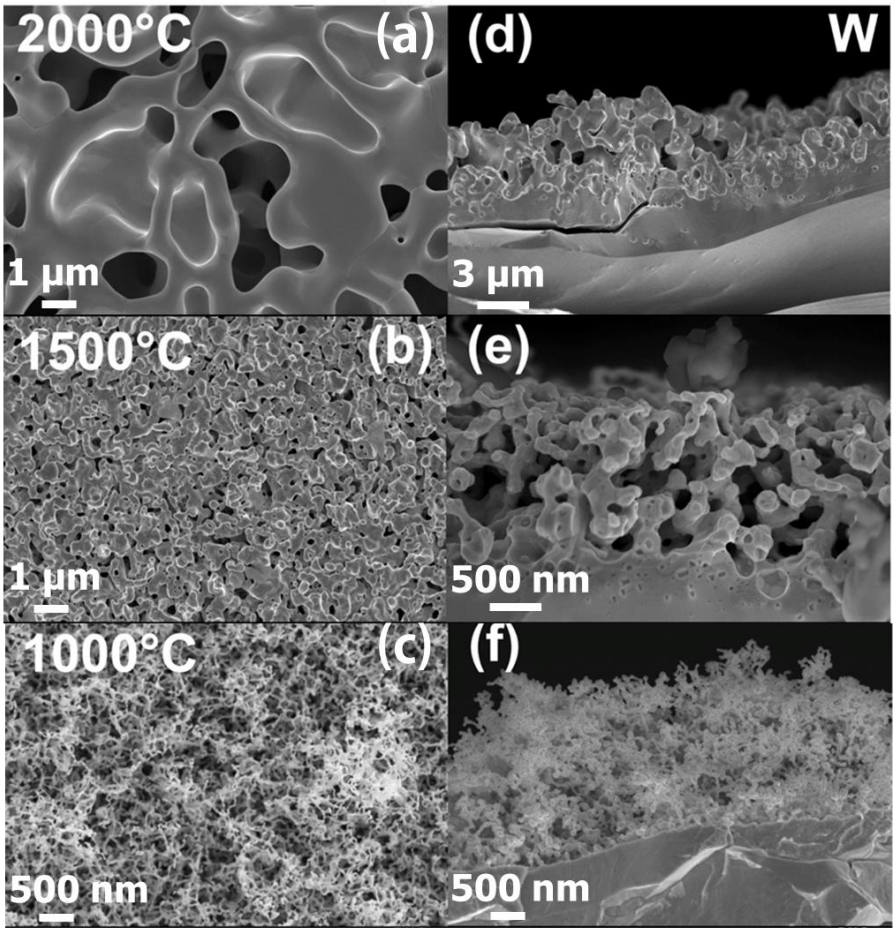

Figure 3.2 *SEM images of showing the evolution of the helium-induced surface morphology changes of tungsten surfaces as a function of the surface temperature during plasma exposure (E_{ion}=45 eV). For each temperature, top-views and cross-sections are shown on the left and right sides, respectively. The exposure duration was 1000 s for the samples prepared at 1500 °C and 2000 °C, and 500 s for the sample prepared at 1000 °C. Adapted from ref. [122].*

After treatment with low-energy helium ions, the tungsten surfaces exhibit a nanostructured surface morphology consisting of nanometric filaments with an open interconnected structure. ***Figure 3.3***(b) illustrates the typical morphology observed for a surface temperature of 1500 °C. The formation mechanism of such structures has been studied in detail, and appears linked to the formation and coalescence of helium bubbles in the near-surface region inducing swelling of the surface.[127] At 1500 °C, the nanoscopic filaments have a diameter of 100-200 nm (***Figure 3.3***a, b). We recently showed that these filaments have a crystalline inner structure.[122] The formation of such nanostructures occurs when the particle flux to the surface during processing is sufficiently high[147], i.e., when the helium

concentration in the near-surface region during the plasma processing is high enough for helium bubbles to grow and coalesce. With a porosity of up to 90%, the nanostructured tungsten absorbs between 94% and 97% of light in the visible range, whereas the polished targets reflect more than 50% of the light (***Figure 3.4***a,d and ***Figure 3.5***a). Although a detailed quantitative analysis of the porosity and specific surface area is beyond the scope of this study, non-oxidized metallic W films made with the same plasma technique by Kajita *et al.* indeed showed porosities of up to 90% at the surface and about 50% near the bottom of the nanostructure.[153] The specific surface area of these metallic W films, as measured by nitrogen adsorption (BET), can be ~20 times higher than the geometrical area.[154]

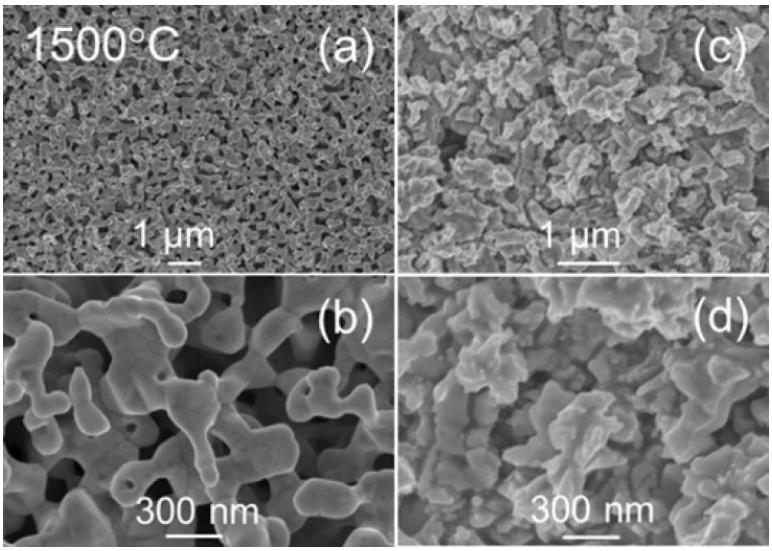

Figure 3.3 *SEM images of plasma-processed tungsten metal at two different magnifications (a,b) and the resulting WO_3 samples after the 2-step anneal (c,d).*

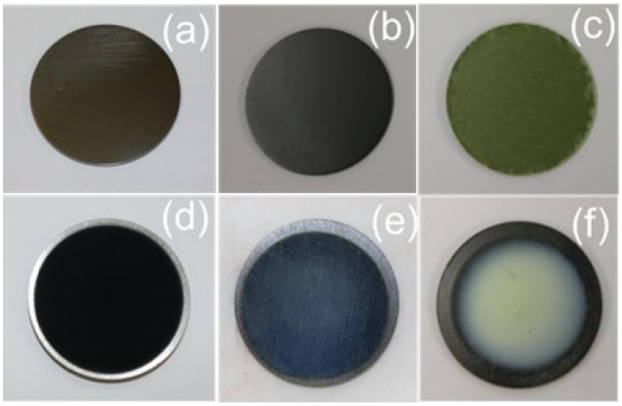

Figure 3.4 *Photographs of (a) polished tungsten, (b) polished tungsten after two-step anneal at 550/450°C, (c) polished tungsten after anneal at 700°C, (d) nanostructured tungsten, (e)*

nanostructured tungsten single-step annealed at 550°C (f) nanostructured tungsten after two-step anneal at 550/450°C.

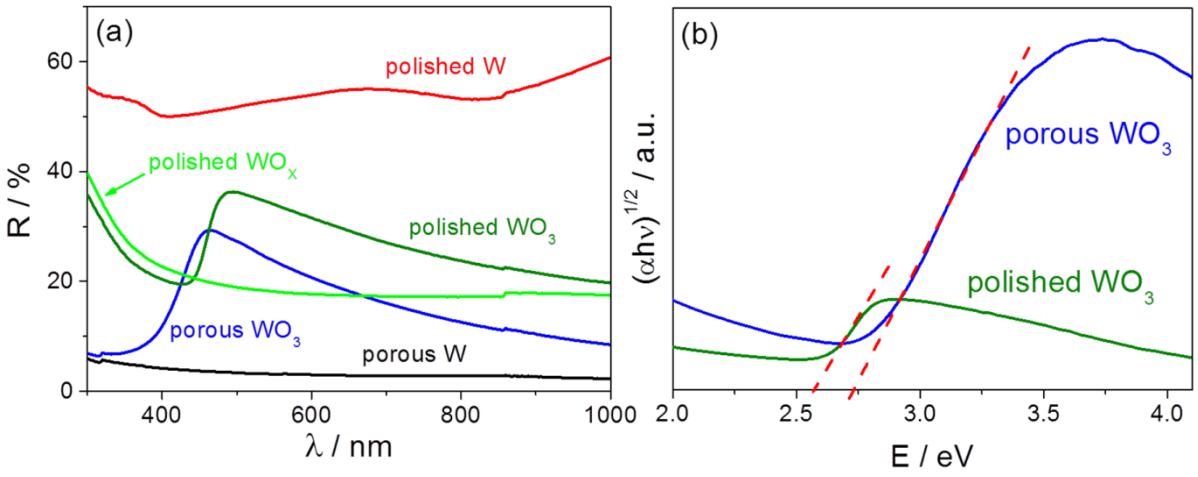

Figure 3.5 *a) Diffuse reflectance measurements of polished tungsten (red), polished tungsten after two-step anneal (green), nanostructured tungsten (black), nanostructured WO_3 after two-step anneal (blue), polished tungsten after anneal at 700°C (olive). b) Kubelka-Munk transformation of the reflectance curves for nanostructured WO_3 after two-step anneal (blue), and for polished W after anneal at 700°C (polished WO_3) (olive).*

After the plasma processing, the tungsten samples are annealed under a flow of oxygen in either one or two steps. This is done with the goal of getting a phase pure m-WO_3 in the nanoporous surface, while preserving the electrical conductivity of the metallic bulk. Moreover, the interfacial defects should be minimized, and should not act as severe recombination centers.

In-situ XRD measurements performed in air between room temperature and 600°C (***Figure 3.6***) reveal that the oxidation of bulk tungsten occurs starting at 500°C. Therefore it was chosen to anneal the samples at 500°C, 550°C or 600°C in air for 8 hours each. XRD measurements on those samples reveal the presence of peaks belonging to the desired monoclinic WO_3 phase (JCPDS reference files WO_3: PCPDF 83-0948) and possibly also the reflections from the 040 plane of a substoichiometric monoclinic $W_{24}O_{68}$ phase (JCPDS reference files PCPDF 36-0103), as shown in ***Figure 3.7***a. Raman spectra collected on the same samples reveal the presence of the W-O bending and W-O stretching modes characteristics for the monoclinic WO_3 phase (***Figure 3.7***b). Moreover, the absence of the 950 cm^{-1} band confirms the 1:3 stoichiometric ratio between W and O.[148] From the combination of XRD and Raman data we can describe our samples as composed of a superficial monoclinic WO_3 phase, and a substoichiometric WO_{3-x} (mostly $W_{24}O_{68}$) at the

interface with the metallic tungsten bulk. The challenge here is to minimize the formation of the interfacial WO_{3-x} layer, which generates defects likely to act as an important recombination center.

A detailed study of the lattice changes as a function of temperature gives useful information for the choice of a selective anneal procedure. By comparing the 2θ position as a function of the temperature, of the tungsten peak and the tungsten oxide peaks in the in-situ measurement of ***Figure 3.6***, it is observed that linear lattice expansion occurs for metallic W upon heating, while the tungsten oxide has a local maximum in unit cell parameters at 450°C. The lattice changes of tungsten and tungsten oxide are shown in ***Figure 3.8***. The observation of a local maximum in cell parameters at 450°C is the starting point towards the development of a two-step anneal procedure, since we may assume that at the maximum lattice volume the oxygen exchange is most efficient. Thus the first step is carried out at 550°C for 2 hours to obtain the desired monoclinic WO_3 (m-WO_3) phase.[128] While high temperatures favor fast crystallization, they also represent more strongly reducing conditions. To minimize the formation of a sub-stoichiometric WO_{3-x}, the sample is subsequently held at 450°C for 4 hours to fully oxidize the substoichiometric part of the sample before cooling down to room temperature. This temperature allows full oxidation of the mesoporous structure, while it is not high enough to promote extensive oxidation in the dense tungsten substrate underneath.

The effect of the two-step treatment can be seen by comparing ***Figure 3.4***e and ***Figure 3.4***f. Samples annealed with a single step at 550°C have a blue color (***Figure 3.4***e), indicating the presence of oxygen vacancies. The same blue color was also observed for annealing temperatures of 500 and 600°C and for a prolonged 8 hour treatment at 550°C, both in air and in O_2 flows (not shown). The blue coloration of the oxygen-deficient WO_{3-x} phase is well known and extensively documented in the literature.[138,149,150,151,152,153,154,155] After the second anneal for 4 h at 450°C the sample turns yellow (***Figure 3.4***f). This corresponds to the color of stoichiometric WO_3, indicating that the porous surface of the sample indeed fully oxidizes at this lower temperature.

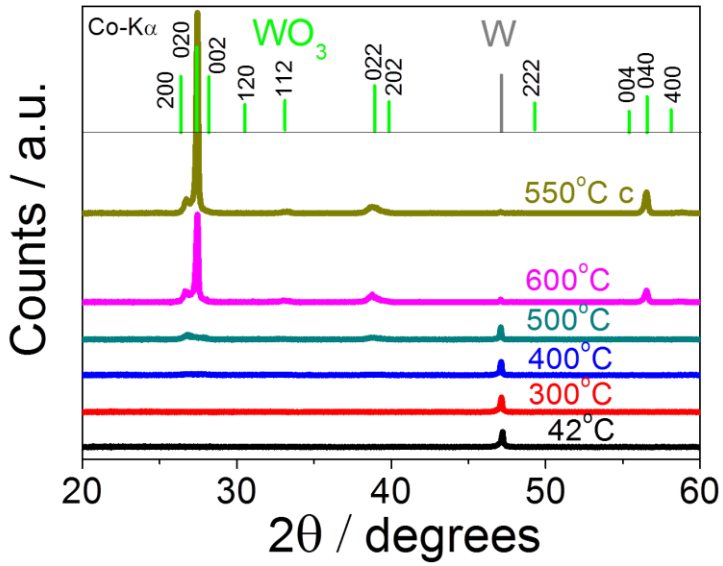

Figure 3.6 *In-situ XRD showing oxidation of bulk tungsten begins above 500°C. Measurements performed in air at atmospheric pressure, temperature ramp rate of 5°C/min, temperature dwell of 20 min prior to XRD measurement. International Centre for Diffraction Data (JCPDS) reference files; W: PCPDF 04-0806; WO_3: PCPDF 83-0948*

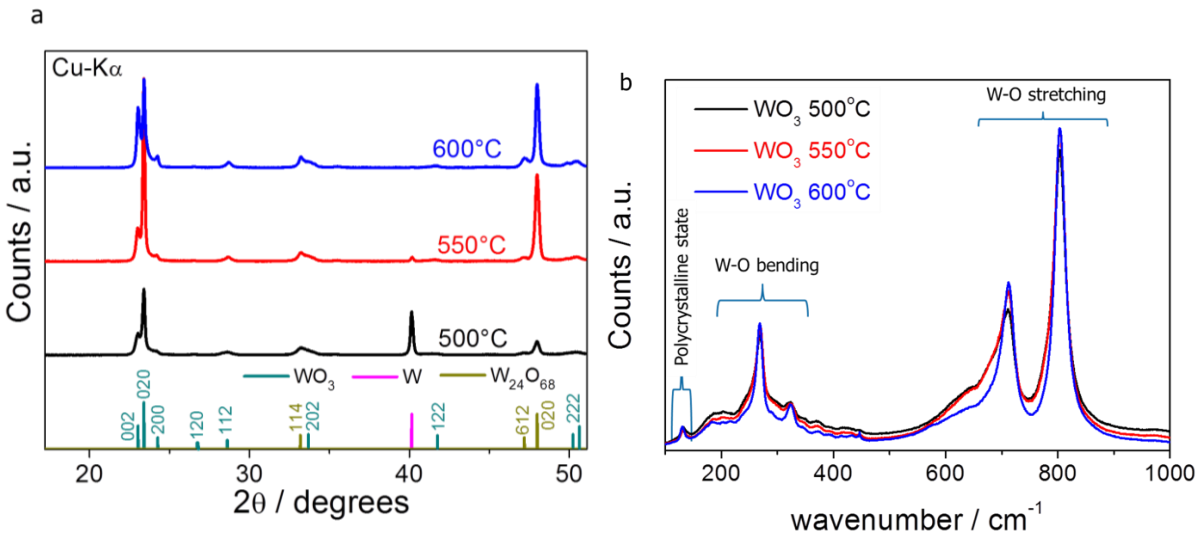

Figure 3.7 *XRD showing the presence of metallic tungsten, monoclinic WO_3 and a substoichiomeric phase identified as $W_{24}O_{68}$. The plasma-treated tungsten disk is converted into WO_3 and $W_{24}O_{68}$ as the temperature increases. JCPDS reference files for W: PCPDF 04-0806; WO_3: PCPDF 83-0948; $W_{24}O_{68}$: PCPDF 36-0103 (a). Raman spectra of the same samples showing the W-O bending and stretching modes characteristics for the monoclinic WO_3 phase. The absence of a band at 950 cm^{-1} indicates that there is no Raman signal from a substoichiometric WO_{3-x}.*

A more detailed analysis of the optical properties is shown in ***Figure 3.5***. After the two-step anneal, the porous WO_3 samples show a sharp decrease of the diffuse reflectance below ~470 nm that marks the optical absorption edge (band gap) of the material (***Figure 3.5***a). In contrast, polished samples annealed under the same two-step procedure do not show such a transition. This suggests that the oxidation of the surface of bulk tungsten is much slower than that of the porous nanostructured material. Firing the polished sample at a much higher temperature (700°C) leads to a greenish coloration of the sample (***Figure 3.4***c) and a sharp decrease in the reflectance below ~480 nm (***Figure 3.5***a) that is consistent with the presence of m-WO_3. X-ray diffraction indeed confirms the formation of a monoclinic WO_3 phase under these conditions (***Figure 3.9***). The fact that this sample looks greenish, i.e., a mixture of yellow and blue, suggests the presence of a significant amount of sub-stoichiometric WO_{3-x} underneath the surface.

The Kubelka-Munk transformation[155,156] of the diffuse reflectance curves, shown in ***Figure 3.5***b, shows bandgap values of 2.7 eV and 2.6 eV for the porous and polished m-WO_3 samples, respectively. In the literature the bandgap energy of WO_3 has been mainly measured by optical absorption, varying from about 2.5 to 3.0 eV[157,158.] According to Berger *et al.,* the bandgap of porous structures is the same as that for compact ones,[129] thus the different morphology cannot explain the different bandgaps in ***Figure 3.5***b. Instead, we attribute the difference to the different annealing conditions. This is consistent with other literature reports showing that the bandgap of WO_3 undergoes a red-shift upon annealing at higher temperatures.[131,132,159]

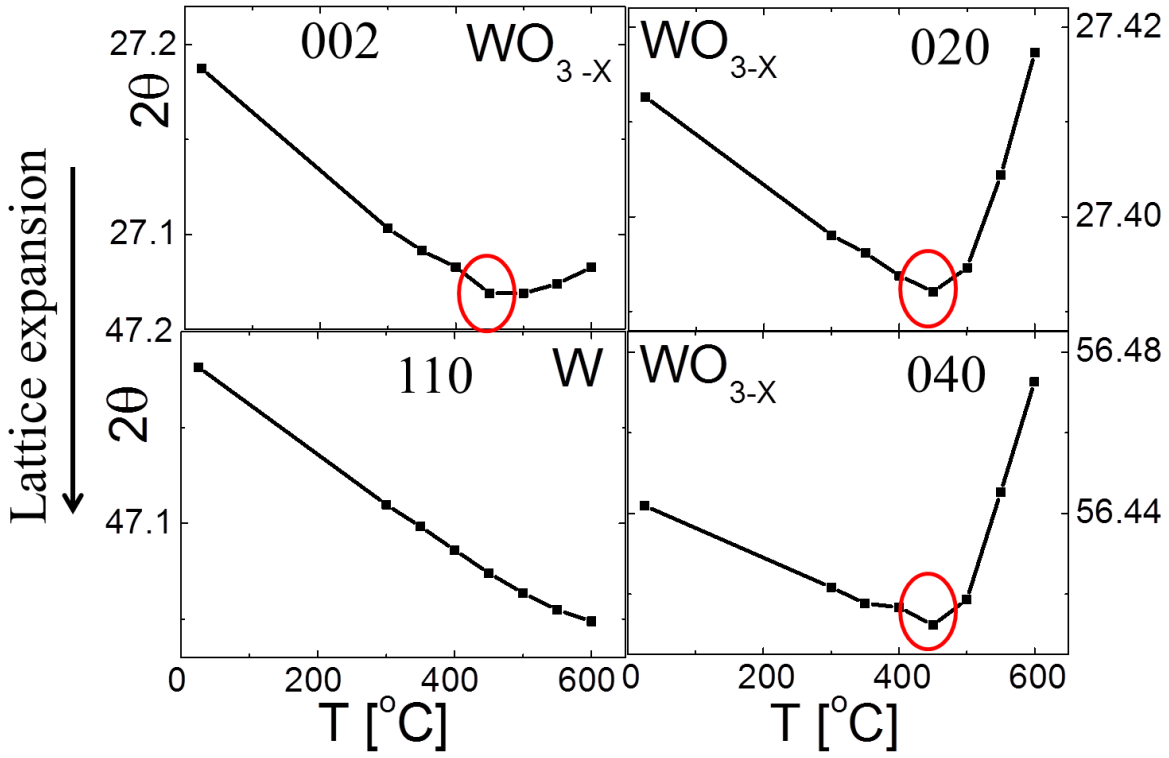

Figure 3.8 *In-situ XRD showing the lattice dynamics of the bulk tungsten and the superficial tungsten oxide as a function of temperature. Measurements performed in air at atmospheric pressure, temperature ramp rate of 5°C/min, temperature dwell of 20 min prior to XRD measurement. International Centre for Diffraction Data (JCPDS) reference files; W: PCPDF 04-0806; WO_{3-x}: PCPDF 36-0103.*

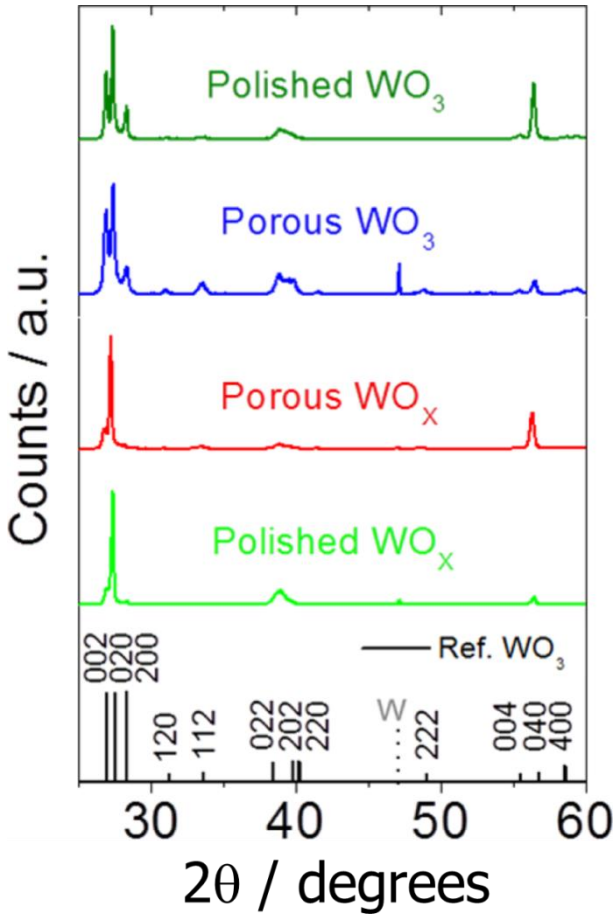

Figure 3.9 *XRD (Co-Kα source) of polished WO_x annealed at 550/450°C (green) – porous WO_x annealed at 550°C (red) – porous WO_3 annealed at 550/450°C (blue) – polished WO_3 annealed at 700°C (olive). During thermal anneal, the nanostructured tungsten is first converted into oxygen deficient WO_{3-x}, and then fully oxidized into WO_3. The latter process remains incomplete in the case of the polished samples. International Centre for Diffraction Data (JCPDS) reference files; W: PCPDF 04-0806; WO_3: PCPDF 83-0948*

The photo-electrochemical activity of the WO_3 samples was determined by measuring the current as a function of applied potential under chopped AM1.5 illumination (***Figure 3.10***). The porous nanostructured WO_3 sample made with the plasma processing method and annealed using the two-step procedure at 550/450°C shows a significantly higher photocurrent plateau value than the polished WO_3 sample annealed at 700°C: 6 times higher at 1.0 V vs. RHE, and 3 times higher at 2.5 V vs. RHE. The higher photocurrent of the nanostructured sample is attributed to three factors related to the morphology, and a fourth factor related to the composition at the bulk-porous interface. The first is the higher specific surface area, which greatly enhances the catalytic activity for water oxidation by creating

many more sites for the chemical reactions, thereby relaxing the requirements for the turnover frequency of each site. This is especially important at higher potentials, where charge separation is efficient and the surface reaction kinetics struggle to keep up with the rapid supply of photo-generated holes. The second factor is the enhanced absorption due to extensive light scattering in the nanostructured material. This is also evident from the smaller reflectance (i.e., larger absorbance) of the nanoporous vs. polished WO_3 in ***Figure 3.5***a. The third factor is the fact that the typical feature size (***Figure 3.2***b,e) is comparable to the minority carrier diffusion length (L_D ~150 nm[124]). This means that the photo-generated holes have no trouble to reach the semiconductor/electrolyte interface before they recombine. An important advantage of the plasma processing technique is that the small feature size is retained even deep within the bulk of the porous film, close to the interface with the metallic tungsten (***Figure 3.2***e). This is especially important when considering the intrinsically low optical absorption coefficient of WO_3 ($1/\alpha$ = 6 μm at λ = 327 nm[124]). The fourth factor is related to the two-step anneal procedure, which ensures a sharper structural change at the interface between the porous WO_3 surface and the compact W bulk, thereby minimizing the formation of the defect-rich WO_{3-x} layer.

A more detailed look at the voltammogram at low potentials of ***Figure 3.10***a reveals that the photocurrent of the nanostructured WO_3 increases more steeply than that of the compact WO_3. This is again a manifestation of the feature size being smaller than the minority carrier diffusion length. Within a distance L_D from the surface, all the holes can reach the electrolyte, even without the presence of an electric field. Thus at low applied potentials (close to V_{FB}), the porous sample will give higher currents because it has a larger surface area, i.e., there are more electron/hole pairs that are created within 150 nm of the surface than for the dense sample. At more positive potentials, the electric field can also separate the electron/hole pairs generated in the bulk of the material, so the difference between the two morphologies becomes less important.

The AM1.5 photocurrent density of our compact WO_3 is similar to the values reported in the literature[129,132,135,137]. In contrast, the photocurrent densities for our plasma-treated nanostructured WO_3 are significantly higher than literature values for porous WO_3 synthesized directly from metallic W (although an accurate quantitative comparison cannot be made due to different experimental conditions).[133]

Both the polished and the nanostructured WO_3 samples show an onset potential of ~0.6 V vs. RHE (***Figure 3.10***b). This is 0.2 V more positive than the flatband potential of WO_3, which

is at +0.4 V vs. RHE.[117] This difference is not unexpected for a metal oxide without a co-catalyst for O_2 evolution. In fact, for most (un-catalyzed) metal oxides the difference between the flatband potential and the photocurrent onset potentials is much larger.

The low photocurrent (0.2 $mAcm^{-2}$ at 1.23 V vs. RHE) of the porous WO_{3-x} sample annealed in a single step at 550°C (***Figure 3.10***a, red curve) is attributed to recombination at structural defects. These defects are presumably the oxygen vacancies that also cause the blue color of the material (***Figure 3.4***e), and were assigned by XRD mostly to a $W_{24}O_{68}$ interfacial phase. Minor changes in the photocurrent upon MeOH addition to the electrolyte (a hole scavenger) rule out the possibility that surface catalysis is a major limitation (see ***Figure 3.11***). Samples annealed in a single step at 500°C and 600°C show an overall comparable performance to the one annealed at 550°C. However, differences are still present and the photocurrent at 1.23 V vs. RHE is higher the lower the temperature. Similarly, the onset potential shifts cathodically from 600°C to 550°C and down to 500°C. This shift does not occur in the presence of 0.1M MeOH, indicating the formation of catalytic limitations when annealing at temperatures higher than 500°C (***Figure 3.11***).

Quantum efficiency measurements (IPCE) in ***Figure 3.12*** confirm the higher photo-response over the whole spectrum of above-bandgap light for the porous WO_3. The efficiency peaks at 370 nm and reaches a value of 22%. The bandgap of 2.65 eV obtained from the Tauc plot of the IPCE photocurrent (inset in ***Figure 3.12***b) matches the value from the diffuse reflectance spectra (***Figure 3.5***b) and values reported in the literature for monoclinic WO_3.

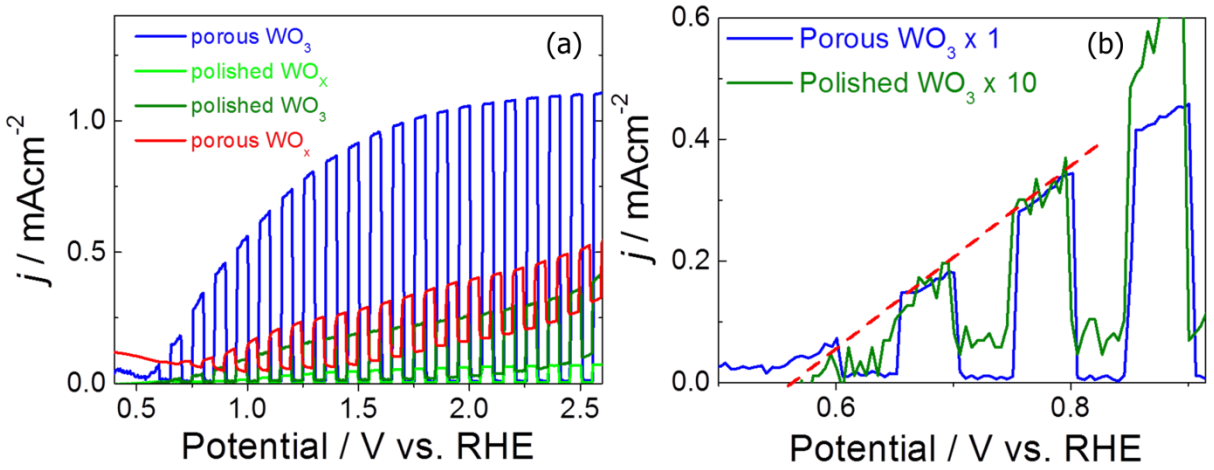

Figure 3.10 *(a) J-V curve under chopped AM1.5 illumination of polished tungsten after two-step anneal (polished WO_x, green), nanostructured WO_3 after two-step anneal (porous WO_3, blue),*

polished tungsten after anneal at 700°C (polished WO_3, olive), and nanostructured WO_X annealed at 550°C (porous WO_x, red). The scan rate was 10 mV/sec. (b) Photocurrent onset potential of ~ +0.6 V vs. RHE for both the porous WO_3 and polished WO_3 (multiplied 10x).

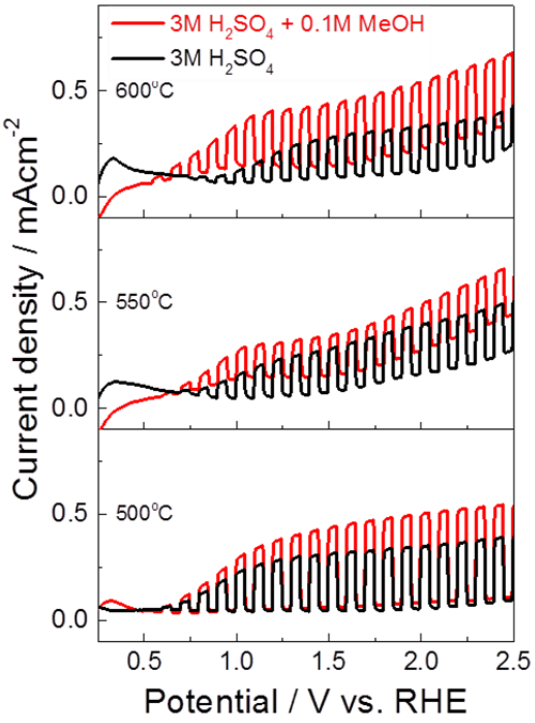

Figure 3.11 *J-V curve under chopped AM1.5 illumination of porous tungsten after single step anneal at 600°C (top), at 550°C (middle), at 500°C (bottom) in a 3M H_2SO_4 electrolyte and with the addition of 0.1M MeOH as a hole scavenger.*

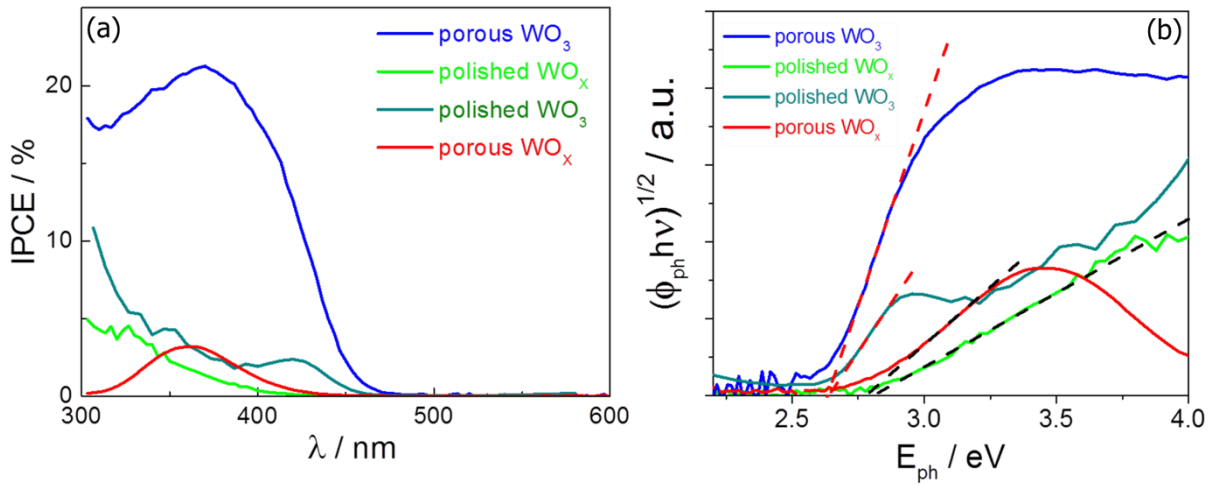

Figure 3.12 *(a) IPCE measured at 1.23 V vs. RHE and 2 nm/sec. (b) bandgap calculation.*

Conclusions

In summary, in this chapter we propose a novel plasma-assisted processing technique to generate surface nanostructures on metals. This top-down approach guarantees good contact between the different crystallites and avoids electrical conductivity limitations. After an optimized two-step anneal procedure that minimizes the concentration of interfacial defects, the mesoporous tungsten surface transforms into nanostructured monoclinic WO_3, while preserving the conductivity of the metallic tungsten bulk. These porous WO_3 films showed photocurrents up to 1 mA/cm^2, which is 5 times higher than dense, non-porous WO_3 samples made from a polished W disc. The excellent control over the feature size with the helium plasma technique along with its effectiveness with a broad range of metals offer an exciting new synthesis route for nanostructured materials for e.g. solar water splitting.

CHAPTER 3 REFERENCES

121. Lewis, N. S.; Nocera, D. G. *Proc. Natl. Acad. Sci. U.S.A.* **2006**, 103, 15729–15735.
122. Chen, X.; Shen, S.; Guo, L.; Mao, S. S. *Chem. Rev.* **2010**, 110, 6503-6570.
123. Zou, Z.; Ye, J.; Sayama, K.; Arakawa, H. *Nature* **2001**, 414, 625-627.
124. Alexander, B.D.; Kulesza, P.J.; Rutkowska, I.; Solarska, R.; Augustynski, J. *J. Mater. Chem.* **2008**, 18, 2298-2303.
125. Van de Krol, R.; Liang, Y.; Schoonman, J. *J. Mater. Chem.* **2008**, 18, 2311-2320.
126. Thomann, I.; Pinaud, B. A.; Chen, Z.; Clemens, B. M.; Jaramillo, T. F.; Brongersma, M. L. *Nano Lett.* **2011**, 11, 3440–3446.
127. Abe, R.; Higashi, M.; Domen, K. *J. Am. Chem. Soc.* **2010**, 132, 11828-11829.
128. Baldwin, M.J.; Doerner, R.P. *Nucl. Fusion* **2008**, 48, 035001–1-6.
129. De Temmerman, G.; Bystrov, K.; Zielinski, J.J.; Balden, M.; Matern, G.; Arnas, C.; Marot, L. *J. Vac. Sci. Technol. A* **2012**, 30, 041306–1-6.
130. Kajita, S.; Saeki, T.; Yoshida, N.; Ohno, N.; Iwamae, A. *Appl. Phys. Express* **2010**, 3, 085204–1-3.
131. Butler, M.A.; *J. Appl. Phys.* **1977**, 48, 5, 1914-1920.
132. Chen, X.; Ye, J.; Ouyang, S.; Kako, T.; Li, Z.; Zou Z. *ACSNano* **2011**, 5, 6, 4310-4318.
133. Santato, C.; Ulmann, M.; Augustynski; J.; *J. Phys. Chem. B* **2001**, 105, 936–940.
134. Santato, C.; Ulmann, M.; Augustynski, *J. Adv. Mater.* **2001**, 13, 511–514.
135. Santato, C.; Odziemkowski, M.; Ulmann, M.; Augustynski, J. *J. Am. Chem. Soc.* **2001**, 123, 10639–10649.
136. Berger, S.; Tsuchiya, H.; Ghicov, A.; Schmuki, P. *Appl. Phys. Lett.* **2006**, 88, 203119–203122.
137. Hsiao, P.-T.; Chen, L.-C.; Lia, T.-L.; Teng, H. *J. Mater. Chem.* **2011**, 21, 19402-19409.
138. Qin, D.-D.; Tao, C.-L.; Friesen, S. A.; Wang, T.-H.; Varghese, O. K.; Bao, N.-Z.; Yang, Z.-Y.; Mallouk, T. E.; Grimes, C. A. *Chem. Commun.* **2012**, 48, 729–731.
139. Hong, S.J.; Jun, H.; Borse, P.H.; Lee, J.S. *Int. J. Hydrogen energy* **2009**, 34, 3234-3242.
140. Baeck, S. H.; Jaramillo, T.; Stucky, G. D.; McFarland, E. W. *Nano Lett.* **2002**, 2, 831-834.
141. Vemuri, R.S.; Engelhard, M.H.; Ramana, C.V. *ACS Appl. Mater. Interfaces* **2012**, 4, 1371−1377.
142. Gissler W.; Memming R. *J. Electrochem. Soc.* **1977**, 124, 1710-1714.
143. Gu, G.; Zheng, B.; Han, W. Q.; Roth, S.; Liu, J. *Nano Lett.* **2002**, 2, 8, 849-851.
144. Spichiger-Ulmann M.; Augustynski J. *J. Appl. Phys.* **1983**, 54, 10, 6061-6064.
145. Cifuentes, S.C.; Monge, M.A.; Pérez, P. *Corros. Sci.* **2012**, 57, 114–121.
146. Van Rooij, G.J.; Veremiyenko, V.P.; Goedheer, W.J.; de Groot, B.; Kleyn, A.W.; Smeets, P.H.M.; Versloot, T.W.; Whyte, D.G.; Engeln, R.; Schram, D.C.; Lopes Cardozo N. *J. Appl. Phys. Lett.* **2007**, 90, 121501, 1-3.
147. Krashenninikov, S.I.; *Phys. Scr.* **2011**, T145, 014040, 1-4.
148. Augustynski et al.; On Solar Hydrogen & Nanotechnology; Wiley, **2010**
149. Al Mohammad, A.; Gillet M. *Thin Solid Films* **2002**, 408, 302–309.
150. Granqvist, C.G. *Sol. Energy Mater. Sol. Cells* **2000**, 60, 201-262.
151. Sato, R.; Kawamura, N.; Tokumaru, H.; *Appl. Surf. Sci.* **2008**, 254, 7676–7678.
152. Wriedt, H.A. *Bull. Alloy Phase Diagr.* **1989**, 10, 368-384.
153. Migas, D. B.; Shaposhnikov, V. L.; Rodin, V. N.; Borisenko, V. E. *J. Appl. Phys.* **2010**, 108, 093713–1-7.
154. Sikka, V. K.; Rosa, C. *J. Corros. Sci.* **1980**, 20, 1201-1219.

155. Murphy, A.B. *Sol. Energy Mater. Sol. Cells* **2007**, 91, 1326-1337.
156. Lopez, R.; Gomez, R. *J. Sol-Gel Sci. Technol.* **2012**, 61, 1–7.
157. González-Borrero, P.P.; Sato, F.; Medina, A.N.; Baesso, M.L.; Bento, A.C.; Baldissera, G.; Persson, G.; Niklasson, G.A.; Granqvist, C.G.; Ferreira da Silva, A. *Appl. Phys. Lett.* **2010**, 96, 061909–1-3.
158. Liu, X.; Wang, F.; Wang, Q. *Phys. Chem. Chem. Phys.* **2012**, 14, 7894–7911.
159. Ahn, K.-S.; Lee, S.-H.; Dillon, A.C.; Tracy C.E.; Pitts, R. *J. Appl. Phys.* **2007**, 101, 093524–1-4.
160. Mi, Q.; Zhanaidarova, A.; Brunschwig, B.S.; Gray, H.B.; Lewis N.S. *Energy Environ. Sci.* **2012**, 5, 5694-5700.
161. Kajita, S.; Yoshida, N.; Yoshihara, R.; Ohno, N.; Yokochi, T.; Tokitani, M.; Takamura, S. *J. Nucl. Mater.* **2012**, 421, 22–27.
162. Yajimaa, M.; Hatanob, Y,; Kajitac, S.; Shib, J.; Harab, M.; Ohno N. *J. Nucl. Mater.* **2013**, 438, S1142–S1145.
163. Bange, K. *Sol. Energy Mater. Sol. Cells* **1999**, 58, 1-131.

Chapter 4

Tantalum (Oxy)Nitride Photoanodes for Solar Water Splitting

4.1 Oxynitrogenography: the Controlled Synthesis of Single Phase Tantalum Oxynitride Photoabsorbers

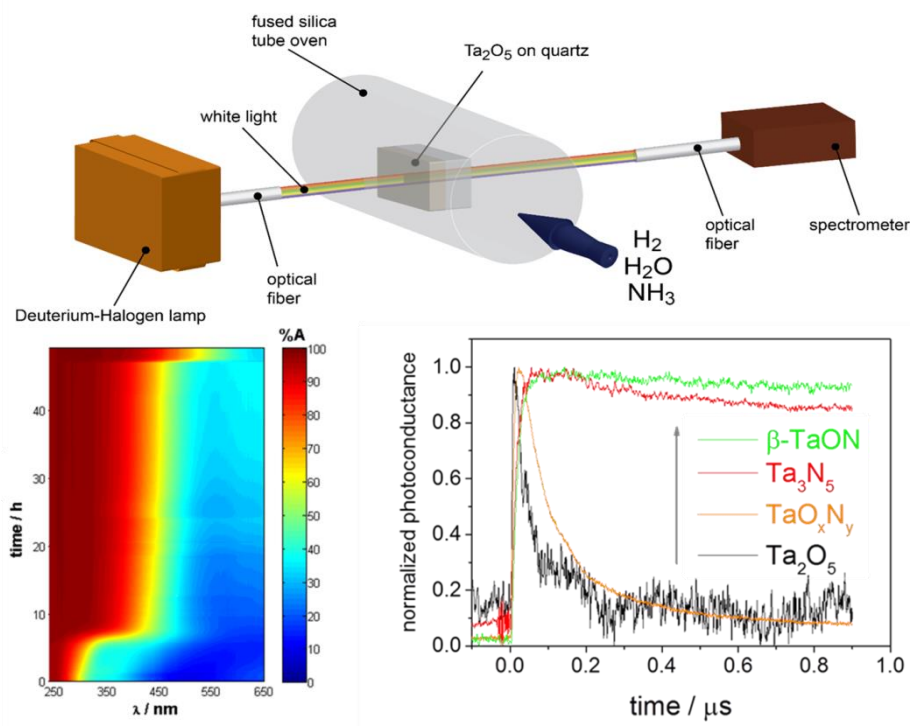

We propose an in-situ UV-vis monitoring technique called 'oxynitrogenography' as an approach towards the controlled and reproducible synthesis of thin films of different Ta-O-N phases, including the elusive β-TaON phase. The optical absorption changes are measured during annealing of the film at increasing NH_3/H_2O ratios, and can be directly correlated to the presence of different phases (Ta_2O_5, β-TaON, mixed TaON-Ta_3N_5, Ta_3N_5) due to the abrupt change in the absorption edge. After additional XRD analysis, the thermodynamic equilibrium conditions to obtain these various phases are determined, and a phase diagram is constructed. We observe that there is a very narrow range of parameters for the thermodynamic stability of the β-TaON phase. We observe that the carrier mobility increases

with the nitrogen content in the sample, from 10^{-5} cm^2/Vs in Ta_2O_5, to 10^{-2} cm^2/Vs in β-TaON and the mixed TaON-Ta_3N_5, until 10^{-1} cm^2/Vs in Ta_3N_5. While the carrier mobility of β-TaON and Ta_3N_5 is comparable to that of $BiVO_4$, the lifetime in the order of milliseconds is comparable to that of crystalline silicon. This is much higher than previously reported and compares favorably with the currently most promising metal oxide-based semiconductors ($BiVO_4$, Fe_2O_3, WO_3, Cu_2O) for photo-electrochemical (PEC) water splitting. Although these long lifetimes may be partly caused by (de-)trapping from shallow trap states, these results clearly demonstrate that a high phase purity is an essential prerequisite for efficient (oxy)nitride-based absorber materials.

This chapter is based on:
de Respinis, M.; Fravventura, M.; Abdi, F. F.; Schreuders, H.; Savenije, T. J.; Smith, W. A.; Dam, B.; and van de Krol, R. *Chem. Mater.*, **2015**, 27 (20), pp 7091–7099.

Introduction

Oxynitrides and nitrides have recently attracted much attention in the field of solar energy conversion.[160] While transition metal oxide semiconductors are particularly appealing candidates for photo-electrochemical conversion of solar energy into storable fuels due to their low-cost, non-toxicity, abundance, and stability towards corrosion, hardly any of them fulfills the requirements to reach the goal of 10% solar-to-hydrogen (STH) conversion efficiency.[39] This is mostly due to their poor carrier conductivity, while in addition their bandgaps are usually too large to efficiently absorb sunlight. To reduce the bandgap, nitrogen is incorporated into metal oxides, leading to nitrogen-doped oxide, oxynitride or nitride phases. This is a promising approach, since the N-2p orbitals are energetically more shallow than the deep O-2p orbitals.[161,162,163,164,177] Among the various nitride and oxynitride compounds considered, tantalum nitride (Ta_3N_5) and tantalum oxynitride (β-TaON) are particularly attractive because of their bandgaps (2.1 eV and 2.4 eV, respectively) and the high energetic position of Ta 5d orbitals, which form the conduction band in these materials. The conduction and valence band edges are in a favorable position to enable hydrogen and oxygen evolution without the need for an externally applied potential (see **Figure 4.1**). Tantalum (oxy-)nitrides suffer from their intrinsic thermodynamic instability when illuminated under the harsh conditions required for water oxidation.[165,166,167] However, this problem seems to be solvable; deposition of an efficient co-catalyst (e.g. CoO_x,[168,169] Co-Pi[170]) on the surface of the tantalum (oxy-)nitrides ensures that the water oxidation reaction is favored over the self-degradation over at least 1 hour. Moreover, important progress has recently been made in prolonging the lifetime of unstable photoelectrodes by depositing thin protective layers.[171,172,173,174,175,176.]

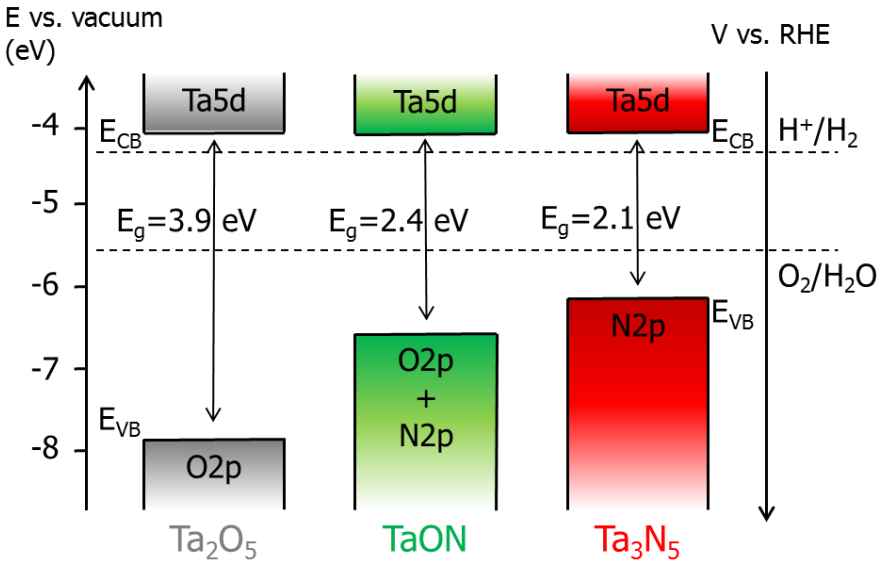

Figure 4.1. *Band diagram of Ta-oxide, Ta-oxynitride and Ta-nitride showing the increase in the energy of the valence band edge on nitridation, after ref. [177]*

The tantalum nitride phase can be readily obtained by nitridation of tantalum oxide under a flow of ammonia.[178,179,180,181,182] The nitridation of tantalum oxide under ammonia flow at high temperature is essentially governed by the reaction of the oxide with ammonia (or decomposed gases) and the competitive reverse reaction with the produced water. Both experimental and calculated thermodynamic diagrams as a function of the oxygen chemical potential have been proposed in the literature and the importance of water is well documented.[183,186] While highly efficient photocatalytic β-TaON particles have been reported in the literature, the ability to make the desired β-TaON phase depends very sensitively on the nitridation conditions of Ta_2O_5.[166,184] As a result, recipes used by individual groups can be difficult to reproduce in other labs due to small differences in the experimental setups and local conditions, and the material's purity. Moreover, transfer of these recipes to thin films may not be straightforward due to possible strain effects and differences in surface energies. For example, in our previous work we were unable to form single phase β-TaON thin films in either wet or dry ammonia.[185,188] Moreover, while a significant amount of literature is available on its crystal and electronic structure,[186,187,188,189] and photoelectrochemical performance,[166,168] to date a quantitative analysis of the carrier mobility and lifetime of β-TaON is missing.

In our previous approach we attempted to form the β-TaON thin film phase by kinetic quenching of the transformation process from the oxide to the nitride phase in a flow of ammonia.[194] Here we aim to establish a *thermodynamic equilibrium* by controlling the gas

composition, i.e., a balanced supply of nitrogen (in the form of ammonia), hydrogen, and oxygen (in the form of water) and allowing for thermal equilibration, followed by a rapid cooling down to room temperature. Without individual control over both the $p(H_2)$ and the $p(H_2O)$, the thermodynamic conditions are not unambiguously defined and the conversion cannot be controlled to the extend necessary for easy transfer of recipes to other setups – even though the conversion may be perfectly reproducible within the same reactor. In this approach, tantalum oxide thin films are nitridized by ammonolysis in a tube furnace under a controlled flow of ammonia, water and hydrogen, while following the optical transmission of the film in-situ. We call this process, where we exchange oxygen with nitrogen in a controlled and reversible fashion while monitoring the induced changes in the optical absorption of the material, 'oxynitrogenography'. The name is inspired by the 'hydrogenography' combinatorial optical monitoring technique where the metal-hydrogen phase diagram is probed in a similar fashion.[190] The control over the phase transformation process in oxynitrogenography will allow us to identify the conditions needed to produce high-quality metal (oxy)nitrides. We study these films with time-resolved microwave conductivity to quantify for the first time the carrier mobility and lifetime in tantalum oxynitride thin films as a function of the nitrogen content in the material.

Experimental section

Films synthesis: Oxynitrogenography. The synthesis of Ta_2O_5 thin films has been described previously.[179,191,188] In brief, a Ta film (99.95% purity) was sputtered onto fused silica substrates (ESCO S1-UV, 1 mm thick) in 3 µbars partial pressure of Ar (20 ml/min flow) with 100W DC electric power, and a substrate temperature of 400°C. A 5 nm Ti adhesion layer was deposited first, followed by a 60 nm Ta film. After deposition, the samples were oxidized for 5 hours at 650 °C in flowing air to form Ta_2O_5. The nitridation of the Ta_2O_5 thin film was monitored in-situ via optical spectroscopy,[179] as shown in ***Figure 4.2***. The sample is illuminated by a balanced deuterium-halogen lamp (DH-2000-BAL, Ocean Optics) via a solarization-resistant optical fiber / collimator assembly, which provided a nearly parallel beam of light with a diameter of ~5 mm at the sample position. The transmitted light is then collected by another optical fiber /collimator assembly and delivered to a spectrometer (MAYA 2000-Pro, Ocean Optics) with a 200 – 1100 nm detection range. This allowed us to accurately determine the change in the optical absorption edge upon inclusion of nitrogen into the lattice. All oxy-nitridation experiments were performed in a furnace with a fused silica reactor tube at 1100 K.[186] During the oxy-nitridation process, H_2O vapor was introduced

into the oven by a water-saturated flow of Ar carrier gas. A summary of the gas flows used is shown in **Table 4.1**. The same gas flows were used during the cooling-down process.

Table 4.1. *Gas flow parameters as used in the oxynitrogenography experiments. In the leftmost column are the ammonia/hydrogen ratios as reported in Figures 3 and 4. The other columns represent the actual flows used.*

$p(NH_3)/p(H_2)^{3/2}$	5% H_2/Ar (ml/min)	NH_3 (ml/min)	Ar/H_2O (ml/min)
30	44.63	100	0.675
10	80	80	1.21
3	80	24	1.21
1	80	8	1.21
0.3	80	2.4	1.21
0.1	80	0.8	1.21

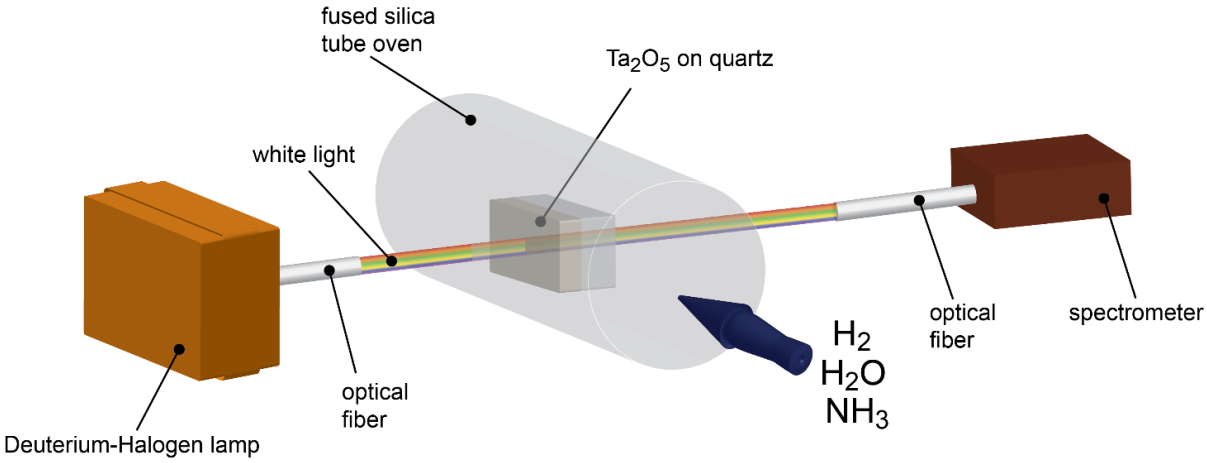

Figure 4.2*. In-situ optical monitoring setup herewith called 'oxynitrogenography'. The Ta_2O_5 thin film is placed in a tube furnace at 1100 K under a controlled gas mixture; the induced change in optical absorption is monitored by in situ UV-vis measurements.*

Structure and morphology. The crystal structure of the samples was determined using a Bruker D8 Advance X-ray diffractometer equipped with LynxEye linear detector in a Bragg-Brentano configuration, and with a cobalt source (Co-Kα_1 λ=1.788965, Co-Kα_2 λ =1.792850). A Perkin Elmer Lambda 900 UV/vis/NIR double-beam spectrophotometer with an integrating sphere was used for diffuse reflectance measurements. The morphology and chemical composition of thin films were investigated with scanning electron microscopy (SEM) and energy dispersive X-ray spectroscopy (EDS), respectively (JEOL JSM-6010LA equipped with a tungsten hairpin filament and an energy dispersive X-ray microanalyser). The samples were

investigated in the secondary electron imaging mode (SEI), using an Everhart-Thornley type of detector. SEM images were collected using the accelerating voltage of 5 kV. The X-ray spectra were recorded with an energy dispersive spectrometer equipped with a silicon-drift detector, using the accelerating voltage of 20 kV. AFM surface scans were performed using an NT-MDT Ntegra system coupled to an NT-MDT P8 XPM controller, with an NT-MDT NSG30 cantilever mounted. Scans were taken in semi-contact mode over an area of 20x20 μm, with a 0.5 Hz frequency and a resolution of 512x512 points. The thickness of the thin films was measured by means of a Dektak step profilometer.

Composition. The composition of the Ta-O-N films was analyzed using X-ray photoelectron spectroscopy (XPS) technique. The samples were placed in the Thermo-Scientific K-Alpha XPS instrument one day prior to the measurements and the instrument was pumped to achieve the appropriate vacuum. The XPS instrument used is equipped with a monochromatic Al-Kα radiation source. We use ion etching to study the depth dependence of the composition.

Optoelectronic properties. Time resolved microwave conductivity (TRMC) measurements were carried out to determine the lifetime and mobility of the photo-generated carriers. For this, the samples were mounted in a microwave cavity cell and placed within the setup described elsewhere.[192,193] The X-band (8.2-12.4 GHz) microwaves are generated using a Gunn diode. The experiments were carried out at 8.44 GHz, the resonant frequencies of the loaded cavity. During the measurements, a change in the microwave power reflected by the cavity upon nanosecond pulsed laser excitation (3.5 ns FWHM), ΔP/P, is monitored and correlated to the photoinduced change in the conductance of the sample, ΔG, by $\Delta P(t)/P = -K\Delta G(t)$. Here, K is the sensitivity factor derived from the resonance characteristics of the cavity and the dielectric properties of the medium. The change in conductance is then associated with the product of the ratio of mobile charge carriers normalized to the number of absorbed photons (φ) and the sum of their mobilities ($\mu_e + \mu_h$) according to the relation $\varphi\Sigma\mu = \frac{\Delta G}{I_0 \beta e F_A}$, where I_0 is the intensity per pulse, e is the elementary charge, β is a factor related to the inner dimensions of the waveguide and F_A is the fraction of incident photons attenuated within the sample.

Results and discussion

To synthesize phase-pure β-TaON, we performed a step-wise nitridation experiment on a Ta_2O_5 sample at 827 °C as illustrated in **Figure 4.3a**. Based on the phase diagram derived

by Swisher and Read[186] we kept the ratio between the partial pressure of water and hydrogen constant at 0.01, while increasing the ratio between the flows of ammonia and hydrogen. Each value of p_{NH_3}/p_{H_2} is kept constant for the time necessary until a thermodynamic equilibrium is obtained (i.e., no more changes in the optical absorption are observed), then increased to the next level (e.g., from 0.03 to 0.1, then to 0.3, and so on). **Figure 4.3b** shows the results of a typical UV-vis measurement. Initially the optical absorption is mostly in the UV range, consistent with the large bandgap of Ta_2O_5 (E_g = 3.9 eV). This phase is stable at p_{NH_3}/p_{H_2} ratios lower than 0.1.

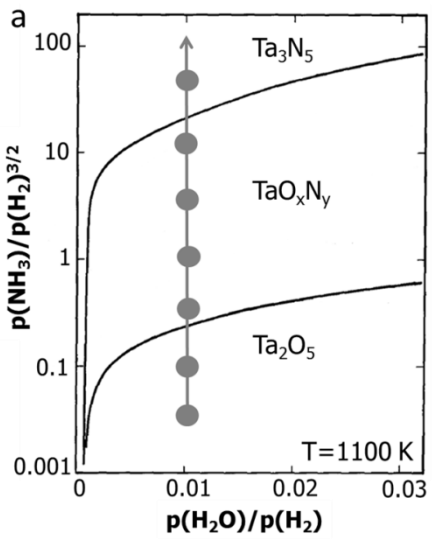
a
100
10
1
0.1
0.001
0
0.01
0.02
0.03
p(NH3)/p(H2)3/2
p(H2O)/p(H2)
Ta3N5
TaOxNy
Ta2O5
T=1100 K

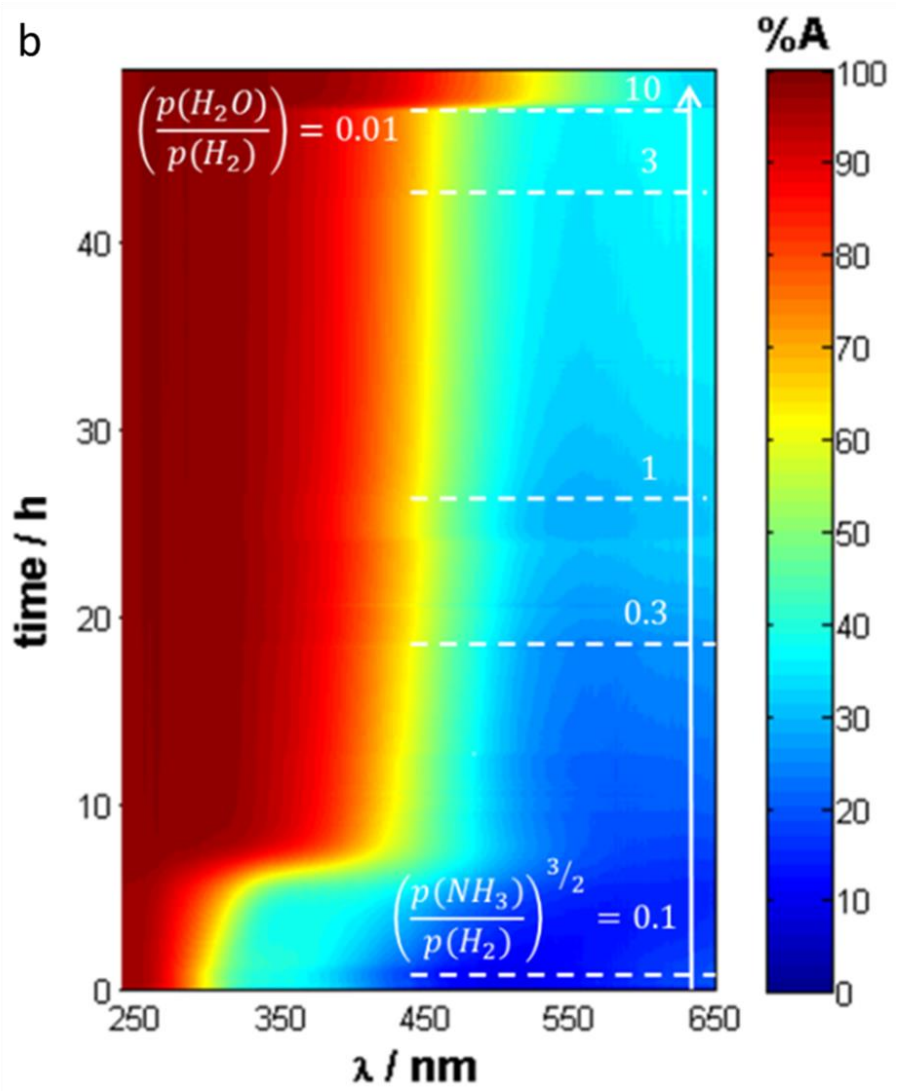
b
%A
100
90
80
70
60
50
40
30
20
10
0
time / h
0
10
20
30
40
250
350
450
550
650
λ / nm
p(H2O)/p(H2) = 0.01
10
3
1
0.3
p(NH3)/p(H2)3/2 = 0.1

Figure 4.3. *(a) Ta-O-N phase diagram after Swisher at al.,[186] indicating the region explored in this work. (b) In-situ optical monitoring of the stepwise nitridation of a Ta_2O_5 thin film. The x axis is the wavelength, the y axis reflects the time in hours. The white dotted lines delimit the areas with a certain NH_3/H_2 partial pressure, as indicated in white. The color indicates the optical absorption through the sample calculated from the measured transmission in percentage (%A = 100 - %T), where red is used to show high absorption and blue to show low absorption.*

After setting the gas ratio p_{NH_3}/p_{H_2} to 0.1, the optical absorption edge slowly redshifts. We attribute this to the diffusion of nitrogen into the Ta_2O_5 lattice. The gradual red shift of the absorption occurs for about 6 hours, until the solubility limit for nitrogen into the Ta_2O_5 phase is reached.[194] At this point, an abrupt red shift in the absorption edge (at t~6 hours) indicates that the sample undergoes a transformation, presumably into an oxynitride phase. Based on the change in optical absorption, it can be inferred that most of the phase transformation occurs within 2 hours. For p_{NH_3}/p_{H_2} ratios in the range of 0.1-3 ($0.1 < p_{NH_3}/p_{H_2} < 3$) the presence of a slow but constant red-shift of the absorption edge hints towards a continuously changing concentration of nitrogen within the oxynitride phase, similar to the case of Ta_2O_5. Alternatively, the red-shift could be due to a local nucleation and growth of Ta_3N_5. To distinguish between these possibilities, X-ray diffraction will be used (*vide infra*). Finally, at $p_{NH_3}/p_{H_2} = 10$ an abrupt change in the absorption edge suggests another phase transformation, presumably to Ta_3N_5 (E_g = 2.1 eV). In this case, the transition is more rapid, and completed in less than an hour.

To confirm the formation and stability of the different Ta-O-N phases, ex-situ XRD measurements were performed on samples removed from the ammonolysis process after equilibration at certain p_{NH3}/p_{H2} ratios, and the results are shown in **Figure 4.4**. The bottom pattern corresponds to the starting material, Ta_2O_5, produced by annealing a Ta film at 650 °C in air. The XRD peaks of this sample match best with the hexagonal δ-Ta_2O_5 phase, shown in blue (the reference file with the Miller indices for each peak is included in the Supporting Information). Upon nitridation at a p_{NH_3}/p_{H_2} ratio of 0.1, a different phase is observed, with diffraction peaks matching the reflections of monoclinic β-TaON (JCPDS #71-0178). When the p_{NH_3}/p_{H_2} ratio is increased to values between 0.3 – 3, additional diffraction peaks belonging to the orthorhombic Ta_3N_5 phase (JCPDS #72-0813) show up. This shows that the gradual redshift of the optical absorption edge in **Figure 4.3** is due to the formation of Ta_3N_5. Finally, at a p_{NH_3}/p_{H_2} ratio of 10, the β-TaON peaks disappear and the Ta_3N_5 peaks

are the only ones present. It should be noted that the nitridation process is fully reversible, i.e., it is possible to start with Ta_3N_5 and form TaON and Ta_2O_5, by lowering the p_{NH_3}/p_{H_2} ratio (**Figure 4.4**). From the XRD results a line phase diagram can be constructed (**Figure 4.5b**). Our phase diagram, in contrast to that of Swisher et al.,[186] suggests that the monoclinic β-TaON phase is only stable in a very narrow range of conditions. Moreover, we find that the phase boundaries (oxide-oxynitride, as well as oxynitride-nitride) occur at lower p_{NH_3}/p_{H_2} ratios. This is tentatively attributed to the fact that our experiments are done on thin PVD films instead of particles, which may lead to different manifestations of stress/strain effects and surface energy contributions.[195] Such effects may also explain the small differences in measured peak positions compared to the reference peaks in **Figure 4.5a**. Another difference is that our films are deposited onto a thin (5 nm) Ti adhesion layer, which may also affect the crystallization behavior. A more detailed study on these effects is, however, beyond the scope of this study.

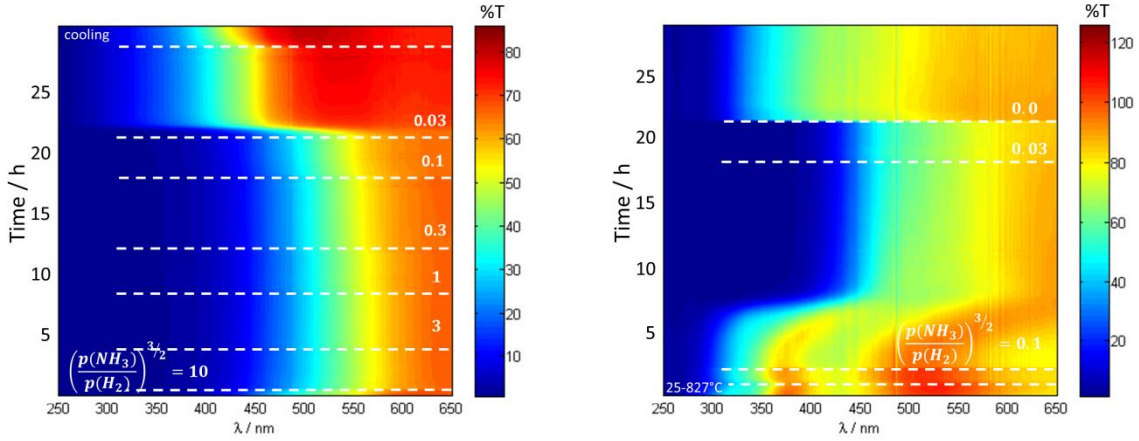

Figure 4.4. *In-situ optical monitoring of the oxidation of a Ta_3N_5 thin film (left), and nitridation and oxidation of a Ta_2O_5 film (right). The x axis is the wavelength, the y axis reflects the time in hours. The white dotted lines delimit the areas with a certain NH_3/H_2 partial pressure, as indicated in white. The color change indicates the light transmitted through the sample in percentage (%T), where red is used to show high transmission and blue to show low transmission.*

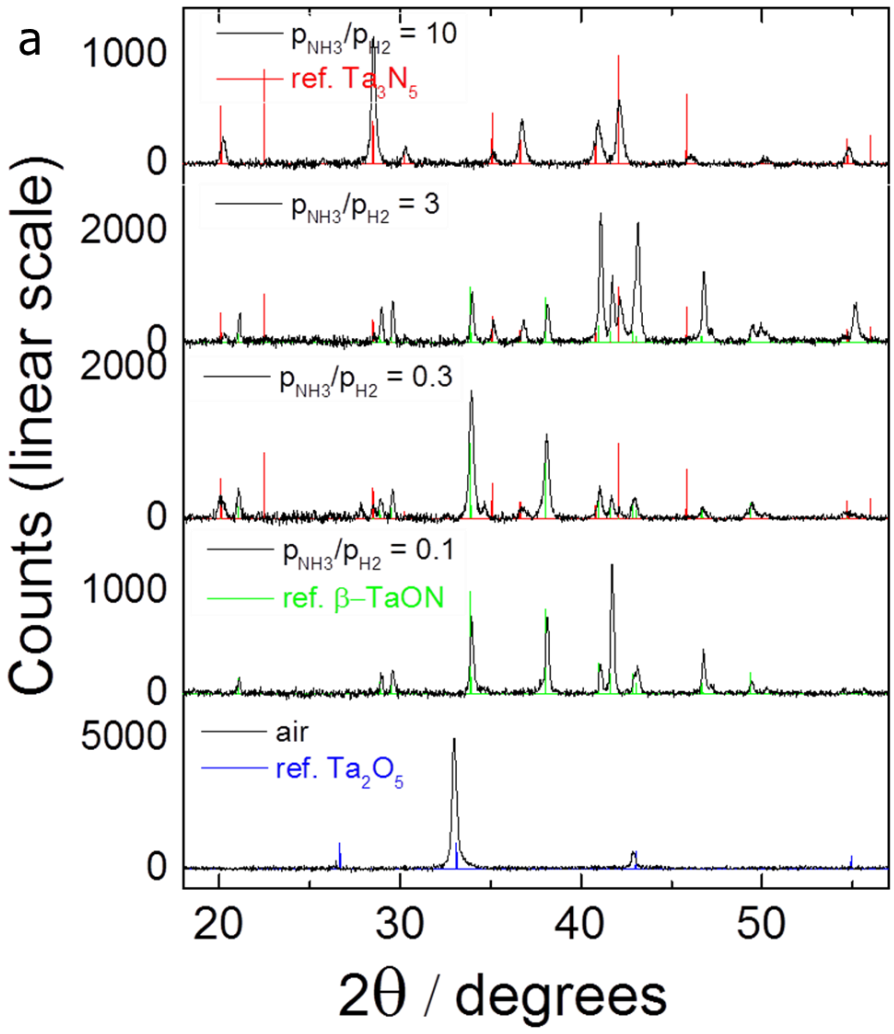
a
p_{NH3}/p_{H2} = 10
ref. Ta_3N_5
p_{NH3}/p_{H2} = 3
p_{NH3}/p_{H2} = 0.3
p_{NH3}/p_{H2} = 0.1
ref. β–TaON
air
ref. Ta_2O_5
Counts (linear scale)
1000
0
2000
0
2000
0
1000
0
5000
0
20
30
40
50
2θ / degrees

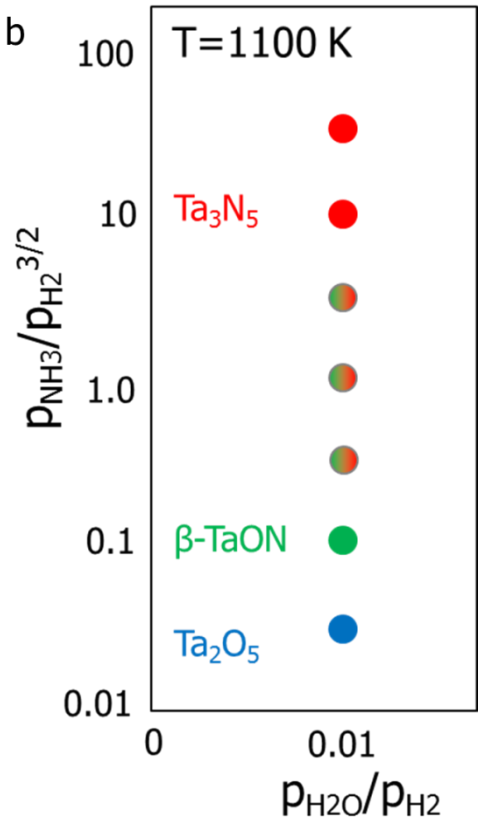

Figure 4.5. *(a) X-ray diffractograms of (from bottom to top): Ta film oxidized in air at 650°C, Ta_2O_5 reference peaks in blue; Ta film annealed at 827°C at p_{NH_3}/p_{H_2}=0.01 and p_{NH_3}/p_{H_2} = 0.1, β-TaON reference peaks in green; Ta film at 0.3 ≤ p_{NH_3}/p_{H_2}≤ 3, β-TaON and Ta_3N_5 reference peaks in green and red, respectively; the top-most pattern belongs to a Ta film annealed at p_{NH_3}/p_{H_2} = 10, Ta_3N_5 reference peaks in red. (International Centre for Diffraction Data (JCPDS) reference files; Ta_2O_5: PCPDF 19-1299; β-TaON: PCPDF 71-0178; Ta_3N_5: PCPDF 72-0813). (b) Line phase diagram showing the partial pressure ratios of the gas mixture and the Ta-O-N phase obtained in this mixture.*

Measurements with a step profilometer reveal that, starting from a Ta thickness of 60 nm, the thickness becomes 175±15 nm in Ta_2O_5, 280±30 nm in β-TaON (p_{NH_3}/p_{H_2}= 0.1), and 225±30 nm in both TaO_xN_y (from hereon we will use this to describe the mixture of TaON and Ta_3N_5 phases obtained at p_{NH_3}/p_{H_2}= 3) and Ta_3N_5 (p_{NH_3}/p_{H_2}= 10). The relative change in thickness between Ta_2O_5, β-TaON and Ta_3N_5 is 1:1.60:1.29, in reasonable agreement with their volume ratios of 1:1.70:1.34. The observation that almost the entire volume change is accommodated by a change in film thickness indicates a good adhesion of the films to the substrate.

SEM and AFM images of the Ta_3N_5 films on quartz reveal a smooth and flat surface, while the β-TaON films present higher surface roughness (**Figure 4.6**). This is possibly related to the

larger lattice expansion of the latter. EDS analysis confirms an increasing N/O ratio as we move to samples exposed at higher p_{NH_3}/p_{H_2} ratios (**Figure 4.7**). A quantitative analysis, however, is hindered by the limited thickness of the films.

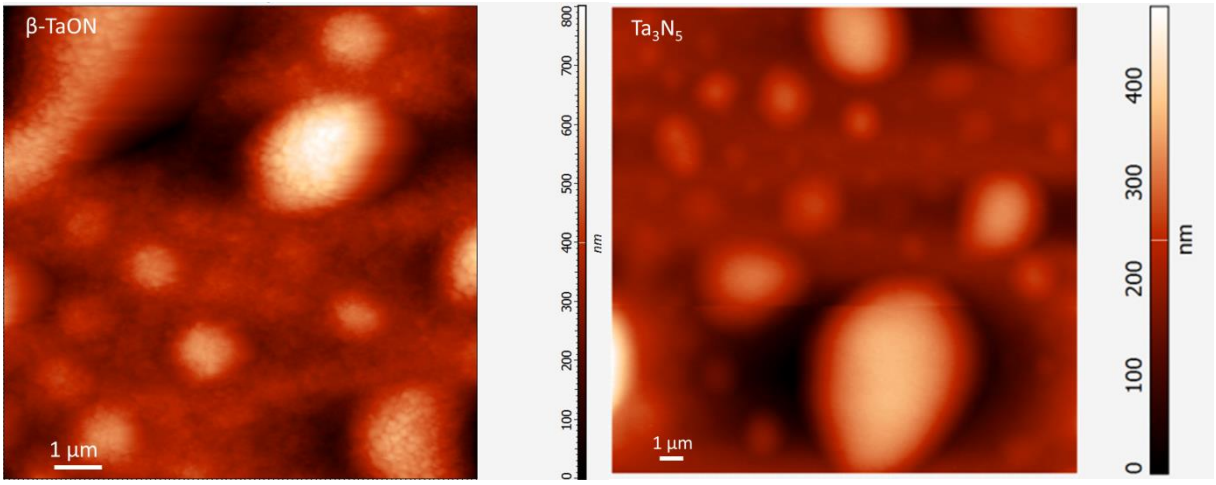

Figure 4.6. *SEM and AFM images of a β-TaON thin film (left), and of a Ta_3N_5 film (right) deposited on quartz.*

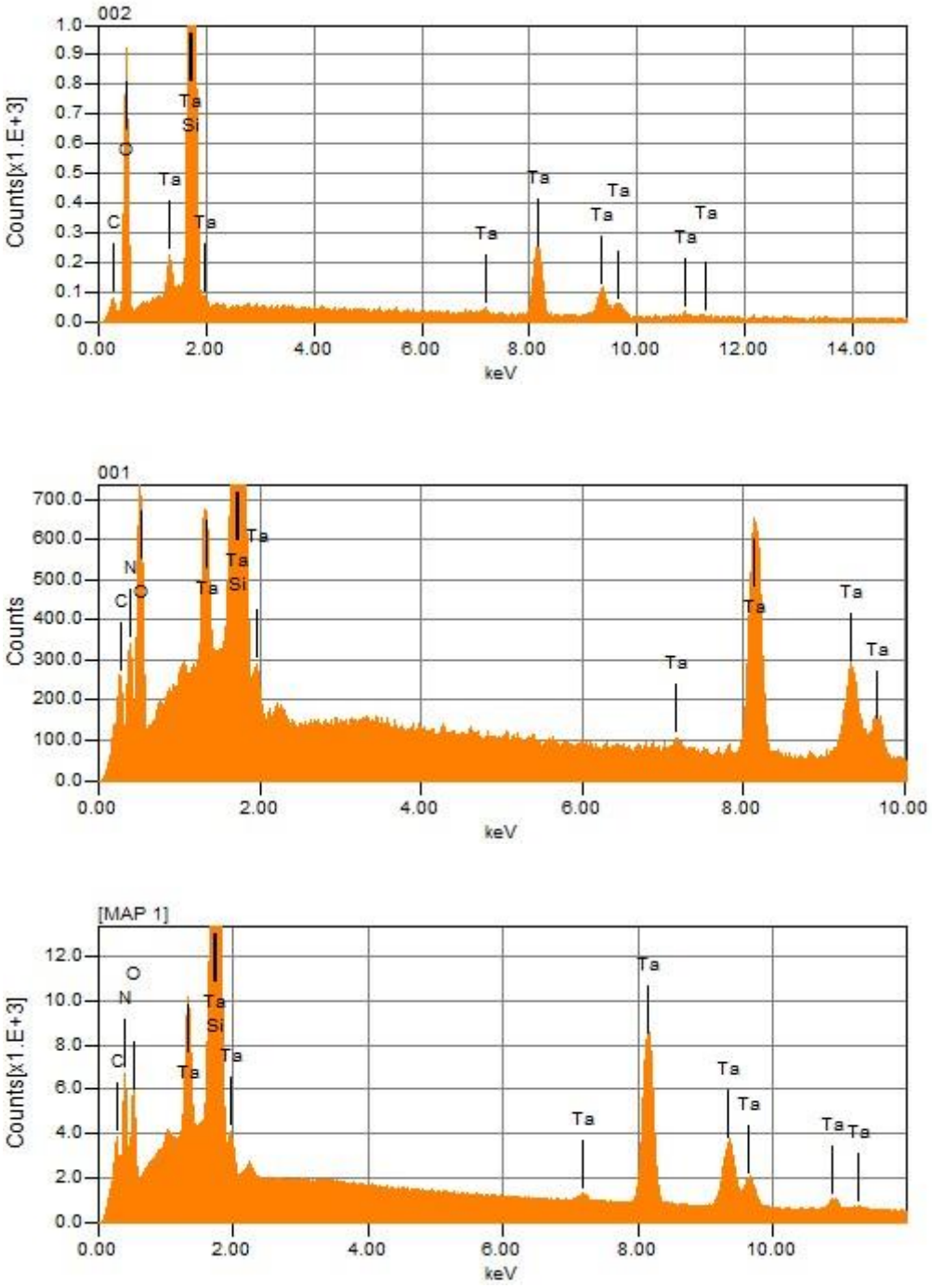

Figure 4.7. *EDS analysis on a Ta_2O_5 (top), β-TaON (middle), and Ta_3N_5 (bottom) thin films deposited on quartz. The intensity ratio N/O of the N and O peaks visible at around 0.5 keV increases as we move to more oxygen poor films.*

XPS analysis was performed to provide a more accurate estimate of the surface and sub-surface composition of Ta, N, O in the Ta-O-N samples deposited on quartz at different N/O ratios. The surface and subsurface composition are both measured, in order to be able to

discriminate between the bulk thermodynamics properties better represented by the subsurface measurement, while the surface composition can be affected by the kinetics of the cool down process. In order to probe the sub-surface composition, the films were ion-beam etched for 10 nm. **Figure 4.8** shows that the Ta4p peak shifts to a lower binding energy as the nitrogen content in the samples increases. This is in agreement with other studies, and is attributed to the larger electronegativity of O compared to N.[196,197] Thus, the electron density around the Ta atoms increases as the N/O ratio increases, which implies that the Ta-N bond is less polar than the Ta-O bond. The O 1s peak also shifts to lower energies with increasing N/O ratio. Although the shift is much smaller, it suggests that the Ta-O bond also becomes more covalent in character upon increasing nitrogen content. This covalency would positively affect the charge carrier mobility of the nitride samples compared with the more oxygen rich oxynitride and oxide samples (vide infra), as more de-localized charges are more mobile than in the small polaron hopping mechanism typical of oxides. Furthermore, the lower binding energy with increasing N/O ratios, observed also on the surface, explains the lower chemical stability of these compounds compared to that of the oxide phase. Despite the increased covalency upon nitrogen incorporation, Ta_3N_5 still has a substantial ionic character.

Figure 4.9 shows the surface XPS measurements of the Ta-O-N thin films, where the C 1s peak (285.2 eV) was used as a standard to calibrate the binding energies. Sample charging was observed for the Ta_2O_5, β-TaON and for the mixed phase TaON-Ta_3N_5 samples, while no charging was observed in the Ta_3N_5 film. This can be understood in terms of the carrier's mobility, highest in the Ta_3N_5 film (see TRMC section). A comparison with the sub-surface data shows that the surfaces of β-TaON, of the mixed phase TaON-Ta_3N_5 and of Ta_3N_5 are oxygen rich. This can be explained with the fact the reactivity of ammonia decreases quicker than the reactivity of water vapor while cooling down from 827 °C. A similar observation was reported in the literature for Ta_3N_5 photoanodes, which formed a surface passivation layer with composition $Ta_{3-x}N_{5-y}O_y$, including amount of Ta vacancies and O impurities. The thickness of the passivation layer was estimated to be less than 15 nm.[198] In contrast, another study on Ta_3N_5 photocatalysts shows the presence of a thin surface layer of TaN instead of oxygen impurities. A possible explanation for this discrepancy may be the differences in the conditions for the cooling down process.[199] It should be realized that the composition of the surface will have a major influence on the photocatalytic activity of the film. Since a detailed systematic study of the surface properties as a function of e.g. cooling

rates is beyond the scope of this study, we decided to focus our efforts on the bulk properties of the Ta-O-N films.

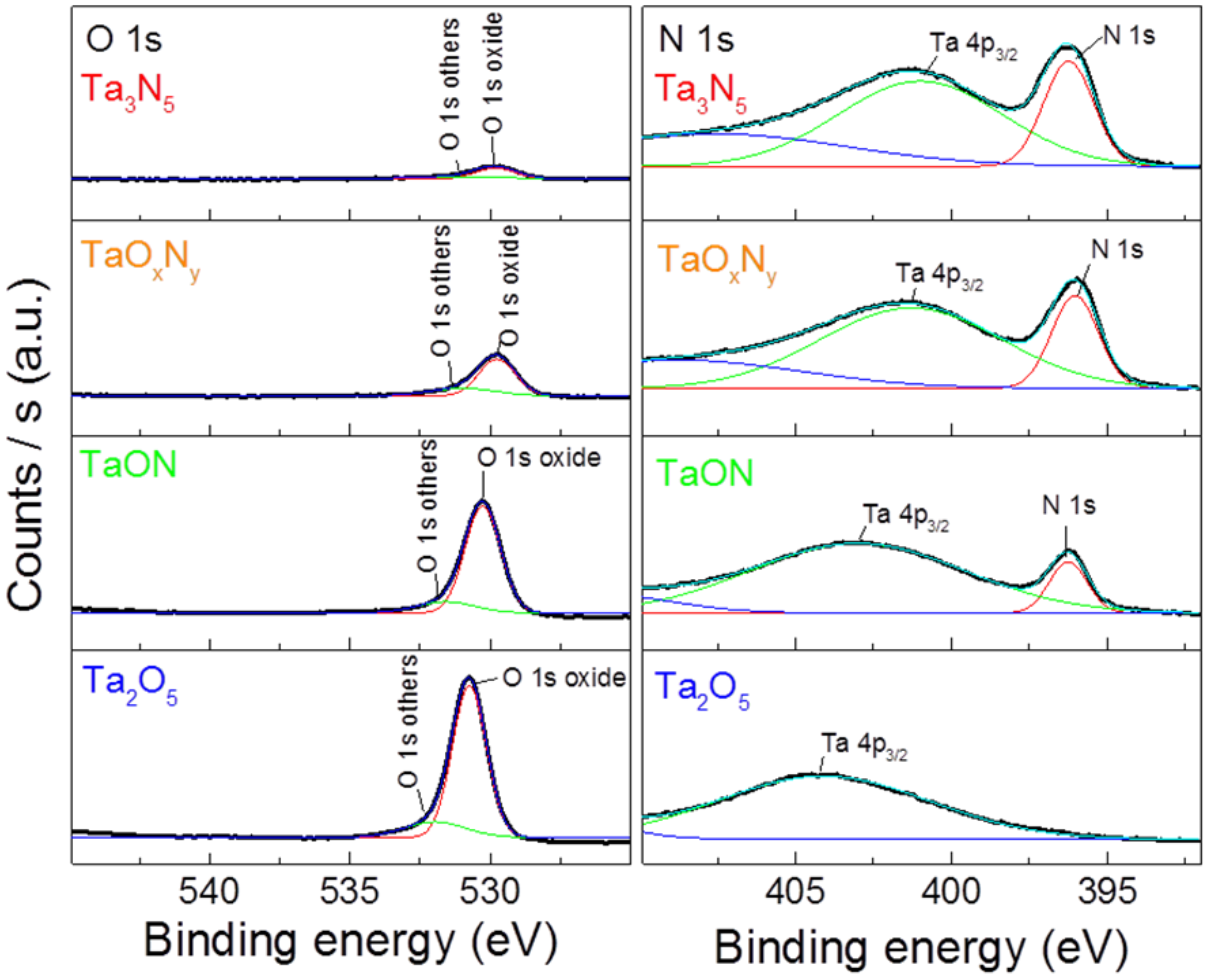

Figure 4.8. *XPS data at 10 nm from the surface showing the O 1s and N 1s signals of (from bottom to top): Ta film oxidized in air at 650°C, Ta_2O_5 in blue; Ta film annealed at 827°C at p_{NH_3}/p_{H_2}=0.01 and p_{NH_3}/p_{H_2} = 0.1, β-TaON in green; Ta film at 0.3 ≤ p_{NH_3}/p_{H_2}≤ 3, mixed TaON and Ta_3N_5 in orange; the top-most pattern belongs to a Ta film annealed at p_{NH_3}/p_{H_2} = 10, Ta_3N_5 in red. The Ta 4p peaks shift to lower binding energies as the nitrogen content in the film increases. The Ta_3N_5 samples contains some O impurities.*

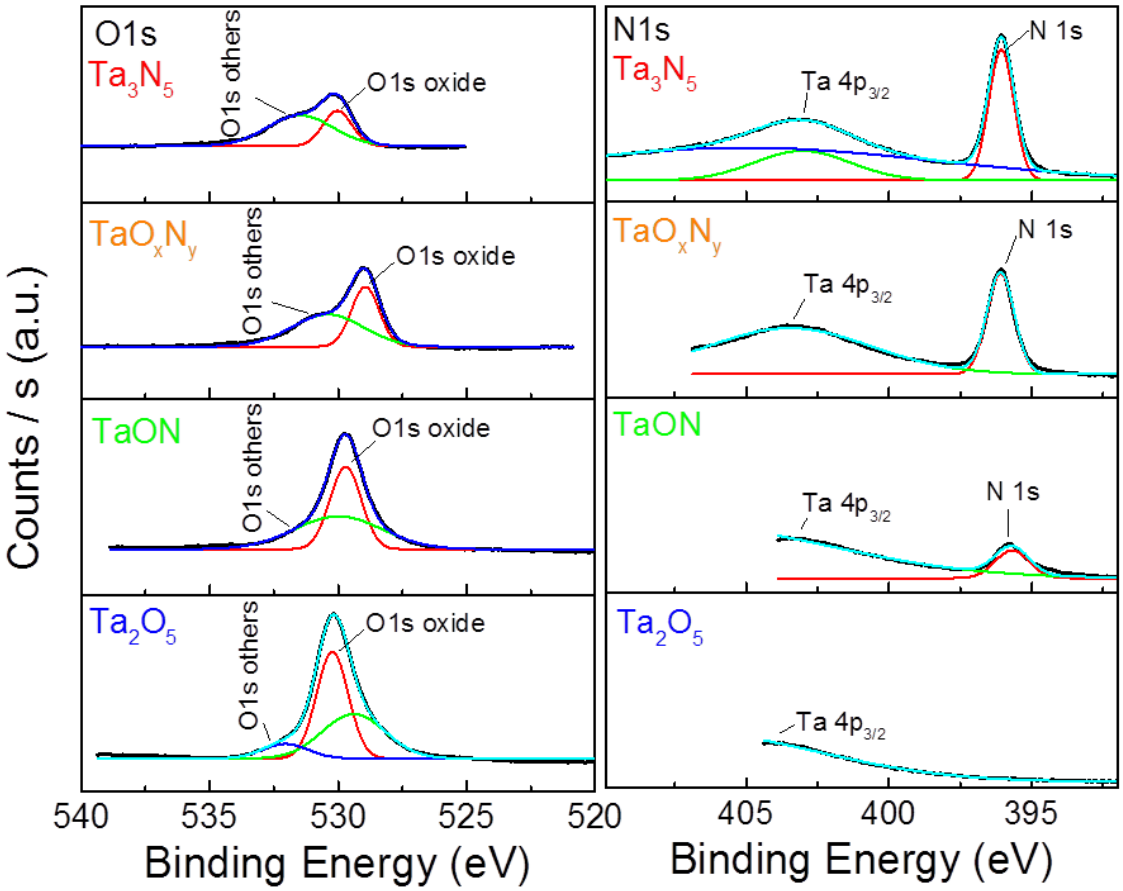

Figure 4.9. *XPS surface data showing the O-1s and N-1s signals of (from bottom to top): Ta film oxidized in air at 650°C, Ta_2O_5 in blue; Ta film annealed at 827°C at p_{NH_3}/p_{H_2}=0.01 and p_{NH_3}/p_{H_2} = 0.1, β-TaON in green; Ta film at 0.3 ≤ p_{NH_3}/p_{H_2} ≤ 3, mixed TaON and Ta_3N_5 in orange; the top-most pattern belongs to a Ta film annealed at p_{NH_3}/p_{H_2} = 10, Ta_3N_5 in red. Sample charging was observed for the Ta_2O_5, β-TaON and for the mixed phase TaON-Ta_3N_5 samples, while no charging was observed in the Ta_3N_5 film. The C1s peak (285.2 eV) was used as a standard to calibrate the binding energies.*

To characterize the carrier transport properties of our Ta-O-N films, we performed time resolved microwave conductivity (TRMC). With this technique, the carrier mobility and lifetime can be quantitatively determined. The presence of the 5 nm Ti adhesion layer is not expected to greatly influence the results since TiN films (even in partially oxidized form) show metallic conductivities. Hence, the carrier lifetimes due to excitations in this part of the film will be very short (fs – ps) and will not show up in the TRMC signal.

Figure 4.10 shows the microwave photoconductance of Ta_2O_5, β-TaON (p_{NH3}/p_{H2} = 0.1), TaO_xN_y (TaON mixed with Ta_3N_5, p_{NH3}/p_{H2} = 3), and Ta_3N_5 (p_{NH3}/p_{H2} = 10) as a function of incident photon fluence per laser pulse. For each material, the photon fluence was increased

until a signal-to-noise ratio of at least 10:1 was achieved. With a laser pulse at a wavelength of 300 nm and low photon fluence (10^{11}-10^{13} photons cm^{-2} $pulse^{-1}$), the maximum photoconductance values for β-TaON and Ta_3N_5 are 1.0 $\cdot 10^{-2}$ cm^2/Vs and 8.0 $\cdot 10^{-2}$ cm^2/Vs, respectively. At higher light intensities the photoconductance decreases, which is attributed to fast non-geminate electron-hole recombination. At lower light intensities, the photoconductance is not expected to change, so the values mentioned above are also valid for AM1.5 illumination conditions ($\sim 10^9$ photons per pulse per cm^2). For TaO_xN_y the photoconductance is of the same order of magnitude as in the single phase β-TaON. However, it shows a distinctively different behavior; it increases as the photon fluence is increased to 6 $\cdot 10^{13}$ photons cm^{-2} $pulse^{-1}$, and then flattens out at higher light intensities. This behavior is typical for the presence of trap states, which first have to be filled before the charges can be fully mobile.[193,200] These defect states are presumably of two natures: heterogeneous grain boundaries and substitutional N_O defects formed under nitrogen-rich environment, where N_O represents a nitrogen on a site in TaON that is normally occupied by oxygen (e.g. due to N-O site exchange). For Ta_2O_5 a signal can be measured only at the highest fluence, and its value is 2 $\cdot 10^{-5}$ cm^2/Vs, three orders of magnitude smaller than in the nitrogen-rich phases.

Photoconductance values for a laser pulse at 450 nm are shown in **Figure 4.11.** The photoconductance values at 450 nm for the Ta_3N_5, TaON and Ta_2O_5 films are comparable to the ones recorded at 300 nm, respectively. However at 450 nm there is no clear dependence of the photoconductance on the laser fluence.

While no literature photoconductance data exist for β-TaON, relatively low photoconductance values for Ta_3N_5 were predicted by a theoretical study by *Morbec et al.* who considered the high anisotropicity of the material with the large electron and hole effective masses as a possible cause for low mobility values.[201] Moreover, while material purity and crystalline quality of sputtered thin films is usually much better than those made from solution processing, to the best of our knowledge no electrical conductivity (mobility) studies have been reported on solution processed Ta_3N_5 or TaON films. Thus the comparison of our films is only to films that have been made with similar vacuum-based techniques. An experimental work by *Ziani et al.* concluded that the mobility of their reactive magnetron sputtered Ta_3N_5 was in the range 1-4 cm^2/Vs which is two orders of magnitude higher values than measured in our study.[202] The same values were reported for their mixed TaON-Ta_3N_5 films. On the other hand, their reported lifetime was in all cases in the order of 3-9 ps, 10 orders of magnitude lower than measured in our study (see below). This discrepancy could be due to

differences in the crystallinity (slightly higher in their case), phase purity and the nature of grain boundaries (enormously more sites for recombination in their case).

The observation of a higher photoconductance in Ta_3N_5 than in β-TaON seems at odds with a recent first-principle study of the intrinsic defects and electronic conductivity of TaON, which predicted a better electronic conductivity for TaON than for the nitride and oxide phases due to the different type of dominant defect in TaON (the O_N antisite instead of O or N vacancies, or Ta interstitials in Ta_2O_5 and Ta_3N_5).[203] The photoconductivity can be related to the crystallinity of the film. The XRD analysis indicates a comparable degree of crystallinity in β-TaON, Ta_3N_5 and the mixed TaON-Ta_3N_5 films, with a higher degree of crystallinity in the Ta_2O_5 film. As the photoconductivity for our thin films shown in **Figure 4.10** seems not to be correlated to the degree of crystallinity, we can exclude crystallinity as the main cause of higher photoconductivity in the more N-rich thin films. Instead, we believe the higher photoconductivity of the Ta_3N_5 is simply due to the more delocalized nature of the N2p orbitals compared to the O2p orbitals. The stronger electron affinity of oxygen in TaON leads to a more ionic nature of the bonds, resulting in a charge transport mechanism that is governed by small polaron hopping.[101,204,205,206,207] As an example to show the potential of oxynitrides and the importance of a high control over the crystal structure, it is interesting to mention that Hall mobility values as high as 17 cm^2/Vs have been reported for epitaxially synthesized anatase TaON, a polymorph of β-TaON.[208]

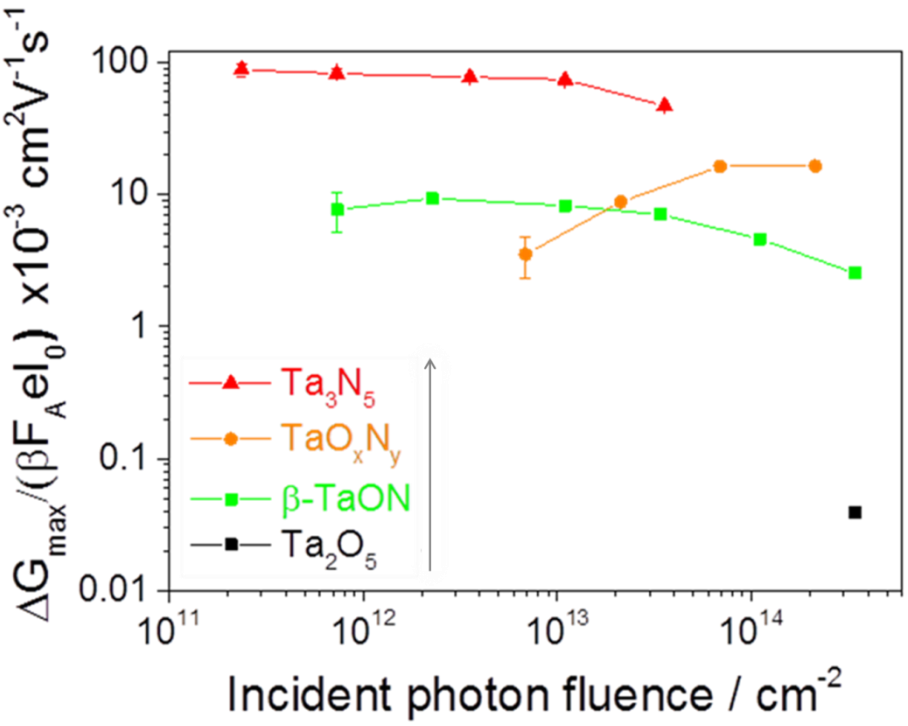

Figure 4.10. *Time-Resolved Microwave Conductance signal of Ta_2O_5 (Ta annealed in air), β-TaON (p_{NH3}/p_{H2} = 0.1), TaO_xN_y (p_{NH3}/p_{H2} = 3), and Ta_3N_5 (p_{NH3}/p_{H2} = 10) as a function of incident photons per laser pulse of 3.5 ns at 300 nm. AM1.5 illumination is equivalent to an incident number of photons per pulse of ~10^9 cm^{-2}.*

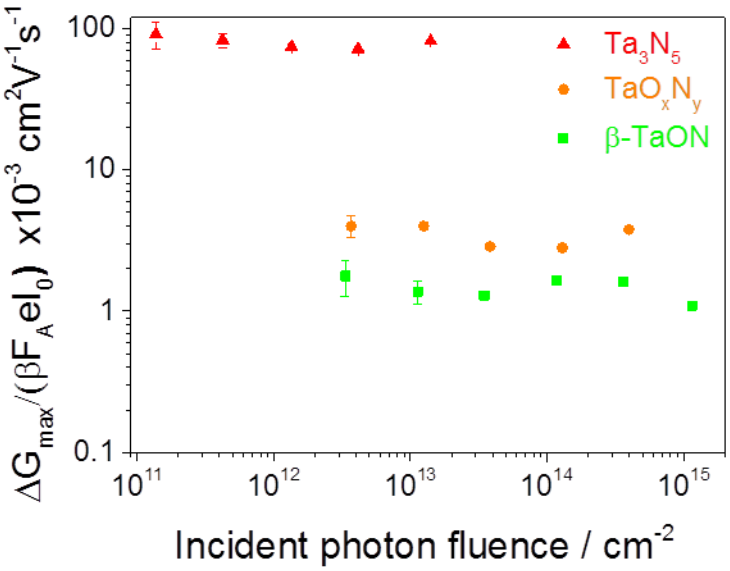

Figure 4.11. *Time-Resolved Microwave Conductance signal of β-TaON (p_{NH3}/p_{H2} = 0.1), TaO_xN_y (p_{NH3}/p_{H2} = 3), and Ta_3N_5 (p_{NH3}/p_{H2} = 10) as a function of incident photons per laser pulse of 3.5 ns at 450 nm. AM1.5 illumination is equivalent to an incident number of photons per pulse of ~10^9 cm^{-2}.*

Figure 4.12a shows the normalized TRMC transients of Ta_2O_5, β-TaON, TaO_xN_y and Ta_3N_5 at 300 nm. The combined lifetime of the photo-generated holes and electrons can be obtained by fitting the decay of the signal.[209] The weak Ta_2O_5 signal decays very rapidly and becomes indistinguishable from the noise after 300 ns. An exponential fit to the decay of the β-TaON signal indicates the presence of a fast component with a decay constant of 5 μs, a medium component of 120 μs, and a long component with a lifetime of 4 ms. The relative magnitudes of these contributions are 12%, 30% and 58%, respectively. These lifetimes are exceptionally long compared to other photoanode materials. In fact, after 1000 μs (the limit of our instrumentation) the TRMC signal for β-TaON is still ~50% of the initial value (**Figure 4.12b**).

In the Ta_3N_5 sample, while the carrier mobility is one order of magnitude higher than β-TaON, the lifetime of the carriers is comparable. The decay of the signal can be fit by a fast decay of 5 μs, a medium one at 120 μs, and the long component of 4 ms. The relative magnitudes of these contributions are 40%, 20% and 40%, respectively (**Figure 4.12c**).

In the TaO_xN_y sample (a mix of TaON/Ta_3N_5 phases as shown by XRD) – despite having a similar mobility as β-TaON – the TRMC signal has completely vanished after just a few μs. Given the long lifetime of the phase pure samples we attribute this to the presence of recombination sites at the grain boundaries between the β-TaON and the Ta_3N_5 phases. The extremely long lifetime of the charge carriers in the stoichiometric β-TaON and Ta_3N_5 compared to the drastically reduced lifetime in the mixed TaON/Ta_3N_5 sample (TaO_xN_y in the graphs), confirms the need for single phase materials to achieve high performance.

With a 450 nm laser pulse, similar decay values as the ones observed at 300 nm are obtained for β-TaON and Ta_3N_5. The TaO_xN_y, however, exhibits a longer lifetime under a 450 nm laser pulse compared to its value at 300 nm, as the signal is still alive after 10 μs (**Figure 4.13**)

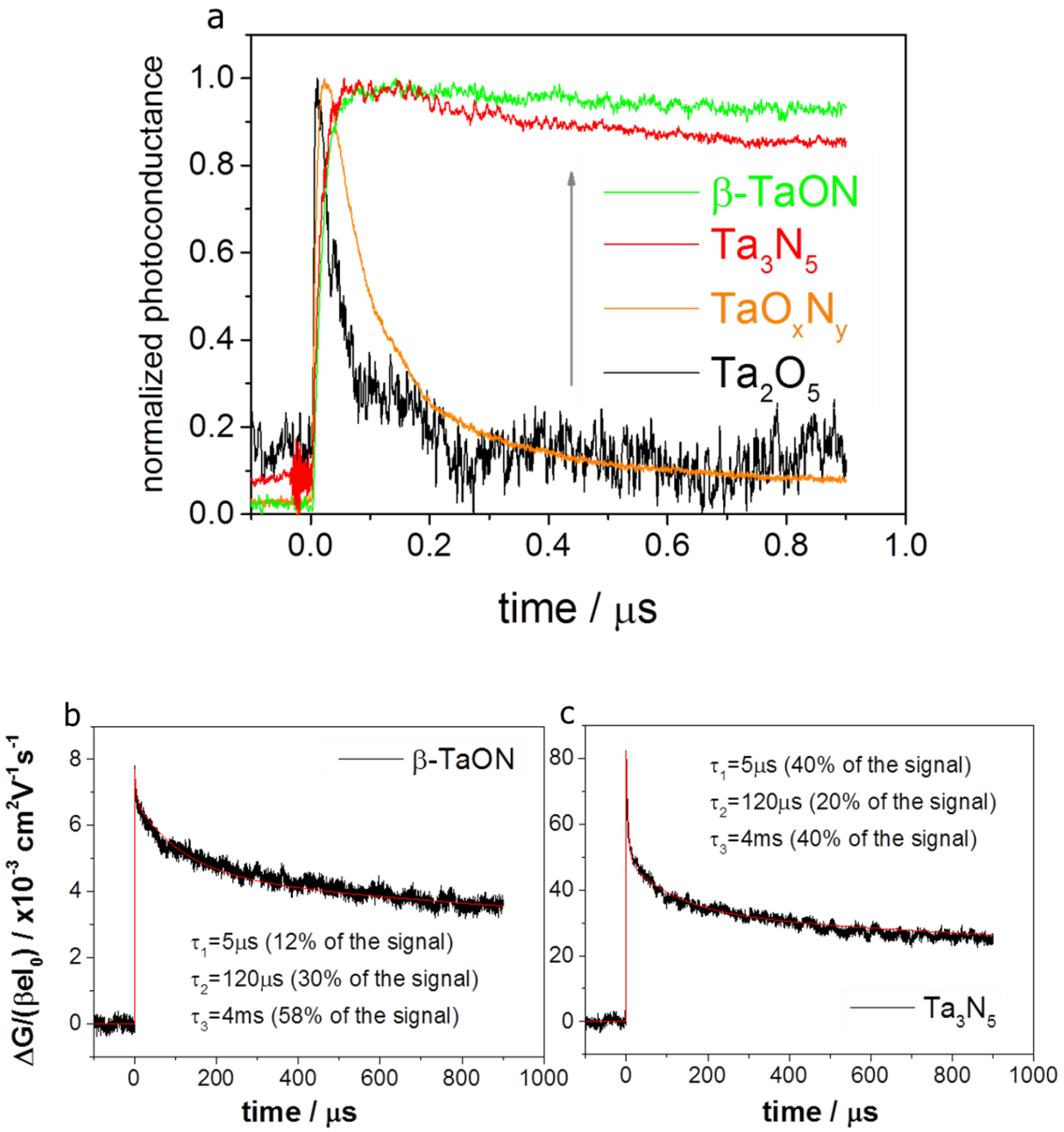

Figure 4.12. *(a) Normalized photoconductance Ta_2O_5, β-TaON, TaO_xN_y (mixed TaON-Ta_3N_5), and Ta_3N_5. (b-c) TRMC decay signal for the lifetime of charge carriers in β-TaON (b) and Ta_3N_5 (c) with the fitting to their decay. Laser pulse of 3.5 ns at 300 nm.*

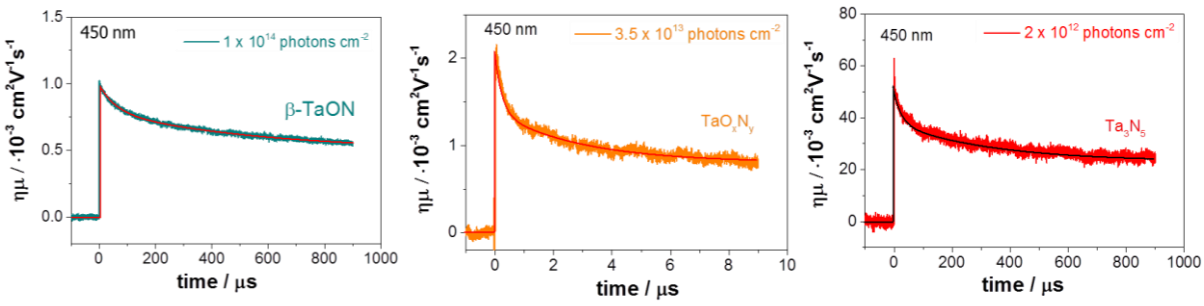

Figure 4.13. *TRMC decay signal of β-TaON (p_{NH3}/p_{H2} = 0.1), TaO_xN_y (mixed TaON-Ta_3N_5, p_{NH3}/p_{H2} = 3), and Ta_3N_5 (p_{NH3}/p_{H2} = 10). Average over 100 traces. Laser pulse of 3.5 ns at 450 nm. The timescale for the mixed TaON-Ta_3N_5 sample is 10 μs, for the β-TaON and Ta_3N_5 samples it is 1000 μs.*

A summary of the semiconducting properties for various photoanode materials is illustrated in **Table 4.2**, which shows a comparison of the carrier mobilities, lifetimes, and diffusion lengths. With a lifetime in the order of ms, the photo-generated carriers in β-TaON and Ta_3N_5 live much longer than in most metal oxides. This would suggest that these materials are highly defect-tolerant, similar to e.g. CdTe. However, the long TRMC lifetime may have multiple explanations. The most straightforward recombination process is at grain boundaries and surfaces. With an apparent carrier diffusion length of tens of μm (**Table 4.2**), a film thickness of a few hundred nm, and a crystallite size between 20-30 nm (as estimated from the Scherrer equation), the charge carriers would be certain to hit these defects many times. Since it seems unlikely that this can occur without recombination, one should consider alternative explanations for the long lifetime. These explanations usually involve the presence of trap states. Since the TRMC signal does not increase with photon fluence, filling of deep traps does not seem to play a role for β-TaON and Ta_3N_5 under the current conditions. Instead, we tentatively attribute the long lifetime to the presence of shallow traps. These shallow trap states are not directly involved in electron-hole recombination (which occurs between mobile carriers); instead, the long lifetime reflects the time necessary for the carriers to escape the shallow traps, after which they become 'available' for recombination. The presence of shallow traps is indeed consistent with the modest mobility, which is a consequence of the fact that the carriers not only experience transport through the conduction or valence band, but also spend a certain amount of time in the trap. Since de-trapping is a thermally activated process, temperature-dependent TRMC measurements would provide more detailed insights. However, this is beyond the scope of this study.

It should be noted that the presence of shallow traps means that one should be careful when interpreting the apparent carrier diffusion lengths shown in **Table 4.2** for β-TaON and

Ta_3N_5. If the lifetime indicated by the TRMC signal is indeed determined by the de-trapping rate from shallow traps, it means that the actual lifetime of the free charge carriers in the conduction and valence bands is much shorter, and that their mobility is higher. As a result, the true carrier diffusion length is likely to be shorter, and would also depend on the ability of the carriers to move around while residing in the shallow trap state.

Table 4.2. *Comparison of carrier mobility, lifetime, diffusion length of several photoanode materials for solar water splitting.*

Photoelectrode material	**Carrier mobility, μ ($cm^2V^{-2}s^{-1}$)**	**Carrier lifetime, τ**	**Diff. length, L (nm)**	**Method/reference**
Fe_2O_3	0.5	3 ps	2-4	TAS[210,211,212]
WO_3	10	1-9 ns	150-500	Space-charge model[213]
Cu_2O	6	40 ps	25	THz spectroscopy[214]
$BiVO_4$	0.044	40 ns	70	TRMC[Error! Bookmark not defined.]
Ta_3N_5	4.4	7.3 ps	9	TAS, Hall effect[202]
Ta_2O_5	0.000022	5 ns	0.5	TRMC[this study]
TaON-Ta_3N_5	0.014	7.5 μs	520	TRMC[this study]
β-TaON	0.01	2.3 ms	8000 (*)	TRMC[this study]

Ta_3N_5	0.08	1.6 ms	18000 (*)	TRMC[this study]

(*) See text

Conclusions

In conclusion, in this chapter we demonstrated the use of 'oxynitrogenography' as a technique towards the controlled and reproducible synthesis of phase pure Ta-O-N phases, including the elusive β-TaON phase. The method shows that the solubility range is smaller than expected, which implies that this quasi-equilibrium approach is necessary to obtain phase pure samples. The high quality of the films is confirmed by their electronic properties as probed with TRMC. We observe that the carrier mobility increases with the nitrogen content in the sample, from 10^{-5} cm^2/Vs in Ta_2O_5, to 10^{-2} cm^2/Vs in β-TaON and the mixed TaON-Ta_3N_5, up to 10^{-1} cm^2/Vs in Ta_3N_5. While the carrier mobility of β-TaON and Ta_3N_5 is comparable to that of $BiVO_4$, the apparent lifetime in the order of milliseconds is comparable to that of crystalline silicon. This would make it superior by three orders of magnitude to that of other Ta_3N_5 reported in the literature, as well as to that of the most promising metal oxide-based semiconductors ($BiVO_4$, Fe_2O_3, WO_3, Cu_2O) under investigation in photo-electrochemical (PEC) water splitting. Moreover, these results suggest a carrier diffusion length of the order of tens of μm, much longer than the optical absorption depth. However, some care must be taken when interpreting these results, as the possibility of carrier (de-)trapping into and from shallow trap states may alter the picture. Nevertheless, the extremely long-lived TRMC signal for the stoichiometric β-TaON and Ta_3N_5, compared to that of the mixed TaON/Ta_3N_5 samples, confirms the need for single phase materials to realize high energy conversion efficiencies for these promising photoanode materials.

4.2 Tantalum Nitride Thin Films with Al_2O_3 Surface Layer for High Performance Solar-driven Water Oxidation

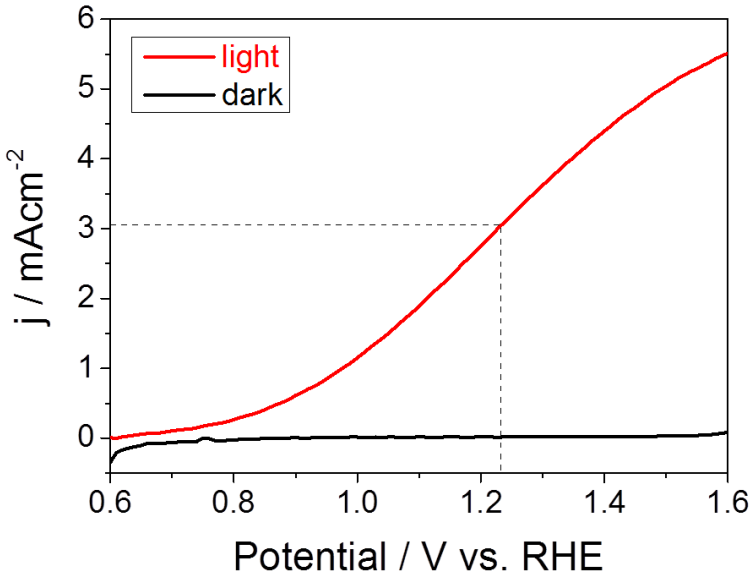

The development of a reliable method to synthesize efficient thin film Ta_3N_5 photoanodes has been hindered by the unavoidable growth of undesired interfacial phases during the synthesis process. Moreover, the intrinsic instability in water under illumination is a major hurdle for its use in photoelectrochemical water splitting. In this study Ta_3N_5 photoanodes of different thicknesses were synthesized by radiofrequency (RF) reactive sputter deposition of Ta_2O_5 onto a Pt-coated quartz substrate, followed by a nitridation at 1100 K in a controlled flow of NH_3, H_2O and H_2. The assembly was then catalyzed by multilayered, multifunctional coating of a 2 nm Ni layer, $Ni(OH)_2$-$Co(OH)_2$, and Co-phosphate. To protect the Ta_3N_5 against corrosion we investigated the addition of interfacial atomic layer deposited (ALD) films of either 3 nm TiO_2 or 3 nm Al_2O_3 films in between the Ta_3N_5 and the catalyst layers. The use of ALD interfacial layers is novel for Ta_3N_5. The optimal conditions were found in a Ta_3N_5 thickness of 580 nm coated with a 3 nm Al_2O_3 interfacial layer. As a result, a current density of 3 $mAcm^{-2}$ was measured at the reversible potential for water oxidation during photoelectrochemical water splitting. Finally the same surface treatment applied to TaON samples resulted in a photoelectrochemical performance one order of magnitude lower than with Ta_3N_5. We hypothesize that as compared to Ta_3N_5 the performance of TaON-Pt for water splitting is more negatively affected by the presence of secondary crystal phases due to the interaction of the Pt-quartz substrate during the growth process.

Introduction

The search of cheap and efficient photoelectrodes for the direct conversion of solar energy into chemical fuels such as hydrogen has led to the investigation of metal oxynitrides and nitrides.[160] Among the various nitride compounds considered, tantalum nitride (Ta_3N_5) is particularly attractive because of its nearly ideal bandgap for water splitting (2.1 eV).[215] Moreover the conduction and valence band edges are in a favorable position to theoretically enable hydrogen and oxygen evolution without the need for an externally applied potential.

The tantalum nitride phase can be readily obtained by nitridation of tantalum oxide under a flow of ammonia.[216,217,218] In the literature, Ta_3N_5 photoanodes have been synthesized via thermal nitridation of tantalum oxide films[220,221] or powders,[222,223] electrochemical anodization followed by thermal nitridation to form nanorods or nanotubes,[217,219,224] reactive sputtering,[225] vapor phase hydrothermal processes,[218] reverse homogeneous precipitation to form an oxide precursor,[226] and atomic layer deposition.[227,228] While virtually all the techniques above promote a well-controlled growth of high quality materials, the reported photoelectrochemical performance varies enormously. One reason for this variation is related to the discovery of a substoichiometric layer which forms at the surface of the Ta_3N_5 already prior to the immersion in water.[235,237] Surface exfoliation treatments have proven to be successful in removing the undesired surface layers and increase the performance.[219] Moreover, optimization of light absorption and charge transport via nanostructuring also lead to a performance improvement.[220,221,222,223]

A second reason for the difficulty in comparing performances is due to the different methods used to stabilize tantalum nitride when illuminated under the conditions required for water oxidation.[224,225] To compensate for that drawback, different water oxidation catalysts,[226,227] usually in multilayered configuration, are employed by the various research groups working on this material.[228,229] While progress has recently been made in prolonging the lifetime of unstable photoelectrodes by depositing thin protective layers by atomic layer deposition, this route is still unexplored for Ta_3N_5.[230,231,232,233,234,176.]

We have recently established a synthesis method called 'oxynitrogenography' to obtain single phase β-TaON and Ta_3N_5. During the synthesis, we approach *thermodynamic equilibrium* by controlling the gas composition, i.e., a balanced supply of nitrogen (in the form of ammonia), hydrogen, and oxygen (in the form of water) and allowing for thermal equilibration.[235] The goal of this work is to investigate the effects of ultra-thin interfacial layers, in between the Ta_3N_5 and the catalyst layers, to the photoelectrochemical performance of the Ta_3N_5 (and

TaON) films deposited with the oxynitrogenography technique onto Pt-coated quartz substrates.

Experimental section

Film synthesis: The synthesis of Ta_3N_5 thin films has been described previously.[235,191] In brief, a Ta film (99.95% purity) was sputtered onto fused silica substrates (ESCO S1-UV, 1 mm thick) in 3 μbars partial pressure of Ar (20 ml/min flow) with 100W DC electric power, and a substrate temperature of 400°C. A 5 nm Ti adhesion layer was deposited first, followed by the Ta film. After deposition, the samples were oxidized for 5 hours at 650 °C in flowing air to form Ta_2O_5. All nitridation experiments were performed in a furnace with a fused silica reactor tube at 1100 K.[186] During the nitridation process, H_2O vapor was introduced into the oven by a water-saturated flow of Ar carrier gas. The same gas flows were used during the cooling-down process.

Intermediate protection layers: Ultrathin amorphous TiO_2 layers (3 nm) were deposited onto the Ta_3N_5 films using a homemade thermal atomic layer deposition (ALD) system described previously.[176] The TiO_2 ALD was carried out at a substrate temperature of 150 °C using tetrakis(dimethylamino)-titanium (TDMAT) and H_2O (T_{H_2O} = 25 °C) as the Ti and O precursors, respectively. The pulsing times are 5 s and 10 ms for Ti and O precursors, respectively. Each precursor was purged for 30 seconds after the pulse. The growth rate measured by ellipsometry was 0.8 Å per cycle. The Al_2O_3 ALD was performed at 100 °C in a FlexAl ALD reactor using trimethylaluminum (TMA) and oxygen plasma as precursors. An ALD cycle consists of 0.75 s TMA exposure, 3 s N_2 purge, 2.5 s O_2 plasma exposure and 3 s N_2 purge. At the experimental conditions, the growth rate of Al_2O_3 is approximately 0.14 Å per cycle. The number of cycles is adjusted to obtain the desired thickness.

Catalyst deposition: The multilayer catalyst is deposited as follows. Firstly a 2 nm Ni film (99.95% purity) is sputter deposited in a PREVAC sputter chamber in 3 μbars partial pressure of Ar (15 SCCM flow) with 100W radio frequency power, for a deposition rate of 1 nm/50 s. Secondly, the samples are subsequently immersed into a mixed solution of 0.1 M $Ni(NO_3)_2$ and 0.1 M NaOH for 30 min, followed by a mixed solution of 0.1 M $Co(NO_3)_2$ and 0.1 M NaOH for 30 min, then washed with demineralized water and dried in N_2. Lastly the photoanodes are held potentiostatically at 1.0 V vs. Ag/AgCl for 3 min in a phosphate solution (pH = 7.1) with 0.5 mM $Co(NO_3)_2$.

Structure and morphology. The crystal structure of the samples was determined using a Bruker D8 Advance X-ray diffractometer equipped with LynxEye linear detector in a Bragg-Brentano configuration, and with a cobalt source (Co-Kα_1 λ=1.788965, Co-Kα_2 λ =1.792850). A Perkin Elmer Lambda 900 UV/vis/NIR double-beam spectrophotometer with an integrating sphere was used for diffuse reflectance measurements. Kelvin Probe Force Microscopy (KPFM) measurements were performed with a tip velocity of 2 μm/s in 2 x 2 μm^2 scans, 6 μm/s in 6 x 6 μm^2 scans, modulation potential 1 V, lift height 50 nm, scan rate 0.5 Hz, box temperature 28 °C. During KPFM measurements, illumination was provided by a Ushio SP9 spot cure unit with monochromator and fiber, center wavelength 365 nm, window 10 nm, lamp power 100%, intensity measured perpendicular: ~230 $\mu W/cm^2$, incidence angle: ~30°. The thickness of the thin films was measured by means of a Dektak step profilometer.

Photoelectrochemical characterization. Photoelectrochemical characterization was carried out in an aqueous 1M KOH (99%, Sigma-Aldrich) solution. The solution was purged with nitrogen prior and during the measurements to remove any dissolved oxygen. The working area of the electrodes exposed to the electrolyte was 28.3 mm^2 (6 mm diameter) for all samples. Potential control was provided by a potentiostat (EG&G PAR 283) in a three-electrode cell with a fused silica window. An Ag/AgCl electrode (XR300, Radiometer Analytical) and a coiled Pt wire were used as the reference and counter electrodes, respectively. White-light photocurrent densities were measured under simulated AM1.5 solar illumination (100 mW/cm^2) with a Newport Sol3A Class AAA solar simulator (type 94023A-SR3), whereas quantum efficiencies were measured with a 300 W Xe-arc lamp (L.O.T. Oriel LSB530U) coupled into a grating monochromator (Acton SpectraPro 150i). An electronic shutter (Uniblitz LS6) and high-pass colored glass filters (Schott, two filters of 3 mm thickness each) were placed between the monochromator and the sample to remove second-order diffracted light. The intensity of the monochromatic light was measured with a calibrated photodiode (Ophir PD300-UV).

Ta_3N_5 Results

For the (photo)electrochemical characterization of the Ta_3N_5 samples, two film thicknesses of 225 nm and 580 nm were chosen and samples were deposited on either Pt-coated quartz or Si. As an alternative to Pt, researchers have also reported the use of Ta foils as a conductive substrate for Ta_3N_5.[221] However, these foils were not chosen here because they flaked off during the nitridation process. XRD analysis of the Ta_3N_5-quartz and Ta_3N_5-Pt-quartz films is

shown in **Figure 4.2.1.** The material is mostly phase pure when deposited onto the quartz substrate. The preferential orientation of the films depends on the thickness. While films on quartz are single phase, the XRD of Ta_3N_5 films grown on Pt-coated quartz substrates show the presence of unidentified secondary phases. While not directly recognized in our X-Ray diffractograms, the presence of interfacial phases such as Ta_2N and Ta_5N_6 has been observed in the literature when Ta_3N_5 nanorods were grown onto a Ta substrate.[223]

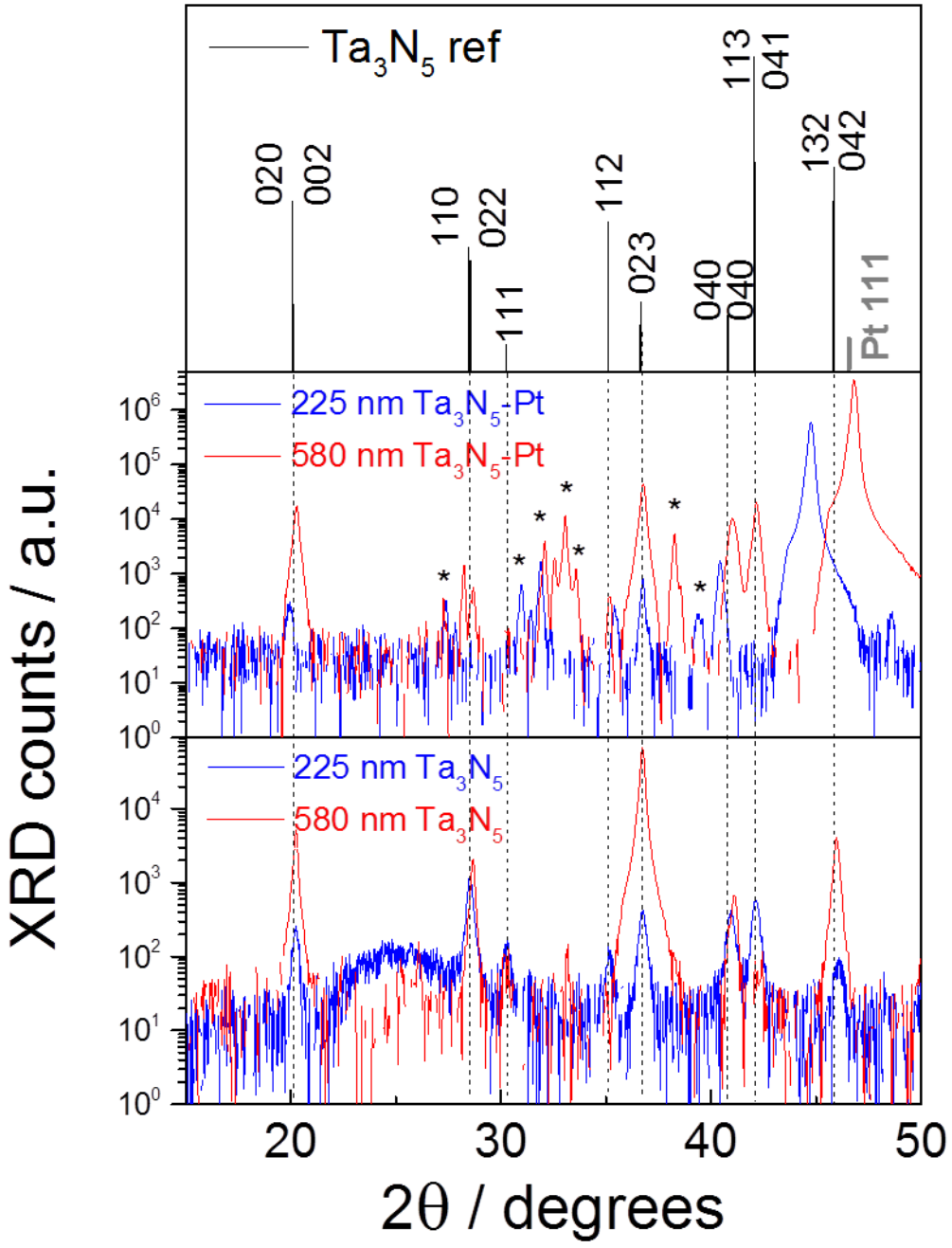

Figure 4.2.1. *X-ray diffractograms of Ta_3N_5 of 225 nm and 580 nm on quartz substrate (bottom) and on Pt-quartz (center). Y axis in logarithmic count scale. Ta_3N_5 and Pt reference peaks are shown in the top panel (International Centre for Diffraction Data. Ta_3N_5: PCPDF 72-0813; Pt: PCPDF 04-0802). An asterisk marks an unknown peak.*

We first test the semiconducting properties of our 225 nm Ta_3N_5-Pt-quartz electrodes. As explained in more detail in Chapter 2.2, the photovoltage generated by a semiconductor upon illumination is an important parameter, which relates to the semiconductor's efficiency to convert photons, of energy greater than its bandgap, into mobile charges at a given energy. The effective energy of the charges extracted from the semiconductor is given by its photovoltage, which is a quantity always smaller than the bandgap. Clearly, the more efficient the semiconductor (i.e., the less recombination), the larger the photovoltage will be. We use 2D Kelvin Probe Force Microscopy (KPFM) to provide information about the shift in the Fermi level on the surface of a solid in the dark and under illumination, i.e. the surface photovoltage. For measurements on unstable photoanodes such as Ta_3N_5, the advantage of the KPFM technique, compared to other (photo)electrochemical methods to measure the photovoltage, lies in the fact that KPFM measurements can be performed in air. The KPFM analysis on the Ta_3N_5-Pt-quartz reveals the formation of a 15 mV built-in surface photovoltage when measured under chopped UV illumination (λ = 365 nm, 200 $\mu W/cm^2$) while scanning the surface profile (see Figure 4.214.2). The relatively small shift in the Fermi level here reported is consisted with what expected at such low light intensities (low compared to AM1.5) based on the bandgap of Ta_3N_5.[236] This means, that our material is photoactive.

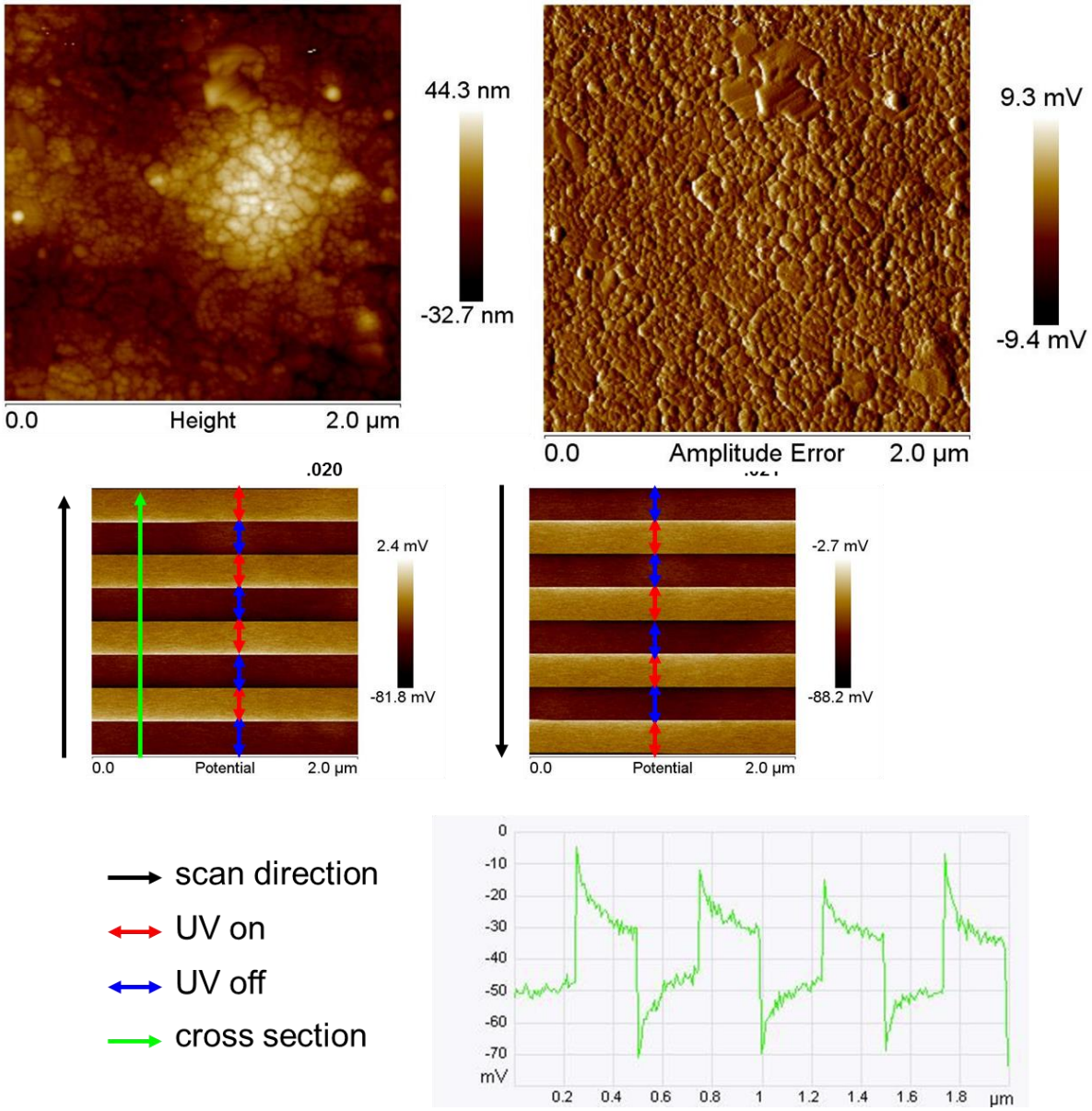

Figure 4.214.2. *AFM and amplitude signal (top), KPFM images under chopped UV illumination (λ = 365 nm, 200 µW/cm^2) while scanning the surface profile (bottom) of a Ta_3N_5 thin film deposited on Pt-quartz.*

Cyclic voltammetry for the bare Ta_3N_5-Pt samples in 1 M KOH in the dark reveals non negligible current at potentials below 1.5 V vs. RHE, which cannot be ascribed to water splitting (**Figure 4.2.3**). The intense redox activity present anodically and cathodically around 0.85 vs. RHE are tentatively assigned to oxidation of the Ta_3N_5 film and reduction of oxygen gas that is formed at positive potentials. The JV curve under illumination overlaps with the JV curve in the dark up to 1.0 V vs. RHE. Above this potential a photocurrent of 0.15 mAcm^{-2} at 1.23 V vs. RHE and up to 1 mAcm^{-2} at 1.6 V vs. RHE is generated. The rather positive onset potential at 1.0 V vs. RHE is somewhat unexpected considering the nearly

ideal band edge position of Ta_3N_5. It can be caused by a) poor catalytic activity of Ta_3N_5, b) surface recombination. The latter may be caused by a non-ideal semiconductor / liquid interface possibly caused by the reported growth of a superficial substoichiometric layer. Such a layer can introduce a potential barrier, act as a recombination center, and can be responsible for a poor catalytic activity.[228,229,237,219,235] We notice also that the current density is one order of magnitude lower than the theoretical saturation current density of Ta_3N_5, 13 $mAcm^{-2}$, estimated by its bandgap. Limited current density can be caused by a) limited light absorption, b) recombination. The recombination can occur in the bulk due to poor diffusion length and at the interfaces. Based on the amount of light absorbed, the expected current density would be 6.1 $mAcm^{-2}$ for our 225 nm Ta_3N_5. This value is about one half of the theoretical value. Considering the recombination, in Chapter 4.1 we calculated a long carrier diffusion length of the order of µm in our Ta_3N_5-quartz thin film measured by TRMC. However the long lifetimes are most likely due to trapping and detrapping phenomena. That means that calculated diffusion lengths may be over-estimated, and bulk recombination may still play an important role.[235] However, when Ta_3N_5 is grown on Pt-quartz secondary phases appear according to XRD. These extra phases may alter the picture by creating extra recombination centers. In Chapter 4.1 we found that the surface of Ta_3N_5 is in reality N-deficient and O-rich. Therefore, recombination may also take place at the interface with the surface substoichiometric layer. Furthermore, in the same chapter we identified the presence of shallow trap states which can be associated to the interfacial layer. In conclusion, we tentatively ascribe the modest current density of our bare Ta_3N_5 to both bulk as well as interfacial recombination. As we conveyed in **Chapter 4.1**, a high phase purity is an essential prerequisite for efficient (oxy)nitride-based absorber materials.

Successive JV cycles in **Figure 4.2.3** show decreasing photocurrent. This observation, together with the significant current generated in the dark, reveals the profound photo-electrochemical instability of the bare Ta_3N_5 photoelectrodes. The Ta_3N_5 instability is related to two mechanisms. A light-dependent mechanism for which photogenerated holes oxidize the Ta_3N_5, and an electrochemical instability as demonstrated by the Pourbaix diagram of Ta_3N_5 which shows no regions of stability. Because of this instability, we coated the Ta_3N_5 photoanodes coated with a set of catalytic and surface protection layers. Co-based catalysts are the most widely used on Ta_3N_5 to drive the water oxidation reaction and thereby improve the lifetime.[219,222,227,228,229,230] In general these Co-based catalysts are electrodeposited. However, since the films are intrinsically unstable in aqueous solutions, we chose to avoid the use of electrodeposition directly on the bare Ta_3N_5 samples. Instead, the catalytic layers

consist of a) firstly an ultrathin sputter deposited 2 nm Ni film; b) then the photoanode is dip coated with $Ni(OH)_2$ followed by $Co(OH)_2$; c) finally CoP_i is electrodeposited. An ultrathin 2 nm Ni film has been shown to be the optimal thickness to protect and catalyze Si photoanodes in 1 M KOH.[234,233] $Ni(OH)_2$ increased the performance and stability of Ta_3N_5 by acting as a hole-storage layer when used in conjunction with MoO_3 [228] or with $Fe(OH)_2$ [229]. The photoelectrochemical measurements are shown in **Fig. 4.2.4**(a).

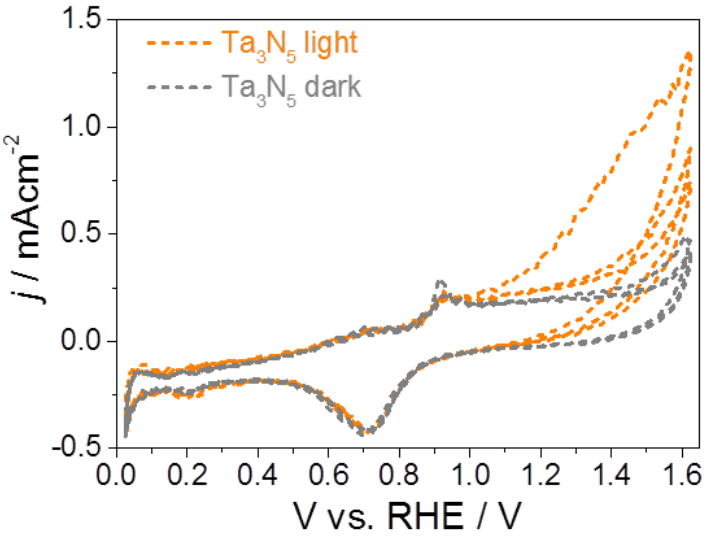

Figure 4.2.3. *JV curve of the bare 225 nm Ta_3N_5 in the dark and under AM1.5 illumination in 1 M KOH. The scan rate is 50 mV/sec.*

When the catalytic layers are deposited onto Ta_3N_5 the resultant JV characteristic in the dark presents similar redox features at 0.7 and 0.9 V vs. RHE (**Figure 4.4a,** top panel) as the bare Ta_3N_5 sample shown in **Figure 4.2.3**. On top of the Ta_3N_5 redox features, we observe redox peaks at 1.3 and 1.4 V vs. RHE. These features were also observed for the $Ni(OH)_2$ catalysts deposited directly on FTO-coated glass (**Figure 2 in Chapter 2.1**), as well as for $Co(OH)_2$ catalysts. Hence, we attribute the redox peaks in the same potential region (in 1 M KOH) of our Ni-Co catalyst-coated Ta_3N_5 to the catalyst. At a potential larger than 1.5 V vs. RHE, we ascribe the current to the catalytic water oxidation reaction running over the Ni-Co-based catalyst. Under illumination, the catalyst-coated Ta_3N_5 sample shows photocurrent at potential greater than 0.9 V vs. RHE. This potential is 0.1 V cathodic of the onset potential of the bare Ta_3N_5. The second and third JV cycles show a photocurrent which is comparable to the first cycle, indicating an improved photoelectrochemical stability compared to the bare Ta_3N_5 sample. The presence of the catalyst redox peaks indicates that the Ta_3N_5 film is not compact, and that part of the catalyst is directly deposited onto the Pt substrate.

Since the Ta_3N_5 redox activity is occurring also in the presence of the catalyst layers, we conclude that the catalysts do not offer enough protection. As a possible solution, we apply an extra ultrathin (3 nm) TiO_2 or Al_2O_3 layer. This extra protection layer is deposited in between the semiconductor and the Ni.

The addition of a 3 nm TiO_2 interfacial layer leads to a decrease current density of the Ta_3N_5 as well as the catalyst features during the cyclic voltammetry in the dark (**Fig. 4.2.4a,** middle panel). The photocurrent generated under illumination is comparable to that of the catalyzed-Ta_3N_5 sample. Moreover, successive cycles lead to a decrease in photocurrent density. Given the stability of the TiO_2 layer in 1 M KOH as reported in the literature,[231,232] this observation suggests the presence of pinholes or defects through which water molecules or atomic oxygen (or molecules) can diffuse.

The use of a 3 nm Al_2O_3 interfacial layer instead of TiO_2 offers a substantial improvement (**Fig. 4.2.4a,** bottom panel). In the dark (dotted lines), it suppresses the Ta_3N_5 redox features without affecting the catalyst redox features. Under illumination, it promotes a 50 mV cathodic shift of the photocurrent onset potential compared to the catalyzed-Ta_3N_5 sample. In addition, it leads to a photocurrent density of 0.5 $mAcm^{-2}$ at 1.23 V vs. RHE. Multiple cycles reveal a reasonably constant photocurrent density despite a small increase of the Ta_3N_5 reduction peak at 0.65 V vs. RHE.

The incident photon-to-current conversion efficiency (IPCE) data in **Figure 4.4 (b)** show an unchanged efficiency when the TiO_2 interfacial layer is present between the Ta_3N_5 and the catalyst, compared to the base case. In contrast, a large increase in IPCE is observed in the presence of the Al_2O_3 interfacial layer. We hypothesize that the Al_2O_3 layer not only offers protection against photocorrosion, but also reduces the surface recombination and/or creates a more favorable band alignment when in contact with Ni, thus forming a better metal-insulator-semiconductor interface. [238,239,240,241]

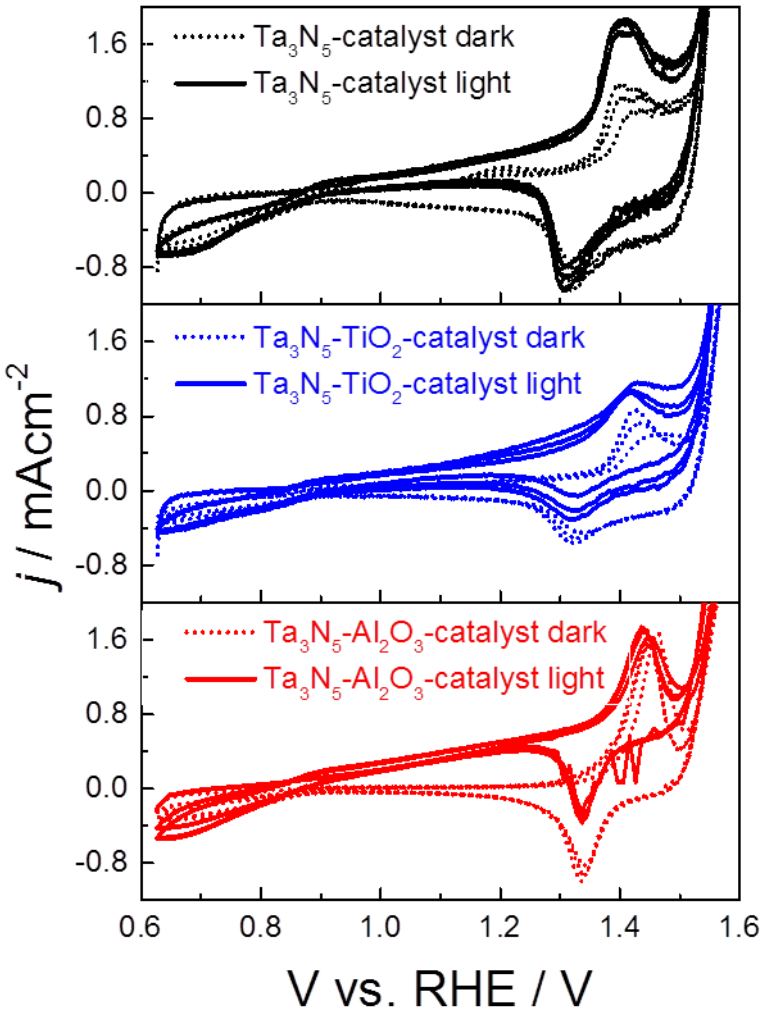
Ta3N5-catalyst dark
Ta3N5-catalyst light
Ta3N5-TiO2-catalyst dark
Ta3N5-TiO2-catalyst light
Ta3N5-Al2O3-catalyst dark
Ta3N5-Al2O3-catalyst light
j / mAcm-2
V vs. RHE / V

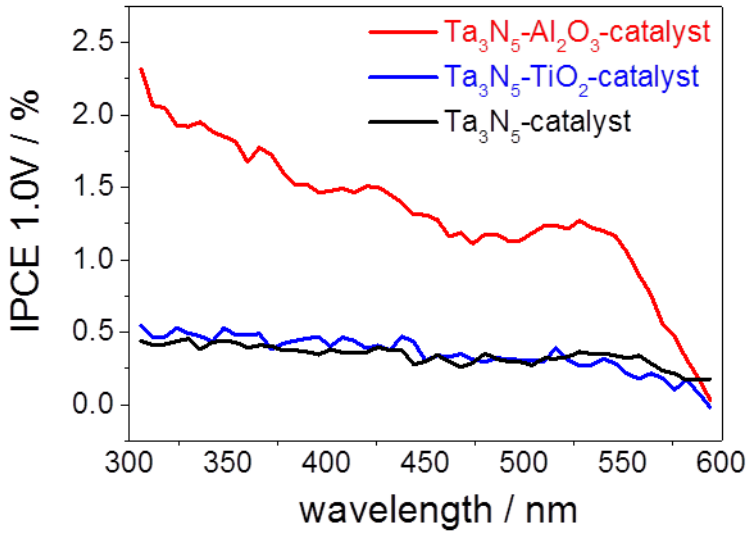
Ta3N5-Al2O3-catalyst
Ta3N5-TiO2-catalyst
Ta3N5-catalyst
IPCE 1.0V / %
wavelength / nm

Figure 4.2.4. *a) JV curves in the dark and under AM1.5 illumination in 1 M KOH of: 225 nm catalyst-coated Ta_3N_5 photoanodes; catalyst-coated Ta_3N_5 photoanodes with a TiO_2 interfacial layer; catalyst-coated Ta_3N_5 photoanodes with a Al_2O_3 interfacial layer. The scan rate is 50 mV/sec. b) Incident photon-to-current conversion efficiency (IPCE) at 1.0 V vs. RHE in 1 M KOH for a 225 nm Ta_3N_5 catalyzed with a Ni-NiCo-CoPi (black), with an additional 3 nm TiO2 interfacial layer (blue) and with a 3 nm Al_2O_3 interfacial layer (red).*

In order to increase the light absorption, we synthesized a 580 nm Ta_3N_5 photoanode. The thickness is chosen following a previous work by the Jaramillo group which found an optimal thickness of 600 nm for their thin film Ta_3N_5.[221] Due to the interaction with Pt however, we acknowledge that some of our Ta_3N_5 films may contain significant amounts of sub-stoichiometric (non-photoactive) tantalum nitrides, thus reducing the effective thickness of our Ta_3N_5 film. The photoelectrochemical performance of the 580 nm Ta_3N_5 is then tested including the Al_2O_3-protective interfacial layer and the catalyst. The results are shown in **Figure 4.2.5.** In the dark, the voltammogram shows no current at all potentials besides the beginning of a reductive peak negative of 0.6 V vs. RHE. This demonstrates the electrochemical stability of the photoanode in the potential window considered. The absence of the catalyst peaks implicates that at this thickness, the Ta_3N_5 layer is compact and there is no direct deposition of the catalyst onto the Pt substrate. Under illumination, a photocurrent is generated at potentials larger than 0.8 V vs. RHE. It reaches 3 $mAcm^{-2}$ at 1.23 V vs. RHE, while at 1.6 V vs. RHE a saturation current density of 5.5 $mAcm^{-2}$ is obtained. Comparable current density of 3 $mAcm^{-2}$ has been achieved in the literature on photoanodes made via electrophoretic deposition of nanoparticles followed by necking treatment.[227] The highest photocurrent value to date for thin films Ta_3N_5 photoanodes is 5.5 $mAcm^{-2}$ at 1.23 V vs. RHE, reported by Zou et al. This was achieved with thermal nitridation of Ta foils to achieve a Ta_3N_5 thickness of 2.0 μm, followed by a thermal or mechanical exfoliation of the surface layer.[219]

The stability of the photoanode is illustrated by the consecutive scans in **Figure 4.2.5.** The dark scans show overall negligible current in the potential range 0.6-1.6 V vs. RHE, as a proof of the good electrochemical stability of the photoanode. Under illumination, however, the reductive peak at 0.6 V vs. RHE appears together with a 20% decrease of saturation current density at each successive cycle. This degradation could be due to either an instability of the Al_2O_3 protective layers, or its permeability caused by the formation of cracks or pinholes.

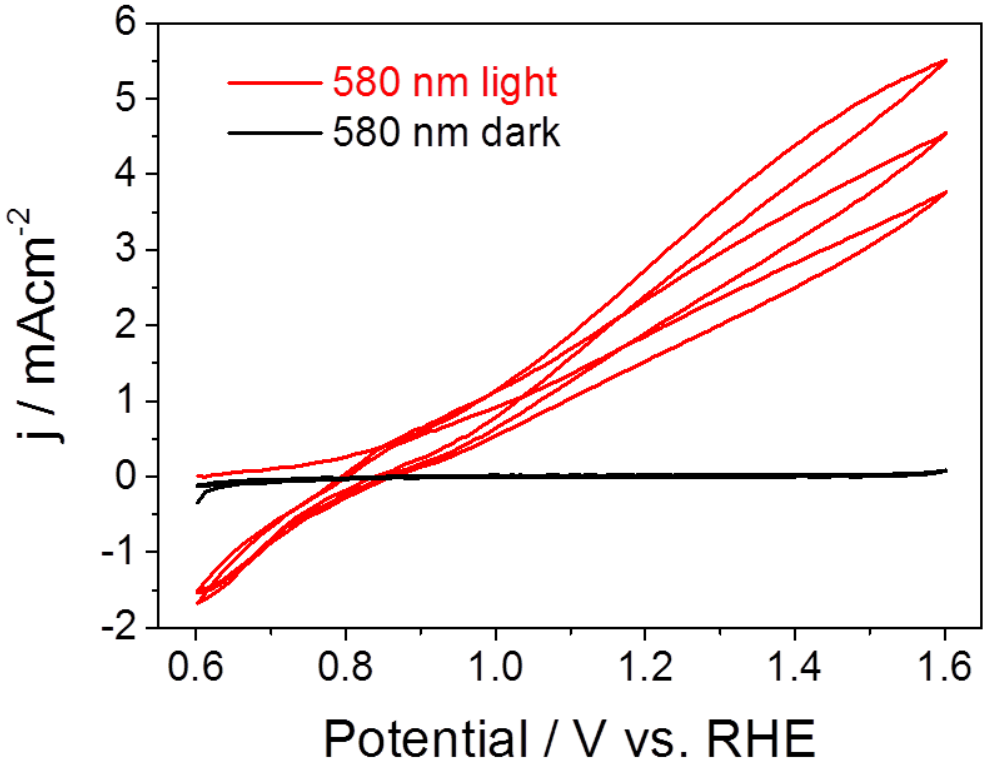

Figure 4.2.5. *JV curves in the dark and under AM1.5 illumination in 1 M KOH of the 580 nm catalyzed Ta_3N_5 photoanodes with a Al_2O_3 interfacial layer. The scan rate is 50 mV/sec.*

Ta_3N_5 Discussion

The photoelectrochemical performance reported herein compares favorably with a good fraction of the literature reports for thin films. This despite the disadvantage of growing the Ta_3N_5 film onto a Pt film, whose interaction generates secondary crystal phases. The difference between the effect of the ALD TiO_2 and the ALD Al_2O_3 layer is somehow counterintuitive. There is ample literature demonstrating that crystalline and amorphous TiO_2 can be used as a generic and effective electron- and hole-conducting protection layer for photocathodes and –anodes, respectively.[232,242,243] Its limited effectiveness in our case could be due to the particular nature of the deposition process for TiO_2 which may generate pinholes or oxygen permeability through the film. Depending on the materials properties of the film, the hole transport mechanism through the TiO_2 layer could be via defect-induced intergap states (substoichiometric film with low degree of crystallinity) or pure tunneling. The

deposition temperature for the TiO_2 layer determines its degree of crystallinity, which in turn controls the conductivity and stability in strongly alkaline media. At the deposition temperature of the ALD process, well below the crystallization temperature of TiO_2 (~400 °C), the deposited film will be amorphous. An optimization of the TiO_2 layer is currently under investigation and will be subject of a separate study. The use of Al_2O_3 as a passivation layer has been investigated to a lesser extent than TiO_2. Thus far it has been used successfully in passivating crystalline Si and photoanodes such as Fe_2O_3. In the former case, the effective surface passivation by Al_2O_3 films has mainly been attributed to a high negative fixed charge density in the Al_2O_3.[244] A negative fixed charge density is shown to be especially beneficial for the passivation of highly doped p-type c-Si as the bulk minority charge carriers, the electrons, are effectively shielded from the c-Si surface. In the case of Fe_2O_3, the Al_2O_3 coverage was reported to promote a decrease in the work function of Fe_2O_3 to a value lower than that of the catalyst. The overlayer thus aids in extracting electrons during the water oxidation reaction.[245] Thus, the improvement by our Al_2O_3 layer can be due to chemical passivation of surface recombination centers, and/or by improving the interfacial energetics between the Ta_3N_5 and the catalyst. Based on the available data, we are currently unable to distinguish between these possibilities.

While promising, the performance herein reported is still far from ideal with respect to the onset potential and the photocurrent density. In the literature, different approaches have proven successful to tackle each of the two issues separately. It has been shown that the mechanical removal of the surface substoichiometric layer in Ta_3N_5 photoanodes improves the photocurent density, but unexpectedly does not improve the onset potential.[219] Nanostructuring as well can bring the photocurrent density to higher values because of the better light absorption and charge transport. However nanostructuring has the drawback of increasing the density of surface states which prevent the onset potential to shift cathodically.[220,223,226,222] The need for multifunctional surface layers that can store holes, passivate the surface, and catalyze the electrochemical reactions is becoming increasingly important in the direct solar water splitting community, and is not limited to Ta_3N_5. Based on the concept of multi-functionality, p-type Co_3O_4-$Co(OH)_2$ bilayers[226] and p-type $Ni(OH)_2$-MoO_3 bilayers[228] were successfully used to lower the onset potential of Ta_3N_5 to values close to 0 V vs. RHE. A detailed mechanistic explanation for this remarkable shift is, however, still lacking. It has been related to the work function of the chosen materials which matches the energy of the holes in the Ta_3N_5.[226,228] While not mentioned in these articles, we notice that a p-n junction may have formed between the n-type Ta_3N_5 and the p-type bilayers. Such a

junction would increase the built in photovoltage and, therefore, the charge separation in the bulk material. In our case, the presence of a tunnel oxide such as Al_2O_3 prevents the formation of a p-n junction.

The photoelectrochemical stability of the thermodynamically instable Ta_3N_5 has yet not found a solution in the literature as well as in this study. The rate of decomposition varies greatly depending on the rate of extraction of the photogenerated holes from Ta_3N_5. The 2 nm Ni pre-catalyst layer has been used successfully in the literature to passivate Si, GaAs and GaP photoanodes, also in synergy with TiO_2.[242,234] It is known that Ni readily converts into $Ni(OH)_2$ in alkaline media, which in turn becomes NiOOH at the oxidizing potentials required for water oxidation. The knowledge of the nature of the Ni-based layer in terms of its phase (β, γ) and water tightness could shine light on its passivation properties and the underlying reason for its modest effectiveness in the present case. While it increases the photocurrent density, our ALD-deposited Al_2O_3 layer gives limited protection towards corrosion. Preliminary XPS data for a Ta_3N_5 film covered with Al_2O_3 layers of 1, 3 or 5 nm show the presence of the Ta and N peaks of comparable intensities at all thicknesses. While not conclusive (the electronic escape distance is in the order of few nm) the XPS data cannot exclude the presence of pinholes through the Al_2O_3 layer. Increasing the thickness of the layer could extend the lifetime of the Ta_3N_5, albeit at the expenses of hole conductivity. Furthermore, according to its Pourbaix diagram Al_2O_3 converts into AlO_2 at sufficiently positive potentials in alkaline media. This would make it unsuitable as a passivation layer for Ta_3N_5. However, the water tightness of the top Ni layer could inhibit the Al_2O_3 conversion process.

TaON Results

Here we present the photoelectrochemical results we obtained for TaON. Just like for Ta_3N_5 the deposition of TaON onto Pt-quartz gives rise to secondary crystal phases. Moreover, some of the β-TaON peaks are missing in the X-ray diffractogram of **Figure 4.2.6**, which would suggest that we do not have the desired β-TaON phase. Unlike in Ta_3N_5, KPFM analysis under chopped UV illumination (λ = 365 nm, 200 μW/cm^2) shows negligible built-in surface photovoltage, which is undistinguishable from the background noise (see **Figure 4.2.7**). The absence of surface photovoltage indicates extensive charge recombination. Such recombination could take place a) at the semiconductor/electrolyte interface, b) at the interface with the back contact, c) in the bulk of the material, d) at grain boundaries. This origin is investigated by correlating the photoelectrochemical results for different surface

modifications or with alternative substrates, with the structural data from XRD measurements. For photoelectrochemical measurements, we decorated the TaON-Pt-quartz photoanodes with IrO_x nanoparticles as a water oxidation catalyst (the bare TaON yielded no photocurrent). This choice was made to allow for an easy comparison to earlier work on this material. Moreover, functionalization with IrO_x has proven to be effective in scavenging holes away from the TaON surface to drive the water oxidation reaction.[246] The linear sweep voltammogram under chopped illumination in **Figure 4.2.8** shows that the material is photoelectrocatalytically active. The photocurrent falls short of 0.3 $mAcm^{-2}$ at the reversible potential for water oxidation of 1.23 V vs. RHE and is moderately dependent on the applied potential. The inset displays the potential region in proximity of 0 V vs. RHE, where the material shows reduced yet non-negligible photoresponse. A photoresponse in this potential region can be expected due to the band position of TaON which straddle the water oxidation and reduction potentials. While an onset potential near 0 V vs. RHE is a promising result, the origin of the photocurrent could be due to either water splitting, photocorrosion, or a combination of them. A stability measurement is therefore performed to clarify this aspect and the result is shown in **Figure 4.2.9**. For the stability measurement, the IrO_x-catalyzed TaON-Pt-quartz photoanode is compared with a NiOOH-catalyzed TaON-Pt-quartz photoanode, another effective catalyst for water oxidation in alkaline environments. In both cases, the photocurrent spikes to ~0.2 $mAcm^{-2}$ when the shutter is opened, then decays exponentially to about a tenth of the initial value after 600 s. At 500 s in the TaON-IrO_x curve, the shutter was closed for 30 s and then re-opened. This was done to check whether the photocurrent would recover to its initial value upon reopening the shutter. This did not happen, instead the photocurrent followed the decay curve. This observation supports a decrease in current due to material degradation rather than to an artifact such as e.g. reduced active area due to bubble formation. Electrochemically-induced pH gradients can also be excluded in this strongly alkaline electrolyte (1 M KOH).

Following literature reports that a graphite-like coating can increase the stability of photoelectrodes by acting as a charge separator and spacer,[247,248] we have also made use of graphite as intermediate layer between the semiconductor and the catalyst layers. In **Figure 4.2.9** we show that the addition of graphite has positive effect on the decay rate.

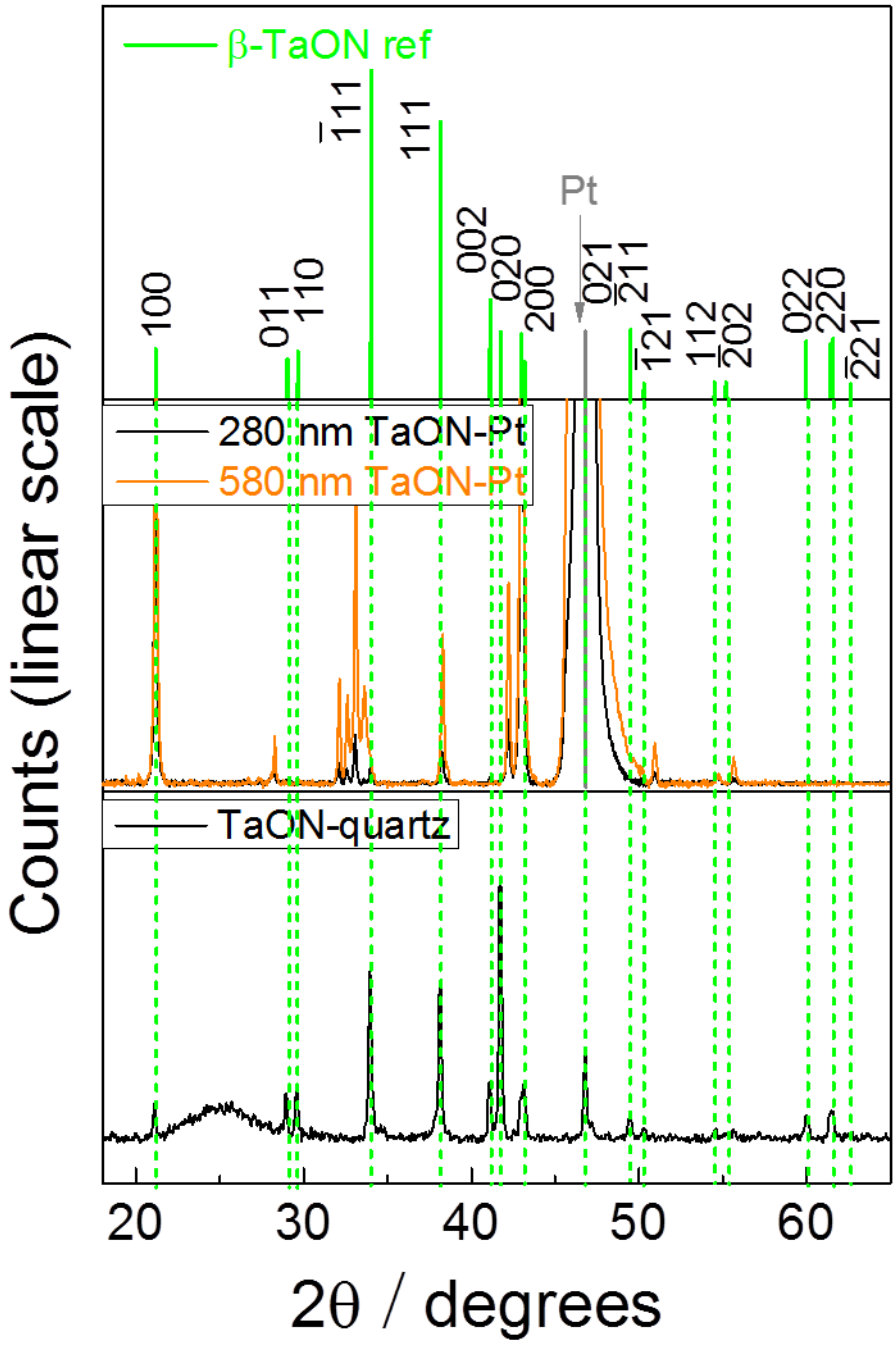

Figure 4.2.6. *X-ray diffractograms of TaON of 280 nm and 580 nm on Pt-quartz substrate (center) and on quartz (bottom). β-TaON and Pt reference peaks are shown (top). International Centre for Diffraction Data. β-TaON: PCPDF 71-0178; Pt: PCPDF 04-0802. The broad peak at 25° is due to the quartz substrate.*

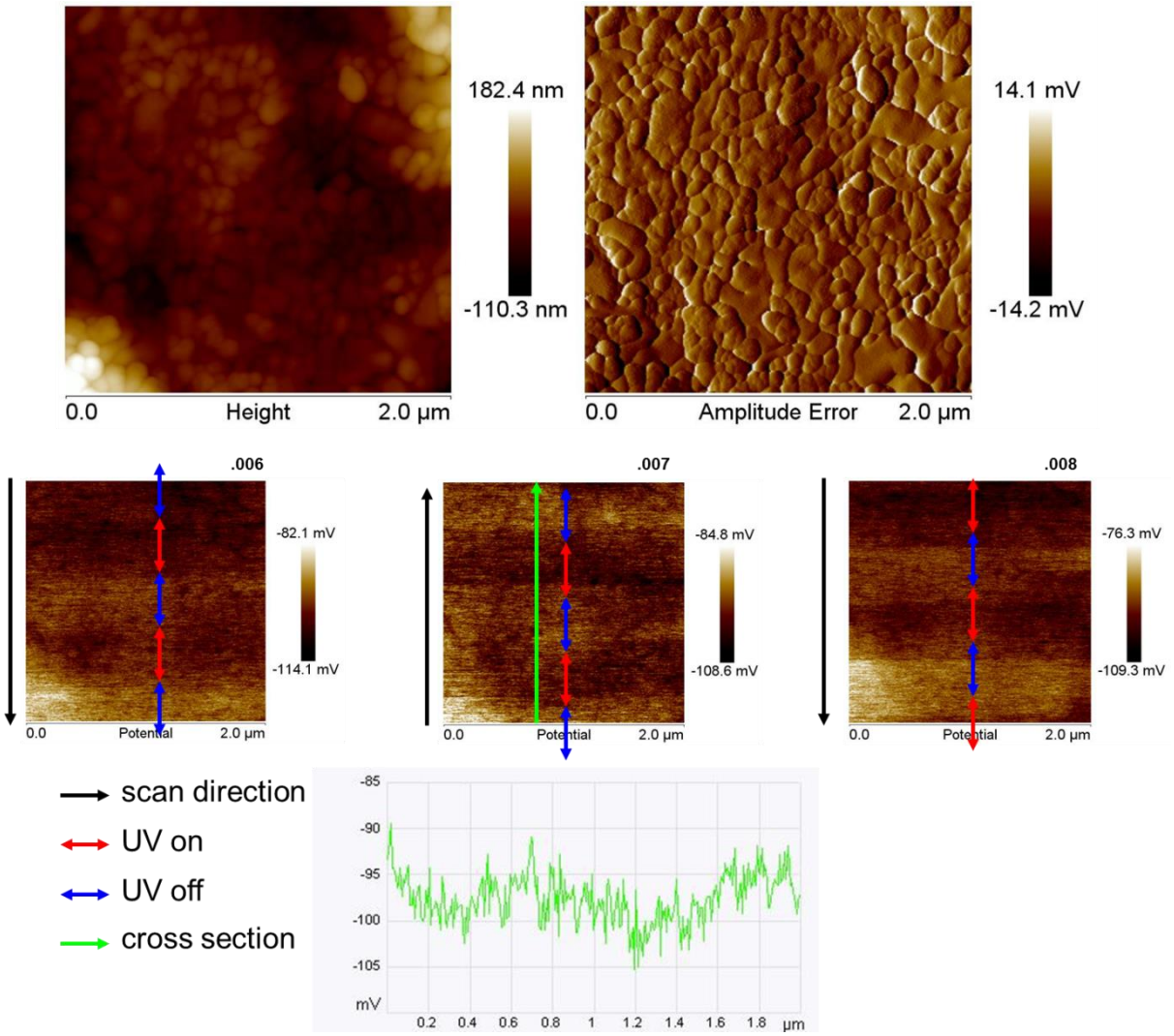

Figure 4.2.7. *AFM and amplitude signal (top), KPFM images under chopped UV illumination (λ = 365 nm, 200 µW/cm²) while scanning the surface profile (bottom) of a TaON thin film deposited on Pt-quartz.*

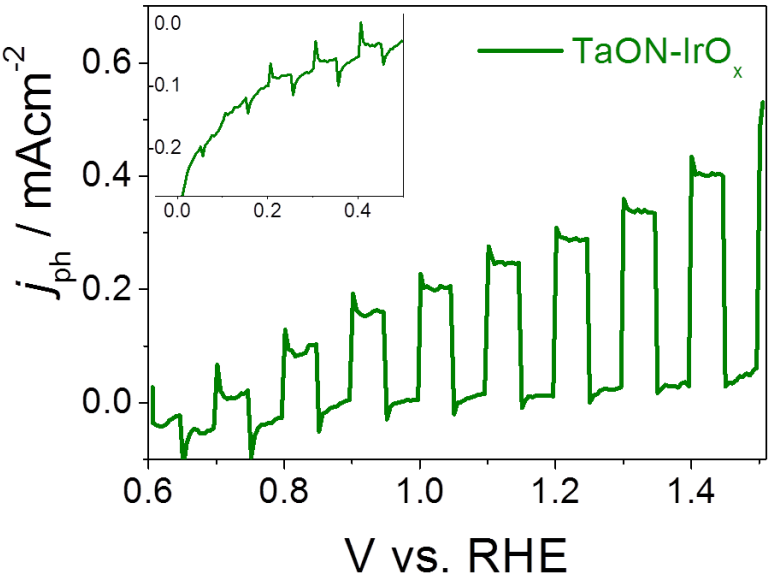

Figure 4.2.8. *Linear sweep voltammetry of IrO_x catalyzed 280 nm β-TaON–Pt–quartz (inset in the proximity of 0V vs. RHE) under chopped AM1.5 illumination. The scan rate is 10 mV/sec.*

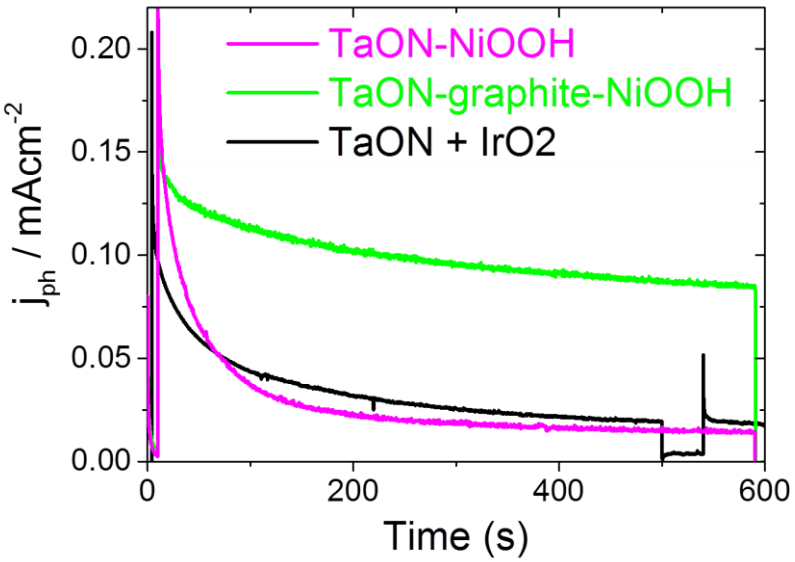

Figure 4.2.9. *Chronoamperometry at 1.23 V vs. RHE under AM1.5 illumination of a IrO_x- and a NiOOH-catalyzed TaON-Pt-quartz photoanodes, the latter with and without a graphite layer at the TaON-NiOOH interface. Measurements performed in 1 M KOH. At 500 s in the TaON-IrO_x curve, the shutter was closed for 30 s and then re-opened.*

Following the work done on Ta_3N_5, we synthesized TaON thin films of thickness of 360 nm and 580 nm for improved light absorption. Also, we coated the photoanodes with the same Ni-$Ni(OH)_2$-$Co(OH)_2$-CoP_i catalyst with an Al_2O_3 interfacial layer of identical thickness (3 nm) as done successfully on Ta_3N_5. The resulting linear voltammetric measurements in the anodic direction are shown in **Figure 4.2.10**. The dark scans for the 360 and 580 nm TaON films display the development of a cathodic current at potentials lower than 0.9 V vs. RHE. The cathodic current could be assigned to reduction of the catalytic layer, as shown for the Ta_3N_5 case in **Figure 4.4(a)** Similarly, anodic current appears at potentials greater than 1.0 V vs. RHE. While the graphs overlap in the cathodic region V < 0.9 V vs. RHE, the anodic dark current is reduced in the 580 nm sample at V > 1.0 V vs. RHE. The latter observation indicates that a thicker layer gives better coverage of the underlying Pt. Under illumination, extra anodic current develops. For the 580 nm sample the current is higher than for the 360 nm sample and reaches 0.15 $mAcm^{-2}$. Like in the case of Ta_3N_5, under illumination the thicker samples do not show the oxidative (and reductive) peaks around 1.4 V vs. RHE. Those peaks were ascribed to the presence of regions where deposition of the catalyst directly onto the Pt surface occurred.

With the Ni-$Ni(OH)_2$-$Co(OH)_2$-CoP_i catalyst and the Al_2O_3 interfacial layer, the stability significantly improves. After one hour at 1.23 V vs. RHE under AM1.5 illumination, the photoelectrochemical performance is 20% less than its initial value as shown in **Figure 4.2.11**.

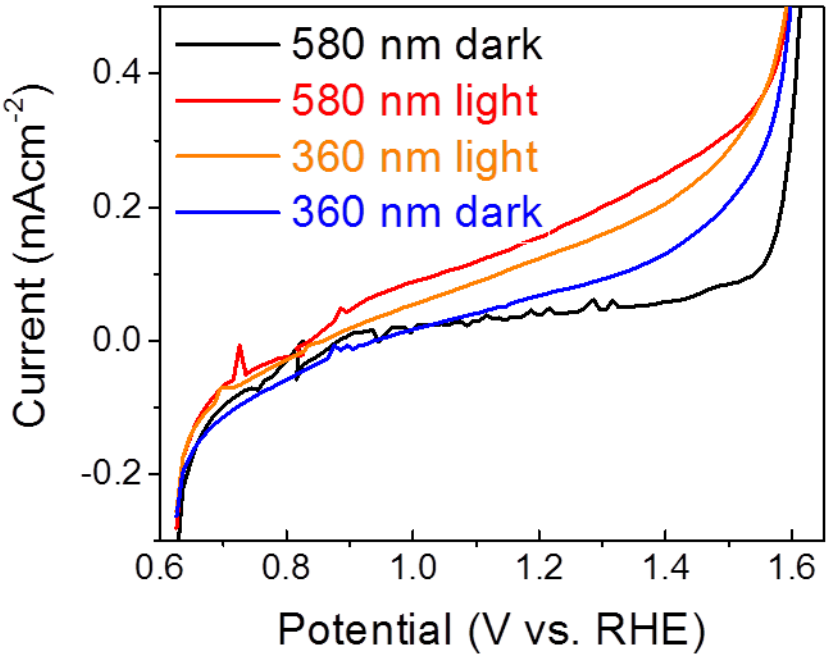

Figure 4.2.10. *JV curves in the dark and under AM1.5 illumination in 1 M KOH of 360 and 580 nm TaON-Pt-quartz photoanodes catalyzed by Ni-Ni(OH)$_2$-Co(OH)$_2$-CoP$_i$ with a Al$_2$O$_3$ interfacial layer. The scan rate is 50 mV/sec.*

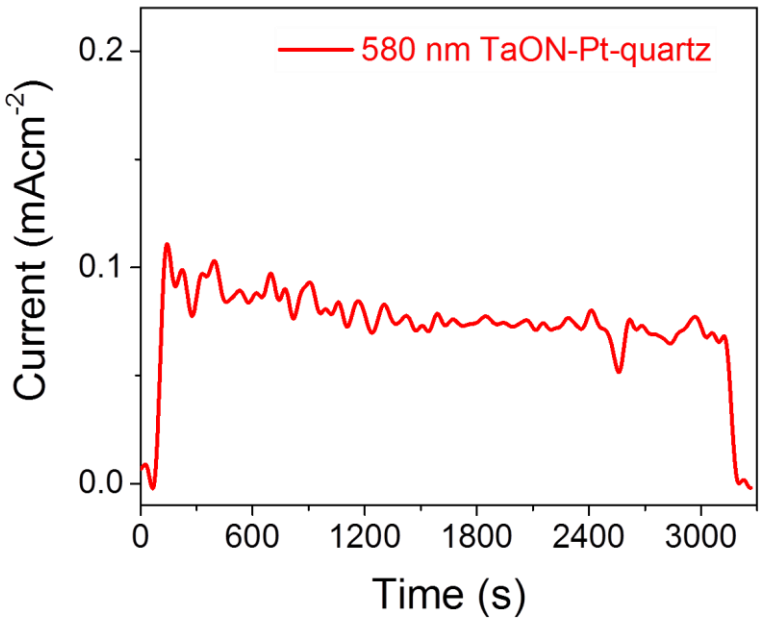

Figure 4.2.11. *Chronoamperometry at 1.23 V vs. RHE under AM1.5 illumination in 1 M KOH of 580 nm TaON-Pt-quartz photoanodes catalyzed by Ni-Ni(OH)$_2$-Co(OH)$_2$-CoP$_i$ with a Al$_2$O$_3$ interfacial layer.*

Unlike the case of Ta_3N_5, the maximum photocurrent generated by TaON is a full order of magnitude lower, irrespective of the thickness. Since we can exclude light absorption as the main factor limiting the performance of our 580 nm TaON-based photoanodes, the reason for the limited photocurrent is recombination. The recombination may occur 1) at the semiconductor-liquid interface, 2) at the semiconductor-Pt interface, 3) in the bulk of the semiconductor, or 4) at grain boundaries. The addition of the same surface modifications which worked effectively in Ta_3N_5 did not improve the performance comparably in our TaON-Pt-quartz photoanodes. Possible causes for recombination at the surface are slow charge extraction (i.e., poor catalysis), and the presence of surface states. Hole capture by these surface states may compete with the water oxidation process. While not conclusive, the modest photocurrents, even in the presence of a good water oxidation catalyst (the Ni-$Ni(OH)_2$-$Co(OH)_2$-CoP_i) and an effective passivation layer such as Al_2O_3, suggest that the charge extraction and surface recombination may not be the primary limiting factor. Recombination can also take place in the bulk and at the back contact, the metal / semiconductor interface. The stringent requirements posed on substrate by the high-temperature TaON synthesis method greatly limit the choice of usable materials. In this study, TaON samples were deposited on Pt-coated quartz, which fulfils the requirements. As an alternative to Pt-coated quartz, researchers have also reported the use of Ta foils as a conductive substrate for Ta_3N_5.[221] However, these foils were not chosen here because they failed as a substrates for β-TaON, possibly due to the greater mismatch in expansion coefficient of β-TaON compared to Ta_3N_5.[249] X-ray analysis in **Figure 4.2.6** showed the presence of secondary phases when the TaON film is grown onto Pt-quartz, while phase purity is achieved when TaON is deposited directly on the quartz substrate. We believe the secondary phases can have a negative effect on the semiconducting properties of the TaON film, thereby reducing its PEC performance. We have therefore deposited our TaON films onto different substrates such as n-type and p-type Si, TiN and $SrRuO_3$-$SrTiO_3$. In all cases, however, the substrate lost its electrical conductivity after the TaON synthesis process, resulting in low current during the voltammograms. If we replace the quartz substrate with a Si substrate, leaving Pt as conductive layer, we also notice that the PEC activity of the TaON-Pt is suppressed. This is shown in **Figure 4.2.12** where we compare the performance of two identical electrodes deposited onto either quartz or Si. When deposited on Si, no photoactivity is detected. This may be due to the formation of platinum-silicates at high temperatures, which could affect the conductivity of the substrate, but the exact reason is

beyond the scope of this study. In any case, this example illustrates the strong influence of the substrate material underneath the Pt film on the PEC performance of TaON-based thin film photoanodes.

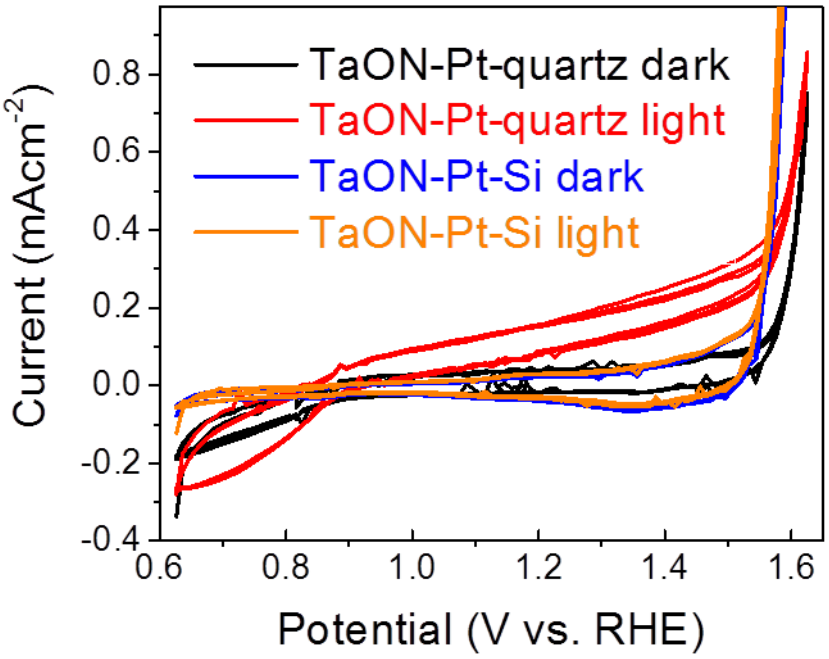

Figure 4.2.12. *JV curves in the dark and under AM1.5 illumination in 1 M KOH of 580 nm TaON-Pt photoanodes catalyzed by Ni-Ni(OH)$_2$-Co(OH)$_2$-CoP$_i$ with a Al$_2$O$_3$ interfacial layer. The layers are deposited either on quartz or on Si substrate. The scan rate is 50 mV/sec.*

TaON Discussion

Our TaON and Ta_3N_5 thin films have been grown on the same substrates and treated with the same surface modification. Yet the photoelectrochemical performance differs substantially. We speculate that this discrepancy is caused by the lower tolerance to secondary phases of TaON compared to Ta_3N_5. With the "oxynitrogenography" technique we have shown the existence of a narrow range of parameters which enables the formation of a phase pure β-TaON.[235] This phase was associated with high carrier lifetime by the TRMC analysis. Mixed phases, however, showed poor semiconducting properties. Next to this, the growth of both TaON and Ta_3N_5 onto Pt-quartz lead to the formation of unidentified secondary phases. The stringent requirements for the formation of a high quality TaON compared to Ta_3N_5 may explain the different overall film properties in the presence of high

amounts of impurities. A possible solution to the problem is to synthesize the TaON separately from the substrate for PEC measurements. The TaON film could be then transferred to the substrate in a second stage. This approach however has to deal with the possible poor contact between the TaON and the substrate itself.

Conclusions

In conclusion, in this chapter we demonstrated the use of Ta_3N_5 synthesized by high-temperature nitridation in a $NH_3/H_2O/H_2$ gas mixture for photoelectrochemical water splitting. We showed that growing Ta_3N_5 onto Pt-quartz alters the phase purity of the film compared to its growth onto quartz. We also showed for the first time the use of atomic layer deposited TiO_2 and Al_2O_3 overlayers for Ta_3N_5. The presence of the Al_2O_3 interfacial layer between the Ta_3N_5 and the Ni-$Ni(OH)_2$-$Co(OH)_2$-CoP_i catalyst increases the charge extraction rate by two-fold compared to the Ta_3N_5-catalyst and to the Ta_3N_5-TiO_2-catalyst configurations. As a result a promising 5.5 $mAcm^{-2}$ at 1.6 V vs. RHE was achieved with a 580 nm Ta_3N_5 photoanode with Al_2O_3-Ni-$Ni(OH)_2$-$Co(OH)_2$-CoP_i surface multilayers. When the same recipe is applied to TaON, a photocurrent of only 0.2 $mAcm^{-2}$ at 1.23 V vs. RHE is measured. We hypothesize that this discrepancy is caused by the lower tolerance to secondary phases of TaON compared to Ta_3N_5.

160. Maeda, K. (Oxy)nitrides with d0-electronic configuration as photocatalysts and photoanodes that operate under a wide range of visible light for overall water splitting *Phys. Chem. Chem. Phys.* **2013**, *15*, 10537-10548.
161. Navarro Yergo, R. M.; Consuelo Alvarez Galvan, M.; de Valle, F.; Villoria de la Mano, J. A.; Fierro, J. L. G. Water Splitting on Semiconductor Catalysts under Visible-Light Irradiation *ChemSusChem* **2009**, 2, 471-485.
162. Fakhouri, H.; Pulpytel, J.; Smith, W.; Zolfaghari, A.; Mortaheb, H. R.; Meshkini, F.; Jafari, R.; Sutter, E.; Arefi-Khonsari, F. Control of the visible and UV light water splitting and photocatalysis of nitrogen doped TiO2 thin films deposited by reactive magnetron sputtering *Appl. Catal. B-Environ.* **2014**, *144*, 12-21.
163. Baker, M.A.; Fakhouri, H.; Grilli, R.; Pulpytel, J.; Smith, W.; Arefi-Khonsari, F. Effect Of Total Gas Pressure And O2/N2 Flow Rate On The Nanostructure Of N-Doped Tio2 Thin Films Deposited By Reactive Sputtering *Thin Solid Films* **2014**, *552*, 10-17.
164. Smith, W.; Fakhouri, H.; Pulpytel, J.; Mori, S.; Grilli, R.; Baker, M. A.; Arefi-Khonsari, F. Visible Light Water Splitting via Oxidized TiN Thin Films *J. Phys. Chem. C* **2012**, *116*, 15855-15866.
165. Chen, S.; Wang, L. W. Thermodynamic Oxidation and Reduction Potentials of Photocatalytic Semiconductors in Aqueous Solution *Chem. Mater.* **2012**, *24*, 3659-3666.
166. Abe, R.; Higashi, M.; Domen, K. Facile Fabrication of an Efficient Oxynitride TaON Photoanode for Overall Water Splitting into H_2 and O_2 under Visible Light Irradiation *J. Am. Chem. Soc.* **2010**, *132*, 11828–11829.
167. Kristin A. Persson, Bryn Waldwick, Predrag Lazic, and Gerbrand Ceder, Prediction of solid-aqueous equilibria: Scheme to combine first-principles calculations of solids with experimental aqueous states. *Physical Review B* **2012**, 85, 235438.
168. Higashi, M.; Domen, K.; Abe R. Highly Stable Water Splitting on Oxynitride TaON Photoanode System under Visible Light Irradiation *J. Am. Chem. Soc.* **2012**, *134*, 6968–6971.
169. Liao, M.; Feng, J.; Luo, W.; Wang, Z.; Zhang, J.; Li, Z.; Yu, T.; Zou, Z. Co3O4 Nanoparticles as Robust Water Oxidation Catalysts Towards Remarkably Enhanced Photostability of a Ta3N5 Photoanode *Adv. Func. Mater.* **2012**, *22*, 3066-3074.
170. Li, Y.; Zhang, L.; Torres-Pardo, A.; González-Calbet, J. M.; Ma, Y.; Oleynikov, P.; Terasaki, O.; Asahina, S.; Shima, M.; Cha, D.; Zhao, L.; Takanabe, K.; Kubota, J.; Domen, K. Cobalt phosphate-modified barium-doped tantalum nitride nanorod photoanode with 1.5% solar energy conversion efficiency. *Nat. Commun.* **2013**, *4*, 2566.
171. Liu, R.; Zheng, Z.; Spurgeon, J.; Yang X. Enhanced photoelectrochemical water-splitting performance of semiconductors by surface passivation layers *Energy Environ. Sci.* **2014**, 7, 2504-2517.
172. Hu, S.; Shaner, M. R.; Beardslee, J. A.; Lichterman, M.; Brunschwig, B. S.; Lewis N. S. Amorphous TiO2 coatings stabilize Si, GaAs, and GaP photoanodes for efficient water oxidation *Science* **2014**, *344*, 1005-1009.
173. Mei, B.; Pedersen, T.; Malacrida, P.; Bae, D.; Frydendal, R.; Hansen, O.; Vesborg, P. C. K.; Seger, B.; Chorkendorff, I. Crystalline TiO_2: A Generic and Effective Electron-Conducting Protection Layer for Photoanodes and –cathodes *J. Phys. Chem. C*, **2015**, *119*, 15019–15027.
174. Mei, B.; Permyakova, A. A.; Frydendal, R.; Bae, D.; Pedersen, T.; Malacrida, P.; Hansen, O.; Stephens, I. E. L.; Vesborg, P. C. K.; Seger, B.; Chorkendorff I. Iron-Treated NiO as a Highly Transparent p-Type Protection Layer for Efficient Si-Based Photoanodes *J. Phys. Chem. Lett.* **2014**, *5*, 3456–3461.
175. Kenney, M. J.; Gong, M.; Li, Y.; Wu, J. Z.; Feng, J.; Lanza, M.; Dai H. High-Performance Silicon Photoanodes Passivated with Ultrathin Nickel Films for Water Oxidation *Science* **2013**, 342, 836-840.
176. Digdaya, I. A.; Han, L.; Buijs, T. W. F.; Zeman, M.; Dam, B.; Smets, A. H. M.; Smith, W. A. Extracting large photovoltages from a-SiC photocathodes with an amorphous TiO2 front surface field layer for solar hydrogen evolution *Energy Environ. Sci.* **2015**, *8*, 1585-1593.
177. Maeda, K.; Domen, K. New Non-Oxide Photocatalysts Designed for Overall Water Splitting under Visible Light *J. Phys. Chem. C* **2007**, 111, 7851-7861.

178. Lu, D.; Hitoki, G.; Katou, E.; Kondo, J. N.; Hara, M.; Domen, K. Porous Single-Crystalline TaON and Ta_3N_5 Particles *Chem. Mater.* **2004**, *16*, 1603-1605.
179. Orhan, E.; Tessier, F.; Marchand, R. Synthesis and energetics of yellow TaON *Sol. State Sci.* **2002**, *4*, 1071-1076.
180. Kerlau, M.; Merdrignac-Conanec, O.; Guilloux-Viry, M.; Perrin, A. Synthesis of crystallized TaON and Ta3N5 by nitridation of Ta2O5 thin films grown by pulsed laser deposition *Sol. State Sci.* **2004**, *6*, 101-107.
181. Henderson, S. J., Hector, A. L. Structural and compositional variations in Ta3N5 produced by high-temperature ammonolysis of tantalum oxide *J. Sol. State Chem.* **2006**, *179*, 3518-3524.
182. Hara, M.; Takata, T.; Kondo, J. N.; Domen, K. Photocatalytic reduction of water by TaON under visible light irradiation *Catal. Tod.* **2004**, *90*, 313-317.
183. Hara, M.; Sautet, P.; Nurlaela, E.; Raybaud, P.; Cavallo, L.; Domen, K.; Basset J.-M.; Takanabe, Tuning the properties of visible-light-responsive tantalum (oxy)nitride photocatalysts by non-stoichiometric compositions: a first-principles viewpoint K. *Phys. Chem. Chem. Phys.* **2014**, *16*, 20548-20560.
184. Gao, Q.; Giordano, C.; Antonietti, M.; Controlled Synthesis of Tantalum Oxynitride and Nitride Nanoparticles *Small* **2011**, *7*, 23, 3334–3340.
185. Dabirian, A.; van't Spijker, H; van de Krol, R. Wet ammonia Synthesis of Semiconducting N:Ta2O5, Ta3N5 and β-TaON Films for Photoanode Application *Energy Procedia* **2012**, *22*, 15-22.
186. Swisher, J. H.; Read, M. H. Thermodynamic properties and electrical conductivity of Ta_3 N_5 and TaON *Metallurgical Transactions* **1972**, 3, 489-495.
187. Yashima, M.; Lee, Y.; Domen, K. Crystal Structure and Electron Density of Tantalum Oxynitride, a Visible Light Responsive Photocatalyst *Chem. Mater.* **2007**, *19*, 588-593.
188. Fang, C. M.; Orhan, E.; de Wijs, G. A.; Hintzen, H. T.; de Groot, R. A.; Marchand, R.; Saillard, J.-Y.; de With, G. The electronic structure of tantalum (oxy)nitridesTaON and Ta_3N_5 *J. Mater. Chem.* **2001**, *11*, 1248–1252.
189. Chen, S. Y.; Wang, L. W. Intrinsic defects and electronic conductivity of TaON: First-principles insights. *Applied Physics Letters* **2011**, *99*, 222103.
190. Gremaud, R.; Broedersz, C. P.; Borsa, D. M.; Borgschulte, A.; Mauron, P.; Schreuders, H.; Rector, J. H.; Dam, B.; Griessen, R. Hydrogenography: An Optical Combinatorial Method To Find New Light-Weight Hydrogen-Storage Materials *Adv. Mater.* **2007**, *19*, 2813–2817.
191. Dabirian, A.; van de Krol, R. Resonant optical absorption and defect control in Ta3N5 photoanodes *Appl. Phys. Lett.* **2013**, *102*, 033905.
192. Carneiro, J. T.; Savenije, T. J.; Mul, G. Experimental evidence for electron localization on Au upon photo-activation of Au/anatase catalysts. *Phys. Chem. Chem. Phys.* **2009**, *11*, 2708-2714.
193. Kroeze, J. E.; Savenije, T. J.; Warman, J. M. Electrodeless determination of the trap density, decay kinetics, and charge separation efficiency of dye-sensitized nanocrystalline TiO2. *J. Am. Chem. Soc.* **2004**, *126*, 7608-7618.
194. Dabirian, A.; van de Krol, R.; High-Temperature Ammonolysis of Thin Film Ta2O5 Photoanodes: Evolution of Structural, Optical, and Photoelectrochemical Properties *Chem. Mater.* **2015**, *27*, 708-715.
195. Mooij, L. P. A.; Baldi, A.; Boelsma, C.; Shen, K.; Wagemaker, M.; Pivak, Y.; Schreuders, H.; Griessen, R.; Dam, B. Interface Energy Controlled Thermodynamics of Nanoscale Metal Hydrides *Adv. Energy Mater.* **2011**, *1*, 754.
196. Hara, M.; Chiba, E.; Ishikawa, A.; Takata, T.; Kondo, J. N.; Domen, K. Ta3N5 and TaON Thin Films on Ta Foil: Surface Composition and Stability *J. Phys. Chem. B* **2003**, *107*, 13441-13445.
197. Chun, W.-J.; Ishikawa, A.; Fujisawa, H.; Takata, T.; Kondo, J. N.; Hara, M.; Kawai, M.; Matsumoto, Y.; Domen, K. Conduction and Valence Band Positions of Ta2O5, TaON, and Ta3N5 by UPS and Electrochemical Methods *J. Phys. Chem. B* **2003**, *107*, 1798–1803.
198. Li, M.; Luo, W.; Cao, D.; Zhao, X.; Li, Z.; Yu, T.; Zou Z. A Co-catalyst-Loaded Ta3N5 Photoanode with a High Solar Photocurrent for Water Splitting upon Facile Removal of the Surface Layer *Angew. Chem. Int. Ed.* **2013**, *52*, 11016–11020.

199. Nurlaela, E.; Ould-Chikh, S.; Harb, M.; del Gobbo, S.; Aouine, M.; Puzenat, E.; Sautet, P.; Domen, K.; Basset, J.-M.; Takanabe, K. Critical Role of the Semiconductor–Electrolyte Interface in Photocatalytic Performance for Water-Splitting Reactions Using Ta3N5 Particles *Chem. Mater.* **2014**, *26*, 4812.
200. Fravventura, M. C.; Deligiannis, D.; Schins, J. M.; Siebbeles, L. D. A., Savenije, T. J. What Limits Photoconductance in Anatase TiO2 Nanostructures? A Real and Imaginary Microwave Conductance Study *J. Phys. Chem. C* **2013**, *117*, pp 8032–8040.
201. Morbec, J. M.; Narkeviciute, I.; Jaramillo, T. F.; Galli, G. Optoelectronic properties of Ta3N5: A joint theoretical and experimental study *Phys. Rev. B* **2014**, *90*, 155204.
202. Ziani, A.; Nurlaela, E.; Dhawale, D. S.; Silva, D. A.; Alarousu, E.; Mohammed, O. F.; Takanabe, K. Carrier dynamics of a visible-light-responsive Ta3N5 photoanode for water oxidation *Phys. Chem. Chem. Phys.*, **2015**, *17*, 2670-2677.
203. Chen, S.; Wang, L.-W. Thermodynamic Oxidation and Reduction Potentials of Photocatalytic Semiconductors in Aqueous Solution *Appl. Phys. Lett.* **2011**, *99*, 222103.
204. Rettie, A. J. E.; Lee, H. C.; Marshall, L. G.; Lin, J.-F.; Capan, C.; Lindemuth, J.; McCloy, J. S.; Zhou, J.; Bard, A. J.; Buddie Mullins, C. Combined Charge Carrier Transport and Photoelectrochemical Characterization of BiVO4 Single Crystals: Intrinsic Behavior of a Complex Metal Oxide *J. Am. Chem. Soc.* **2013**, *135*, 11389–11396.
205. Rettie, A. J. E.; Chemelewski, W. D.; Lindemuth, J.; McCloy, J. S.; Marshall, L. G.; Zhou, J.; Emin, D.; Buddie Mullins, C. Anisotropic small-polaron hopping in W:BiVO4 single crystals *Appl. Phys. Lett.* **2015**, *106*, 022106.
206. Ravensbergen, J.; Abdi, F. F.; van Santen, J. H.; Frese, R. N.; Dam, B.; van de Krol, R.; Kennis, John T. M. *J. Phys. Chem. C* **2014**, *118*, 27793–27800.
207. Pala, R. A.; Leenheer, A. J.; Lichterman, M.; Atwater, H. A.; Lewis, N. S. Measurement of minority-carrier diffusion lengths using wedge-shaped semiconductor photoelectrodes *Energy Environ. Sci.* **2014**, *7*, 3424-3430.
208. Suzuki, A.; Hirose, Y.; Oka, D.; Nakao, S.; Fukumura, T.; Ishii, S.; Sasa, K.; Matsuzaki, H.; Hasegawa, T. High-Mobility Electron Conduction in Oxynitride: Anatase TaON *Chem. Mater.* **2014**, *26*, 976.
209. Savenije, T.J.; Van Veenendaal, P.A.T.T.; de Haas, M.P.; Warman, J.M.; Shropp, R.E.I.; Spatially resolved photoconductive properties of profiled polycrystalline silicon thin films *J. Appl. Phys*. **2002**, *91*, 5671.
210. Joly, A. G.; Williams, J. R.; Chambers, S. A.; Xiong, G.; Hess, W. P.; Laman, D. M. Carrier Dynamics in α-Fe2O3 (0001) Thin Films and Single Crystals Probed by Femtosecond Transient Absorption and Reflectivity *J. Appl. Phys.* **2006**, *99*, 053521.
211. Cherepy, N. J.; Liston, D. B.; Lovejoy, J. A.; Deng, H. M.; Zhang, J. Z. Ultrafast Studies of Photoexcited Electron Dynamics in γ- and α-Fe2O3 Semiconductor Nanoparticles *J. Phys. Chem. B* **1998**, *102*, 770−776.
212. Kennedy, J. H.; Frese, K. W., Jr. Photoxidation of Water at α-Fe2O3 Electrodes. J. Electrochem. Soc. **1978**, *125*, 709−714.
213. Butler, M. A. Photoelectrolysis and Physical Properties of the Semiconducting Electrode WO3 J. Appl. Phys. **1977**, *48*, 1914−1920.
214. Paracchino, A.; Brauer, J. C.; Moser, J. E.; Thimsen, E.; Gratzel, M. Synthesis and Characterization of High-Photoactivity Electro-deposited Cu2O Solar Absorber by Photoelectrochemistry and Ultrafast Spectroscopy *J. Phys. Chem. C* **2012**, *116*, 7341−7350.
215. Seitz, L. C.; Chen, Z.; Forman, A.; Blaise, J.; Pinaud, A.; Benck, J. D.; Jaramillo, T. F. Modeling Practical Performance Limits of Photoelectrochemical Water Splitting Based on the Current State of Materials Research *ChemSusChem* **2014**, 7, 1372 – 1385
216. Lu, D.; Hitoki, G.; Katou, E.; Kondo, J. N.; Hara, M.; Domen, K. Porous Single-Crystalline TaON and Ta_3N_5 Particles *Chem. Mater.* **2004**, *16*, 1603-1605.
217. Kerlau, M.; Merdrignac-Conanec, O.; Guilloux-Viry, M.; Perrin, A. Synthesis of crystallized TaON and Ta3N5 by nitridation of Ta2O5 thin films grown by pulsed laser deposition *Sol. State Sci.* **2004**, *6*, 101-107.
218. Henderson, S. J., Hector, A. L. Structural and compositional variations in Ta3N5 produced by high-temperature ammonolysis of tantalum oxide *J. Sol. State Chem.* **2006**, *179*, 3518-3524.

219. Li, M.; Luo, W.; Cao, D.; Zhao, X.; Li, Z.; Yu, T.; Zou, Z. A Cocatalyst-Loaded Ta3N5 Photoanode with a High Solar Photocurrent for Water Splitting upon Facile Removal of the Surface Layer DOI: 10.1002/anie.201305350
220. Dang, H. X.; Hahn, N. T.; Park, H. S.; Bard, A. J.; Mullins, C. B.. Nanostructured Ta3N5 Films as Visible-Light Active Photoanodes for Water Oxidation *J. Phys. Chem. C* **2012**, 116, 19225−19232
221. Pinaud, B. A.; Vesborg, P. C. K.; Jaramillo, T. F. Effect of Film Morphology and Thickness on Charge Transport in Ta3N5/Ta Photoanodes for Solar Water Splitting *J. Phys. Chem. C* **2012**, 116, 15918−15924
222. Cong, Y.; Park, H. S.; Wang, S.; Dang, H. X.; Fan, F.-R. F.; Mullins, C. B.; Bard, A. J. Synthesis of Ta3N5 Nanotube Arrays Modified with Electrocatalysts for Photoelectrochemical Water Oxidation *J. Phys. Chem. C* **2012**, 116, 14541−14550
223. Li, Y.; Takata, T.; Cha, D.; Takanabe, K.; Minegishi, T.; Kubota, J.; Domen, K. Vertically Aligned Ta 3 N 5 Nanorod Arrays for Solar-Driven Photoelectrochemical Water Splitting *Adv. Mater.* **2012**, DOI: 10.1002/adma.201202582
224. Chen, S.; Wang, L. W. Thermodynamic Oxidation and Reduction Potentials of Photocatalytic Semiconductors in Aqueous Solution *Chem. Mater.* **2012**, *24*, 3659-3666.
225. Persson, K.A.; Waldwick, B.; Lazic, P.; Ceder, G. Prediction of solid-aqueous equilibria: Scheme to combine first-principles calculations of solids with experimental aqueous states. *Physical Review B* **2012**, 85, 235438.
226. Hou, J.; Wang, Z.; Yang, C.; Cheng, H.; Jiao, S.; Zhu, H. Cobalt-bilayer catalyst decorated Ta3N5 nanorod arrays as integrated electrodes for photoelectrochemical water Oxidation DOI: 10.1039/c3ee41854e
227. Liao, M.; Feng, J.; Luo, W.; Wang, Z.; Zhang, J.; Li, Z.; Yu, T.; Zou, Z. Co3O4 Nanoparticles as Robust Water Oxidation Catalysts Towards Remarkably Enhanced Photostability of a Ta3N5 Photoanode *Adv. Funct. Mater.* **2012**, *22*, 3066–3074
228. Liu, G.; Fu, P.; Zhou, L.; Yan, P.; Ding, C.; Shi, J.; Li, C. Efficient Hole Extraction from a Hole-Storage-Layer-Stabilized Tantalum Nitride Photoanode for Solar Water Splitting DOI: 10.1002/chem.201500745
229. Wang, L.; Dionigi, F.; Nguyen, N. T.; Kirchgeorg, R.; Gliech, M.; Grigorescu, S.; Strasser, P.; Schmuki, P. Tantalum Nitride Nanorod Arrays: Introducing Ni−Fe Layered Double Hydroxides as a Cocatalyst Strongly Stabilizing Photoanodes in Water Splitting DOI: 10.1021/cm503887t
230. Liu, R.; Zheng, Z.; Spurgeon, J.; Yang X. Enhanced photoelectrochemical water-splitting performance of semiconductors by surface passivation layers **Energy Environ. Sci. 2014**, **7**, 2504-2517.
231. Hu, S.; Shaner, M. R.; Beardslee, J. A.; Lichterman, M.; Brunschwig, B. S.; Lewis N. S. Amorphous TiO2 coatings stabilize Si, GaAs, and GaP photoanodes for efficient water oxidation *Science* **2014**, *344*, 1005-1009.
232. Mei, B.; Pedersen, T.; Malacrida, P.; Bae, D.; Frydendal, R.; Hansen, O.; Vesborg, P. C. K.; Seger, B.; Chorkendorff, I. Crystalline TiO_2: A Generic and Effective Electron-Conducting Protection Layer for Photoanodes and –cathodes *J. Phys. Chem. C*, **2015**, *119*, 15019–15027.
233. Mei, B.; Permyakova, A. A.; Frydendal, R.; Bae, D.; Pedersen, T.; Malacrida, P.; Hansen, O.; Stephens, I. E. L.; Vesborg, P. C. K.; Seger, B.; Chorkendorff I. Iron-Treated NiO as a Highly Transparent p-Type Protection Layer for Efficient Si-Based Photoanodes *J. Phys. Chem. Lett.* **2014**, *5*, 3456–3461.
234. Kenney, M. J.; Gong, M.; Li, Y.; Wu, J. Z.; Feng, J.; Lanza, M.; Dai H. High-Performance Silicon Photoanodes Passivated with Ultrathin Nickel Films for Water Oxidation *Science* **2013**, 342, 836-840.
235. de Respinis, M.; Fravventura, M.; Abdi, F. F.; Schreuders, H.; Savenije, T. J.; Smith, W. A.; Dam, B.; van de Krol, R. Oxynitrogenography: Controlled Synthesis of Single-Phase Tantalum Oxynitride Photoabsorbers *Chem. Mater.* **2015**, 27, 7091–7099
236. Henning, A.; Günzburger, G.; Jöhr, R.; Rosenwaks, Y.; Bozic-Weber, B.; Housecroft, C. E.; Constable, E. C.; Meyer E.; Glatzel, T. Kelvin probe force microscopy of nanocrystalline TiO2 photoelectrodes *Beilstein J. Nanotechnol.* **2013**, 4, 418–428
237. Nurlaela, E.; Ould-Chikh, S.; Harb, M.; del Gobbo, S.; Aouine, M.; Puzenat, E.; Sautet, P.; Domen, K.; Basset, J.-M.; Takanabe, K. Critical Role of the Semiconductor–Electrolyte Interface in Photocatalytic Performance for Water-Splitting Reactions Using Ta3N5 Particles *Chem. Mater.* **2014**, *26*, 4812.

238. Robertson, J. High dielectric constant gate oxides for metal oxide Si transistors *Rep. Prog. Phys.* **2006** 69 327–396
239. Yeo, Y.-C.; King, T.-J.; Hu, C. Metal-dielectric band alignment and its implications for metal gate complementary metal-oxide-semiconductor technology *J. Appl. Phys.* **2002**, 92, 12,
240. Tse, K.; Robertson J. Work function control at metal high-dielectric-constant gate oxide interfaces *Microelectronic Engineering* **2008**, 85 9–14
241. Scheuermann, A. G.; Lawrence, J. P.; Kemp, K. W.; Ito, T.; Walsh, A.; Chidsey, C. E. D.; Hurley P. K.; McIntyre P. C. Design principles for maximizing photovoltage in metal-oxide-protected water-splitting photoanodes *Nature Materials* **2016**, 15, 99-106,
242. Hu, S.; Shaner, M. R.; Beardslee, J. A.; Lichterman, M.; Brunschwig, B. S.; Lewis N. S. Amorphous TiO2 coatings stabilize Si, GaAs, and GaP photoanodes for efficient water oxidation *Science,* 344, 6187
243. Bae, D.; Shayestehaminzadeh, S.; Thorsteinsson, E. B.; Pedersen, T.; Hansen, O.; Seger, B.; Vesborg, P.C.K.; Ólafsson, S.; Chorkendorff, I. Protection of Si photocathode using TiO2 deposited by high power impulse magnetron sputtering for H2 evolution in alkaline media *Solar Energy Materials & Solar Cells* **2016**, 144, 758–765
244. Hoex, B.; Schmidt, J.; Pohl, P.; van de Sanden, M. C. M.; Kessels W. M. M. Silicon surface passivation by atomic layer deposited Al2O3 *Journal of Applied Physics* **2008**, 104, 044903
245. Neufeld, O.; Yatom, N.; Toroker, M. C. A First Principles Study on the Role of an Al2O3 Overlayer on Fe2O3 for Water Splitting, *ACS Catal.*, DOI: 10.1021/acscatal.5b01748
246. Abe, R.; Higashi, M.; Domen, K. *J. Am. Chem. Soc.* **2010**, 132, 11828–11829
247. Hu, J.; Ji, Y.; Shi, Y.; Hui, F.; Duan, H.; Lanza, M. A Review on the use of Graphene as a Protective Coating against Corrosion. *Ann J Materials Sci Eng.* **2014**, 1, 16.
248. Zhang, Z.; Dua, R.; Zhang, L.; Zhu, H.; Zhang, H.; Wang, P. Carbon-Layer-Protected Cuprous Oxide Nanowire Arrays for Efficient Water Reduction *ACS Nano* **2013**, 7, 1709–1717
249. Chun, W. J.; Ishikawa, A.; Fujisawa, H.; Takata, T.; Kondo, J. N.; Hara, M.; Kawai, M.; Matsumoto, Y.; Domen, K. *J. Phys. Chem. B* **2003**, 107, 1798−1803.

Chapter 5

An integrated Photovoltaic-Battery-Electrolyzer for Short and Long Term Conversion and Storage of Solar-Energy

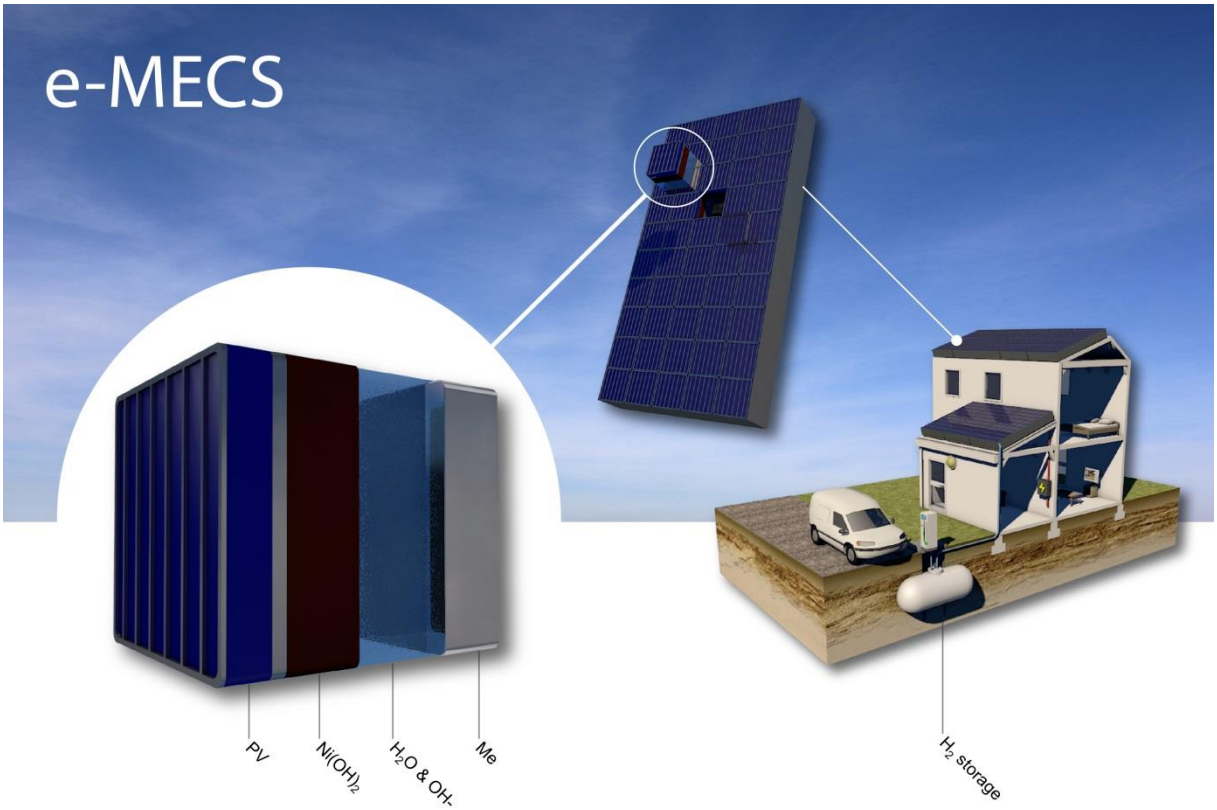

Here, we present a proof-of-principle for an integrated device that is able to convert and store solar energy either in a storage electrode (battery) or in the form of hydrogen gas (H_2 fuel), depending on the intensity of the irradiance. The working principle is that the storage electrode loads at a lower energy than the hydrogen gas formation. The device consists of a photovoltaic (PV) component integrated with a combined battery-electrolyzer cell of the same size. The battery/electrolyzer consists of a Pd-capped hydride-forming $Mg_{0.8}Ti_{0.2}$ cathode and a thick $Ni(OH)_2$ anode, which is powered by either of a triple junction silicon solar cell with an open circuit voltage (OCV) of 1.8 V under 1 sun illumination, or a quadruple junction silicon solar cell with an OCV of 2.3 V under 1 sun illumination. The device performance under varying solar irradiance is compared to the one delivered by the same PV component coupled to an electrolyzer composed of a Pt cathode and a thin $Ni(OH)_2$ anode. With the 4-jn PV cell, the OCV allows for energy storage at all light intensities between 0.1 and 1 sun. With the triple junction PV we show that at low light intensity (10 $mWcm^{-2}$), the most efficient way to use the solar irradiation is by delivering electricity. In the presence of

low light intensity (10 $mWcm^{-2}$), the device is in battery mode and the solar energy is stored by charging the cathode until full loading. Under an irradiance of one sun (100 $mWcm^{-2}$), the device automatically switches to the electrolyzer mode, and the solar energy is stored as a mixture of oxygen/hydrogen gas. Finally, when electric power is needed, the device may be switched back to battery mode to discharge the battery. This last step closes the electrical cycle, and regenerates the device.

This Chapter is based on:
de Respinis, M.; Smith W. A.; Dam, B. Intermittent Solar-Energy Conversion: Modular Electricity-Battery-Electrolyzer Device; patent filed / 2015P00052 NL - application number: 2016294

Rationale

In this section we present the rationale for the technological step from the direct photoelectrochemical approach to water splitting investigated in Chapters 2-4, to the modular PV-battery/electrolyzer concept proposed in Chapter 5. The basis for this rationale are 1) the complications which arise at the metal-semiconductor and semiconductor-catalyst-electrolyte interfaces, 2) the expected decrease in the photovoltage of the photoelectrodes under reduced light intensity, which may inhibit water splitting reactions to proceed, and 3) the fact that the photoelectrochemical H_2 production competes with solar PV, for the same surface area available in e.g. rooftop applications. These three points will be further elaborated below.

1) the metal-semiconductor and semiconductor-catalyst-electrolyte interfaces

The various solid-state approaches to solar water splitting can be grouped according to their interfaces into three groups, a) the properly called PEC approach where there exists at least one semiconductor-electrolyte interface, with proven solar-to-hydrogen (STH) efficiency of 5.2% and stability in the order of hours;[250,78] b) the buried PV-electrolysis where the semiconductors are protected by and separated from the electrolyte by a passivation layer, with proven STH efficiency of 12.4% and stability in the order of tens of hours;[251,252,253] and c) a non-integrated, modular design consisting of a PV component and an electrolyzer, with proven STH efficiency of 22% with the aid of a solar concentrator, and stability in the order of hundreds of hours.[254] Each approach has mostly been pursued by a particular class of materials. Because of the generally good chemical stability against photocorrosion, absorbers based on metal oxides have been employed in a). Si-based photoelectrodes have been used extensively in b). Because of their high efficiency, but also high costs, III-V materials such as GaAs have been often chosen in c).

In Chapters 2-4, we explored different photoelectrodes for the photoelectrochemical water oxidation reaction and in all cases we encountered severe limitations due to the complexity of the interfaces between different materials. Interfacial charge transfer is a key issue when introducing a semiconductor into a liquid electrolyte. As explained in details in a recent review by *Liu et al.*,[255] surface passivation layers can improve the photoelectrode and enhance charge transfer efficiency by suppressing the surface state density, providing an alternative lower energy route for charge transfer through catalytically active sites, protecting photoelectrodes from chemical corrosion. Although significant advantages are

possible through the use of a surface passivation layer, new issues may arise. The surface layer(s) creates new interfaces that must be considered. One example is the development of a metal-insulator-semiconductor (MIS) interface.[256] While a surface layer can improve one property, it may worsen another property simultaneously. To date, the achieved efficiencies of water-splitting by semiconductor-based PEC cells are still lower than that needed in a practical device, due either to a lack of suitable candidate materials, or to stability limitations under harsh reaction conditions. Fortunately, interfacial engineering provides the possibility for the further optimization of PEC systems.

In an attempt to circumvent the limitations posed by the interfaces, in Chapter 5 we pursue research in a different direction where the processes related to light absorption are separated from the electrochemical processes. This has the added benefit that we can more easily optimize the system for fluctuating light intensities.

2) The photovoltage of photoelectrodes under reduced light intensity

A techno-economic analysis performed by the Department of Energy (DOE) of the USA, showed that the main driver for the cost of the H_2 produced by a PEC device is its efficiency.[257] However, a sensitivity analysis of the levelized cost of hydrogen performed internally in our group revealed that actually the incoming solar irradiance and the operating costs can be even bigger knobs to turn.[258] While the behavior of PV modules at different light conditions (direct/diffuse, irradiance, tilting angle) has been investigated thoroughly, most research on PEC devices aims at maximizing the performance and stability under AM1.5G illumination (1000 W/m^2). While some research has been done on the behavior of a single photoelectrode under reduced light intensity,[259] to the best of our knowledge no studies exist on the behavior at the system level. Since the state-of-the-art PEC devices for solar water splitting are rapidly approaching the targets in terms of efficiency and stability under 1 sun illumination, it is of paramount importance to investigate the device behavior under the realistic conditions of fluctuating irradiance.

In recent years, models have been developed to quantify the loss mechanisms in PEC water splitting based on the current state of materials research to calculate the maximum solar-to-hydrogen (STH) conversion efficiencies.[215,260,261] Among others, we find the work by *Jaramillo's group* of particular relevance. Their quantitative sensitivity analysis for each loss mechanism and each absorber configuration shows a profound impact of both on the resulting STH efficiencies, which reaches 25% for the highest performance materials in a dual stacked configuration (see also **Figure 5.01a**).[215] In all the studies however, the

performance was calculated assuming AM1.5G illumination (1000 W/m^2). A flow chart indicating the constants and variables is shown in **Figure 5.01b**. However the assumed AM 1.5G illumination is met on average, in Europe, for less than 20% of the daily hours per year.

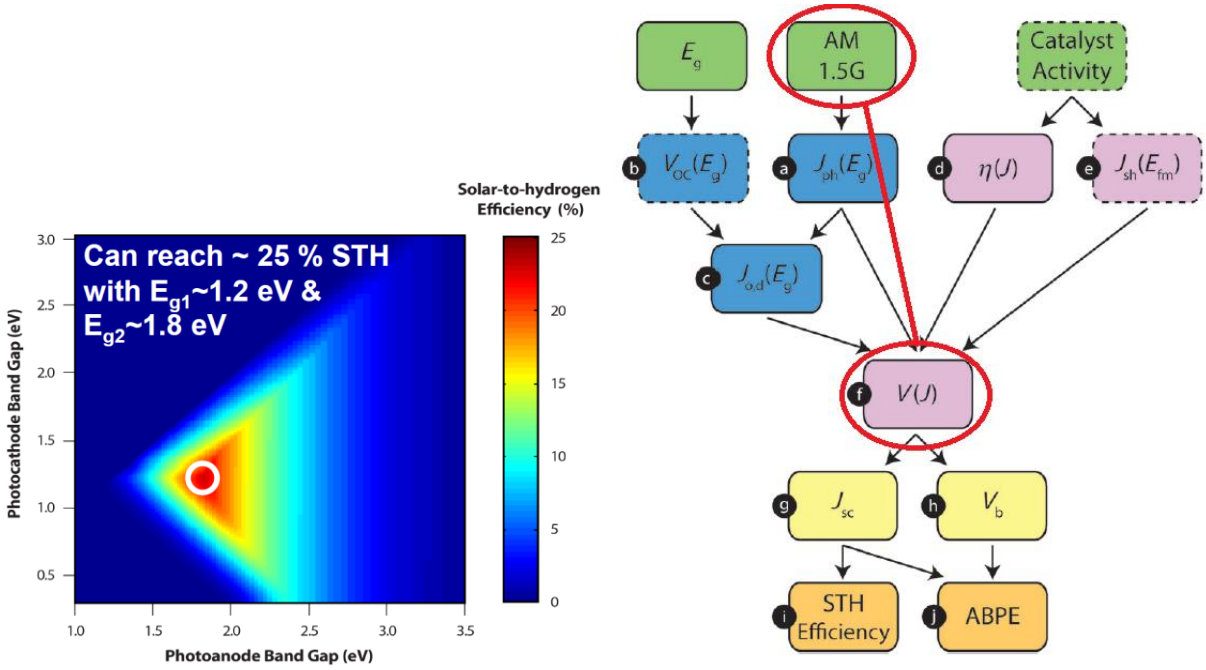

Figure 5.01. *(a) STH efficiency contour plots for dual stacked absorber configuration as a function of the band gaps of the top and bottom absorbers. It takes into account: a) reaction overpotentials (H_2 and O_2); b) entropic losses (V_{ph} < E_g); c) Shunt losses. b) Flowchart outlining calculation steps. Continuous lines indicate constants, dashed lines indicate variables. In red we marked the constant illumination and its effect on the JV characteristic. (Adapted from ref. [215])*

To split water using sunlight, small- and wide-bandgap semiconductors can be combined to provide enough photovoltage and photocurrent to run the catalytic reactions. The energy diagram of a tandem absorber PEC water splitting system is shown in **Figure 5.02**. In the PEC (and PV-electrolysis) approach, the operating point of the device is defined as the intersection between the J-V curves of the photoelectrodes. As we will show in more detail in Chapter 5, when the light intensity is reduced the saturation current density of a photoelectrode J_{sat} decreases linearly while the photovoltage V_{ph} decreases logarithmically. As the V_{ph} decreases, so does the operating point of the device. **Figure 5.03a** shows a schematic image for the operating point for a double absorber PEC solar water splitting device under AM1.5 illumination. When optimized, the reaction JV curve intersects the PV JV curve close to its maximum power point. **Figure 5.03b** illustrates the schematic diagram for a double absorber for PEC water splitting under reduced illumination. The power output

under reduced illumination reduces, and the operating point follows until eventually water splitting is no longer possible. This implies that much larger bandgap materials need to be used to ensure continuous operation during the larger part of the day. We believe the light intensity factor should be taken into account in future sensitivity analyses performed by the PEC water splitting community. In Chapter 5 we propose a novel approach which might enable the energy storage also at low light intensity. This is done adding an electrochemical storage functionality to one of the electrodes. The device then combines chemical storage by the production of H_2 via electrolysis of water, with electrochemical storage in the form of a Ni-MH type of battery using a MgTi hydride-based electrode. To enable the utilization of reduced light intensities, the loading of the MgTi electrode occurs at a lower energy than the hydrogen gas formation.

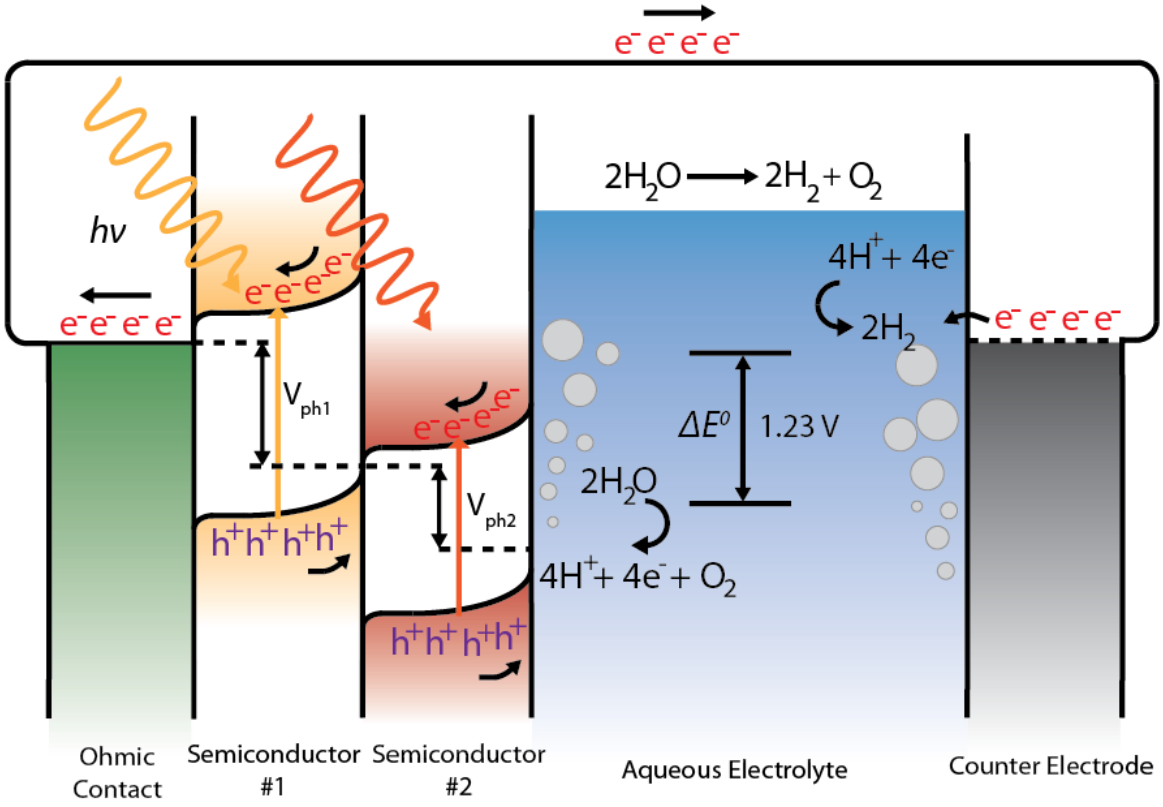

***Figure 5.02**. Energy diagram of a tandem absorber PEC water splitting system showing the photovoltage (V_{ph}) generated by the semiconductor under illumination.*

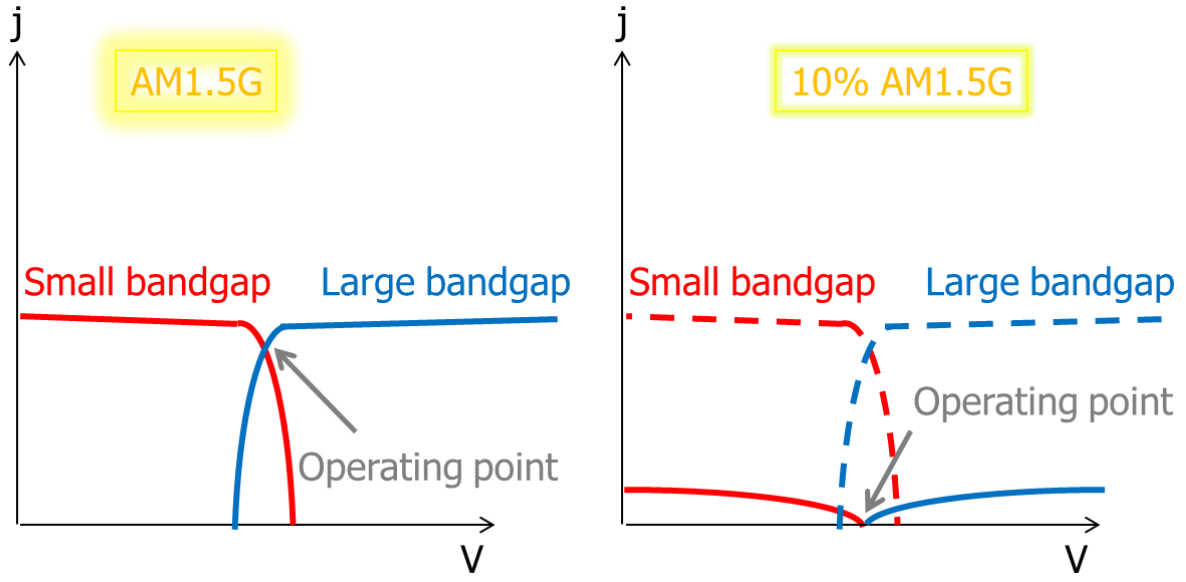

Figure 5.03. *Schematic illustrating the operating point for solar water splitting under AM1.5 illumination for a double absorber for PEC water splitting (a). The power output under reduced illumination reduces, and the operating point follows until eventually water splitting is no longer possible. The cases of a double absorber for PEC water splitting (b) are shown.*

3) Electricity generation and its storage

The main rationale for the development of a photoelectrochemical water splitting research line is the need for storage of solar energy, due to its intermittent character. The most efficient way to use solar energy is by converting it into electricity, to be used directly. The second most efficient way would be to store it in batteries. Thirdly, to store it in the form of chemical bonds, e.g. hydrogen gas. Next to this, the availability of surface area exposed to sunlight is limited, especially in densely populated areas. Therefore, dedicating a certain surface area exclusively for hydrogen generation, could potentially represent a limiting factor for the direct PEC approach. This rationale sets the basis for the development of a research project with an alternative approach. The modular PV-battery/electrolyzer concept proposed in Chapter 5 should enable both electricity generation as well as storage in one integrated device.

Introduction

The energy sector is facing a deep transformation nowadays. This transformation is related to the shift from a fossil-fuel based society to a so-called renewables based society. The drivers for such a transformation are: a) the depletion of easily accessible fossil fuel resources, b) the socio-economical consequences of air pollution and climate changes, c) the expected increase in energy demand, and d) the projected further shift of the population from rural areas to metropolitan areas. In this context, the energy demand is highly fluctuating and so are the renewable energy sources. One of the greatest sustainable energy challenges is to match the fluctuating curves of supply and demand (**Figure 5.1**). The objective of this work is to demonstrate a device that is able to adapt to varying illumination conditions and convert solar energy into either chemical or electrical energy.

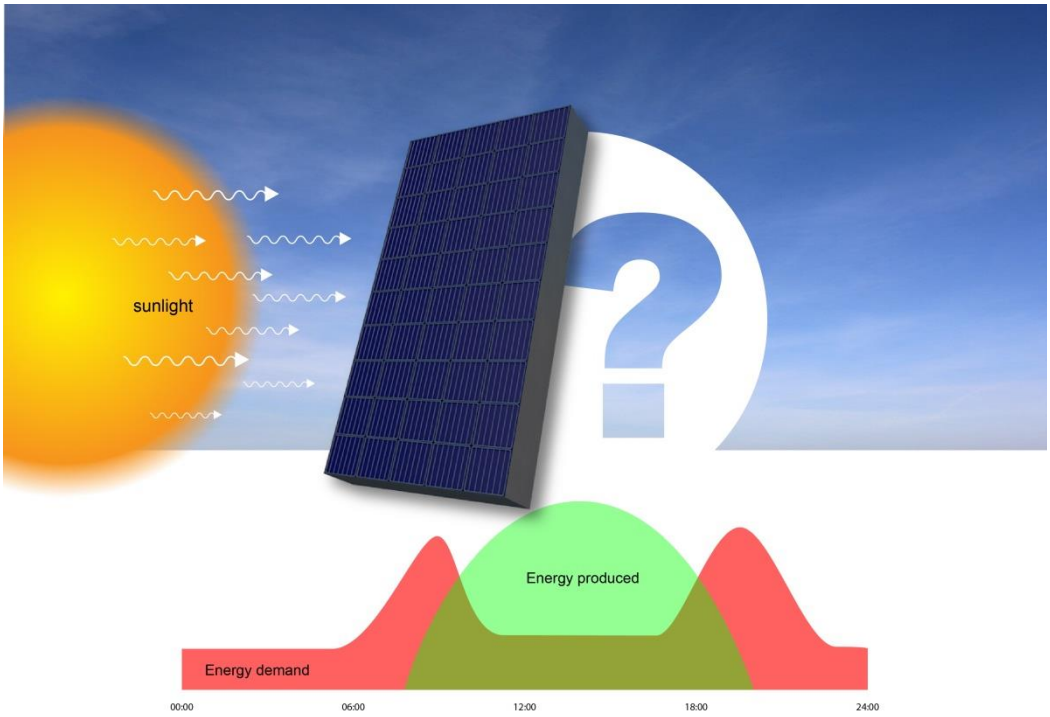

Figure 5.1. *Schematic illustrating the mismatch in the hourly electricity consumption in a household and production from a rooftop photovoltaic system.*

The experience gained with the expansion of rooftop solar PV has shown that the peak of solar electricity production coincides with hours of little household demand. On the other hand, in the evening hours, when the electricity demand peaks, there is limited to no electricity production from the PV cell. In addition, there is a seasonal mismatch between sustainable energy production and demand (see e.g. *F. Mulder)*[36]. While batteries can deal with short-term energy fluctuations, chemical storage in the form of e.g. H_2 will be of

paramount importance for seasonal storage and as a fuel for mobile applications.[36] At present the storage of solar electricity into batteries or into hydrogen through electrolysis, is generally not cost competitive. Thus it would be greatly beneficial to extend the efficiency and operational activity of these storage devices. A rather unexplored way to do so is by optimizing the energy conversion efficiency of solar-powered battery or electrolyzer systems under variable illumination conditions. While extensive data exist for the effect of fluctuating irradiance on the PV output power, limited information is available about when the PV module is directly coupled to a storage device. The direct coupling of a PV cell to batteries or electrolyzers presents the additional challenge of matching the voltage generated by the PV cell to the potential required to run the electrochemical reactions.

Pioneering work by *J. Schoonman* in the early 1980's, illustrated the possibility to combine solar hydrogen production and storage into one photo-electrochemical (PEC) device.[262,263] In this device he integrated a solid state electrode $SrTiO_3$, a proton conducting solid electrolyte and a hydride forming metal ZrH_y. The use of the solid-state electrolyte prevented the oxidation of the metal hydride which served as a hydrogen storage medium/battery. An interesting idea for a photo-rechargeable metal hydride/air battery was proposed in 2001,[264] with the work by *K. Akuto et al.* which showed that a metal oxide photoanode such as $SrTiO_3$ enables photorecharging and plays a pivotal role for the prevention of self-discharge of the $LaNi_{5-x}Al_xH_n$ anode. Recently, research on devices that combine photo-generated hydrogen production (chemical storage) and electrical storage functionalities was renewed.[265,266] Research by *Xia et al.* proposes the use of the pseudocapacitive properties of a $Ni(OH)_2$ combined with a TiO_2 photoanode to store the energy of the photogenerated holes for supercapacitor application, with Pt as hydrogen evolving cathode. Specific capacitances of 482 F/g at 0.5 A/g and 287 F/g at 1.0 A/g were obtained with their $TiO_2/Ni(OH)_2$ nanorod arrays.[265] The work by *Bora et al.* illustrates the possibility to use a hematite-NiO/α-$Ni(OH)_2$ heterostructure as a photoanode where $Ni(OH)_2$ improves the electrocatalytic current density by 16 times and simultaneously provides charge storage capacity.[267] *Danko et al.* proposed the use of a TiO_2-based hybrid photoanode and $LaNi_5$-based metal hydride cathode for photoelectrochemical water decomposition. The comparison with a Pt cathode reveals a photoconversion increase from 2% to 3% when Pt was substituted by the metal hydride cathode. The works described above shows that energy storage via multifunctional (photo-)electrochemical cells could be potentially advantageous compared to a (photo-)electrochemical water splitting cell. Moreover their work sets the basis for the investigation

of multifunctional energy storage cells coupled directly to a renewable source such as a photovoltaic cell.

Research has also been conducted on the system level by combining PV modules with electrolyzers and batteries, both experimentally[271] and theoretically.[268,269,270]

Research performed by General Motors shows that operating at the maximum power point of the PV module is the optimum condition for both the electrolyzer and the battery module.[271] This observation suggests that, for conventional Li batteries and electrolyzers, a choice has to be made on whether to store the solar energy as electricity or chemically. Moreover, in a combined PV-storage system, efficiency arguments recommend the direct use of electricity to be prioritized over its storage and reconversion. If during the daily hours the electricity production from the PV system exceeds the electricity demand, the electricity generated should first meet the consumption and then the remaining fraction can be stored. This is shown conceptually in **Figure 5.2**. However, this remaining power is going to be lower than, and in some cases not enough, to charge the battery nor to run the electrolyzer system designed to handle the power generated at full sun illumination. An analogous situation occurs when the light intensity fluctuates seasonally or due to various weather conditions. At low light intensity as well as under diffuse irradiance, the voltage generated by the PV drops and it may not be enough to run the reactions. While the PV power output equals the product of current and voltage, which is a monotonically increasing function of the light intensity, to run the water splitting reactions at a current density greater than 1 $mAcm^{-2}$ a minimum potential of ~1.6 V is required. The mismatch described in the two examples is of a major concern as it will reduce the operative hours of the device. One option would be to oversize the PV module in order to supply the required power (voltage) to the electrolyzer. Alternatively a power conversion device must be supplied to the module. This increases the overall balance of costs for the system.

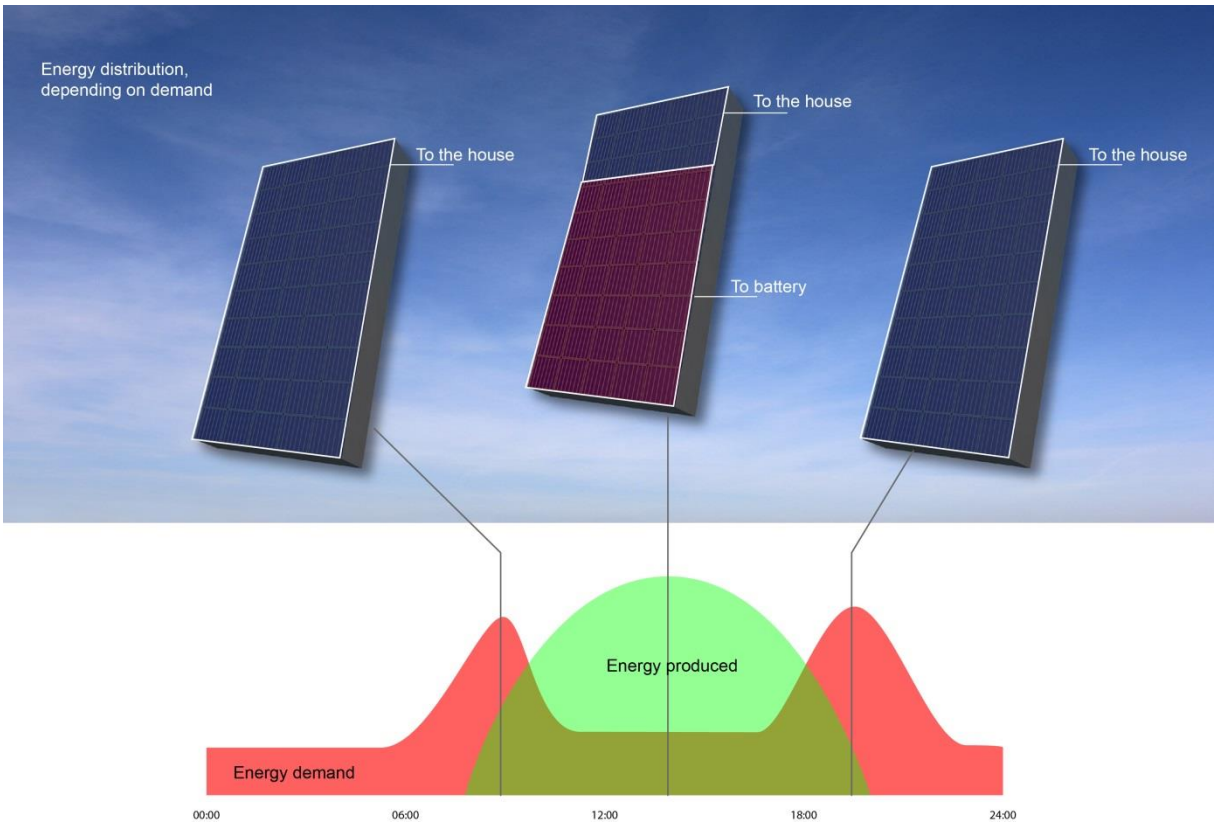

Figure 5.2. *Schematic of an hourly household energy consumption (red) and the electricity production by a PV system (green). When the demand is higher than the electricity production by the PV system, all panels contribute to meet the demand. When the electricity production exceeds the demand, part of it will be stored for later use.*

The common conclusion here is the need to operate storage devices at the maximum power point (MPP) of the solar cell. Since a battery directly connected to a PV array would practically never operate at the MPP, a DC-DC converter is needed. This requirement to operate at the MPP seems to exclude the possibility to perform both the electrical (daily) storage and the chemical (seasonal) storage in one system, unless the converter adapts to the kind of storage needed. An independent research carried on at the Centre for European Policy Studies (CEPS) on the potential market penetration of the Tesla's Powerwall argued that the high upfront costs provide an unfavorable starting point for a disruptive development of lithium-ion home battery. Moreover, its limited storage volume makes it impossible to reach 100% self-sufficiency. A minority of consumers might aim for 100% self-sufficiency by installing multiple batteries and oversizing the solar array, but this is not economically feasible and therefore unlikely to attract a mass-market.[37]

Here, we demonstrate the behavior of a solar device composed of a PV cell combined with an integrated battery/electrolyzer cell under varying light intensity. Since the battery

charging requires a lower voltage than the electrolyzer, we obtain: a) the integration of electrical and chemical storage in one device; b) a self-regulating system where the electrical (daily) storage is prioritized over the chemical (seasonal) storage; c) an increased device efficiency at moderate light intensity compared to PV-electrolysis, due to the fact that the battery components have a lower threshold potential than the water splitting process. We chose two PV cells with an open circuit voltage (OCV) of 2.3 V and 1.8 V. The former to test the PV-battery/electrolyzer device operating near the MPP of the solar cell. The latter to simulate the behavior of the battery/electrolyzer cell under limited applied potential. When the solar cell with larger OCV is used, the performance of the battery/electrolyzer is comparable to that of the electrolyzer at all light intensities. At low light intensity (10 mW/cm^2), the open circuit voltage of the PV is reduced from 2.3 V to 2.1 V. This potential is enough to charge the battery and to perform the water splitting reactions and the performance is limited by the current density generated by the solar cell. When the solar cell with the smaller OCV is used, at low light intensity (10 mW/cm^2), the open circuit voltage of the solar cell is reduced from ~ 1.8 V down to ~1.4 V. At this reduced potential neither the charging of the battery nor the water splitting reactions, can proceed. Therefore, electricity generation is the most efficient conversion process. At or above a moderate light intensity (50 mW/cm^2), the charging of the battery component is prioritized over the production of H_2. When the battery is fully charged, the hydrogen evolution will take place. With a fluctuating applied potential, the electricity is stored partly as electrical storage into the battery and partly as chemical storage in the form of H_2. Finally, the energy stored in the battery can be released by discharging the electrodes. This closes the electric cycle, and regenerates the electrodes in the device.

Experimental section

PV synthesis: We used triple junctions solar cells of 1 cm^2 where the absorber layers are amorphous silicon/nanocrystalline/nanocrystalline and quadruple junctions of 1 cm^2 where the absorber layers are amorphous silicon/amorphous silicon/nanocrystalline/nanocrystalline. Each of these cells have a p-i-n structure. p and n supporting layers are SiO_x doped with boron and phosphorous respectively. They were deposited by PECVD in a textured glass. The front contact is 300 nm Al (the front lines) and the back contacts are 100 nm Ag, 30 nm Cr and 500 nm Al.

Cathode synthesis: The synthesis of MgTi thin films has been carried out by sputter depositing a film of controlled composition of Mg and Ti targets (99.95% purity) onto FTO-

coated glasses substrates (TEC-15, 15 Ω/sq; Hartford Glass Co.) in 3 μbars partial pressure of Ar (20 ml/min flow) with 100 W DC electric power, and a substrate temperature of 400°C. A 5 nm Ti adhesion layer was deposited first, followed by the MgTi film. The same parameters were used for the deposition of the Pd catalyst. Moreover the MgTi-Pd electrode is coated with 150 nm sputtered PTFE film. The same parameters were used for the deposition of the Pt film of 10 nm thickness.

Anode synthesis: Prior to the deposition process the substrates were cleaned by three successive cycles of ultrasonic rinsing in a 10% aqueous triton solution, acetone and isopropanol, for 15 min each time. All the chemicals were used as received, without any further purification. The water used to prepare all solutions was deionized and ultrafiltrated by a Milipore Milli-Q system (resistivity > 18.2 MΩ · cm). The electrodeposition was performed in a single compartment electrochemical cell, using an Ag/AgCl (sat. KCl, sat. AgCl) (XR300, Radiometer Analytical) as reference electrode and a coiled Pt wire as a counter electrode. All potentials are reported versus the reversible hydrogen electrode (RHE), calculated according to the equation (5.1):

$$E_{RHE} = E_{Ag/AgCl}\,(sat.KCl) + E^{0}_{Ag/AgCl}\,(sat.KCl) + 0.0591\,\Delta pH \qquad (5.1)$$

Where E_{RHE} is the potential versus RHE, $E_{Ag/AgCl}\,(sat.KCl)$ is the potential applied or measured experimentally, $E^{0}_{Ag/AgCl}\,(sat.KCl)$ is the standard potential of the Ag/AgCl (sat. KCl) versus the normal hydrogen electrode (0.1976 V), and ΔpH accounts for the difference in pH of the working solution respect to the normal hydrogen electrode (pH zero). The electrodeposition was performed with a potentiostat / galvanostat (EG&G PAR 283). NiOOH was synthesized by electro deposition at 300 microA/cm^2 of a solution containing 0.005 M $NiSO_4$ (J.T. Baker ≥98.0%) and 0.015 M $(NH_4)_2SO_4$ (Sigma Aldrich ≥99.0%) for 10 and 30 minutes.[272] The pH was adjusted by adding NH_4OH (Sigma Aldrich) until a pH of 8.5 was reached. Above a pH of 8 amine complex ions are formed and the colour changes from green to light blue. After electrodeposition, the sample is gently dried under a nitrogen stream before it is placed in a furnace. A heat treatment of 15 minutes at 250ºC with a heating ramp of 5ºC per minute and under a stream of air improves the catalyst by evaporating structural water. The time for NiOOH electrodeposition was calculated according to the real surface area of the working electrode and chosen as 2 min for the electrolyzer and 30 min for the battery/electrolyzer. Theoretical estimation of time needed to fabricate NiOOH films of desired thickness is difficult, since water oxidation reaction can readily occur at potentials facilitating NiOOH deposition.

Electrochemical measurements: The same setup as described in the previous section was used for voltammetric measurements. The polarization curves were obtained by cyclic voltammetry in 1 M KOH.

Device testing: Photoelectrochemical characterization was carried out in an aqueous 1 M KOH (pH ~13.6). The solution was purged with nitrogen prior and during the measurements to remove any dissolved oxygen. The working area of the electrodes exposed to the electrolyte was 28.3 mm^2 (6 mm diameter) for all samples. The potential of the working electrode was controlled by a potentiostat (EG&G PAR 283). In three-electrode measurements, a coiled Pt wire and an Ag/AgCl electrode (XR300, saturated KCl and AgCl solution; Radiometer Analytical) were used as the counter and reference electrodes, respectively. Cyclic voltammetry measurements were performed with a scan rate of 50 mVs^{-1}, unless otherwise stated. White light photocurrent measurements were performed under simulated AM1.5 solar illumination (100$mWcm^2$) with a Newport Sol3A Class AAA solar simulator (type 94023 ASR3). Reduced illumination is achieved by interposing optical density filters in the light path in front of the PV cell. Electrical contact to the sample was made using a silver wire and graphite paste. In the two electrode configuration, the PV cell was connected directly to the electrochemical cell. The potentiostat was used as the ammeter in the current versus time measurements. The electrochemical cell was sealed and made air tight. The cell was continuously purged with a constant N_2 flow rate and vented directly into the gas-sampling loop of a gas chromatograph (GC, Interscience) in order to enable periodic quantification (every 18 minutes) of the gas-phase products. A schematic of such experimental setup is depicted in **Figure 5.3**. A schematic energy diagram in the PV and electrochemical cell is shown in **Figure 5.4**.

Gas chromatography testing: The sensitivity of the GC is tested, with the cell in the electrolyzer mode, by consecutive galvanostatic measurements of 0.1, 0.3 and 1 mA for 72 minutes each in order to collect 4 data points at each current. The partial current density of O_2 (and H_2) production is calculated from the GC peak area according to equation 5.2:[273]

$$j_{O_2} = \frac{peak\ area}{\alpha} \cdot flow\ rate \cdot \frac{2Fp_0}{RT} \cdot (electrode\ area)^{-1} \qquad (5.2)$$

where α is a conversion factor based on calibration of the GC with a standard sample, p_0 = 1.013 bar and T = 273.15 K. The Faradaic efficiency (FE) can then be calculated from the total measured current as $j_{O_2} = j \cdot FE$.

In Figure 5.5A we show the voltage response of the cell to the galvanostatic input. At 0.1 mA, the increase in potential over time is attributed to the charging of the electrodes. At 0.3 and 1 mA the potential decreases over time. This is attributed to an increased water oxidation efficiency as the Ni electrode is overcharged, in agreement with recent literature findings.[75,67,274] In **Figure 5.5**B we show the O_2 and H_2 measurements by the GC at each current. At 0.1 mA no H_2 is detected, while the O_2 concentration increases and saturates to a level of about 12%. At 0.3 and 1 mA H_2 is detected and increases to ~100% within the 72 minutes of the measurement. More data points would be needed to confirm saturation. The O_2 detection follows a comparable trend as at 0.1 mA, saturating at ~12%. This indicates that an adjustment in the calibration is required. Therefore, later in this chapter we will rely on the H_2 measurement for a qualitative analysis.

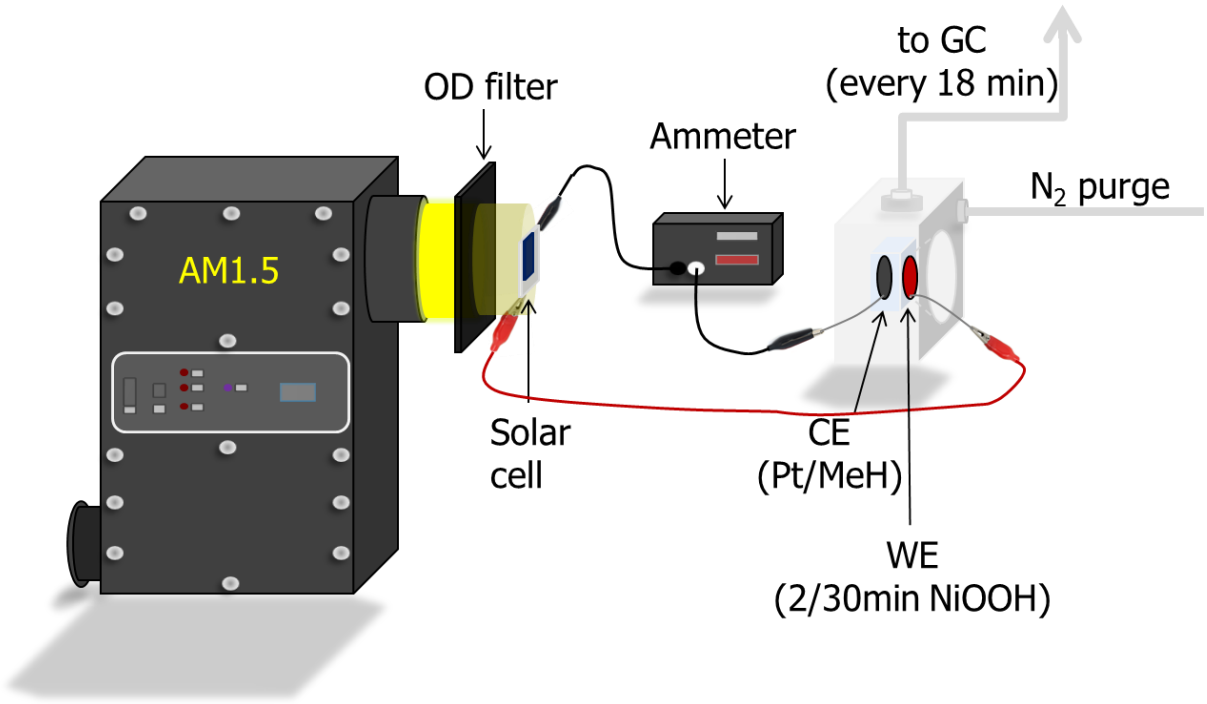

Figure 5.3. *Schematic for the bias-free solar hydrogen/battery setup. The light intensity is controlled by placing optical density filters between the solar simulator and the solar cell. The solar cell is coupled to the electrochemical cell and a current meter is connected in series. The solar cell and the electrodes have a surface area of 1 cm^2. The time for NiOOH electrodeposition was chosen as 2 min for the electrolyzer and 30 min for the battery/electrolyzer. A nitrogen gas purges constantly the electrochemical cell, and the gas evolution is measured every 18 minutes by a gas chromatograph.*

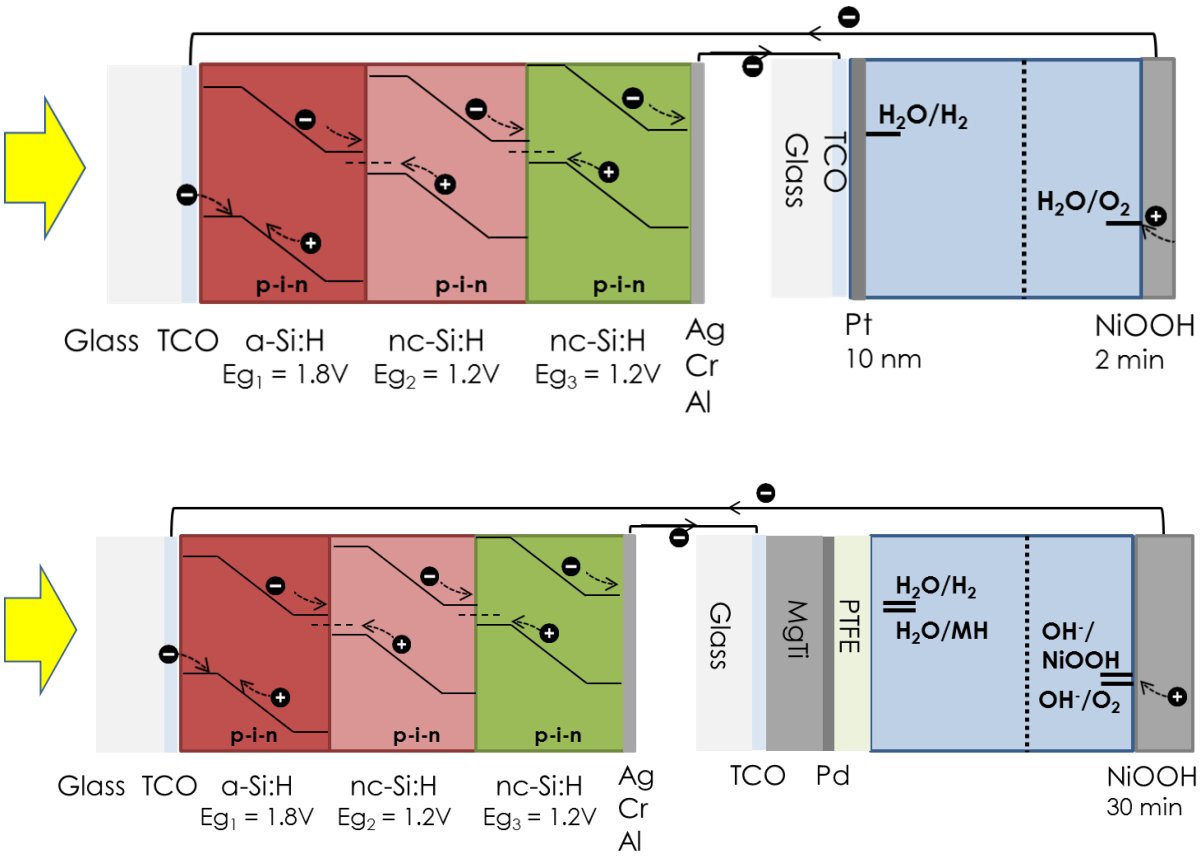

Figure 5.4. *Device components and schematic energy diagram with the available redox couples for the PV electrolysis configuration (top), and for the PV battery/electrolysis configuration (bottom).*

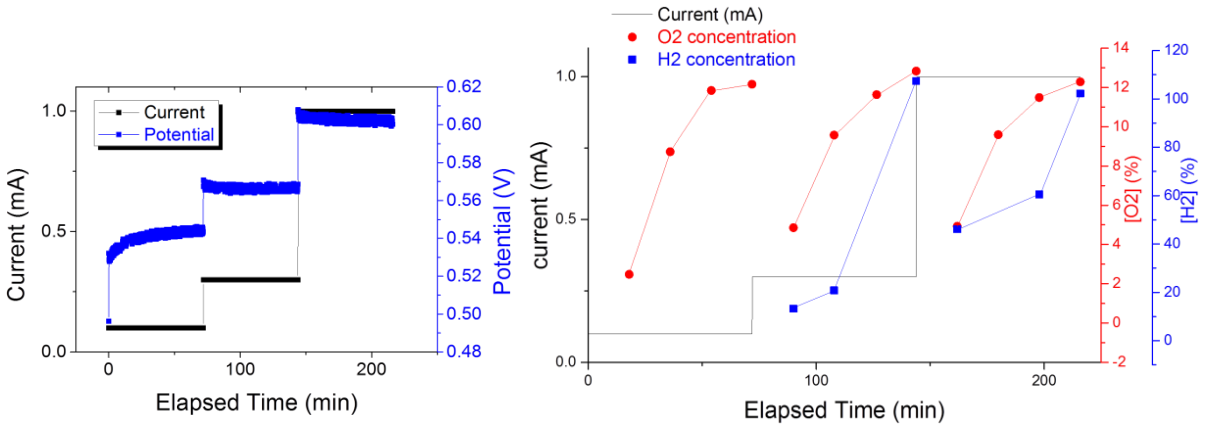

Figure 5.5. *GC test. A) Two electrode voltage response to a galvanostatic current (0.1 mA, 0.3 mA and 1 mA) of the electrolyzer. B) Hydrogen and oxygen evolution during the galvanostatic measurement as detected by the GC.*

Results

In this section we first introduce the theory of the change in open circuit potential of solar cells under varying light intensity. Then we describe the expected change in the operating point of the coupled PV-battery/electrolyzer, as an effect of a reduced power from the PV. This section proceeds with the results of the tests on the PV-electrochemical device. The following performance measurements have been investigated:

- under standard conditions of AM1.5 illumination with the PV and electrochemical cell chosen such that the operating point is on the maximum power point (MPP) of the PV.

- In order to simulate the different light intensities associated to twilight-midday and cloudy-sunny conditions, we have applied optical density filters (OD 0.3 = 50% transmittance, OD1 = 10% transmittance) in front of the solar cell.

- (Rapidly) changing weather conditions have been simulated by cyclic voltammetry at different scan rates.

- The splitting of the output of the solar system between electricity generation and storage leads to a lower-than-optimal power directed to the storage. This is simulated by coupling a solar cell with lower open circuit potential, to the electrochemical part

- The discharge of the battery component is tested in the dark with the solar cell as a resistor.

A. The effect of light intensity on PV-electrolysis.

To understand the behavior of a PV powered electrolysis device, we first discuss the variation of the open circuit potential of the solar cell in relation to the water splitting process that is run by an electrolyzer. The photocurrent vs. potential (JV) curve of a solar cell is the superposition of the current vs. potential (IV) curve of the solar cell diode in the dark with the light-generated current. The JV relationship for the solar cells is:

$$J = J_0 \left[exp\left(\frac{qV_A}{kT}\right) - 1 \right] - J_{sc} \qquad (5.3)$$

Where J_0 is the dark saturation current, the diode leakage current density in the absence of light (a measure of the recombination in a device), q the electron charge, V_A is the potential

between the terminals, k the Boltzmann constant, T the temperature and J_{sc} the short circuit current.

At $V_{oc} \rightarrow J = 0$, therefore the JV relationship becomes

$$0 = J_0 \left[exp\left(\frac{qV_{oc}}{kT}\right) - 1 \right] - J_{sc} \tag{5.4}$$

And the open circuit potential (V_{oc}) can be isolated as in

$$V_{oc} = \frac{kT}{q} ln\left(\frac{J_{sc}+J_0}{J_0}\right) \approx \frac{kT}{q} ln\left(\frac{J_{sc}}{J_0}\right) \tag{5.5}$$

The approximation in equation 5.5 holds when J_{sc} is much larger than J_0, which is normally the case. If the light intensity decreases by i.e. a half, we expect the J_{sc} to also decrease by half. From equation 5.5 we observe that V_{oc} decreases too, with a logarithmic dependence on the J_{sc}. The experimental data for the triple junction solar cell of 1 cm^2 that we use for the storage device are shown in **Figure 5.6.**

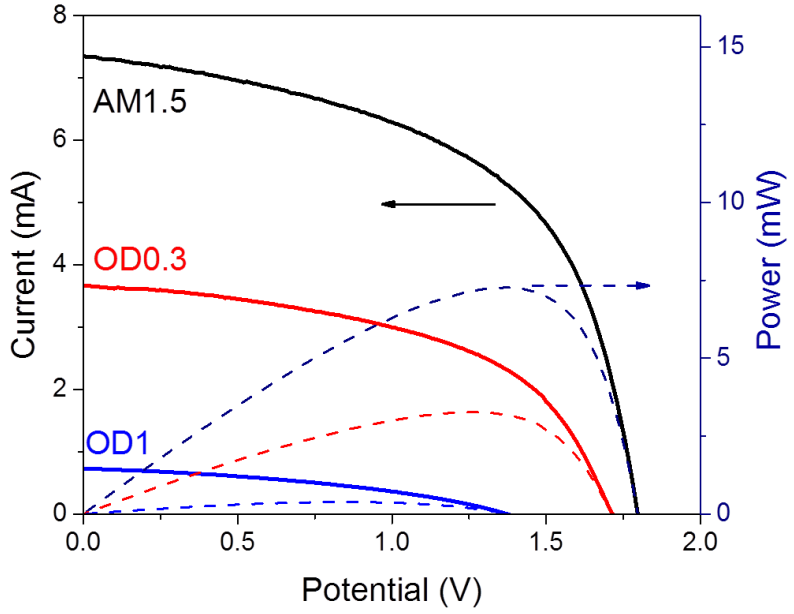

Figure 5.6 *current-voltage characteristic of the triple junction a:Si–nc:Si–nc:Si of 1 cm^2. As the light intensity decreases, both the current density and the OCV are reduced (solid lines); the corresponding power curve is also shown (dashed lines).*

The solar cell efficiency as a function of light intensity can be written as

$$\eta_{PV}^{1sun} = \frac{J_{sc} \cdot V_{oc} \cdot FF}{P_{light}} \quad \Longrightarrow \quad \eta_{PV}^{0.5sun} = \frac{{}^{1}/_{2} J_{sc} \cdot (V_{oc} - \Delta V) \cdot FF}{{}^{1}/_{2} P_{light}} < \eta_{PV}^{1sun} \tag{5.6}$$

With the assumption that the fill factor (FF) does not change significantly under varying light intensity at constant temperature, the solar cell efficiency decreases as the light intensity decreases. In real cases like in **Figure 5.6** also the fill factor decreases, which leads to a further decrease in efficiency. The further away the fill factor is from unity, the more pronounced the lowering of the OCV upon reduced illumination will be.

Next we analyze what happens to an electrolyzer when it is coupled to a PV cell under fluctuating illumination. This connection is not trivial, since for the electrolyzer the potential delivered and not the power of the PV is critical. The efficiency for solar energy conversion to chemical products such as hydrogen, is called solar-to-fuel (STF) or solar-to-hydrogen (STH) efficiency and is given by

$$\eta_{STH} = \frac{I_{photo} \cdot V_{redox} \cdot \eta_{FE}}{P_{in}} \tag{5.7}$$

V_{redox} in photoelectrochemical water splitting is usually taken to be 1.23 V (at room temperature), based on a Gibbs free energy change for water splitting of 237 kJ/mol. However, in an isolated system such as our electrochemical cell, the thermoneutral potential of 1.48 V should be used (286 kJ/mol). η_{FE} is the Faradaic efficiency, the efficiency for the photo-generated electrons and holes that are actually used for the water splitting reaction. In the case of a modular PV-electrolysis approach, the power input P_{in} in equation 5.7 is the power of light that is incident on the solar cell. P_{in} is defined as:[254]

$$P_{in} = \frac{I_{OP} \cdot V_{OP}}{\eta_{PV}} \tag{5.8}$$

Therefore η_{STH} can be written as

$$\eta_{STH} = \frac{I_{photo} \cdot V_{redox} \cdot \eta_{FE} \cdot \eta_{PV}}{I_{OP} \cdot V_{OP}} \tag{5.9}$$

Equation 5.9 shows that the efficiency for solar water splitting is related to the efficiency of the PV module. However, to run the water splitting reactions a minimum potential is required. Since at low light intensity as well as under diffuse irradiance, the generated PV-voltage drops, the voltage matching between the PV and the electrolyzer is of a major concern as the lack of it will reduce the operative hours of the device.

In **Figure 5.7** the coupling of a solar cell to an electrolysis cell is visualized. The solar cell should provide enough voltage to run the electrocatalytic reactions. Considering the overpotential to be added to the V_{redox}, the solar cell should have a maximum power point around 1.8-2.0 V. In the PV-electrolysis approach, the operating point of the device is defined as the intersection between the J-V curve of the solar cell and that of the reactions over the electrodes.

When the light intensity decreases, both the J_{sc} and V_{oc} of a PV module decrease, and so does the operating point of an integrated electrochemical device when a load is directly connected to the PV. Translated into practical terms, this means that in the mornings or during cloudy days the water splitting reactions may proceed at very low efficiency, or even not occur. **Figure 5.7**a shows a schematic image for the operating point for solar water splitting under AM1.5 illumination for a PV+electrocatalyst system. The highest efficiency is achieved when the reaction JV curve intersects the PV JV curve at its maximum power point. **Figure 5.7**b illustrates the solar water splitting under 10% of the AM1.5 illumination for a PV+electrocatalyst system. The power output under reduced illumination reduces, and the operating point follows until eventually water splitting is no longer possible.

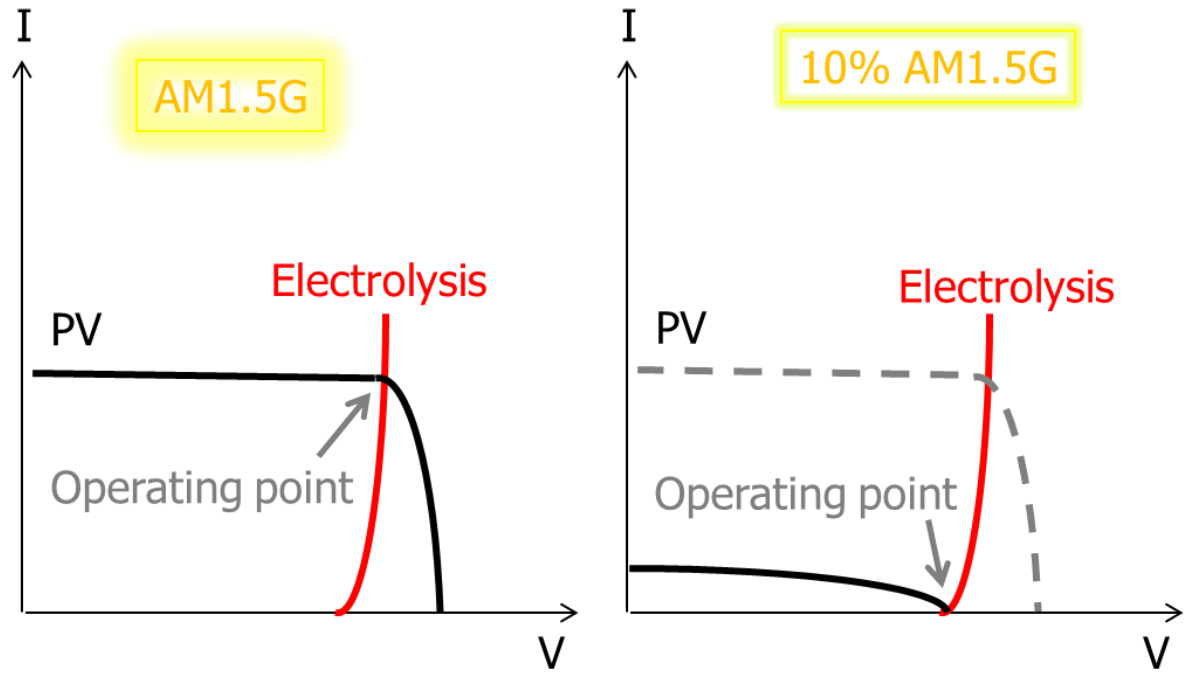

Figure 5.7. *Schematic illustrating the operating point for solar water splitting under AM1.5 illumination for a single absorber PV+electrocatalyst system (a). The power output under reduced*

illumination reduces, and the operating point follows until eventually water splitting is no longer possible (b).

One important observation is related to how to ensure that the intersection of the IV curves, for the PV and the electrolyzer, occurs at the maximum power point of the PV. Firstly, the solar cell must provide a voltage greater than the onset potential for water splitting, taken as 1.48 V. Secondly one should know that the steepness of the IV curve for a given electrolyzer is related to the surface area of its electrodes. Thirdly, the current density of a given solar cell is proportional to its illuminated area. In conclusion, intersecting the IV characteristics at the maximum power point of the PV cell can be obtained by optimally sizing the PV and the electrolyzer components. In this study, we chose to have all components of the same size 1 cm^2.

B. Observed behavior of a Si-based PV-electrolysis cell

Now we demonstrate the concept of Figure 5.7 using a triple junction a:Si–nc:Si–nc:Si with an OCV under 1 sun of 1.8 V. Such a voltage is enough to run the water splitting reactions in an electrolyzer consisting of a Pt cathode and a thin $Ni(OH)_2$ anode. The IV curve of the PV and that of the electrolyzer intersect at ~1.7 V, as shown in Figure 5.8. Applying an OD0.3 filter (50% light transmission in the visible) the PV IV curve intersects the electrolyzer JV curve at ~1.6 V. At these conditions the water splitting reactions are still possible, although they proceed at a lower rate than under full illumination. With an OD1 filter (10% light transmission) the OCV of the PV decreases to <1.4 V, which is less than the required voltage to perform the water splitting reactions and hence no hydrogen would be produced.

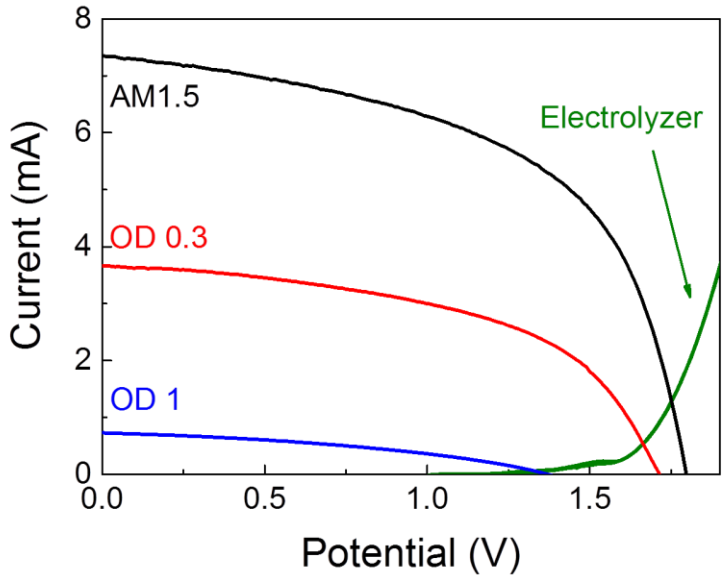

Figure 5.8 *Current-voltage characteristic of the triple junction a:Si–nc:Si–nc:Si at different light intensity, together with the JV characteristic (two electrode measurement) for the overall water splitting via the Pt-NiOOH electrolyzer obtained independently. The schematic for this design configuration is shown in Figure 5.4 top.*

The overlay of the voltammograms obtained from independent experiments carried out on the solar cell and the electrolyzer is a conceptual illustration of how the coupling of PV and electrolysis would work. Based on this the operating current should be over 1 mA under 1 sun, and around 0.4 mA with a OD0.3 filter (Figure 5.8). The actual current output from the PV-electrolyzer device is shown in Figure 5.9. It reveals that the actual values are one order of magnitude lower. After an initial spike, the current relaxes to a roughly steady value for the remaining 4000 s of the measurement. Possibly, the increasing temperature of the solar cell plays an important role in decreasing the potential output of the solar cell as shown in Figure 5.9A. In addition to that, in the long measurement, poor bubble removal and mass transport limitations caused by the geometry of the specific cell could also be involved. Overall, the steady-state value under 1 sun, 60 μA/cm^2, lowers more than linearly under a OD0.3 filter to 20 μA/cm^2. Moreover, negligible current is measured with a OD1 filter. The negligible current at low light intensity is consistent with the schematic representation in Figure 5.7, where we indeed proposed that under reduced irradiation there will be no voltage matching between the PV module and the electrolyzer. One possible solution to allow the electrochemical reactions to occur also at low light intensity would be to increase the size of the PV module or to employ an additional power conversion device. Coupling a quadruple

junction a:Si–a:Si–nc:Si–nc:Si solar cell which has an OCV under 1 sun of 2.3 V to the electrolyzer we find an operating point at 2.0 V, close to the maximum power point of the solar cell (see Figure 5.10A). This quadruple junction solar cell has a better fill factor than the triple junction, therefore the OCV under reduced illumination decreases less significantly and goes from 2.3 V under 1 sun to 2.1 V under 10% illumination (OD1 filter). In this case, the potential provided by the PV cell is always enough to drive the electrolyzer and the PV-electrolyzer device performance is limited by the current generated by the PV. The actual current output from this PV-electrolyzer device at varying light intensity is shown in Figure 5.10B. At all light intensity, the current matches the value expected from the intersection of the JV curves and scales linearly with the light intensity.

In Figure 5.10B we also observe that the current density shows a slight decrease, which is more pronounced at higher light intensity. This decay can be attributed to the temperature effect on the PV potential. An increase in temperature (e.g. due to prolonged exposure to AM1.5) would result in a decrease of the OCV.

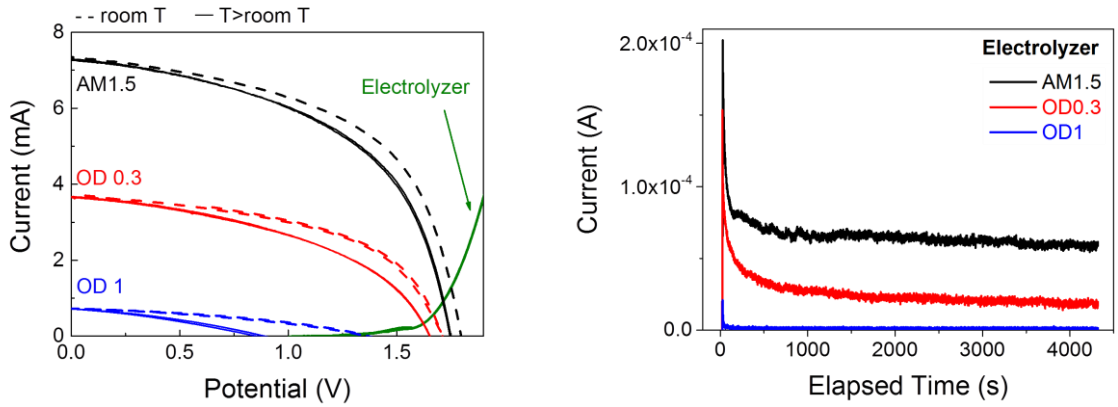

Figure 5.9. *A) Current-voltage characteristic of the triple junction a:Si–nc:Si–nc:Si at different light intensity, together with the JV characteristic (two electrode measurement) for the overall water splitting via the Pt-NiOOH electrolyzer. Dashed lines show the JV characteristic before the long term measurement of Figure 5.7B, thus called room temperature (RT). The solid lines are after the measurement during which the solar cell has heated up, thus called T > RT). B) Chronoamperometric measurements for the PV-electrolyzer configuration (Figure 5.4 top) under different light intensity: 1 sun (black), a 50% OD filter (red), and a 90% OD filter (blue). The current with a 90% filter becomes negligible. Experiments performed at increasing light intensity.*

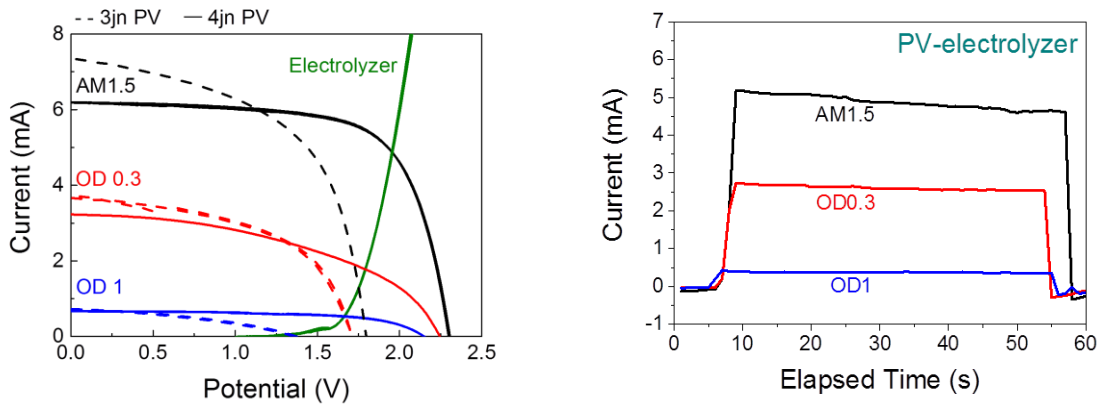

Figure 5.10. *A) Current-voltage characteristic of the quadruple junction a:Si–a:Si–nc:Si–nc:Si (4jn PV, solid lines) at different light intensity, together with the JV characteristic (two electrode measurement) for the overall water splitting via the Pt-NiOOH electrolyzer. Dashed lines show the JV characteristic for the triple junction a:Si–nc:Si–nc:Si (3jn PV). B) Chronoamperometric measurements for the PV-electrolyzer configuration (Figure 5.4 top) under different light intensity: 1 sun (black), a 50% OD filter (red), and a 90% OD filter (blue). Experiments performed at increasing light intensity.*

C. Building a battery/electrolysis cell (to be used under varying solar conditions)

The choice of hybrid electrodes for storage and electrolysis

An alternative approach for PV-electrolysis consists of implementing additional battery functionalities to the electrolyzer. The idea of our combined battery/electrolysis cell is that the potential for loading the battery is lower than that required to split water. Therefore it will enable the electrical storage of solar energy under low light condition, i.e. with OD0.3 and OD1. The practical challenge is to find materials that can work as efficient oxygen and hydrogen evolution catalysts, while showing storage behavior at potentials more advantageous than the respective water splitting reactions. Moreover they have to be stable in aqueous environment.

Here, we propose the use of a hydride-forming Pd-capped $Mg_{0.8}Ti_{0.2}$ cathode, and a $Ni(OH)_2$ anode. Commercial NiMH batteries employ a $Ni(OH)_2$ positive electrode and a mischmetal-based MH as negative electrode. In this proof-of-concept study we replace the mischmetal-based electrode, which is expensive and difficult to fabricate, with a cheap and environmentally friendly Mg-based electrode. The Mg-based electrode is an excellent hydrogen absorber since it exhibits a very high gravimetric storage capacity of about 2200

mAh/g (7.6 wt% hydrogen).[276] However, it suffers from low sorption kinetics, and instability towards oxidation. The oxidation of the film can be effectively prevented by depositing a thin film of Pd, which also acts as a catalyst for the hydrogen sorption. It has been shown that alloying Mg with rare earth elements increases the hydrogen sorption kinetics. *Niessen et al.* revealed that the hydrogen uptake and release kinetics of Mg thin films can be enhanced significantly by alloying Mg with 20% Ti, while keeping an excellent gravimetric capacity (> 6 wt% hydrogen) up to six times that of the MischMetal-based materials.[275] Recently, *Xin et al.* investigated electrochemically a series of Pd-capped Mg_xTi_{1-x} films and revealed that $Mg_{0.85}Ti_{0.15}$ and $Mg_{0.72}Ti_{0.28}$ performed best in terms of short activation period, resistance to corrosion, cyclic stability and large discharge capacity up to 80% after 150 cycles.[276]

The Ni electrode, with the $Ni(OH)_2 \rightleftharpoons NiOOH$ redox couple, is known for its electro-chromic properties and its use as an electrode in the Ni-based batteries such as Ni-MH and Ni-Fe.[75,277,278,279] It has a theoretical capacity of 289 mAh/g, its discharging is a downhill reaction which releases energy. Moreover, it has been shown that NiOOH acts as an efficient water oxidation catalyst.[280] Of importance for the purpose of this work, it also operates in alkaline media just as the metal hydride cathode. Those properties set the basis for the use of this material in our system.

The goal of increasing the solar energy conversion and storage under low light conditions can be achieved if the potential for loading the battery is lower than that required to split water. In the following section we will analyze the thermodynamics and kinetics for the hydrogen evolution reaction (the electrolyzer), compared to the reaction for metal hydride formation (the battery). Afterwards, the oxidation reaction will be discussed.

In (photo-)electrochemical water splitting the (photo-generated) electrons are used to perform the hydrogen evolution reaction (HER). This is a well-studied electrochemical reaction and it is understood it proceeds by one of two mechanisms. Each mechanism consists of two primary steps, and begins with the Volmer reaction (5.1) according to:

(5.1) $M + H_2O + e^- \rightleftharpoons MH_{ad} + OH^-$

(5.2) $MH_{ad} + H_2O + e^- \rightleftharpoons H_2\,(g) + OH^-$

The second reaction is called the Heyrovsky reaction. Alternatively, the Volmer reaction (5.1) followed by the Tafel step (5.3):

(5.3) $2\,MH_{ad} \rightleftharpoons 2\,M + H_2\,(g)$

Where M is a hydrogen active metal site. With this approach it has been shown that the formation, or reductive desorption of intermediate hydride species presents a large energy barrier to the overall hydrogen evolution reaction.[42]

On the other hand, when hydrogen is electrochemically stored in a metal hydride, the reaction path becomes:

(5.1) $M + H_2O + e^- \rightleftharpoons MH_{ad} + OH^-$

(5.4) $MH_{ad} \rightleftharpoons MH_{abs}$

From the reaction mechanisms it follows that the hydrogen evolution and the metal hydride formation are initiated in the same way with the adsorption of one H atom from the surrounding water onto one available metal site via reaction (5.1). This step is followed by the absorption of the H via reaction (5.4) for the formation of a metal hydride. For the hydrogen evolution, a second water molecule and a second electron are involved via reaction (5.2) or (5.3).

Experimentally, the polarization curve of the Pd-$Mg_{0.8}Ti_{0.2}$ electrode is shown in the reductive side of **Figure 5.11**. In this curve we assign the peak at -0.15 V vs. RHE to the metal hydride formation, and the peak at more negative potential to H_2 evolution on the Pd surface. We observe that the formation of the metal hydride (MH) phase occurs at less cathodic potential than H_2 evolution. In particular, its onset potential is at +0.18 V vs. RHE. This value is consistent with earlier electrochemical observations on MgTi systems.[281,282,283] This observation means that the electrochemical hydrogen absorption $MH_{ad} \rightleftharpoons MH_{abs}$ (reaction(5.4)) is thermodynamically more favorable than both reactions (5.2) and (5.3). The reaction energy for the charging of the electrode is thus +0.18 V vs RHE, while that for the hydrogen evolution is 0.0 V vs. RHE. Hence, for the cathode, our goal of loading the battery component at potentials higher than that required to evolve hydrogen is feasible.

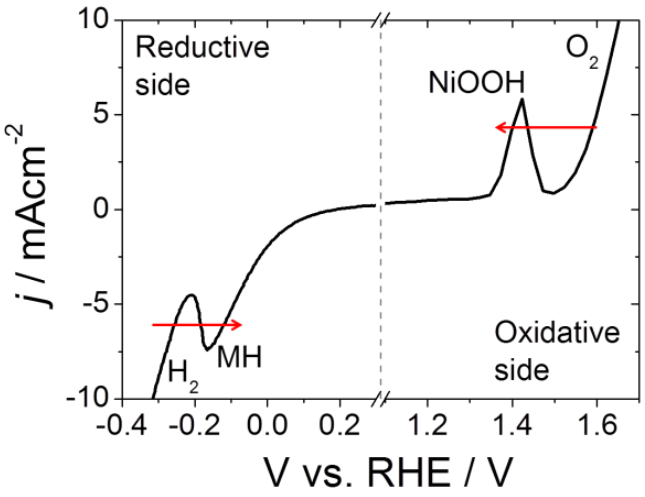

Figure 5.11 *The half-cell reactions at the anode (oxidation) and cathode (reduction) as a function of the applied potential. At the cathode side the formation of the metal hydride occurs at more anodic potential than the hydrogen evolution reaction, and at the anode side the formation of the NiOOH compound requires less energy than the oxygen evolution reaction. Measurements performed in 1 M KOH. The scan rate was 50 mV/s in the oxidative side, and 5 mV/s in the reductive side (due to different electrode capacity).*

However, we also have to compare the battery behavior in the anode. Therefore, we will analyze the electrochemistry for the oxygen evolution reaction (OER) (the electrolyzer), compared to the reaction for the formation of a NiOOH species from a $Ni(OH)_2$ electrode (the battery). If the OER is to be performed by a catalyst based on earth-abundant elements, it will require a minimum of ~0.3-0.4 V overvoltage, η, to obtain currents in excess of $8mAcm^{-2}$. The reason for such a high overpotential can be due to the binding energies of the water oxidation intermediates during the four proton-coupled-electron-transfer (PCET) reaction required for the H_2O/O_2 redox couple (OH^-/O_2 in alkaline media):[48,284,45,46]

(5.5) $$4OH^- \rightleftharpoons O_2 + 2H_2O + 4\mathbf{e}^-$$

On the other hand, the charging/discharging of the Ni electrode proceeds according to:

(5.6) $$Ni(OH)_2 + OH^- \rightleftharpoons NiOOH + H_2O + \mathbf{e}^-$$

While the Ni charging/discharging reaction (5.6) involves the transfer of a single proton and electron, the OER reaction (5.5) is a four PCET reaction, making it kinetically more favorably.

Experimentally, the polarization curve of the Ni electrode is shown in the oxidative side of Figure 5.11. Consistent with other reports,[75,277,285] we assign the peak at +1.4 V vs. RHE to the oxidation of the $Ni(OH)_2$ electrode to NiOOH, and the current increase at more positive

potentials to O_2 evolution. Therefore the formation of the NiOOH phase occurs at less anodic potential than O_2 evolution. Considering the onset potential, the $Ni(OH)_2$ → NiOOH reaction has an onset at ~1.35 V vs. RHE, whereas the OER has an onset at 1.5 V vs. RHE. This half-cell measurement proves that also for the anode, the battery component loads at potentials lower than that required to split water.

When the Ni and the MgTi electrodes are used in an electrochemical cell one can measure the overall two electrode JV curve for the battery/electrolyzer concept. As the metal hydride (MH) formation starts at 0.18 V vs. RHE, and the NiOOH forms at 1.35 V vs. RHE, the open circuit potential (OCV) of the battery is 1.17 V. On the other hand, a minimum ΔV of 1.48 V is required to perform water splitting. The resulting JV curve is shown as the orange curve in **Figure 5.12**, where it is compared to the overall electrolyzer's JV curves shown as the green curve. Clearly, the onset potential for the battery mode is 200-300 mV smaller than for the electrolysis mode. This reflects the earlier onset potential for the loading of the MgTi-Pd-PTFE electrode compared to the H_2 evolution at the Pt electrode (see also **Figure 5.13**). The lower slope of the JV curve for the MgTi-Pd-PTFE reflects the higher resistivity of the electrode compared to Pt. Clearly, now the electrodes can be charged when the potential provided by the PV cell is too low to induce electrolysis. In **Figure 5.13** the half-cell JV characteristics are shown. The JV for the thicker Ni electrode (30 min deposition) overlaps that for the thinner one (2 min deposition), except for a small peak before the onset for water oxidation. This confirms that the thickness of the Ni electrode does not contribute significantly to the water oxidation activity of the electrolyzer and battery/electrolyzer configuration.

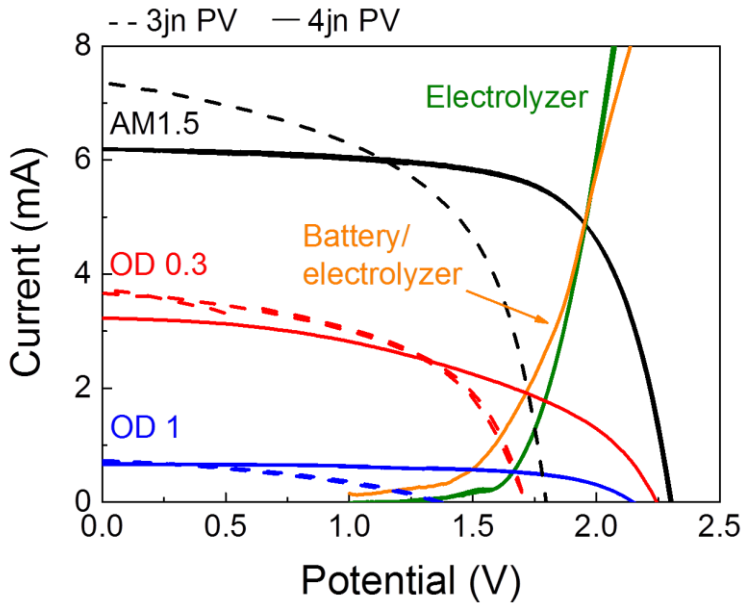

Figure 5.12 *Current-voltage characteristic of the quadruple junction a:Si–a:Si–nc:Si–nc:Si (4jn PV, solid lines) at different light intensity. Dashed lines show the JV characteristic for the triple junction a:Si–nc:Si–nc:Si (3jn PV). The two electrode JV characteristic for the overall water splitting via the Pt-NiOOH electrolyzer (green), and the two electrode JV characteristic for the MeH-NiOOH battery/electrolyzer (orange). Note, that each curve is obtained in an independent measurement. The schematic for the PV-battery/electrolyzer configuration is shown in Figure 5.4 bottom.*

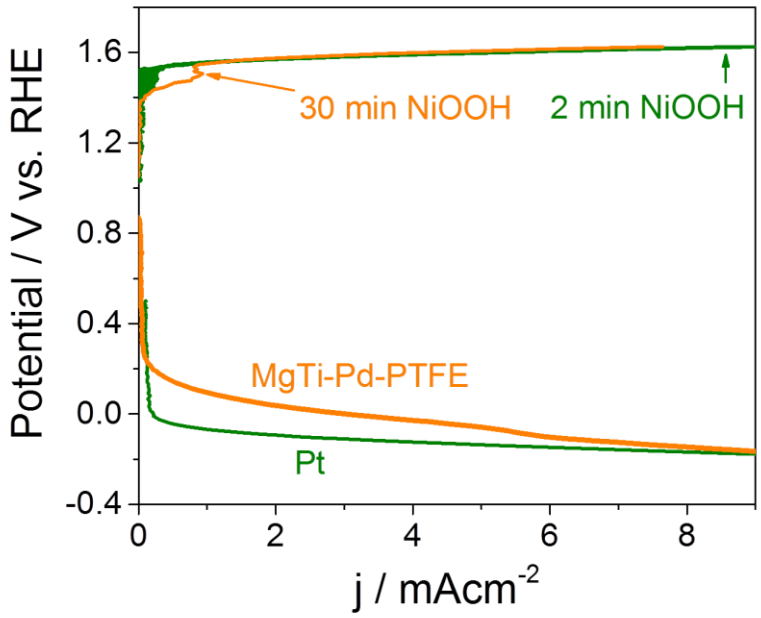

Figure 5.13. *Half-cell JV characteristics of the 2 min and 30 min NiOOH, the 10 nm Pt and the MgTi-Pd-PTFE electrodes. Scans taken at 10 mV/s for the cathodes and 50 mV/s for the anodes.*

D. PV-battery/electrolysis cell: effect of light intensity and comparison with a PV-electrolysis cell

To verify the actual performance of the battery/electrolyzer cell we powered it by the triple junction PV cell and measured the output as a function of increasing light intensity, Figure 5.14. At all light intensities, the current generated in the cell is lower than expected from the individual measurements shown in Figure 5.12. This is consistent with what was observed in the PV-electrolyzer system described above (Figure 5.8 and Figure 5.9) With an OD1 filter (10% light transmitted) the PV cell generates an OCV of 1.4 V. This potential is not sufficient to perform the water splitting reactions, however it is just enough to intersect the IV curve for the battery/electrolyzer in the two electrode measurement of Figure 5.12. Therefore, in the measurement of Figure 5.14 the measured current is limited to few μA. While limited, the measured current represents an improvement compared to the PV-electrolyzer system (Figure 5.14). With an OD0.3 filter (50% light transmission), after the initial spike, the current decays within 200 seconds to a plateau at around 500 μA. Thereafter, the current decays to a second plateau value of about 100 μA. This indicates the exhaustion/completion of one redox process and a stabilization of a second process. We assign the two electrochemical processes to firstly the loading of the battery component until its full capacity is reached, and secondly the electrochemical hydrogen production via water splitting. The last measurement is performed under full sun, AM1.5 illumination. The chronoamperometric measurement for the PV battery/electrolyzer shows a decay similar to that observed in the PV electrolyzer. However the current stabilizes at 150 μA, a value twice as high the 75 μA measured for the PV electrolyzer under the same conditions. This observation indicates that the hydrogenated electrode is more efficient in electrolysis at that current density.

The current in the PV-battery/electrolyzer configuration is always higher than in the PV-electrolyzer configuration. Remarkably, the current for the PV-battery/electrolyzer with a 50% OD filter has a step-like behavior. It is 20x higher than for the PV-electrolyzer for the initial 1500 s, then decreases to ~ 3x the value for the PV-electrolyzer. The initial higher current is attributed to the charging of the MgTi and the Ni battery electrode, until full charge is achieved (we will show later in Figure 5.21 that the capacity of the MgTi is orders of magnitude larger than that of Ni).

The performance of the battery/electrolyzer device coupled to the quadruple junction a:Si–a:Si–nc:Si–nc:Si solar cell is shown in Figure 5.15. The current (5.5 mA) measured through the device matches the value expected from the intersection of the JV curves of the PV end the battery/electrolyzer as in Figure 5.12. The current is initially always higher than for the PV-electrolyzer configuration. Interestingly, under 1 sun illumination (AM 1.5), the current drops by about 1 mA after 10 seconds of illumination. This drop in current seems reproducible as has been measured again after turning off and on the experiment. A galvanostatic discharge measurement for the MgTi electrode revealed that the electrode was not fully loaded at the end of the measurement. Therefore we tentatively attribute the drop in current to a shift in the functionality of the not fully loaded MgTi electrode from battery mode to electrolyzer mode. Alternatively, the battery at the anode side ($Ni(OH)_2 \rightarrow NiOOH$) is fully charged, while the MgTi is not. In Figure 5.21 we will show that the capacity of the Ni anode is too small to sustain 5.5 mA current for 10 seconds, thus ruling out the latter option.

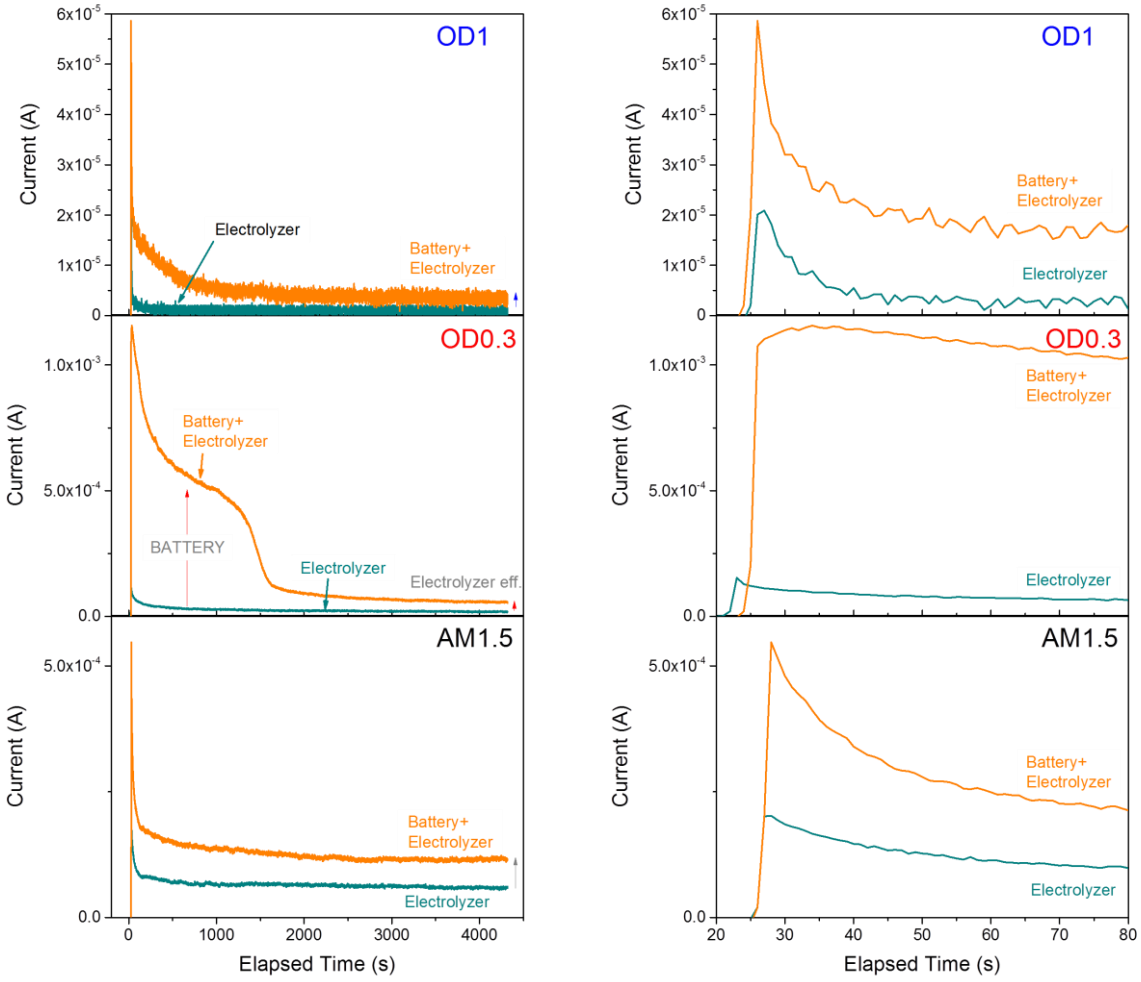

Figure 5.14. *A) Chronoamperometric measurements for the triple junction PV-battery/electrolyzer as in Figure 5.4 bottom, and the PV-electrolyzer configuration as in Figure 5.4 top under different light intensity: 1 sun (black), a 50% OD filter (red), and a 90% OD filter (blue). Experiments performed at increasing light intensity. B) Zoom in over the first minute of the chronoamperometric measurement.*

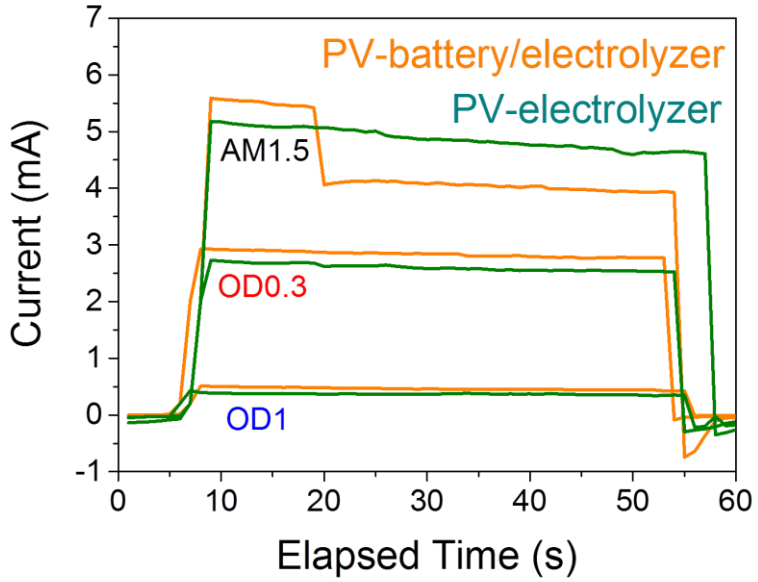

Figure 5.15. *Chronoamperometric measurements for the quadruple junction PV-battery/electrolyzer as in Figure 5.4 bottom, and the PV-electrolyzer configuration as in Figure 5.4 top under different light intensity: 1 sun (black), a 50% OD filter (red), and a 90% OD filter (blue). Experiments performed at various light intensities.*

E. PV-battery/electrolysis cell: prove for battery loading at moderate light intensity

To verify our interpretation of the behavior of the triple PV configuration using the OD0.3 filter (Figure 5.14), we performed a gas chromatography (GC) measurement of the evolving gases. In Figure 5.16 we plot the chronoamperometric measurement together with the hydrogen concentration as detected by the GC. No hydrogen is detected in the first 1500 seconds. Hydrogen is detected only thereafter and its concentration increases with time. Clearly no hydrogen is produced at the high current plateau. Hence, we conclude that at OD0.3 conditions first the battery component is loaded until its full capacity is reached. It is then followed by the electrochemical hydrogen production via water splitting. The higher current measured in the former process is explained by the lower potential required for the battery loading and the consequent higher current at the operating point as shown in Figure 5.12.

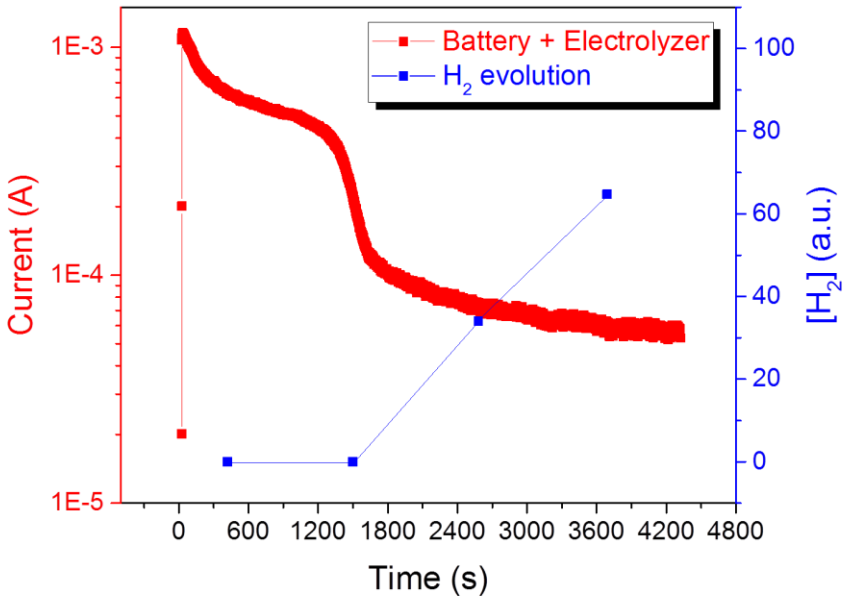

Figure 5.16. *Chronoamperometric measurements for the PV-battery/electrolyzer with a 50% OD filter (red) as in Figure 5.14. H_2 concentration measured by the GC (blue). No H_2 is detected after 420 and 1500 seconds. H_2 detection starts from 2580 seconds, and increases at the 3660th second. The GC data support the interpretation of an initial higher current due to the $Mg_{0.8}Ti_{0.2}$ charging, until full charge is achieved. Thereafter, the current is going to hydrogen evolution.*

F. PV-battery/electrolysis cell: energy storage upon rapidly changing potential

In **Figure 5.14** and **Figure 5.16** we showed that at moderate light intensity (OD0.3) the battery/electrolyzer device favors the loading of the battery component over the electrolysis of water. Moreover, once fully charged, the $Mg_{0.8}Ti_{0.2}H_2$-Pd-PTFE battery electrode acts as an efficient hydrogen evolution catalyst. Since in reality the solar irradiance may change quickly, in this section we investigate the storage behavior under a rapidly changing applied potential. In **Figure 5.17** we show the linear sweep voltammetry of the electrode at different scan rates. At a scan rate of 5 mV/s the battery electrode shows an onset potential at +0.2 V vs. RHE and a peak at -0.15 V vs. RHE, which is attributed to the hydrogenation of the electrode. At V < -0.22 V vs. RHE the current density increases in value which is attributed to the hydrogen evolution. The two processes appear separate and can be distinguished with ease (blue). At a scan rate of 10 mV/s the battery electrode shows again an onset potential at 0.2 V vs. RHE, however there is no local maximum of current density.

To understand whether the current goes to battery charging or to hydrogen evolution, we have calculated the integral of the JV curves in **Figure 5.17** for the hypothetical hydrogen uptake and release for samples of MgTi of two thicknesses, 200 nm and 400 nm. The integral is calculated assuming all the current under the charging/discharging curves goes to the sorption of hydrogen into/out of the MgTi. When comparing the hydrogen uptake (current IN) to the hydrogen release (current OUT), the current consumed during hydrogen uptake is always higher. Considering that the hydrogen release during discharge is on average at least 90% of the hydrogen uptake as shown in the galvanostatic measurement of **Figure 5.19**, the results indicate that during rapid increase in bias, part of the current does not go to MH formation, but to H_2 evolution.

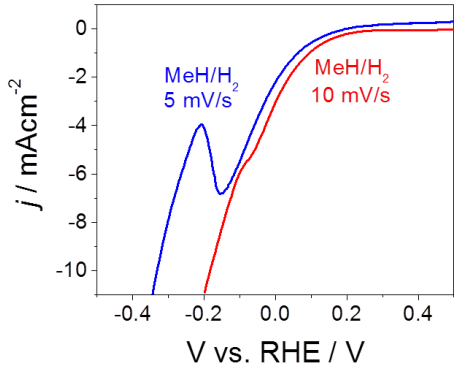

Figure 5.17. *Linear sweep voltammetry of the $Mg_{0.8}Ti_{0.2}$ battery electrode at different scan rate.*

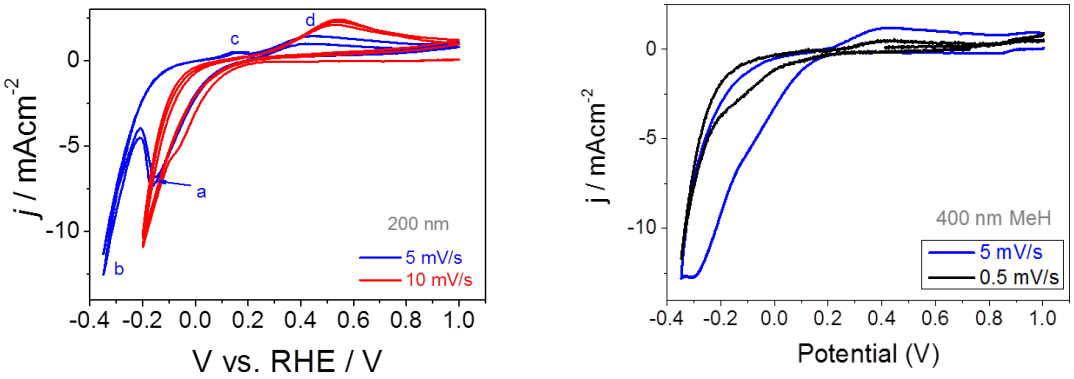

Figure 5.18. *Polarization curves of the MgTi electrodes at different scan rates. Four features are distinguishable: a) hydrogen uptake into the MgTi electrode; b) hydrogen evolution; c) hydrogen release from the Pd catalyst; d) hydrogen release from the MgTi electrode.*

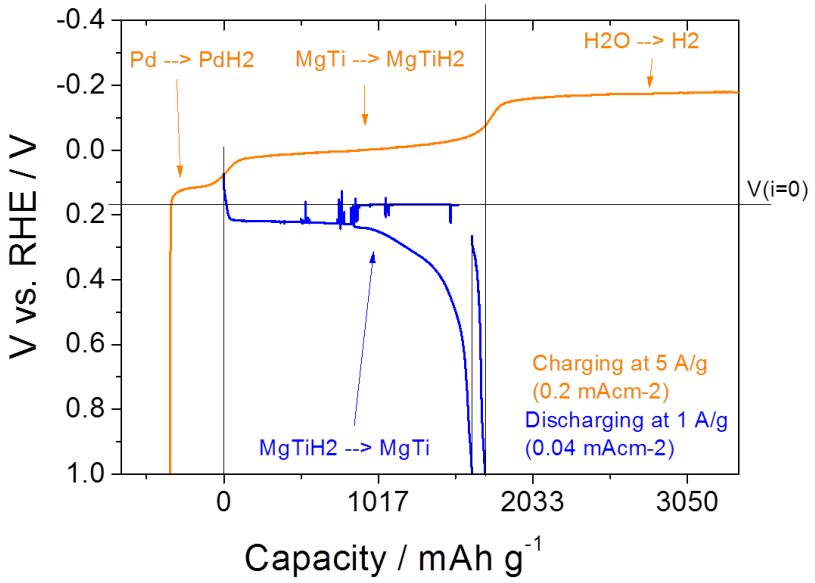

Figure 5.19. *Galvanostatic charging and discharging of the MgTi electrode (see Appendix 1). Horizontal line indicates the open circuit potential. Total discharge time was ~6000 s.*

G. PV-battery/electrolysis cell: battery discharge. Capacity limited by Ni electrode

Thus far we have shown the energy storage properties of the PV-battery/electrolyzer device as a function of the light intensity, and we have compared them to a PV-electrolyzer configuration. In this section we show that when electricity generation is needed, the device can be switched to discharge the battery and generate electricity.

In **Figure 5.20** we show the chronoamperometric measurement performed in the dark by discharging the battery electrodes through the solar cell used as a small resistor. A small however not negligible current is flowing through the circuit.

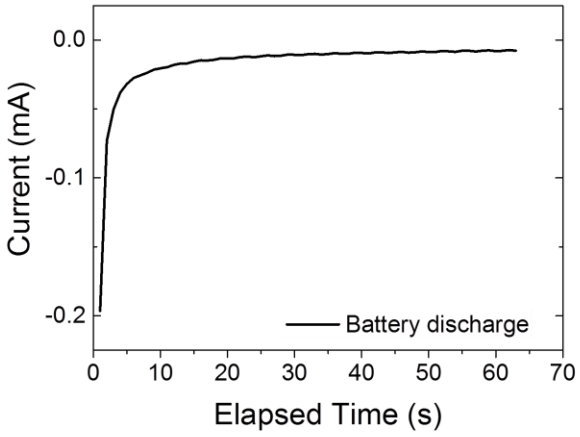

Figure 5.20. *Chronoamperometric measurement for the discharging of the battery electrodes through the solar cell.*

The discharge current shown in **Figure 5.20** is modest, and much lower than expected from the capacity of the MgTi electrode shown in **Figure 5.19**. We try to understand the reason for this by performing charge/discharge measurements for each electrode separately. **Figure 5.21** shows chronopotentiometric measurements for the charge and discharge of the Ni-based and the metal hydride electrodes. **Figure 5.22** compares the time course of the potential of the Ni electrode during discharge, relative to that of the MgTi electrode. Depending of the chosen discharge current for the Ni electrode, there will be no potential difference between the Ni and the MgTi electrodes after 4 s at -30 μA, or after 26 s at -3 μA. The discharge current of the MgTi electrode is chosen as +50 μA. This current density gives a lower limit for the time of potential equilibration between the two electrodes.

Moreover we observe that the time necessary to fully discharge the Ni electrode is in the order of tens of seconds. This time is three orders of magnitude shorter than the time that would be needed to discharge the metal hydride electrode if it were fully loaded. The timescale for the discharge of the Ni electrode is comparable to the time at which the discharge of the full battery occurs, as shown in **Figure 5.20**. Therefore, we conclude that the battery capacity is limited by the capacity of the Ni electrode. The low capacity of the Ni electrode, despite its thickness, suggests that the Ni film deposited directly onto FTO is not porous enough to be fully charged. As a result only the surface is used in the $Ni(OH)_2$ / NiOOH redox cycling.

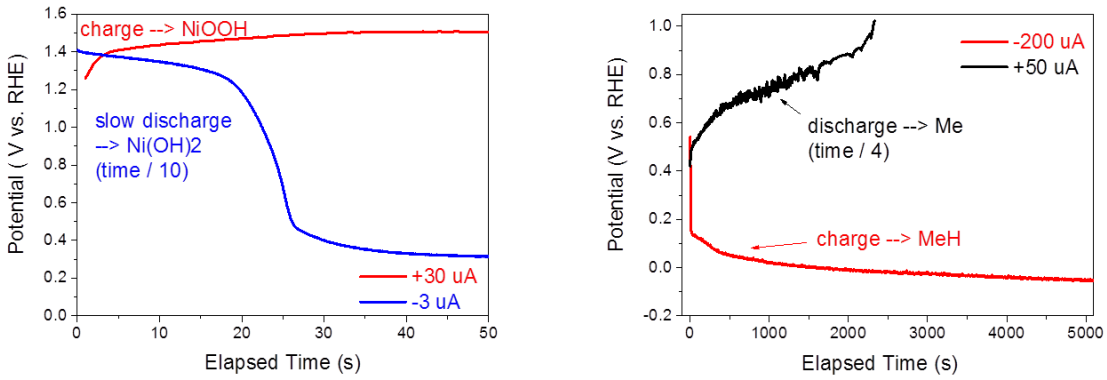

Figure 5.21. *Three electrodes galvanostatic charge/discharge of the Ni electrode (left), and of the* $Mg_{0.8}Ti_{0.2}$ *electrode (right).*

The intersection of the charging/discharging curves in Figure 5.21 is a good approximation of the potential for the given reversible redox couple, either $Ni(OH)_2$ / NiOOH (left), or $Mg_{0.8}Ti_{0.2}$ / $Mg_{0.8}Ti_{0.2}H_2$ (right). A steady potential over a certain time indicates the time for which a certain reaction is occurring, and can be interpreted as the capacitance of the electrode for the given redox reaction. An abrupt change in potential over time indicates the shift to a different reaction which enables the given current density to be maintained. The x-axis scale in the left and right plots differs by 3 orders of magnitude, and the current density by 1. This illustrates that the discharging capacity is limited by the Ni electrode.

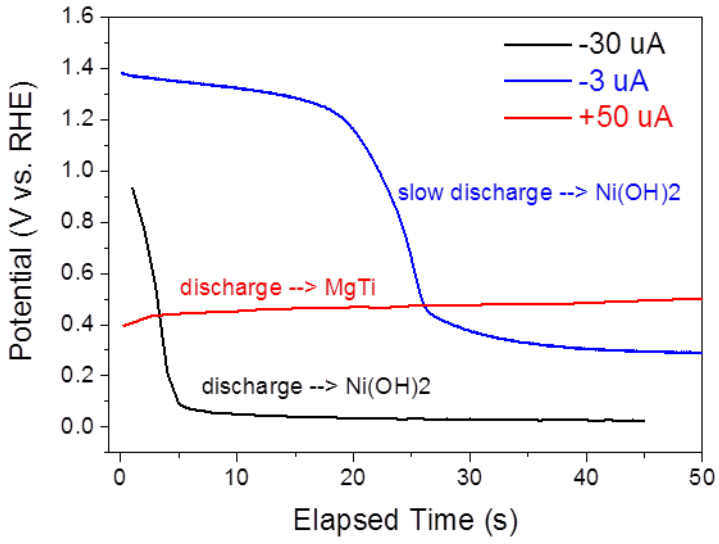

Figure 5.22. *Three electrodes galvanostatic discharge of the Ni electrode and of the* $Mg_{0.8}Ti_{0.2}$ *electrode at different discharge current. The intersection of the discharging curves represents the*

moment where there is no potential difference between the electrodes. It is therefore a good indication of the time necessary to discharge the battery.

H. **PV-battery/electrolysis cell: schematic overview under operation**

The results shown in **Figures 5.12-5.16** illustrate the performance of the PV-battery/electrolyzer device. **Figure 5.23** shows a schematic diagram of the proposed device in various stages of operation. The electro-chromic properties of both the anode and the cathode are used to visualize the charging/discharging processes.

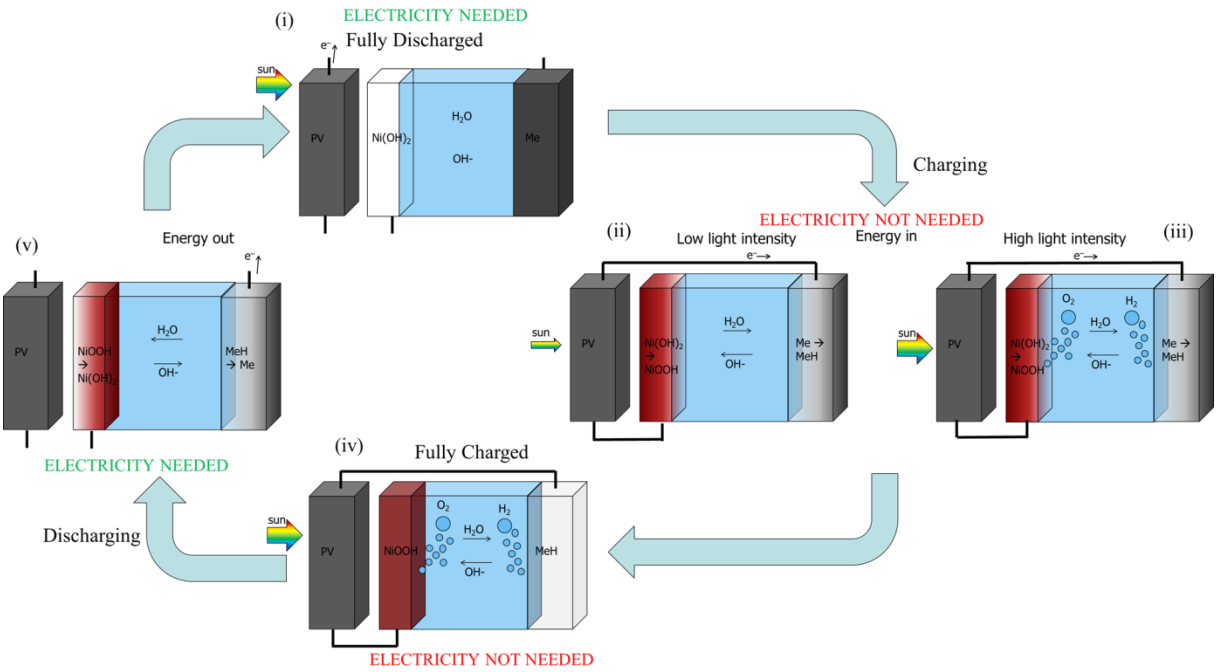
(i)
ELECTRICITY NEEDED
Fully Discharged
sun
e⁻
PV
Ni(OH)2
H2O
OH-
Me
Charging
ELECTRICITY NOT NEEDED
(ii)
Low light intensity
Energy in
(iii)
High light intensity
(v)
Energy out
NiOOH → Ni(OH)2
MeH → Me
Me → MeH
ELECTRICITY NEEDED
(iv)
Fully Charged
Discharging
O2
H2
ELECTRICITY NOT NEEDED

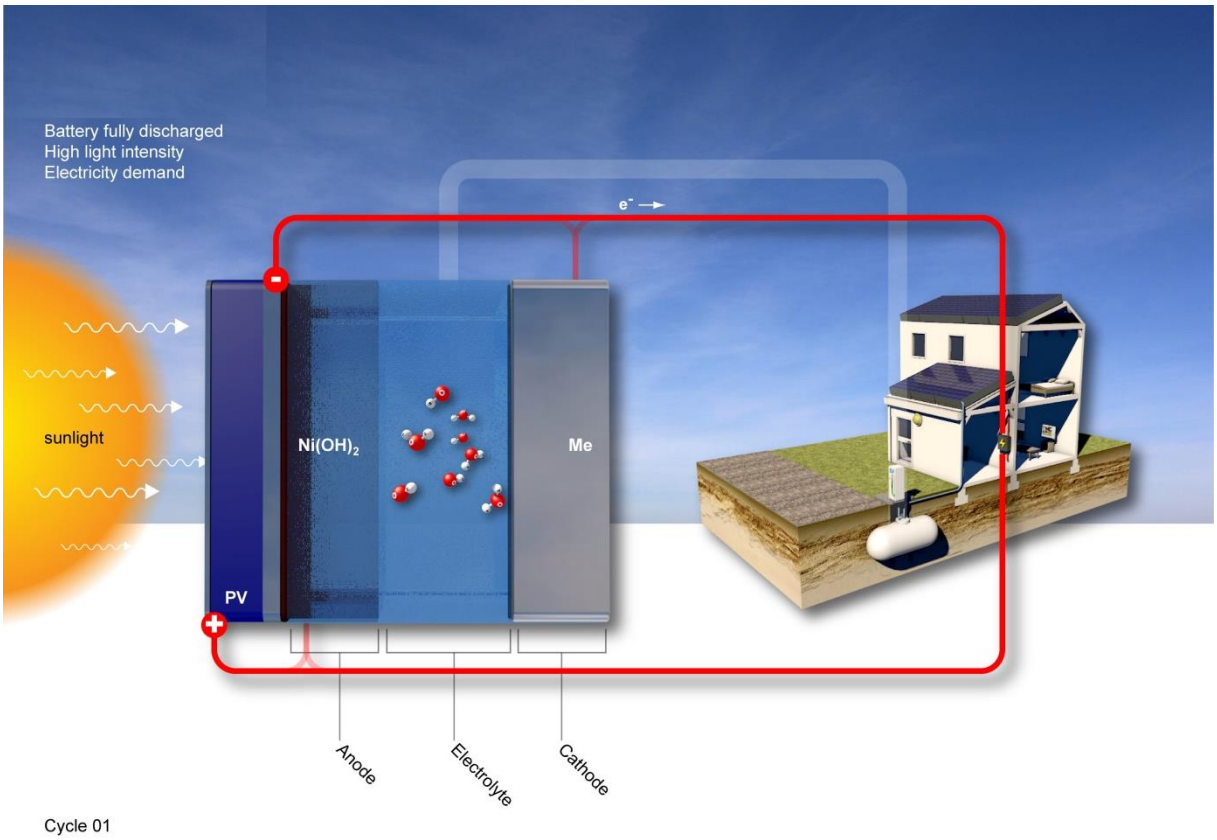
Battery fully discharged
High light intensity
Electricity demand
e⁻
sunlight
Ni(OH)2
Me
PV
Anode
Electrolyte
Cathode

Cycle 01

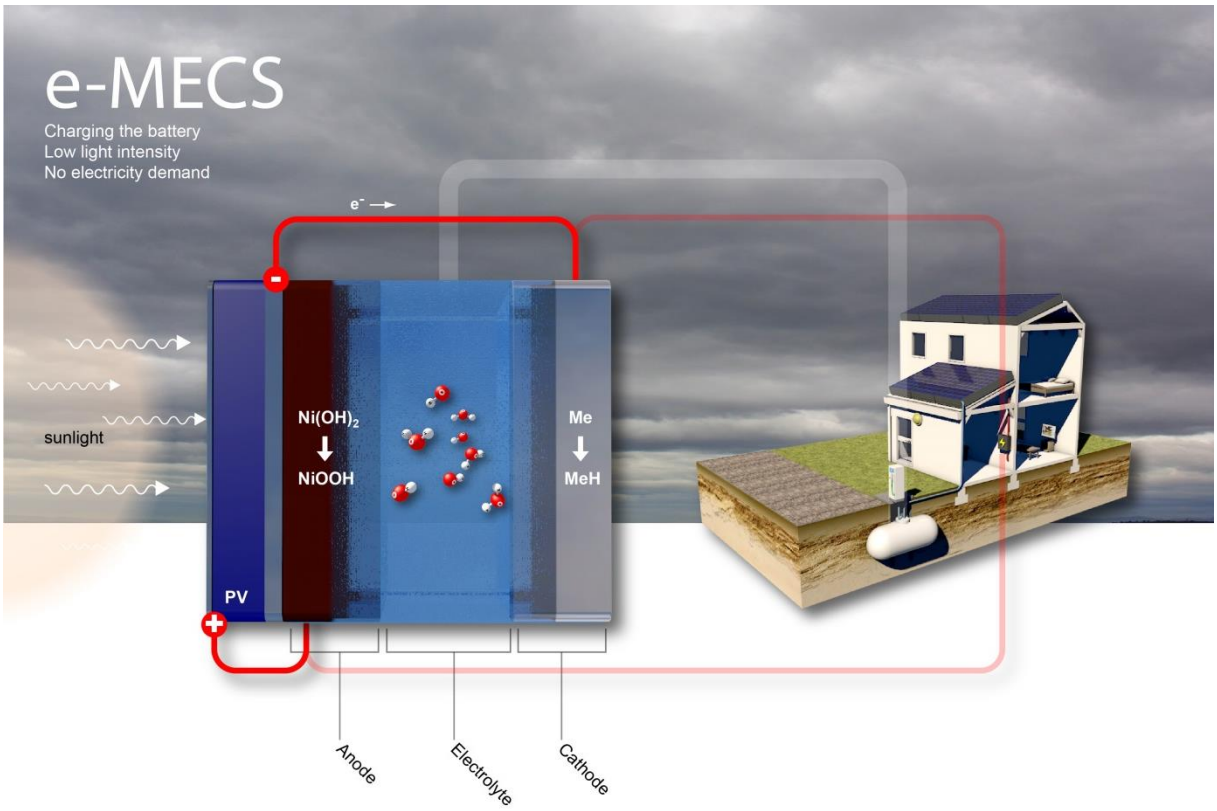

Cycle 02

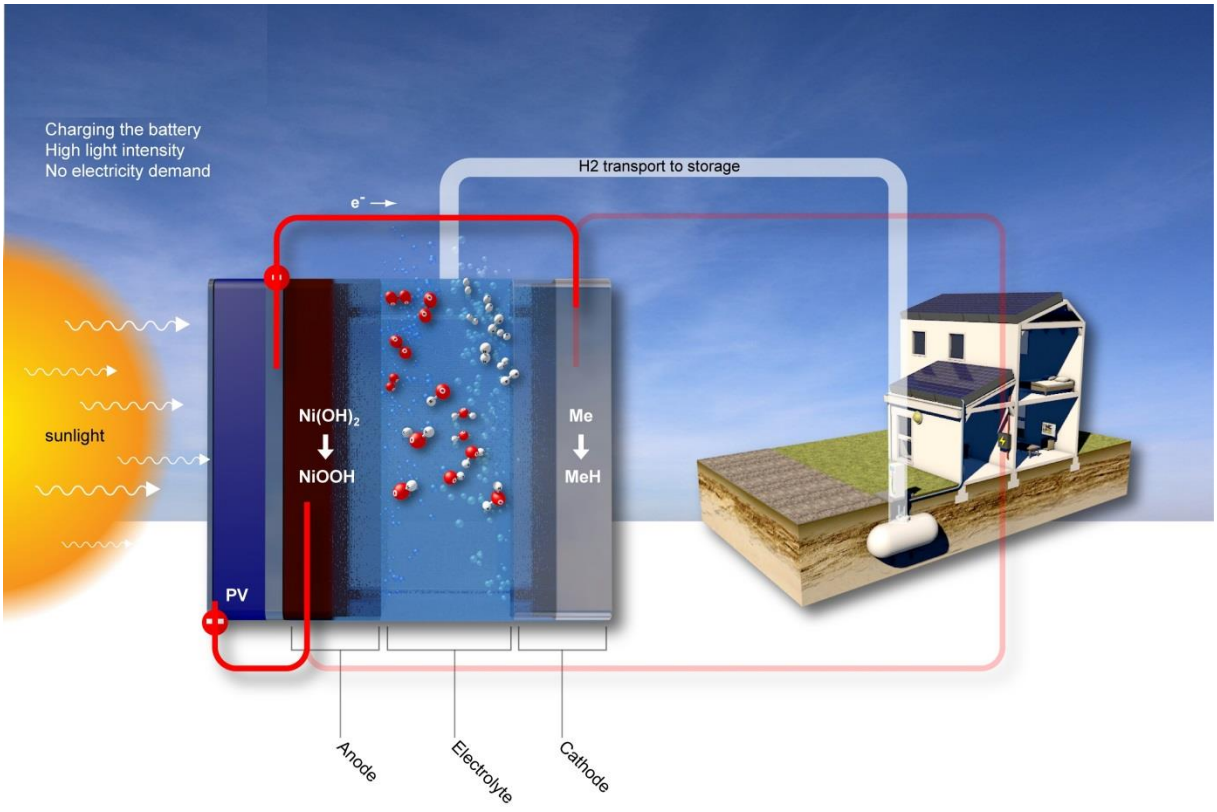

Cycle 03

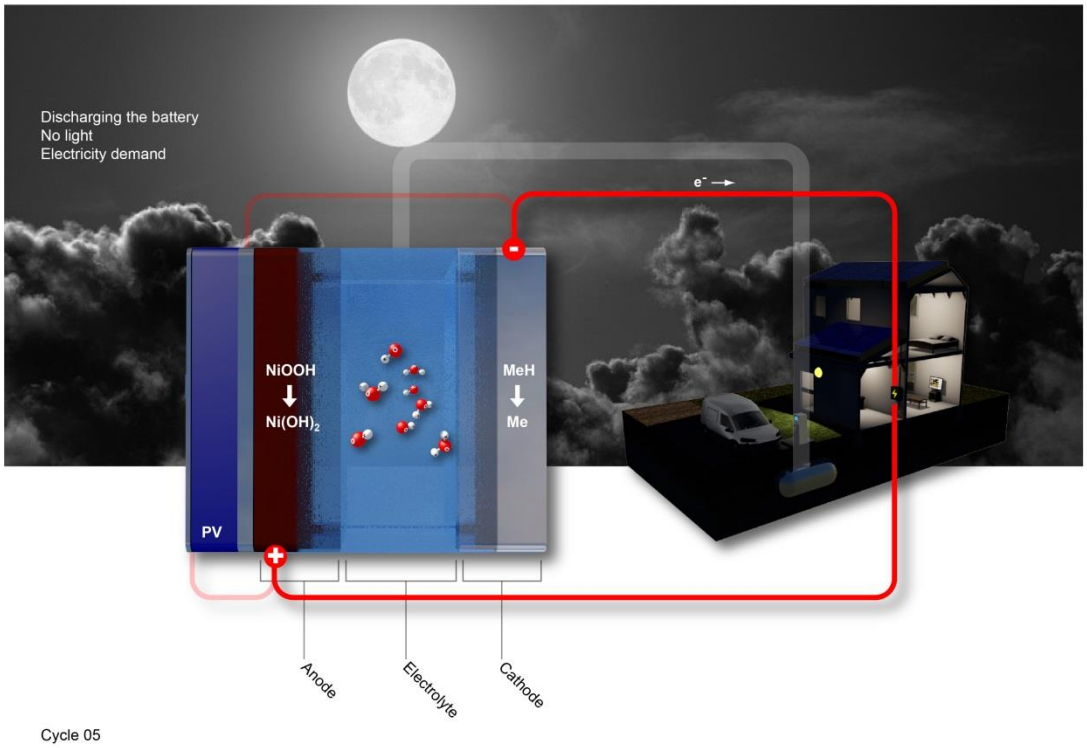

Figure 5.23.[3] *Schematic diagram of the device under operation. (i)-Cycle 01: the electricity demand is greater than the PV production → the PV is connected directly to the house; (ii)-Cycle 02: low power output from the PV (e.g. cloudy day) and production exceeds demand → (part of) the PV is connected to the battery/electrolyzer and charges the battery; (iii)-Cycle 03: high power output from the PV and production exceeds demand → (part of) the PV is connected to the battery/electrolyzer which performs electrolysis (H_2 is then transported to storage tank); (iv): when the battery component is full, electrolysis can still proceed; (v)-Cycle 05: demand exceeds PV production (e.g. at night) → the energy stored in the battery can be released to power the house.*

When the electrochemical cell is fully discharged (i-Cycle 01) the Ni-based anode is in its low-energy state $Ni(OH)_2$, and the hydrogen-absorbing metal cathode is in the metallic state. If the electricity from the PV component is needed, a switch disconnects the electrochemical part and directs the electricity to the users. If electricity is not needed the electrochemical cell is connected to the PV, and the device begins charging its electrodes (ii-Cycle 02) and storing energy according to $Ni(OH)_2$ → NiOOH at the anode, and Me → MH at the cathode. When the solar irradiance increases and the solar cell provides enough power, the device gradually switches from battery mode to electrolysis mode for the hydrogen production (iii-

[3] Cycle 01, Cycle 02, Cycle 03, Cycle 05: Figures by YORVIK.nl

Cycle 03) just like in a conventional electrolyzer, with OER and HER running over the efficient NiOOH and Pd catalysts, respectively (iv). When electricity is needed and no power comes from the PV, the energy stored into the battery is released by closing the circuit with the load. The energy release occurs by discharging the Ni-based electrode according to $Ni(OH)_2 \leftarrow NiOOH$, and the MeH electrode via the reaction $Me \leftarrow MH$ (v-Cycle 05). When the battery electrodes are fully discharged the cell is back at the initial point (i).

Discussion

The device concept proposed in this work offers the possibility, after optimization, to configure the PV module and the battery electrodes precisely to meet the end-user's need. The optimal size will provide enough energy during peak hours (of solar irradiance) to charge the battery component to such an extent that covers the daily needs also during winter times. The excess output from the PV in the summer will be converted into chemical energy, stored as H_2. This can be used as a fuel to power a vehicle. We consider as an example a residential house with a surface availability of 100 m^2 for installation the PV-battery/electrolyzer device. The electricity daily loading curve is as show in **Figure 5.24**. The solar irradiance is the one available in Delft, The Netherlands, estimated to be 1050 $kWh/m^2 \cdot yr$. The solar panels efficiency is taken as 15% and generate 11805 kWh/yr. The household consumption is considered to be the average value for The Netherlands, 3000 kWh/yr. The fraction of the electricity provided directly by the PV is taken to be 1/3 of the total daily consumption, thus 1000 kWh/yr. The remaining 2000 kWh/yr is to be indirectly provided after storage in a battery or as H_2. This equals to 5.5 kWh/day. In order to store (and release) such an amount of power from our MgTi electrode, we can consider as a maximum thickness the one used in commercial NiMH batteries. From the literature one can find that 290 μm is the normal thickness for the metal hydride electrode in Ni-MH batteries.[286] Calculations on a per gram basis show that our MgTi film has a 1700 mAh/g capacity at 1 A/g discharge rate (as in **Figure 5.19**). Using the same surface area of 100 m^2 as for the solar PV, assuming a 90% battery efficiency, 100 m^2 of 290 μm thick MgTi electrode can store up to 24.1 kWh/day, which is greater than the 5.5 kWh/day required. The next question one may wonder is whether the power output from the PV in the winter is enough to charge the battery to such an extent to cover the daily electricity household consumption. If not, the hydrogen stored in the summertime can be used via a fuel cell to back-up the electricity shortage. Taking Delft (The Netherlands) as an example, the PVGIS website[287] tells us that on average the daily power output in December is 10.40 kWh/day, which is 31% that of the yearly average of 32.3 kWh/day.[287] Given the average electricity

consumption of 8.2 kWh/day, a battery with 90% efficiency (but also 80%) will be able to meet the consumption needs. Therefore, the hydrogen produced can be used e.g. to power an electrical/fuel cell vehicle.

For the 2000 kWh/yr provided by the battery we consider a conversion efficiency of the battery component to be 90%, thus 2222 kWh/yr from the PV are needed to cover the 2000 kWh/yr consumption from the daily storage. The remaining 1000 kWh/yr are provided directly by the PV. All the above considered, of the 11800 kWh/yr produced yearly by the 100 m^2 PV panels, 3222 kWh/yr are used to cover the 3000 kWh/yr consumption. This leaves 8578 kWh/yr available for e.g. charging a fuel cell or an electric vehicle. We consider the case of a fuel cell vehicle. With an electrolyzer conversion efficiency of 60%, 5147 kWh/yr are stored into H_2. We consider moreover 200 kWh of H_2 is stored in one full tank which guarantees 600 km driving range. Therefore, 5147 kWh/yr are enough to provide 43 full tank filling and drive 25700 km. The results above are summarized in **Figure 5.25**.

In conclusion, 100 m^2 of 15% efficient solar panels coupled with an optimized battery/electrolyzer device with 90% efficiency as a battery and 60% efficiency as electrolyzer, are enough to power a typical residential house in The Netherlands throughout the year. Additionally, enough H_2 is produced to provide 43 full tank filling and drive 25700 km with a H_2 vehicle.

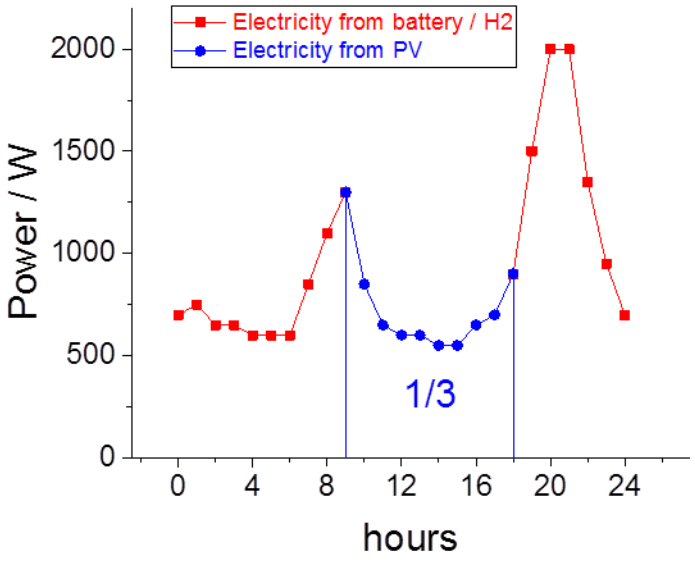

Figure 5.24. *Daily load profile of a residential house.[288,289] The fraction of the electricity provided directly by the PV is taken to be 1/3 of the total daily consumption. The remaining electricity is to be provided by the battery or H_2.*

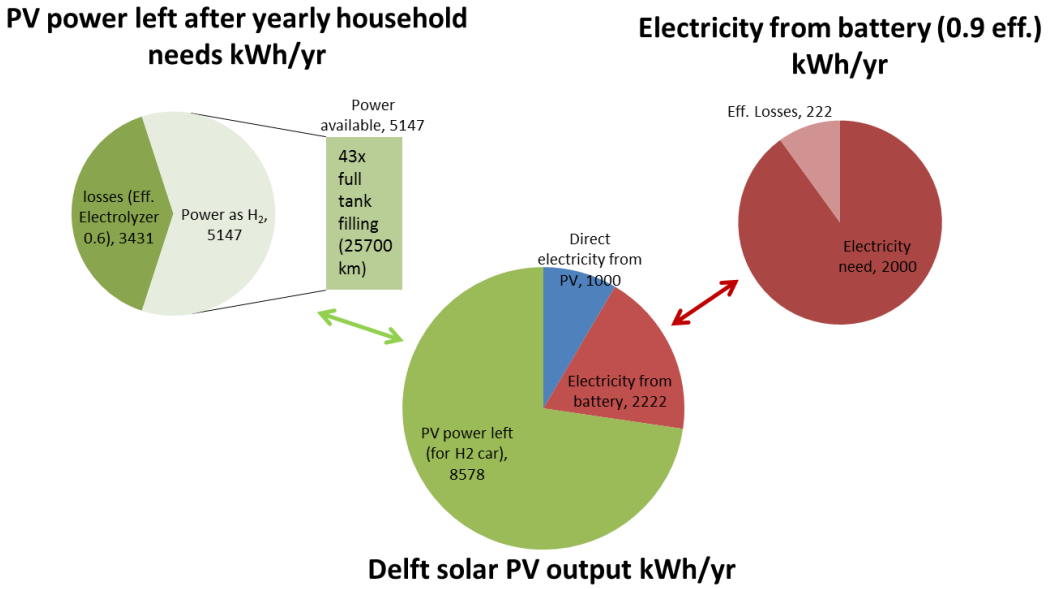

Figure 5.25. *Utilization of the 11800 kWh/yr provided by the PV according to its final use. Amounts calculated considering energy losses.*

Since the initial cost of batteries (let alone that of the electrolyzers) is an important factor limiting their market penetration, the use of easy-to-fabricate and abundant elements such as MgTi and Ni based electrodes holds promise for the scaling up of the technology.

However an alternative material for the Pd catalytic layer should be found. The materials proposed in this proof-of-concept study should not be considered as the final choice. In fact, the materials used in commercial PV and Ni-Fe, Ni-MH and Ni-hydrogen batteries could be employed for pilot plant studies. Another advantage of the proposed system is the limited electronics and balance-of-plant costs needed to operate.

Conclusions

In this chapter, we presented a proof-of-principle of a device that is able to convert solar energy either in electricity or to hydrogen, depending on the intensity of the irradiance. The device consists of a PV component integrated with a combined battery-electrolyzer cell. The battery/electrolyzer consists of a Pd-capped hydride-forming $Mg_{0.8}Ti_{0.2}$ cathode and a thick $Ni(OH)_2$ anode, which is powered by either of a triple junction a-Si–nc-Si–nc-Si with an OCV of 1.8 V under 1 sun, or a quadruple junction a-Si–a-Si–nc-Si–nc-Si with an OCV of 2.3 V under 1 sun. The quadruple solar cell is chosen to test the PV-battery/electrolyzer device operating near the MPP of the solar cell. The triple solar cell is chosen to simulate the behavior of the battery/electrolyzer cell under limited applied potential. The working principle is that the storage electrode loads at lower potential than that needed for water electrolysis. The battery component loads with a ΔV of 1.17 V and the electrolyzer operates with a ΔV of 1.48 V. The device performance under varying solar irradiance is compared to the one delivered by the same PV component coupled to an electrolyzer composed of a Pt cathode and a thin $Ni(OH)_2$ anode. When the solar cell with larger OCV is used, the performance of the battery/electrolyzer is comparable to that of the electrolyzer at all light intensities. At low light intensity (10 mW/cm^2), the open circuit voltage of the PV is reduced from 2.3 V to 2.1 V. This potential is enough to charge the battery and to perform the water splitting reactions and the performance is limited by the current generated by the solar cell. When the solar cell with the smaller OCV is used, at low light intensity (10 mW/cm^2), the open circuit voltage of the PV is reduced from ~ 1.8 V down to ~1.4 V. At this reduced potential neither the charging of the battery nor the water splitting, can proceed. Therefore, electricity generation is the most efficient process. At moderate light intensity (50 mW/cm^2) and above, the charging of the battery component is prioritized over the production of H_2. When the battery is fully charged, the hydrogen evolution will take place. With a fluctuating applied potential, the electricity is stored partly as electrical storage into the battery and partly as chemical storage in the form of H_2. Finally, when electric power is needed, the device may be

switched back to battery mode to discharge the battery. This last step closes the cycle, and regenerates the device.

The Mg-based cathode has a discharging capacity of 1700 mAh/g, comparable to that of what reported in the literature. The capacity of our Ni electrode instead is considerably lower than that reported in other studies and limits the battery discharge capacity. The cyclic stability of the Mg electrode has not been tested and should be investigated.

Since the local storage of solar electricity into batteries or hydrogen is currently not cost competitive with the electricity prices from the grid, it is of paramount importance to extend the storage capacity and the operational activity of the solar energy storage devices. An unexplored way to do so is by maximizing their energy conversion efficiency under the variable illumination conditions typically experienced daily. The concept device proposed in this work, after optimization, offers the possibility to size the PV module and the battery electrodes precisely to meet the end-user's need. Calculations for a residential house with a surface availability of 100 m^2 for installation the PV-battery/electrolyzer device show that such a system could make the house independent from the grid. Additionally, enough H_2 is produced yearly to provide 43 full tank filling and drive 25700 km with a H_2 vehicle. This is in principle enough for 1 or 2 vehicles.

All the above considered, we believe the proposed flexible solar electricity/battery/electrolyzer device holds promise for application in households.

APPENDIX 1

Hydrogen uptake and release from a MgTi electrode

Number	*Value*
1 electron (e^-)	1.6022×10^{-19} C
Number of Avogadro (NA)	6.0221×10^{23} mol^{-1}
Atomic weight of H	1.0081 amu

Charging time: 1575 s – 325 s = 1250 s

Charging at 58µA: 58×10^{-6}A = 58×10^{-6} C/s

So, 58×10^{-6} C/s · 1250 s = 0.0725 C

Amount of electrons: 0.0725 C / 1.6022×10^{-19} C = 4.525×10^{17} electrons

---

Ratio e^- vs. H = 1 : 1, so 4.525×10^{17} atoms of hydrogen

Moles of H = 4.525×10^{17} / NA = 4.525×10^{17} / 6.0221×10^{23} mol^{-1} = 7.514×10^{-7}

Weight of H (g): 7.514×10^{-7} / 1.0081 = 7.454×10^{-7} gram

Weight of $Mg_{0.80}Ti_{0.20}$

Number	*Value*
Density $Mg_{0.80}Ti_{0.20}$ (ρ)	2.291 g/cm^3

Diameter surface (D)	6	mm	=	0.6 cm
Thickness of layer (h)	200	nm	=	2.0×10^{-5} cm

$V\ (cm^3) = ¼\ \pi \cdot D^2 \cdot h = ¼\ \pi \cdot (0.6\ cm)^2 \cdot 2.0 \times 10^{-5}\ cm = 1.8 \times 10^{-6}\ \pi\ cm^3$

Weight of MgTi (g): $V \cdot \rho = 1.8 \times 10^{-6}\ \pi\ cm^3 \cdot 2.291\ g/cm^3 = 1.296 \times 10^{-5}$ gram

Mass ratio H vs MgTi

Weight of H / weight of MgTi · 100% = 7.454×10^{-7} g / 1.296×10^{-5} g = 5.75%

REFERENCES CHAPTER 5

250. Khaselev, O.; Turner, J. A. A Monolithic Photovoltaic-Photoelectrochemical Device for Hydrogen Production via Water Splitting *Science* **1998**, 280, 425-427.
251. Han, L.; Abdi, F. F.; van de Krol, R.; Liu, R.; Huang, Z.; Lewerenz, H.-J.; Dam, B.; Zeman, M.; Smets, A. H. M. Efficient Water-Sp litting Device Based on a Bismuth Vanadate Photoanode and Thin-Film Silicon Solar Cells *ChemSusChem* **2014**, 7, 2832 – 2838.
252. Khaselev, O.; Bansal, A.; Turner J. A. High-efficiency integrated multijunction photovoltaic/electrolysis systems for hydrogen production *Int. J. Hydrogen Energy* **2001**, 26, 127-132
253. Wang, H.; Deutsch, T. G.; Welch, A.; Turner, J. A. Stability of Illuminated p-GaInP2 Semiconductor Photoelectrode *Int. J. Hydrogen Energy* **2012**, 37, 14009-14014
254. Bonke, S. A.; Wiechen, M.; MacFarlane, D. R.; Spiccia, L. Renewable fuels from concentrated solar power: towards practical artificial photosynthesis *Energy Environ. Sci.* **2015**, 8, 2791-2796
255. Liu, R.; Zheng, Z.; Spurgeon, J.; Yang X. Enhanced photoelectrochemical water-splitting performance of semiconductors by surface passivation layers *Energy Environ. Sci.* **2014**, 7, 2504-2517.
256. Scheuermann, A. G.; Lawrence, J. P.; Kemp, K. W.; Ito, T.; Walsh, A.; Chidsey, C. E. D.; Hurley, P. K.; McIntyre, P. C. Design principles for maximizing photovoltage in metal-oxide-protected water-splitting photoanodes *Nature Materials* **2016**, 15, 99-106
257. Pinaud, B. A.; Benck, J. D.; Seitz, L. C.; Forman, A. J.; Chen, Zhebo; Deutsch, T. G.; James, B. D.; Baum, K. N.; Baum, G. N.; Ardo, S.; Wang, H.; Miller, E.; Jaramillo, T. F. Technical and economic feasibility of centralized facilities for solar hydrogen production via photocatalysis and photoelectrochemistry *Energy Environ. Sci.* **2013**, 6, 1983-2002
258. Victoria, M.; Smith, W.A.; Jacobs, J.F.; Vermaas, D.A.; de Respinis, M.; Digdaya, I.A.; Sudhölter, E.J.R.; Dam, B. A technologically and economically feasible solar-driven water-splitting device for hydrogen production; submitted
259. Lin, Y.; Battaglia, C.; Boccard, M.; Hettick, M.; Yu, Z.; Ballif, C.; Ager, J. W.; Javey, A. Amorphous Si Thin Film Based Photocathodes with High Photovoltage for Efficient Hydrogen Production *Nano Lett.* **2013**, 13, 5615–5618
260. Prevot, M. S.; Sivula, K. Photoelectrochemical Tandem Cells for Solar Water Splitting *J.Phys.Chem.C* **2013**, 117, 17879−17893
261. Doscher, H.; Geisz, J. F.; Deutsch, T. G.; Turner, J. A. Sunlight absorption in water–efficiency and design implications for photoelectrochemical devices *Energy Environ. Sci.* **2014**, 7, 2951.
262. Schoonman, J. *Ber. Bunsenges. Phys. Chem.* **1982**, 86, 660-664.
263. Schoonman, J.; Kiliaan, H.S. *Solid State lonics* **1983**, 9 & 10, 1087-1092.
264. Akuto, K.; Sakurai, Y. *J. Electrochem. Soc.* **2001**, 148, 2, A121-A125.
265. Xia, X.; Luo, J.; Zeng, Z.; Guan, C.; Zhang, Y.; Tu, J.; Zhang, H.; Fan, H.J. *Scientific Reports* **2012**, 2, 981, 1-6.
266. Danko, D.B.; Sylenko, P.M.; Shlapak, A.M.; Khyzhun, O.Y.; Shcherbakova, L.G.; Ershova, O.G.; Solonin, Y.M.; *Sol. Energy Mater. Sol. Cells* **2013**, 114, 172-178.
267. Bora, D. K.; Braun, A.; Erni, R.; Muller, U.; Dobeli, M.; Constable, E. C. *Phys. Chem. Chem. Phys.* **2013**, 15, 12648-12659.
268. Morvaj, B.; Dragicevic, T.; Krajcar, S. Controllable photovoltaic grid power injection with an assistance of energy storage system, Fourth International Conference on Power Engineering, Energy and Electrical Drives (POWERENG), **2013**
269. Borowy, B.; Salameh, Z. M. Methodology for optimally sizing the combination of a battery bank and PV array in a Wind/PV hybrid system, *IEEE Transactions on Energy Conversion* **1996**, 11, 367 - 375
270. Tummuru, N.R.; Mishra, M. K.; Srinivas, S. Integration of PV/battery hybrid energy conversion system to the grid with power quality improvement features *IEEE International Conference on Industrial Technology (ICIT)*, **2013**
271. Kelly, N. A.; Gibson, T. L.; Cai, M.; Spearot, J. A.; Ouwerkerk D. B. Development of a renewable hydrogen economy: Optimization of existing technologies *International Journal of Hydrogen Energy* **2010**, 35, 892–899
272. Morisaki, S.; Kawakami, K.; Baba, N. Formation of Nickel Oxyhydroxide Thin Films by Electrodeposition and Their Electrochromic characteristics, *Japanese journal of Applied Physics* **1988**, 27, 314-318

273. Li, C. W.; Kanan, M. W. CO2 Reduction at Low Overpotential on Cu Electrodes Resulting from the Reduction of Thick Cu2O Films *J. Am. Chem. Soc.*, **2012**, 134, 7231–7234
274. Diaz-Morales, O.; Ferrus-Suspedra, D.; Koper, M. T. M. The importance of nickel oxyhydroxide deprotonation on its activity towards electrochemical water oxidation *Chem. Sci.* **2016** DOI: 10.1039/c5sc04486c
275. Niessen, R. A. H.; Notten, P. H. L. *Electrochem. Solid-State Lett.* **2005**, 8, 10, A534-A538.
276. Xin, G.; Yang, J.; Fu, H.; Zheng, J.; Li, X. *Int. J. Hydrogen Energy* , 38, 10625-10529.
277. Hall, D. S.; Lockwood, D. J.; Bock, C.; MacDougall, B. R. Nickel hydroxides and related materials: a review of their structures, synthesis and properties *Proc. R. Soc. A* **2014***,* 471:201407
278. Chen, J.; Bradhurst, D. H.; Dou, S. X.; Liu, H. K. Nickel Hydroxide as an Active Material for the Positive Electrode in Rechargeable Alkaline Batteries *Journal of The Electrochemical Society* **1999**, 146, 3606-3612
279. Freitas, M.B.J.G. Nickel hydroxide powder for NiO·OH/Ni(OH)$_2$ electrodes of the alkaline batteries *Journal of Power Sources* **2001**, 93, 163-173
280. Subbaraman, R.; Tripkovic, D.; Chang, K.-C.; Strmcnik, D.; Paulikas, A. P.; Hirunsit, P.; Chan, M,; Greeley, J.; Stamenkovic, V.; Markovic N. M. Trends in activity for the water electrolyser reactions on 3d M(Ni,Co,Fe,Mn) hydr(oxy)oxide catalysts, *Nature Mater.* **2012**, 11, 550–557
281. Vermeulen, P.; Niessen, R.A.H.; Notten, P.H.L. Hydrogen storage in metastable MgyTi(1-y) thin films *Electrochem. Comm.* **2006**, 8, 27-32.
282. Vermeulen, P.; Niessen, R. A. H.; Borsa, D. M.; Dam, B.; Griessen, R.; Notten, P. H. L. Effect of the Deposition Technique on the Metallurgy and Hydrogen Storage Characteristics of Metastable MgyTi(1−y) Thin Films, *Electrochem. Solid-state Lett.* **2006**, 9, A520-A523.
283. Vermeulen, P.; Ledovskikh, A.; Danilov, D.; Notten, P.H.L. Thermodynamics and kinetics of the thin film magnesium–hydrogen system *Acta Mater.* **2009**, 57, 4967-4973.
284. Dau, H.; Limberg, C.; Reier, T.; Risch, M.; Roggan, S.; Strasser, P. *ChemCatChem* **2010**, 2, 724.
285. Dennis A. Corrigan The Catalysis of the Oxygen Evolution Reaction by Iron Impurities in Thin Film Nickel Oxide Electrodes *J. Electrochem. Soc.* **1987,** 134, 377-384.
286. Pan, Y.H.; Srinivasan, V.; Wang, C.Y. An experimental and modeling study of isothermal charge/discharge behavior of commercial Ni–MH cells *Journal of Power Sources* **2002**, 112, 298–306
287. http://re.jrc.ec.europa.eu/pvgis/apps4/pvest.php
288. Mohammad Sameti et al. Simulation of a ZEB Electrical Balance with a Hybrid Small Wind/PV. *Sustainable Energy*, **2014**, 2, 5-11.
289. Taufiqul Arif, M.; Oo, A. M. T.; Shawkat Ali, A. B. M. Estimation of Energy Storage and Its Feasibility Analysis, *Energy Storage - Technologies and Applications*, **2013**

Summary

Resource scarcity and climate change have severe socio-economic and geo-political consequences. The approach needed for tackling them consists of moving away from a dependence on fossil-fuel resources and relying on decentralized energy production based on renewables. It is likely that our society will experience such a transformation of the energy sector in the coming decades.

Because renewable energy sources such as solar and wind typically present daily and seasonal fluctuations, technologies for short term and long term energy storage have to be developed. In this thesis we investigated materials and devices for the conversion and storage of solar energy. We pursued this research via two approaches: a) the direct conversion of solar energy into hydrogen and oxygen in a (photo)electrochemical (PEC) cell and b) an integrated device - composed of a photovoltaic (PV) cell and a battery/electrolyzer - for combined solar electricity production with electrical storage and chemical storage. The electrical storage is best suited for the short term, while the chemical storage can in principle provide the long term storage and serve as fuel for transportation. In the PEC approach, we focused on the oxygen evolving electrode, where the energetically more difficult reaction of the water splitting is performed.

The conversion of renewable (solar) energy into fuels such as hydrogen, alcohols, hydrocarbons, etc. is highly desirable as a means of energy storage. The water splitting process plays a pivotal role in the renewable production of fuels. In all approaches, water is oxidized to oxygen releasing protons and electrons for the fuel production reactions. However the efficiency of the water oxidation reaction is low, limited by its high overpotential and slow kinetics. In **Chapter 2.1** we firstly discussed the thermodynamic reasons of the overpotential, by introducing the concepts of free energy diagram, the Sabatier principle and the scaling relations. Since four individual one-electron reaction steps of 1.23 eV each are needed for water oxidation, the total energy change is 4.92 eV. In this case, the reaction would occur at zero overpotential. However the difference in the energetics of two of the reaction intermediates (HO* and HOO*) is a constant equal to 2.98 eV (should be 2.46 eV). This difference between actual catalysts and an ideal one, gives a minimum thermodynamic overpotential of $\frac{2.98-2.46}{2}$ = 0.26 V. This constant is the basis of the scaling relationships, which makes it impossible to change any of these binding energies

independently. To avoid the limitations defined by the scaling relation, the challenge is to find a way to modify oxide surfaces or the electrochemical interface, such that the relative stability of HOO* and HO* changes. 3D structures such as in layered catalysts may provide a viable route to allow for water splitting with low overpotential.

Experimentally we used three different first-row transition-metal catalysts (Co, Fe, Ni) to illustrate the effect on the catalytic activity of 1) metal catalytic sites, 2) electrolyte anions, pH, and catalyst thickness. Our results showed that increasing the specific surface area of the catalyst layer (via the thickness) is beneficial until ohmic losses prevail. This is true as long as the catalyst is electrically connected throughout its thickness and in contact with the electrolyte. Moreover, the water oxidation reaction over catalysts with a double-hydroxide structure are favored in alkaline media compared to a neutral electrolyte. Furthermore, we have shown that certain catalysts such as CoPi possess a peak in catalytic activity at a certain pH.

Electrocatalysts were investigated as electrodes, and in combination with a light absorbing semiconductor as photoelectrodes. The class of semiconductors of choice is metal oxides ($BiVO_4$, WO_3, Ta_2O_5) because of the non-toxicity, inexpensiveness and stability towards oxidation. As drawbacks they have *poor catalytic activity, poor visible light absorption* and *low charge carrier mobility*. In this thesis we aimed at understanding the underlying reasons for these drawbacks in order to develop strategies for their mitigation. In **Chapter 2.2** we investigated the PEC performance of $BiVO_4$ photoanodes for water oxidation in neutral pH. We modified its surface with catalysts belonging to three different co-catalysts groups: a ruthenium derived aqua complex $[(cy)Ru^{II}(bpy)OH_2]^+$ molecular catalyst (RuCat); metallic nanoparticles of RuO_2; a porous Co double hydroxide in a phosphate buffer (CoPi). The trend in electrocatalytic activity of the catalysts is RuO_2→CoPi→RuCat, however the PEC activity is found to be reversed, RuO_2-$BiVO_4$→CoPi-$BiVO_4$→RuCat-$BiVO_4$. This shows that the electrocatalytic activity of a catalyst cannot be used to determine its effectiveness as a co-catalyst. The self-limited thickness of the molecular catalyst results in a light absorption of only 5% across the UV-vis-NIR spectrum, which allows for a higher saturation current density under front illumination as compared to CoP_i. Despite the limited thickness of RuCat, the RuCat-$BiVO_4$ photoanode shows a 0.1 V more cathodic onset potential compared to CoP_i-$BiVO_4$. We attributed this to the larger distance between the conduction band electrons in $BiVO_4$ and the reaction center (Ru), compared to the distance with Co. The smaller onset potential and the high co-catalytic activity at small thicknesses, make the use of molecular

catalysts an interesting proposition when designing a heterojunction tandem device where light must first pass through the catalyst layer.

The mismatch of metal oxides between the absorption depth of visible light (up to several micrometers) and the distance that the photo-generated charge carriers can travel before they recombine (between 1 and few hundreds of nanometers) can be overcome via morphology control, i.e. nanostructuring. One of the main challenges in developing highly efficient nanostructured photoelectrodes is to achieve good control over the desired morphology and good electrical conductivity. In **Chapter 3** we proposed a novel plasma-assisted processing technique to generate surface nanostructures on tungsten. This top-down approach guarantees good contact between the different crystallites and avoids electrical conductivity limitations. After an optimized two-step anneal procedure that minimizes the concentration of interfacial defects, the mesoporous tungsten surface transforms into nanostructured monoclinic WO_3, while preserving the conductivity of the metallic tungsten bulk. These porous semiconducting WO_3 films showed photocurrents up to 1 mA/cm^2, which is 5 times higher than dense, non-porous WO_3 samples made from a polished W disc.

The poor carrier conductivity of metal oxides, and their inefficiency in absorbing significant portions of the visible part of sunlight, can be addressed by nitrogen incorporation into metal oxides, leading to nitrogen-doped oxide, oxynitride or nitride phases. In **Chapter 4.1** we demonstrated the use of 'oxynitrogenography' as a technique towards the controlled and reproducible synthesis of phase pure Ta-O-N phases, including the elusive β-TaON phase. The method shows that the solubility range of O and N is smaller than expected, which implies that a quasi-equilibrium approach is necessary to obtain phase pure samples. The high quality of the so formed films is confirmed by their electronic properties as probed with TRMC. We observed that the carrier mobility increases with the nitrogen content in the sample, from 10^{-5} cm^2/Vs in Ta_2O_5, to 10^{-2} cm^2/Vs in β-TaON and the mixed TaON-Ta_3N_5, up to 10^{-1} cm^2/Vs in Ta_3N_5. While the carrier mobility of β-TaON and Ta_3N_5 is comparable to that of $BiVO_4$, the apparent lifetime in the order of milliseconds is comparable to that of crystalline silicon. This would make it superior by three orders of magnitude to that of other Ta_3N_5 reported in the literature, as well as to that of the most promising metal oxide-based semiconductors ($BiVO_4$, Fe_2O_3, WO_3, Cu_2O) under investigation in photo-electrochemical (PEC) water splitting. Moreover, these results suggest a carrier diffusion length of the order of tens of μm, much longer than the optical absorption depth. However, some care must be taken when interpreting these results, as the possibility of carrier (de-)trapping into and from

shallow trap states may alter the picture. Nevertheless, the extremely long-lived TRMC signal for the stoichiometric β-TaON and Ta_3N_5, compared to that of the mixed TaON/Ta_3N_5 samples, confirmed the need for single phase materials to achieve high energy conversion efficiencies for these promising photoanode materials.

For (photo-)electrochemical measurements, the semiconductors have to be deposited or grown onto a conductive substrate. The development of a reliable method to synthesize efficient thin film TaON and Ta_3N_5 photoanodes has been hindered by the unavoidable growth of undesired interfacial phases during the synthesis process. In **Chapter 4.2** we showed that growing Ta_3N_5 onto Pt-quartz alters the phase purity of the film compared to its growth onto quartz. We also showed for the first time the use of atomic layer deposited TiO_2 and Al_2O_3 overlayers for Ta_3N_5. The presence of the Al_2O_3 interfacial layer between the Ta_3N_5 and the chosen Ni-$Ni(OH)_2$-$Co(OH)_2$-CoP_i catalyst increases the charge extraction rate by two-fold compared to the Ta_3N_5-catalyst and to the Ta_3N_5-TiO_2-catalyst configurations. As a result a promising 5.5 $mAcm^{-2}$ at 1.6 V vs. RHE was achieved with a 580 nm Ta_3N_5 photoanode with Al_2O_3-Ni-$Ni(OH)_2$-$Co(OH)_2$-CoP_i surface multilayers. When the same recipe is applied to TaON, a photocurrent of only 0.2 $mAcm^{-2}$ at 1.23 V vs. RHE is measured. We hypothesize that this discrepancy is caused by the lower tolerance to secondary phases of TaON compared to Ta_3N_5.

In conclusion, our PEC investigation reveals that 1) in the materials considered, the drawbacks can be mitigated via optimized semiconductors-catalyst junctions, via nanostructuring, and via bandgap engineering, 2) the conductor-semiconductor and semiconductor-catalyst-electrolyte interfaces are key factors influencing the performance and lifetime of the device and 3) the ideal semiconductors/catalysts combinations are yet to be found.

From a device perspective, the intrinsic limitations of the direct photoelectrochemical approach to water splitting, include i) complications which arise at the semiconductor-catalyst-electrolyte interfaces, ii) the expected decrease in the photovoltage under reduced light intensity and iii) the fact that the photoelectrochemical H_2 production competes with solar PV, for the same surface area available. As a possible way to overcome the issues above, in **Chapter 5** we have developed a proof-of-principle of a device that is able to convert solar energy either in electricity or to hydrogen, depending on the intensity of the irradiance. Furthermore, interfacial limitations are circumvented in the proposed integrated device, where the solid-state processes (i.e., light absorption and charge separation) are

separated from the electrocatalytic processes of electrical/chemical storage. Compared to a pure photo-electrochemical approach, this approach has the further advantages of a) enabling electricity production and electrical storage, and b) improved compatibility with the daily and seasonal variations of light intensity.

The device consists of a PV component integrated with a combined battery-electrolyzer cell. The battery/electrolyzer consists of a Pd-capped hydride-forming $Mg_{0.8}Ti_{0.2}$ cathode and a thick $Ni(OH)_2$ anode, which is powered by either of a triple junction a-Si–nc-Si–nc-Si with an OCV of 1.8 V under 1 sun, or a quadruple junction a-Si–a-Si–nc-Si–nc-Si with an OCV of 2.3 V under 1 sun. The working principle is that the storage electrode loads at lower potential than that needed for water electrolysis. In fact, the battery component has a ΔV of 1.17 V and the electrolyzer operates with a ΔV of 1.48 V. The experiments show that at low light intensity (10 mW/cm^2), the OCV of the PV is reduced from ~1.8 V down to ~1.4 V. At this reduced potential we do not detect significant current. This suggests that neither the charging of the battery nor the water splitting can proceed, due to overpotentials. Therefore, electricity generation is the most efficient process. At moderate light intensity (50 mW/cm^2) and above, the charging of the battery component is prioritized over the production of H_2. When the battery is fully charged, the hydrogen evolution will take place. With a fluctuating applied potential, the electricity is stored partly as electrical storage into the battery and partly as chemical storage in the form of H_2. When the solar cell with larger OCV is used, the performance of the battery/electrolyzer is comparable to that of the electrolyzer at all light intensities, up to > 5 $mAcm^{-2}$ bias-free.

In this prototype device, Earth-abundant materials such as Si (solar cell), Mg, Ti and Ni (electrochemical cell) constitute the main components. Moreover, the fabrication of Si solar cells is a well-developed industrial process and electrodes in the electrochemical cell are deposited with cheap and scalable techniques such as Physical Vapor Deposition (PVD) and electrodeposition. As drawbacks, 1) triple or quadruple junction solar cells are needed to provide the required potential for the electrochemical reactions, 2) the capacity of the chosen Ni electrode is limited, and 3) Pd, a rare-Earth element, is used as a catalyst for the Mg-based electrode. Lastly, the cyclic stability has not been tested. With all the above considered, we believe that the concept device proposed in this work, after optimization, offers the possibility to size the PV module and the battery electrodes precisely to meet the end-user's need. A patent on this device is pending.

Samenvatting

Bron schaarste en klimaatveranderingen hebben ernstige socio-economische en geopolitieke consequenties. Om dit te kunnen veranderen, zullen we minder afhankelijk moeten worden van fossiele brandstoffen en moeten kunnen vertrouwen op gedecentraliseerde energie productie, op basis van duurzaamheid. Het is waarschijnlijk dat een dergelijke transformatie in de komende decennia zal plaatsvinden in onze maatschappij.

De productie van duurzame energie, uit bronnen zoals de zon en de wind, kennen dagelijkse fluctuaties en schommelingen door seizoenen. Dit zorgt op sommige dagen voor een overschot aan elektriciteit, op anderen aan een te kort. Daarom moeten er technieken worden ontwikkeld om energie voor de korte en de lange termijn op te slaan. In deze thesis onderzochten we materialen en apparatuur voor de omzetting en opslag van zonne-energie en (zonne-)elektriciteit. We streefden in dit onderzoek twee doelen na. In het eerste doel onderzochten we de directe omzetting van water naar waterstof en zuurstof, via zonne-energie in een foto-elektrochemische (PEC) cel. In deze benadering hebben we onze aandacht gevestigd op het ontwikkelen en bestuderen van een elektrode, die met behulp van zonne-energie zuurstof kan maken. We hebben ons gericht op dit deel van de reactie omdat dit een ingewikkeldere reactie is, energetisch gezien, dan de productie van waterstof. In het tweede doel onderzochten we een geïntegreerd apparaat – bestaande uit een fotovoltaïsche (PV) cel en een accu/elektrolysecel – om binnen ditzelfde apparaat de productie van zonne-elektriciteit te combineren met de opslag van deze elektriciteit, middels een accu en via verbindingen met een chemische stof: waterstof. De accu kan het beste worden gebruikt als korte termijn opslag, terwijl de manier die wij hebben onderzocht om waterstof te gebruiken voor energie opslag, beter voor de lange termijn kan worden gebruikt. Tevens kan het in die vorm dienen als een mogelijkheid om de elektriciteit te transporteren.

De omzetting van duurzame (zonne-) energie in brandstoffen zoals waterstof, alcohol, koolwaterstoffen, etc. is een gewenste manier van de energie op te slaan. Het proces om water te splitsen, via water oxidatie tot zuurstof, speelt een belangrijke rol in de productie van duurzame brandstoffen. Aangezien hierbij protonen en elektronen vrij komen, waarmee deze beschikbaar worden voor de reacties voor productie van brandstoffen. Echter de efficiëntie van de reactie van wateroxidatie is laag, want het is gelimiteerd door de hoge

overpotentiaal en de langzame kinetiek. In Hoofdstuk 2.1 bediscussiëren we eerst de thermodynamische oorzaken van deze overpotentiaal, door middel van het introduceren van een 'vrij energie diagram' concept, de Sabatier principe en de schaal-verhoudingen. Er zijn vier individuele 1-elektron reactie stappen tussen de vorming van H2O in O2, in de vorm van de volgende chemische vormen HO*, O*, HOO*. Voor elk van deze stappen is 1.23eV nodig. Dit brengt de totale energie verandering op 4.92 eV. In deze situatie, zou de reactie ontstaan met nul overpotentiaal. Echter het verschil in de energie van twee van de stappen (HO* en HOO*) is constant gelijk aan 2.98 eV (zou 2.46 eV) moeten zijn. Dit verschil tussen de actuele katalysatoren en de ideale vorm geeft minimaal een thermodynamische overpotentiaal van $\frac{2.98-2.46}{2}$ = 0.26V. Deze constante is de basis van de schaal verhoudingen, wat het onmogelijk maakt om een van deze verbindende energieën te veranderen. De uitdaging is om de beperkingen, zoals vastgesteld op de schaalverhouding, te vermijden en dus een manier te vinden om de oxide oppervlakten of de elektrochemische interface te veranderen, zodat de relatieve stabiliteit van HOO* en HO* veranderd. 3D structuren zoals in gelaagde katalysatoren, kunnen mogelijk een manier bieden om water splitsing toe te staan met een lage overpotentiaal.

We hebben met drie verschillende eerste lijn transitie metalen katalysatoren geëxperimenteerd (Co, Fe, Ni) om het effect te illustreren van de katalytische activiteit van 1) metalen katalytische kanten, 2) elektrolyt anionen, pH en de katalytische dikte. Onze resultaten laten zien dat het vergroten van de specifieke oppervlakte gebied van de katalysatorlaag (via de dikte) noodzakelijk is, tot dat ohmische verlies de overhand krijgt. Dit gebeurd zolang als dat de katalysator elektrisch verbonden is door zijn dikte en in contact staat met de elektrolyten. Bovendien wordt de water oxidatie reactie over katalysatoren met een dubbele-hydroxide structuur verkozen in een alkalisch media in plaats van een neurale elektrolyt. Verder laten we zien dat bepaalde katalysatoren, zoals CoPi, een katalytische activiteit bevatten bij een bepaalde pH.

Elektrokatalysatoren werden onderzocht als elektrodes en in combinatie met een licht absorberende semi-geleiders van foto-elektroden. De gekozen groep semi-geleiders is metal oxiderend ($BiVO_4$, WO_3, Ta_2O_5), vanwege hun niet-toxische werking, de lage kosten en stabiliteit in de oxidatie. Helaas echter hebben ze als nadelen: lage katalytische activiteit, lage zichtbare licht absorptie en lage lading dragende mobiliteit. In deze thesis streven we naar het begrijpen van de onderliggende redenen voor deze nadelen, om zodoende strategieën te ontwikkelen om deze nadelen af te kunnen zwakken. In hoofdstuk 2.2 onderzoeken we de prestatie van PEC bestaand uit $BiVO_4$ foto-anoden, voor water oxidatie in

neutrale Ph setting. We veranderen eerst het oppervlak met katalysatoren die behoren tot drie verschillende mede-katalysatoren groepen: een ruthenium zouthydraat $[(cy)Ru^{II}(bpy)OH_2]^+$ moleculaire katalysator (RuCat); metaal nanodeeltjes bestaande uit RuO_2; een poreuze Co-dubbel-hydroxide in een fosfaatbuffer (CoPi). De elektrokatalystische activiteit van de katalysator is gericht naar RuO_2 → CoPi→ RuCat, echter de PEC activiteit blijkt tegengesteld te werken, RuO_2-$BiVO_4$→CoPi-$BiVO_4$→RuCat-$BiVO_4$. Dit laat zien dat de elektrokatalystische activiteit van de katalysator niet kan worden gebruikt om hierbij zijn activiteit als een katalysator te bepalen. De zelflimiterende dikte van de moleculaire katalysator resulteert in een lichtabsorptie van enkel 5% onder het UV-vis-NIR spectrum, wat zorgt voor een hogere verzadiging van de stroomdichtheid bij belichting van de voorkant vergeleken met CoPi. Ondanks de gelimiteerde dikte van RuCat, de RuCat-$BiVO_4$ foto anode laat een 0.1V hogere kathodische begin-potentiaal dan met CoPi-$BiVO_4$. We wijden dit toe aan de grotere afstand tussen de geleidingsband elektronen in $BiVO_4$ en het reactiecentrum (Ru), vergeleken met de afstand met Co. De kleinere begin potentiaal en de hogere co-katalytische activiteit met een lagere dikte maakt het gebruik van moleculaire katalysatoren een interessante optie om een zogenoemde heterojunctie tandem apparatuur te ontwikkelen, waar licht eerst door een katalysator filter heen moet.

Het niet in relatie staan van de absorptie-diepte van zichtbaar licht van metaal oxiden (tot enkele micrometers) en de afstand dat de foto-gegenereerde geleiding drager kan overbruggen, tot ze samenkomen, (tussen 1 en enkele honderdsten van nanometers) kan worden opgelost via morfologische controle, zoals nanostructurering. Eén van de grote uitdagingen in het ontwikkelen van een hoog efficiënte nanogestructureerde foto-elektroden is het bereiken van een goede controle over de gewenste morfologie en goede elektrische geleiding. In hoofdstuk 3 hebben we een nieuwe plasma-gesteunde verwerkingstechniek voorgesteld, om nanostructuren op het oppervlak van wolfraam te genereren. Deze top-down benadering garandeert goed contact tussen de verschillende kristallen en vermijd elektrische geleidingen beperkingen. Na een geoptimaliseerde 2-stappen procedure wat de concentratie van tussenliggende fouten moet minimaliseren, de mesoporeuze wolfraam oppervlak transformeert in een nanogestructureerde, monoklinische WO_3 met behoud van de geleiding van niet-geoxideerd wolfraam in de bulk. De (foto-)elektrische stroom van deze poreuze halfgeleidende WO_3 (zeer dunne) laag bereikt waarden tot 1 mA/cm^2, dat tot 5 keer hoger is dan dichte, niet-poreuze WO_3 samples gemaakt uit een gepolijste Wolfraam schijf.

De slechte elektronen/gaten geleiding van metaal oxiden en hun inefficiëntie om significante delen van zichtbaar zonlicht te absorberen kan worden toegewezen aan de aanwezigheid

van stikstof dat in de metaal oxiden zit, wat lijdt tot de stikstof doping van zuurstof, tot oxynitrides of tot stikstof fases. In Hoofdstuk 4.1 demonstreren we het gebruik van 'oxynigrogengraphy' als een techniek voor het gecontroleerde en reproduceerbare synthese van fase pure Ta-O-N fases, inclusief de moeilijk te behalen β-TaON fase. De methode laat zien dat de reikwijdte van oplosbaarheid van O en N kleiner is dan verwacht, wat impliceert dat de quasi-evenwichts benadering nodig is om de fase pure samples te kunnen verkrijgen. De hoge kwaliteit van de ze gevormde dunne lagen of 'films' is bewezen via hun elektrische kenmerken as onderzocht met TRMC. We observeerden dat de elektronen/gaten mobiliteit werd vergroot als functie van de stikstof concentratie in het sample, van 10^{-5} cm^2/Vs in Ta_2O_5 tot 10^{-2} cm^2/Vs in β-TaON en in mixed TaON-Ta_3N_5 tot 10^{-1} cm^2/Vs in Ta_3N_5. Terwijl de elektronen/gaten mobiliteit van β-TaON en Ta_3N_5 vergelijkbaar is met dat van $BiVO_4$, de waarschijnlijke levensduur, in de grote van milliseconden, is vergelijkbaar met dat van kristallijn silicium. Dit zou het superieur maken (met drie orders van sterkte) ten opzichte van de andere Ta_3N_5 waarover wordt gerapporteerd is in de literatuur, net als ten opzichte van de andere meest belovende op metal oxide gebaseerde halfgeleiders ($BiVO_4$, Fe_2O_3, WO_3, Cu_2O) die worden gebruik in de onderzoeken naar foto-elektrochemische (PEC) water splitsing. Bovendien suggereren deze resultaten dat de elektronen/gaten diffusie lengte in de orde van tientallen μm moet zijn, veel langer dan de optische absorptie van licht. Echter men moet deze resultaten voorzichtig interpreteren gezien de mogelijkheid tot de elektronen/gaten gevangen kunnen worden en kunnen ontsnappen uit ondiepe (potentiaal) toestanden. Desondanks bevestigen de extreem langlevende TRMC signalen voor de stiochiometrische β-TaON en Ta_3N_5, vergeleken met de gemixte TaON/Ta_3N_5 samples, de noodzaak voor het gebruik van materialen bestaande uit een enkelvoudige fase voor het bereiken van een hoge energie omzetting efficiëntie binnen deze veelbelovende fotoanode materialen.

Voor (foto-)elektrochemische metingen, de halfgeleiders moeten worden geplaatst of ingroeien op een geleidend substraat. De ontwikkeling van betrouwbare methoden om een efficiënte dunne laag TaON and Ta_3N_5 fotoanodes te vormen, werd verhinderd door de onvermijdelijke groei van ongewenste fases aan het grensvlak in het vormingsproces. In Hoofdstuk 4.2 laten we zien dat het groeien van Ta_3N_5 op Pt-kwarts de puurheid 'purity' veranderd van de ze laag, vergeleken met de groei op kwarts. We laten ook voor de eerste keer zien dat het gebruik van een atomische-laag aangebrachte TiO_2 en Al_2O_3 deklagen voor Ta_3N_5. De aanwezigheid van de Al_2O_3 liggende laag tussen de Ta_3N_5 en de gekozen Ni-

$Ni(OH)_2$-$Co(OH)_2$-CoP_i katalysator vergroten de ladings-extractie snelheid in tweevoud vergeleken met de Ta_3N_5-katalysator en met de Ta_3N_5-TiO_2-katalysator configuraties. Als een resultaat de veelbelovende 5.5 $mAcm^{-2}$ bij 1.6 V vs. RHE was bereikt met een 580 nm Ta_3N_5 fotoanode met Al_2O_3-Ni-$Ni(OH)_2$-$Co(OH)_2$-CoP_i oppervlakte multilagen. Als we dit zelfde 'recept' toepassen op TaON, meten we een 'fotostroom' van maar 0.2 $mAcm^{-2}$ at 1.23 V vs. RHE. We hypothetiseren dat dit verschil werd veroorzaakt door de lagere tolerantie naar secundaire fases van TaON vergeleken met Ta_3N_5.

In conclusie laat ons PEC onderzoek zien dat 1) de materialen beschouwend, de nadelen kunnen worden overkomen door geoptimaliseerde zogenoemde semiconductor-catalyst junctions, via nanostructurering en via band gap engineering, 2) de geleider-halfgeleider en halfgeleider-katalysator-elektrolyt interfaces zijn hoofdrolspelers in de prestaties en de duur van the device/het apparaat en 3) de ideale halfgeleiders/katalysatoren combinaties moeten nog gevonden worden.

Vanuit een apparatuur perspectief, de intrinsieke beperkingen van de fotoelectrochemische benadering om water te splitsen zijn: i) complicaties die voorkomen uit de halfgeleider-katalysator-elektrolyt interfaces, ii) de verwachte vermindering in fotovoltage onder verminderde lichtintensiteit en iii) het feit dat de fotoelektrochemische H_2 productie concurreert met de solar PV om hetzelfde stuk beschikbare oppervlakte. Als een mogelijke manier om de bovenstaande punten te overwinnen, hebben we in Hoofdstuk 5 een 'proof of principle' device/apparatuur ontwikkeld die het mogelijk maakt om zonne-energie om te zetten in dan wel elektriciteit, dan wel waterstof, afhankelijk van de intensiteit van de straling. Bovendien zijn de beperkingen aan het grensvlak omzeild in het voorgestelde geïntegreerde apparaat, waar de vaste-stof processen (i.e. licht absorptie en lading scheiding) afgezonderd zijn van de elektrokatalyserende processen en van de elektrische/chemische opslag. Vergeleken met een enkele foto-elektrochemische benadering heeft deze benadering vele voordelen, als in a) mogelijkheid van elektrische productie en opslag, en b) verbeterde verenigbaarheid met de dagelijkse en de seizoen variaties op licht intensiteit.

Het apparaat bestaat uit een PV component, welke geïntegreerd zit in een gecombineerde batterij-elektrolysecel. De batterij/elektrolysecel bestaat uit een Pd bedekte hydride-vormende $Mg_{0.8}Ti_{0.2}$ kathode en een dikke $Ni(OH)_2$ anode, wat wordt voorzien bij ofwel een triple junction a-Si–nc-Si–nc-Si met een OCV of 1.8 V onder 1 zon, of een quadruple junction

a-Si–a-Si–nc-Si–nc-Si met een OCV of 2.3 V onder 1 zon. Het werkingsprincipe is dat de opslag elektrode oplaad bij een lagere spanning dan nodig is voor de waterelektrolyze. De accu bevat a ΔV of 1.17 V en de elektrolysecel werkt met een ΔV van 1.48 V. Dit experiment laat zien dat met een lage licht intensiteit (10 mW/cm^2), de OCV van de PV is verminderd van ~1.8 V tot ~1.4 V. Vanaf deze verlaagde spanning kunnen we geen significante stroom meer detecteren. Dit suggereert dat zowel het opladen van de accu, als het splitsen van water niet meer kan continueren, door de overpotentialen. Daarom is de elektriciteit generatie het meest efficiënte proces. Bij middelmatig licht intensiteit (50 mW/cm^2) en meer, het opladen van de accu wordt een hogere prioriteit dan die van de productie van H_2. Wanneer de accu volledig opgeladen is, vind er waterstof vorming plaats. Met een fluctuerende toegepaste potentialen, de elektriciteit is deels opgeslagen in de vorm van elektrische energie in de accu en deels in de chemische vorm als waterstof. Als het zonnepaneel met een lagere OCV wordt gebruikt is de prestatie van de batterij/elektrolysecel vergelijkbaar met dat van de elektrolysecel bij alle licht intensiteiten, tot > 5 $mAcm^{-2}$ zonder bias.

In dit prototype device, de op aarde overvloedige materialen zoals Si (zonnecel), Mg, Ti en Ni (elektrochemische cel) zijn de belangrijkste elementen. Bovendien is de productie van Si zonnepanelen een goed ontwikkeld industrieel proces en de elektroden worden bevestigd met goedkope technieken zoals Physical Vapor Deposition (PVD) en elektrodedepositie. De nadelen, 1) triple or quadruple junction zonnecellen zijn nodig om de vereiste potentiaal voor de elektrochemische reacties te behalen, 2) de capaciteit van de gekozen Ni electrode is beperkt en 3) Pd, a zeldzaam-aarde element, is gebruikt als een katalysator voor de Mg-gebaseerde elektrode. Als laatste is de cyclische stabiliteit nog niet getest. Alle bovenstaande argumenten in acht nemend geloven wij dat we het concept device zoals voorgesteld in deze thesis, na optimalisatie, de mogelijkheid bied tot het maken van een PV module en batterij electrode die precies aansluit op de end-users nodig gebruikt. We zijn in afwachting van het octrooi op dit apparaat.

Acknowledgements

This PhD started with an intercontinental flight San Francisco-Amsterdam in the summer of 2011. I have been invited by Roel van de Krol for the second round of the interview process. During the dinner which followed the interview, I received my job offer and four and a half fantastic years began. I owe big thanks to Roel and Fatwa since I gained a great deal of my knowledge about this fascinating topic called *photoelectrochemical (PEC) water splitting*, during my first year. Fatwa's patience in dealing with my hundreds of questions has been remarkable. Roel's support, deep knowledge, his precise and punctual comments in all my manuscripts, thesis included, have been of enormous help and were much appreciated. During my second year, both Roel and Fatwa continued their academic career in Berlin. All of a sudden, I became the most experienced person working on the topic. The MECS group became my new family at work, providing me with a friendly environment and marvelous critical audience of colleagues and students. I continued under the supervision of Bernard Dam, of whom I will speak later. Among others in the group, I want to thank Hans Geerlings and Wim Haije for offering continuous scientific inputs and for the professional stimula. A special thanks goes to Herman. My research would have never been as quick without his fantastic technical and research support, as well as enjoyable and fun personality. And Joost of course, thanks to him I could operate a great fraction of the in-house setups, which I needed for my research. I owe thanks to the secretary of the section, Heleen, for her infinite kindness and precious work behind the scenes. I thank also Christiaan for kindly proof-reading my Samenvatting. My office, with Bartek and Digda, has been perhaps the most agreeable place in the world to embark such a project. With them I had plenty of insightful scientific discussions, and spent some of the most hilarious and funny moments of the past 4 years. Next to these people, I could have not completed this PhD successfully without the invaluable supervision of Bernard Dam, head of the MECS group. I owe thanks to him for his always constructive critics, his unceasing search for improvements, the reliability, the guidance and his timely and punctual feedback. Equally precious to me has been his support in overcoming the difficult moments (also personal) I encountered during my path. As a bridge between work and private life, I owe special thanks to Aris, and Fabio, and then all the great friends that accompanyied me in my free time. I cannot conclude without thanking Anja, my girlfriend, for her infinite patience and cheer of course, and for her knowledge of, and care for my soul. Ultimo ma non ultimo, il mio debito di riconoscenza più grande è per la mia famiglia. Solo con il vostro immenso affetto e supporto morale nonostante la distanza, sono riuscito a perseguire e realizzare i miei sogni.

Curriculum Vitae

Moreno de Respinis was born on 3 May 1983 in Milano, Italy. His dedication to sustainable development started with an active and devoted membership in an Italian environmentalist association since 2004. He graduated from the University of Milan in 2008 with a degree of Bachelor of Science, majoring in Physics. His passion for sustainability influenced his study choices and in 2011 he completed a M.Sc. in Sustainable Energy with a study line in Hydrogen and Fuel Cells, from the Technical University of Denmark (DTU). He continued his interest on the development of new renewable energy technologies, by undertaking a research project on Solar Fuels at the Lawrence Berkeley National Laboratories (LBNL), in Berkeley, CA, USA. Thereafter, he pursued a Ph.D. research on the conversion and storage of solar energy at the Delft University of Technology (TUDelft), The Netherlands. Following his eagerness to introduce sustainable energy technologies in the society, starting from April 2016 he is working as a postdoctoral researcher on "Co-Evolution of Smart Energy Products and Services (CESEPS)" in the ERA-Net Smart Grids Plus framework[4] of the Horizon2020 program of the European Commission. This project is carried out in the group Advanced Research on urban Innovations in Sustainability and Energy (ARISE) lead by prof. dr. Angèle Reinders, Department of Design, Production and Management, University of Twente.

[4] http://arisetogether.nl/2016/02/era-net-smart-grids-plus-project-approved/

List of Publications

1) M. de Respinis, W.A. Smith, B. Dam, Intermittent Solar-Energy Conversion: Modular Electricity-Battery-Electrolyzer Device, *in preparation*

2) M. Victoria, W.A. Smith, J.F. Jacobs, D.A. Vermaas, M. de Respinis, I.A. Digdaya, E.J.R. Sudhölter, B. Dam, A technologically and economically feasible solar-driven water-splitting device for hydrogen production, *submitted*

3) S. Emin, M. de Respinis, T. Mavric, B. Dam, M. Valant, W. A. Smith Photoelectrochemical water splitting with porous α-Fe2O3 thin films prepared from Fe/Fe-oxide nanoparticles, *Applied Catalysis A, General.* DOI: http://dx.doi.org/10.1016/j.apcata.2016.06.007

4) M. de Respinis, M. Fravventura, F.F. Abdi, H. Schreuders, T.J. Savenije, W.A. Smith, B. Dam, R. van de Krol, Oxynitrogenography: Controlled Synthesis of Single-Phase Tantalum Oxynitride Photoabsorbers *Chem. Mater.*, 2015, 27 (20), pp 7091–7099

5) M. de Respinis, K. S. Joya, H. J. M. De Groot, F. D'Souza, W. A. Smith, R. van de Krol, B. Dam, Solar Water Splitting Combining a BiVO4 Light Absorber with a Ru-based Molecular Co-catalyst, *J. Phys. Chem. C* 2015, 119, 7275-7281.

6) S. Emin, M. de Respinis, M. Fanetti, W. Smith, M. Valant, B. Dam, A simple route for preparation of textured WO3 thin films from colloidal W nanoparticles and their photoelectrochemical water splitting properties, *Appl. Cat. B*, 2014, 166, 406-412

7) P.A. Szilagyi, I. Weinrauch, H. Oh, M. Hirscher, J. Alcañiz, P. Serra-Crespo, M. de Respinis, B.J. Trzesniewski, F. Kapteijn, H. Geerlings, J. Gascon, B. Dam. A. Grzech, R. van de Krol, Interplay of Linker Functionalization and Hydrogen Adsorption in the Metal–Organic Framework MIL-101, *J. Phys. Chem. C*, 2014, 118 (34), 19572–19579

8) M. Zhang, M. de Respinis, H.M. Frei; Time-resolved observations of water oxidation intermediates on a cobalt oxide nanoparticle catalyst, *Nature Chemistry 6, 362–367 (2014)*

9) A.W. Maijenburg, A.N. Hattori, M. De Respinis, C.M. McShane, K.-S. Choi, B. Dam, H. Tanaka, J.E. ten Elshof; Ni and p-Cu_2O nanocubes with a small size distribution by templated electrodeposition and their characterization by photocurrent measurement, *ACS Appl. Mater. Interfaces*, 2013, 5 (21), 10938–10945

10) M. de Respinis, G. De Temmerman, I. Tanyeli, M.C.M. van de Sanden, R.P. Doerner, M.J. Baldwin, R. van de Krol, Efficient Plasma-Route to Nanostructure Materials: Case Study on m-WO_3 for Solar Water Splitting *ACS Appl. Mater. Interfaces*, 2013, 5 (15), 7621–7625

11) H. Wang, I. Thomann, A. J. Forman, Y. Li, M. Sunkara, M. de Respinis, Hematite (α-Fe_2O_3) as a Photoelectrode for Photoelectrochemical Hydrogen Production, *PEC white papers*, DOE 2013 (http://www1.eere.energy.gov/hydrogenandfuelcells/pdfs/pec_white_papers.pdf)

Patent application

M. de Respinis, W.A. Smith, B. Dam, Intermittent Solar-Energy Conversion: Modular Electricity-Battery-Electrolyzer Device, *patent filed / 2015P00052 NL - application number: 2016294*

This thesis is printed on Cyclus paper. Cyclus paper is made exclusively from 100% recycled fibre, it has natural shade without OBA's, and it is manufactured according to the most stringent environmental certifications.